Delft University of Technology

Master Thesis

Modeling of dynamic ductile fracture propagation using cohesive zone elements

Author:
O.R. van der Meulen BSc.

Supervisors:
Dr. ir. J. Mediavilla Varas
Dr. ir. J. Weerheijm
Prof. Dr. ir. L.J. Sluys
Dr. ing. A. Romeijn

April 22, 2009

Modeling of dynamic ductile fracture propagation using cohesive zone elements

A thesis submitted in partial fulfilment of the requirements for attaining the degree of Master of Science at the Delft University of Technology. Research performed at, and under supervision of TNO Defense, Security and Safety Rijswijk

Oege Ronald van der Meulen
February 2009

In memory of my friend,
Hendrik Sinnema

Acknowledgment

The author gratefully acknowledges the contribution of the EU Vulcan project and the Dutch Delft Cluster project “Bijzondere Belastingen” (CT01.21), for providing vital test data. Support from my supervisor, Dr. ir. J. Mediavilla Varas was invaluable to the research performed. Special thanks go to all the people at TNO Defence, Security and Safety for providing a enjoyable work environment and practical support.

Abstract

An important property shared by rupturing pressure vessels and gas pipe lines alike, is the fact that the extent of resulting damage is a function of the rate of fracture. While this dependence is well known, accurate calculation methods for this are not available for all geometries and materials.

In an effort to derive an improved fracture velocity estimate in ductile materials, a numerical cohesive zone approach is followed; a layer of interface elements describing a possible fracture path and relating a fracture opening to a resulting traction according to a specific constitutive formulation and cohesive properties. These cohesive properties were determined for aluminium 2024 T3 and simulations were performed to research the methods potential to accurately predict the rate of fracture of a number of actual experiments on centre cracked panels and pressurized barrels.

A considerable difference was found between the speed of fracture as observed in experiments and in the simulations. A possible explanation for this discrepancy can be an increased amount of energy dissipation in the fracture process zone at higher fracture rates. This increase originates from a rate dependence of the cohesive properties. To explore the concept of rate dependence, a new type of rate dependent cohesive element material was created for use within the finite element package LS-DYNA using an adapted visco-plastic Perzyna type formulation.

The new cohesive zone material was calibrated and tested against a number of experiments on fracture in pressurized thin walled aluminium cylinders. These showed a greatly improved correlation between the experiments and the simulation as compared to the non rate sensitive approach. The new model was then used to predict the effect of explosives in a pressurized barrel with a pre-existing defect. The simulations were used to establish the explosive quantity needed to induce complete failure in actual experiments performed.

Contents

Nomenclature

The lists below give a short definition of the symbols and abbreviations used in this thesis. The abbreviations and symbols are fully explained when they are first used.

Abbreviations

CVN	Charpy V-notch data points
TSL	Traction separation law

Latin upper case symbols

$A_{\mathrm{N.TSL}}$	Area under the normalized TSL	[-]
$A_{e,\mathrm{max}}$	Area of largest surface 8 noded solid	[mm^2]
C_{pen}	Penalty term for mode I compression	[-]
C_{ts}	Timestep factor in artificial stiffness scheme	[-]
C_{v}	Specific heat	[N/mm^2/K]
E	Young's modulus	[N/mm^2]
E_{shear}	Shear modulus modulus	[N/mm^2]
E_{bulk}	Bulk modulus	[N/mm^2]
G	Critical energy release rate	[N/mm]
G_{1c}	Critical energy release rate at initiation in mode I for plane strain	[N/mm]
H	Triaxiality	[-]
J	Critical energy release rate	[N/mm]
J_{1c}	Critical energy release rate at initiation in mode I for plane strain	[N/mm]
J_e	Elastic part of the mode I J integral	[N/mm]
J_{pl}	Plastic part of the mode I J integral	[N/mm]
K_1	Loading stiffness	[N/mm^3]
K_2	Unloading stiffness, or damage stiffness	[N/mm^3]
K_{1c}	plane strain Critical stress intensity at initiation	[N/mm$^2 m^{1/2}$]
K_c	plane stress Critical stress intensity	[N/mm$^2 m^{1/2}$]
K_{ub}	Upper bound to element stiffness	[N/mm^3]
$\mathbb{N}$	Set containing all natural numbers $\{0, 1, 2, \cdots\}$	
M	Mass matrix	[N/mm^3]
N_{pz}	Exponent (Perzyna parameter)	[-]
$R_{\mathbf{coh}}$	Global cohesive force vector (cz elements)	[N]
$R_{\mathbf{ext}}$	External force vector	[N]
$R_{\mathbf{int}}$	Global internal force vector (bulk elements)	[N]

S	Maximum static traction in mode II / III	[N/mm^2]
T	Maximum static traction in mode I	[N/mm^2]
T^*	Non dimensional temperature, JC model	[-]
U_a	Change in elastic energy	[N mm]
U_P	Change in potential energy	[N mm]
U_γ	Change in surface energy	[N mm]
U_0	Total energy before fracture initiation	[N mm]
U_{ext}	Change in externally performed work	[N mm]
V_e	Volume of finite element	[mm^3]
$\mathbb{Z}$	Set containing all integers $\{\cdots,-2,-1,0,1,2,\cdots\}$	

Latin lower case symbols

c	Speed of fracture propagation	[mm/ms] [m/s]
c_0	Speed of sound	[mm/ms] [m/s]
c_{r}	Speed of Rayleigh surface wave	[mm/ms] [m/s]
c_{s}	Speed of surface waves in shear	[mm/ms] [m/s]
d	Damage variable	[-]
h_{pz}	Work hardening (Perzyna parameter)	[-]
l_e	Smallest dimension of an element	[mm]
q	Work hardening	[-]
q_{I}	Work hardening in mode I	[-]
q_{II}	Work hardening in mode II	[-]
q_{III}	Work hardening in mode III	[-]
$\hat{s}$	Mode II/III traction	[N/mm^2]
$\hat{t}$	Mode I traction	[N/mm^2]
$\hat{t}_{\text{dam}}$	Traction at onset of damage	[N/mm^2]
$\hat{t}_{\text{trial}}$	Trial traction distribution before yield surface check	[N/mm^2]
$\hat{t}_{\mathrm{I}}$	Traction in mode I	[N/mm^2]
$\hat{t}_{\mathrm{II}}$	Traction in mode II	[N/mm^2]
$\hat{t}_{\mathrm{III}}$	Traction in mode III	[N/mm^2]
t_{cz}	Thickness of the cohesive element	[mm]
t_{eq}	Equivalent traction according to some yield criterion model	[N/mm^2]
t_v	Equivalent traction according to von Mises model	[N/mm^2]
u	Displacement	[mm]
$\dot{u}$	First partial derivative to time of u	[mm]
$\ddot{u}$	Second partial derivative to time of u	[mm]
$\dot{u}_{\text{frac}}$	Rate of fracture propagation	[mm/ms] [m/s]

Greek upper case symbols

Γ	Cohesive energy	
Γ_{D}	Dirichlet boundary condition	
Γ_{N}	Neumann boundary condition	
Γ_{N}	Cohesive energy in mode I (normal)	[N mm]
Γ_{T}	Cohesive energy in mode II / III (tangential)	[N mm]

Greek lower case symbols

γ_e	Surface energy per unit area of fracture	[N/mm]
γ_p	plastic dissipation per unit area of fracture	[N/mm]
δ	Cohesive zone opening or jump	[mm]
δ_0	Failure opening in TSL	[mm]
δ_1	End of elastic opening in TSL	[mm]
δ_2	End of static cohesive opening in TSL	[mm]
$\delta_{0,\mathrm{N}}$	Maximum opening in mode I	[mm]
$\delta_{0,\mathrm{T}}$	Maximum opening in mode II / III	[mm]
δ_{eq}	Instantaneous combined opening	[mm]
δ_{I}	Opening in mode I	[mm]
δ_{II}	Opening in mode II	[mm]
δ_{III}	Opening in mode III	[mm]
$\hat{\delta}$	Integrated tangential opening	[mm]
ε	Strain	[-]
ε_{el}	Elastic portion of the strain	[-]
ε_{vp}	Plastic portion of the strain	[-]
ε_{y}	Yield strain	[-]
$\varepsilon_{\mathrm{y,dyn}}$	Dynamic (increased) yield strain, CS model	[-]
$\dot{\varepsilon}^*$	Non dimensional strain rate	[ms^{-1}]
η	Apparent fluidity (Perzyna parameter)	[N ms/mm^2]
λ_0	Normalized failure opening in TSL	[-]
λ_1	Normalized end of elastic opening in TSL	[-]
λ_2	Normalized end of static cohesive opening in TSL	[-]
$\lambda_{\mathbf{dam}}$	Normalized opening at damage onset	[-]
ν	Poisson's ratio	[-]
ρ	Material density	[N/mm^3]
σ	Stress	[N/mm^2]
σ_{H}	Hoop stress	[N/mm^2]
σ_{vm}	Equivalent von Mises stress	[N/mm^2]
σ_y	Yield stress	[N/mm^2]
σ_{ult}	Ultimate stress	[N/mm^2]

Chapter 1

Introduction

The subject of this thesis is: “Modeling of dynamic ductile fracture propagation using cohesive zone elements”. In this introduction, the relevancy of the subject is first discussed in certain areas of application in section 1.1. Section 1.2 then introduces the concept of dynamic-ductile fracture. The last section of the introductory chapter, section 1.3 discusses theoretical bounds to the speed of fracture, and fracture rates as reported in literature.

1.1 Industrial relevance

This research aims to find an improved calculation method for the rate of fracture. This section illustrates the relevancy of knowledge of this quantity in specific fields of engineering.

1.1.1 bleve

The original motivation for starting the research that led to this report is an investigation into the occurrence of *Bleves* in road going pressure vessels at varied degrees of spacial confinement [1]. The term *bleve* is short for *Boiling Liquid Expanding Vapour Explosion* and is not uniquely defined throughout the literature. A bleve for the purpose of this report is defined as:

> “. . . the explosive evaporation process as a consequence of the rupture of a pressure vessel containing a liquefied gas.” [1]

Oxidation of the gas is not considered part of the bleve effect and lies outside the scope of this report. The gas is kept in its liquid state by means of pressurization. The pressure needed is equal to the vapour pressure of the gas at its specific temperature. A dramatic loss of containment will cause a sudden drop of pressure in the pressure vessel and the liquid will boil. The necessary energy for the phase change is extracted from the remaining liquid that is thereby cooled. This process will continue until the remaining liquid is cooled enough for the vapour pressure to be equal to the atmospheric pressure.

For an explosive boiling to take place, the liquid needs to be in a super heated state. The precise temperature limit for this state is a matter of ongoing research and debate, but in super heated liquids, the liquid to gas phase change takes place throughout the liquid through homogeneous nucleation. In this super heated state, the phase change is fast and explosive. This type of explosive evaporation is called flash-evaporation and is the driving force behind the bleve.

When a pressure vessel containing a superheated liquid ruptures, the strength of the resulting pressure wave depends mainly on two factors, the first being the gas release rate. As a superheated liquid is able to transform to its gas state almost instantaneous, the pressure release rate is proportional to the size of the opening in the pressure vessel, which is in turn a function of fracture velocity. The second factor is the level of confinement. The gasses generated from a tanker rupturing in an open half space are better able to escape then when the same tank was rupturing inside a tunnel. This impediment to the gas' escape greatly amplifies the power of the pressure wave and the resulting damage.

Because tunnels are confined spaces by definition, any effort in preventing catastrophic explosions due to bleves in tunnels must be focussed on the gas release rate and thus the rate of fracture. "Pressure release times in the order of 0.5 - 1 seconds are considered ideal" [2]. This translates into fracture propagation rates in the order of 10 - 20 $\frac{m}{s}$. As will be pointed out in section 1.3, speeds observed and calculated, lie well above these values.

1.1.2 Failure of aircraft fuselage

Incidental and intentional pressure hull failure in aeroplanes is another subject where knowing the mechanics of dynamic fracture is important. Designing aircrafts such that fracture can be contained or stopped is obviously important, yet little experimental data on fracture in tests and accidents is available due to security considerations [3]. Publicly available design methods and data do not cover the dynamic fracture behaviour of the aircraft's materials. The EU sponsored Vulcan project aims to increase knowledge in this area. Figure 1.1b shows the results of a test with an internal explosive in a Boeing 747 series aeroplane.

Figure 1.1a shows an example of ductile fracture in an aeroplane fuselage. Although the underlying cause of the accident was fatigue, The resulting continued fracture was dynamic. The fracture was contained by the frame of the aircraft riveted to the fracturing skin, and The aeroplane remained air worthy. Dynamic fracture in aeroplanes may also be triggered by impact from missiles and disintegrating aero-engines [4, 5].

(a) Continued fracture after fatigue

(b) Internal explosion in a Boeing 747

Figure 1.1: Fracture in aeroplanes

1.1.3 Failure in pressurised gas pipes

Foreseen growing energy needs in Europe and the rest of the world are pushing for the exploitation of ever more remote gas fields. Increased volume, distance and progressing technology have made larger diameter, high pressure, pipelines economically attractive. The high strength steel varieties needed to produce these new generation of pipelines API grade X100[1] and up exist, but resistance to fracture is remaining an issue. With pressurised gas pipes, there exists the potential for catastrophic continued fracture to progress unimpeded for great distances. Figures 1.2a and 1.2b illustrate the dramatic consequences of such an event.

To avoid problems with progressive failure in pipes, it is important to make sure that any fracture in the pipe will run slower than the depressurisation front speed of the gas transported within the pipe. If this is the case, the gas pressure will drop ahead of the fracture, releaving the hoop stress on the pipe and slowing the fracture down. As the gas depresurisation rate is unaffected, the fracture will arrest. To design according to this criterion, the industry uses several empirical formulae to predict the fracture rate as a function of internal pressure and making sure this is below the gas depressurisation front speed for the entire design pressure range. The empirical nature of these industry formulae causes them to have validity issues at higher steel grades than used to derive them. Rate dependent cohesive zone models provide an alternative solution strategy to the question of fracture speed and can be used in tweaking the section geometry to assure arrest.

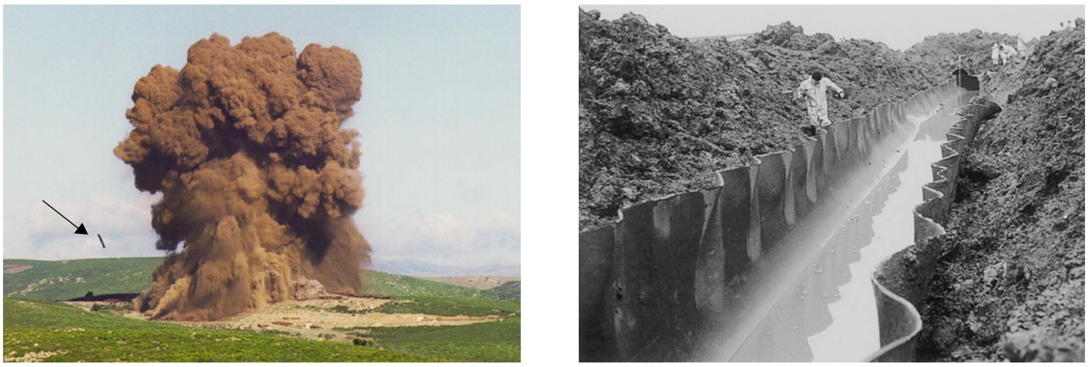

(a) X100 pipe fracturing

(b) Fractured X70 pipe close-up

Figure 1.2: Fracture in pipes

[1]API grades are defined by the American petroleum institute. This is the grading system used throughout the pipe industry, appendix I lists the relevant properties.

1.2 Dynamic-ductile fracture

The question whether a fracture is to be considered dynamic cannot be answered without knowing the relevant scale. For example, at atomic levels, even a quasi-static fatigue fracture is a highly dynamic phenomenon. For the term to be discriminatory, the macroscopic scale needs to be implied; fracture velocities must be considerable compared to the stress wave velocity in the material. In dynamic fracture, inertia of the material plays a large role with kinetic energy levels comparable to the energy of fracture. The higher loading rates associated with dynamic fracture increase the strength and potentially the fracture behaviour. The plastic dissipation of energy leads to an increase of thermal energy that results in a temperature rise in the material that is not present in quasi-static fracture. This increase in temperature may lead to a thermal softening of the material.

Different mechanisms of fracture exist at a microscopic level. Brittle materials tend to fracture *intergranulary*, where the fracture follows the grain boundaries, or in *cleavage*, where the separation occurs along specific crystallographic planes, and through the grains. Ductile fracture is the mechanism associated with most metals at room temperature and usually involves the process known as void nucleation, growth and coalescence. The process starts when under the influence of increased strains, microscopic voids initiate at defects, inclusions and second phase particles (figures 1.3a and 1.3b). These voids grow as the strain continues to increase (figure 1.3c), until the strain is too large for the remaining ligaments between the voids and the material fractures completely in void coalescence (figure 1.3d).

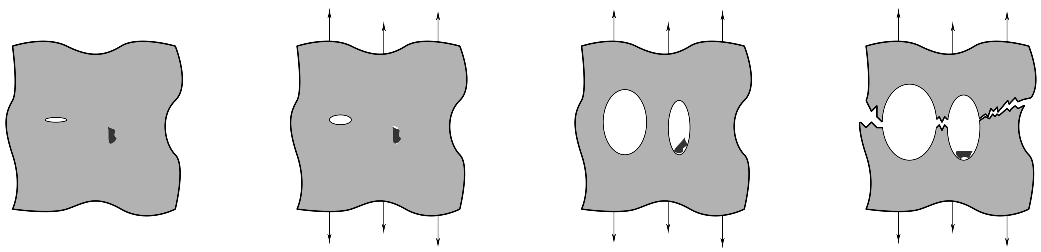

(a) Defects (b) Nucleation (c) expansion (d) Coalescence

Figure 1.3: Ductile fracture process

The ductile fracture process in characterised by a large amount of plastic deformation in the ligaments in between the voids and a high energy dissipation in fracture as compared to to brittle materials. A ductile fracture with a void nucleation, growth and coalescence mechanism can be easily detected in a post mortem examination of the fracture surface. The voids and ligaments form a dimpled surface as illustrated by the scanning electron microscope image of figure 1.4.

1.3 Fracture velocity

Analytical boundaries to the speed at which fracture may propagate exist and will be discussed are section 1.3.1. These are derived for brittle materials, but can be used as an upper bound for more ductile materials. The derived fracture speeds are overconservative however. Experimental

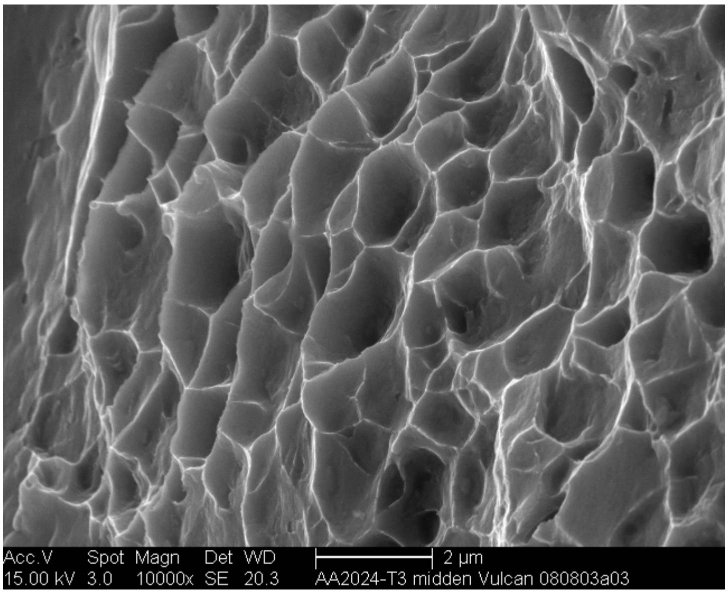

Figure 1.4: Ductile fracture surface

observations show substantially lower fracture speeds in practice, and this is discussed in paragraph 1.3.2.

1.3.1 Theoretical bounds to the rate of fracture

The rate of propagation of any fracture is generally accepted to be bounded by the speed of the surface stress waves in the fracturing medium; this is known as the Rayleigh speed c_{R} [6].

$$c_{\mathrm{R}} = c_s \, \frac{0.862 + 1.14\,\nu}{1 + \nu} \tag{1.1}$$

Where

$$c_s = \sqrt{\frac{E_{\mathrm{shear}}}{\rho}} \tag{1.2}$$

Where E_{shear} is the shear modulus[2]. E_{shear} can be obtained from the Young's modules E and the Poisson's ratio ν by

$$E_{\mathrm{shear}} = \frac{E}{2\,\left(1 + \nu\right)} \tag{1.3}$$

The Griffith model establishes an upper bound for the fracture velocity based on an energy balance consideration [7].

$$c = 0.38\,c_0 \left(1 - \frac{a_0}{a_i}\right) \tag{1.4}$$

Where c_0 denotes the speed of sound in the material, which is equal to

$$c_0 = \sqrt{\frac{E}{\rho}} \tag{1.5}$$

And a_i, a_0 being the instantaneous fracture length and the initial fracture length, respectively. It can be observed that the limit: $\lim_{a_i \to \infty} \left(1 - \frac{a_0}{a_i}\right) = 1$. And therefore for $a_i \gg a_0$, equation (1.4)

[2]For reasons of disambiguation, the more conventional G is not used in this report.

becomes

$$c = 0.38\ c_0 \tag{1.6}$$

A geometry dependent limit to the fracture propagation speed in pipes was derived by Kanninen [8]

$$c = \frac{c_0}{\sqrt[4]{3(1-\nu^2)}} \sqrt{\frac{t_h}{r}} \tag{1.7}$$

Where t_h denotes the pipe wall thickness, r is the pipe radius and c_0 is the speed of sound from equation 1.5. A similar expression by the same author was given in [9], in the form of

$$c = 0.75\ c_0 \sqrt{\frac{t_h}{r}} \tag{1.8}$$

To illustrate the difference in fracture rate as calculated by the different formulae, two different materials which are studied in this work are used in an example calculation, aluminium 2024 T3 and duplex steel DIN 1.4462 are compared. The relevant material properties are listed in table 1.1. The two formulae by Kanninen do not differ substantially from each other in outcome and only equation 1.7 is included. Because the formula is geometry dependent, an example geometry must be assumed. Two example geometries were chosen with dimensions equal to those of the *Vulcan barrel test* introduced in section 3.2 and a representative road going pressure vessel for the Dutch motorways as identified in [10]. These dimensions are listed in table 1.2. The result of these calculations are listed in table 1.3.

Table 1.3 shows a considerable difference between the upper bound fracture rates and the the predictions of the Kanninen formula. Equation 1.7 is somewhat empirical in nature since it is based on a simple model calibrated with test results. The range of validity is not indicated, but it is typically used for steel gas pipes and nuclear reactor design, where the ratio $\frac{t_h}{r}$ is in the range $\frac{1}{30}$ - $\frac{1}{60}$, considerably lower than the value of $\frac{1}{600}$ for the barrel tests. Equation 1.7 and 1.8 cannot hold for arbitrarily high $\frac{t_h}{r}$ ratios; this would imply that uncurved plates can never fracture. Whether the "barrel" geometry falls within the range of validity is doubtful as it does not resemble the typical geometry the formula is used for.

Material	Grade	ρ $\left(\frac{kg}{m^3}\right)$	E $\left(\frac{N}{mm^2}\right)$	E_{shear} $\left(\frac{N}{mm^2}\right)$	ν -
Aluminium	2024 T3	$2.780 \cdot 10^3$	$7.30 \cdot 10^4$	$2.74 \cdot 10^4$	0.33
Duplex steel	1.4462	$7.8 \cdot 10^3$	$2.1 \cdot 10^5$	$8.08 \cdot 10^4$	0.3

Table 1.1: Material properties

Geometry	Name	Radius r (mm)	Thickness t_h (mm)
1	"Barrel"	600	1.0
2	"Tanker"	875	6.5

Table 1.2: Two example geometries

Limit	Equation	Aluminium	Stainless steel
Rayleigh,	eq 1.1	2925	2980
Griffith,	eq 1.6	1947	1972
Kanninen "barrel",	eq 1.7	164	165
Kanninen "tanker",	eq 1.7	345	348

Table 1.3: Calculated velocities in m/s

1.3.2 Reported fracture propagation rates in literature

Hahn

Hahn et al.[11] collected available data from research done on gas pipelines in the nineteen sixties by A. McClure, G. Duffy and R. Eiber [12, 13, 14, 15, 16]. Two steel grades were tested, and all fracture speeds observed were found to be in the range $120 - 240$ m/s for X52 and 240 - 360 m/s for X60. Surprisingly, the internal pressure was found to have little effect and the only mayor difference lay in the fact that it took longer for the fracture to reach its maximum speed. Figure 1.5 shows this for X60. Wall thickness and radius were found to have little effect either, though the authors admitted there to be, to little data to be conclusive.

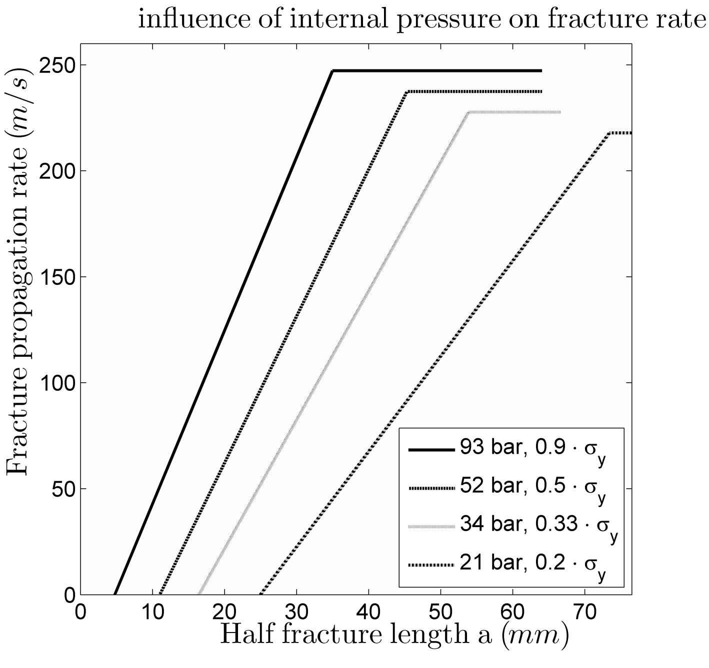

Figure 1.5: Effect of internal pressure on fracture speed

Murtagian

Murtagian et al.[17, 18] performed tests on two different X65 grades steel gas lines. Fracture speeds observed were consistent and ranged up to 660 m/s for $-40°C$, the highest temperature tested. The influence of the $\frac{t_h}{r}$ ratio was examined, and was found to be of influence, Figure 1.6 shows the observed maximum velocities in the test, together with the prediction from equation 1.8. And a linear scaling of equation 1.7. The limited number of tests, seems to be far too limited to warrant the usages of the derived linearly scaled formula in practice. Low temperatures cause materials like steel to fracture in a brittle fashion. Post mortem observations of the fracture surface revealed fracture to have been brittle at initiation but showed an increased amount of ductility as the fracture progressed. Charpy V-notch tests[3] were performed and showed the fracture toughness to be higher (321 $\frac{J}{cm^2}$)than the *ductile* fracture toughness of duplex steel DIN 1.4461 at room temperature (100 - 325 $\frac{J}{cm^2}$)[4].

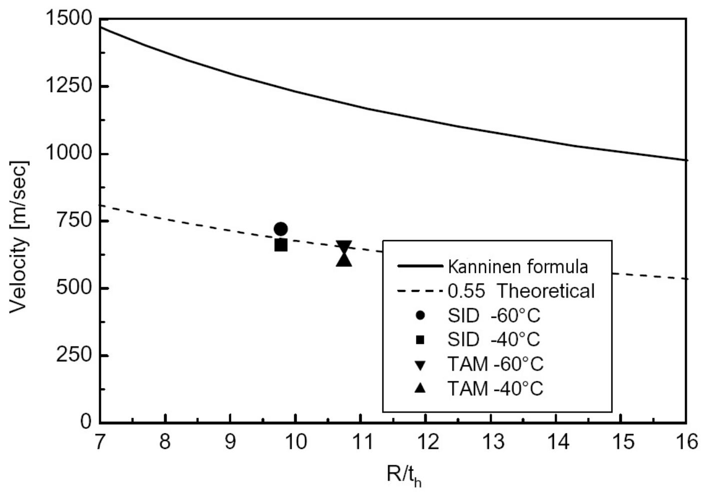

Figure 1.6: Observed fracture speed as a function of $\left(\frac{r}{t_h}\right)$ ratio. [18]

Brauer

Brauer et al.[19] investigated the effectiveness of fibre reinforcements as crack arrestors for steel pipelines of higher-strength steel grades such as X100. The pipe sections had an outer diameter of 914.4 mm and wall thickness of 20 mm. The full scale test showed a fracture velocity of 135 m/s at 600 mm from the the initial notch. It is not clear if this is a stable maximum, or an intermediate value from a fracture still gathering speed.

Demofonti

Demofont et al.[20] performed full scale tests on 3 X100 pipelines with discontinuous properties along their lengths to test fracture arrest formulae. Pipes had an outer diameter of 1422 mm and a 19.1 mm thick wall. Fracture speeds in the 200 - 300 m/s range were reported.

Medina-Velarde

Medina-Velarde et al.[4, 21] performed small scale tests on side cracked, 3 m thick pieces of aluminium 2014A T651, 300 mm long and 120 mm wide. The test setup and geometry resembled that of ASTM norm E1221[22]. Initiation was performed by a wedge shaped projectile fired into a pre machined side notch. Fracture speeds of up to 90 m/s were observed.

[3] See § F.2 for an explanation of the test.
[4] See figure 4.4

1.4 Objective

The main objective of the research presented is the construction of a finite element based solution to obtain estimates on the rate of fracture propagation in ductile materials. Such a tool will be able to predict the geometry dependent rate of fracture as a function of geometry independent material parameters. The solution pursued should incorporate a rate dependent level of energy dissipation in fracture to reflect phenomena observed in practice

1.5 Scope of this Study

The research presented is a part of two more extensive studies. The first being the Delft Cluster project “Bijzondere belastingen” , a study on the magnitude of road tankers carrying liquefied gasses exploding through a mechanism known as a bleve. The second study is concerned with the effects of explosions in aircrafts under the “European 6th Vulcan framework”. Two different materials were selected to be investigated to serve the requirements of both projects. The first material is an aluminium alloy common in commercial aircraft production known as aluminium 2024 with a T3 temper, the second is a duplex steel type used in road tanker construction designated by DIN 1.4462.

A series of tests was performed on these materials by TNO Defence, Security and Safety before the current research was started. Obtaining the necessary material properties is to be done using the results of these tests or from other research already performed. No additional testing is planned or considered part of the current research. Attention is focussed on the development of a new cohesive zone model incorporating the effects of opening rate dependence. The model is to be incorporated in the existing commercial finite element package LS-DYNA through an user defined materials option in the software.

The new user defined cohesive zone element model is to be used in FEM simulations of thin walled structures, therefore a implementation compatible with shell type elements is sought. Unfortunately this is not possible directly within the limitations of the custom material option in LS-DYNA; only eight noded solids are supported at the present. An appropriate interface between the shell type bulk material and the solids of the cohesive zone is required.

1.6 Outline of the thesis

Analytical calculations and experimental observations of the speed of fracture were already discussed in this chapter. Chapter 2 introduces the concept of cohesive zones and other numerical methods to model fracture. Tests performed at TNO are then discussed in chapter 3 and simulations thereof using FEM in chapter 4. A comparison of different available rate sensitive cohesive zone models is presented in chapter 5 as well as the subsequent development of the rate dependent cohesive zone element formulation sought. The model is tested for proper function and validated using parameters obtained from other experiments. In chapter 7 the main conclusions from the research are recapitulated and recommendations for further research and experiments are given.

Chapter 2

Cohesive zones

In this research, cohesive zones are used to model dynamic fracture in FEM simulations. Cohesive zones are first introduced in section 2.1, and described in more detail in section 2.2. Although originally developed as a analytical tool in fracture mechanics, the term cohesive zone shall apply hereafter only to the numerical implementation of the cohesive zone model into discrete cohesive zone elements for usage within finite element simulations, unless indicated otherwise.

2.1 Introduction into cohesive zones

The Cohesive zone model describes fracture by means of a separate interface layer of cohesive zone elements between the continuum elements of the bulk. When fracture progresses, a discontinuum in the continuum mesh appears. Cohesive zone elements are able to exert a traction between the surfaces of the fracture until a certain maximum displacement between the flanks, or maximum opening δ_0 is reached. Tractions are not possible after this point. The cohesive zones exert an equal but opposite traction on both sides of the discontinuity according to a opening dependent function $\hat{t} = f(\delta)$ or *Traction Separation Law* (TSL). Figure 2.1 shows a schematic drawing of this.

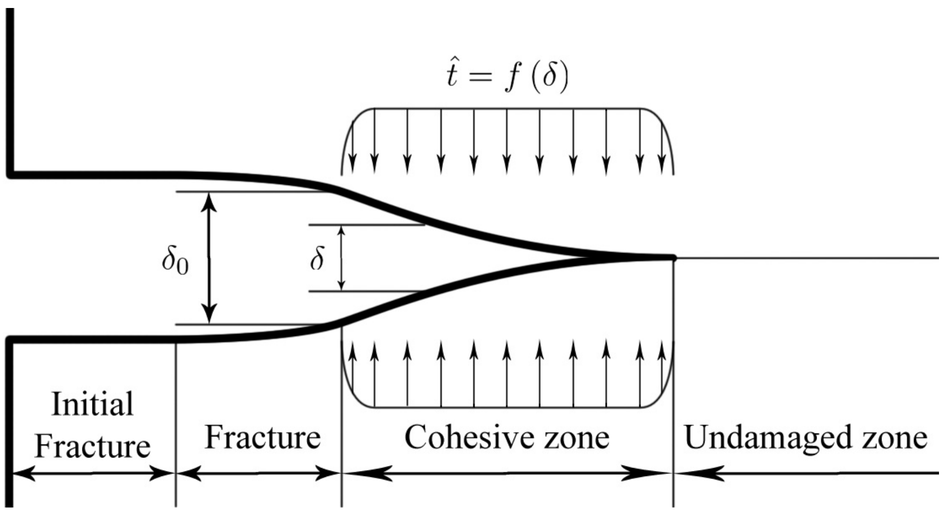

Figure 2.1: The cohesive zone fracture model (after [23])

The exact shape of the TSL may vary, but a typical TSL for ductile fracture as depicted figure 2.2, has three phases, a semi linear elastic start where tractions increase at an increased opening. This is followed by a more constant cohesive traction level caused by plastic yielding of the intervoidal ligaments. The last part describes a decreasing traction as the ligaments begin to fail. The increasing and decreasing slopes of the TSL are also present to avoid the numerical problems associated with a step function TSL approach. Cohesive zones were pioneered by

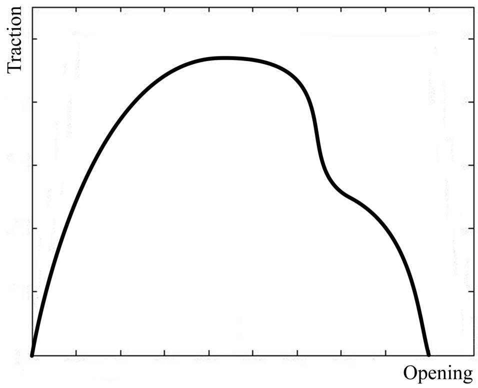

Figure 2.2: Example of a TSL

Dugdale [24] and Barenblatt [25]. Both authors considered a fracture to have a stress free actual length, and a fracture process zone ahead of the physical fracture tip. A cohesive stress was postulated to exist of some fixed quantity σ_0 (Dugdale, figure 2.3a) or a stress as a function of the distance to the fracture tip (Barenblatt, figure 2.3b). This allowed the elastic stress singularity in the crack tip to disappear. The model was generalized by [26] for uncracked bodies to allow for cohesive zones of an arbitrary size. In later years efforts [27, 28] were undertaken to formulate the cohesive laws for metals based on the Gurson constitutive equations [29] concerning growing and coalescing voids in ductile elasto-plastic mediums. Finite element simulations were improved further by comparison with experimental data [30, 31, 32]

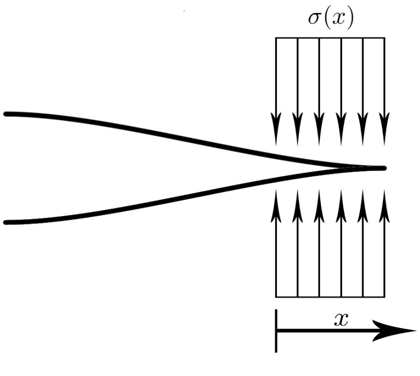

(a) Dugdale

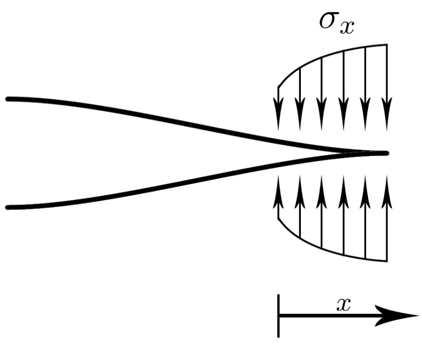

(b) Barenblatt

Figure 2.3: Cohesive zone formulation according to Barenblatt and Dugdale

The opening is defined as the increase in distance between the top and bottom face of the cohesive zone as can be seen in figure 2.4. Cohesive zones usually have a zero thickness. Cohesive zones allow failure according to a certain path. This may be done a priori by defining a failure path in a mesh, as is done throughout this report. If the fracture path is known in advance, cohesive zone interface elements may be placed along all element boundaries. Another possibility is the use of XFEM or a remeshing technique to allow an arbitrary fracture path to form.

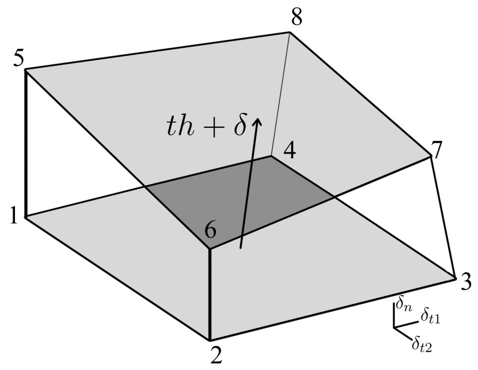

Figure 2.4: Cohesive zone opening definition

Cohesive zones may be defined with a certain normalized TSL, a maximum traction force T and a maximum opening δ_0. The energy dissipated when a cohesive energy is opened up until failure is known as the cohesive energy Γ, this is the integral of the area under the TSL. As can be observed form equation 2.1, T, δ_0 and Γ are not independent of one another. Depending on the author, one property is often not mentioned explicitly. In this report cohesive zones are characterized by their normalized TSL, a maximum traction and a cohesive energy only.

$$\Gamma = \int_0^{\delta} \mathrm{TSL}\left(\delta\right) = \int_0^{\delta_0} T \cdot \mathrm{TSL}_{\mathrm{norm.}}\left(\frac{\delta}{\delta_0}\right) \tag{2.1}$$

Figure 2.5 graphically defines the role of cohesive elements in between a continuum mesh and shows the differences between the constitutive equations for both element types.

2.2 Cohesive zone properties

2.2.1 Modes

In the field of fracture mechanics three different fracture modes are distinguished. Each possible fracture is thought of as being one of, or a combination of these modes. The discriminating feature of these modes is the orientation of a theoretical smooth fracture plane without shear lips in relationship to the applied stresses. A graphic description is given in figure 2.6.

Mode I operates normal to the failure plane and acts in the direction of the normal forces. Mode II and III are associated with in- and out-of-plane shear respectively. Cohesive zones in general and the newly developed cohesive zone model in particular have the possibility of setting different cohesive properties for mode I and mode II/III. The symbols used for the different modes of opening are listed in table 2.1.

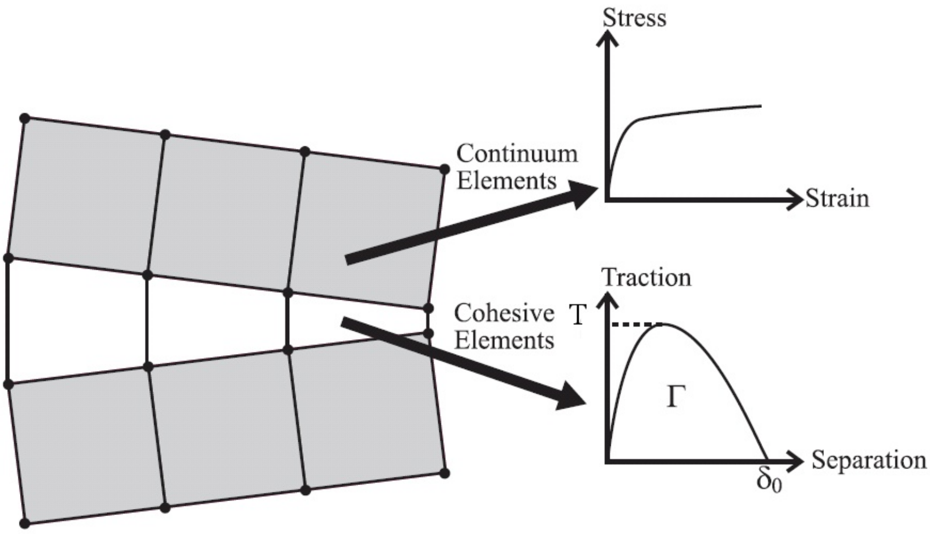

Figure 2.5: Cohesive elements in between an elasto-plasctic continuum element mesh [33]

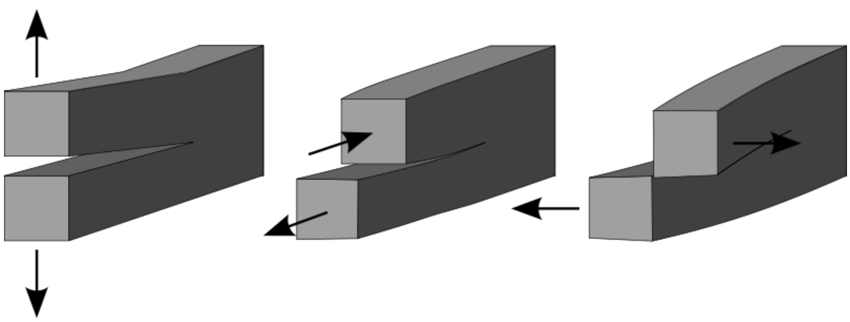

Figure 2.6: Three different modes of fracture defined

	Traction	Maximum traction	Opening	Maximum opening	Energy
mode I	$\hat{t}$	T	δ_{N}	$\delta_{0,\mathrm{N}}$	Γ_{N}
mode II/III	$\hat{s}$	S	δ_{T}	$\delta_{0,\mathrm{T}}$	Γ_{T}

Table 2.1: CZ parameter symbols for different modes

2.2.2 Cohesive energy

The area under the TSL is equal to the cohesive energy Γ, as can be seen in figure 2.7. The cohesive energy represents the amount of energy a cohesive zone can dissipate before it fails. It is equal to the fracture energy, and is therefore a measure of the material ductility. To obtain an (estimate) value for the cohesive energy a number of strategies exist. The cohesive energy is set equal to the value of the J-integral at start of failure in plane strain J_{1c} by many sources [34, 23, 35]. Obtaining J_{1c} requires expensive tests on fatigue pre-cracked specimens of the material at hand. These kind of test results are generally not available in literature. An alternative and less expensive approach is to use LEFM fracture toughness K_{1c} [1] and convert this to an estimate of the cohesive energy. This may be done through the known equation:

$$\Gamma = J_e \approx G_{1c} = \frac{{K_{1c}}^2}{E'} \tag{2.2}$$

Where

$$E' = \begin{cases} E & \text{, For plane stress} \\ \frac{E}{1-\nu^2} & \text{, For plane strain} \end{cases} \tag{2.3}$$

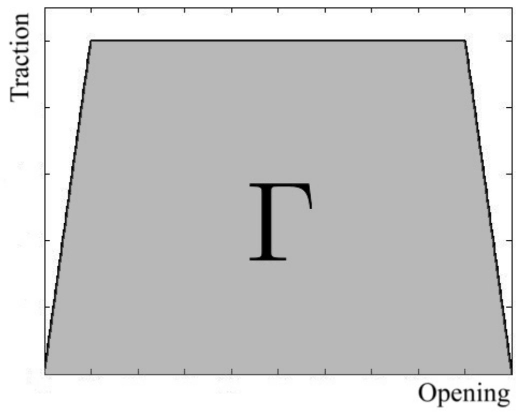

Figure 2.7: The cohesive energy of a TSL

Equation 2.2 is only accurate when there is little or no plastic energy dissipation in the fracture process zone. This is only the case in brittle materials and if used in ductile materials, an overestimation of the true cohesive energy in the order of 200 % too high [34] may be made. This is caused by taking into account the plastic dissipation of the bulk material twice; in the cohesive zone and into a plastic bulk material formulation.

Information on the fracture toughness K_{1c} is available as a tabulated value for many materials, but not all. Experimental derivation of this parameter is much less cumbersome and costly than J_{1c}. But the exclusion of plasticity makes this method less suitable for ductile materials. An even more abundantly available measure of fracture toughness is the Charpy V-notch test data. This value can be obtained through an inexpensive test, but the conversion to a cohesive energy is done by empirical formulae and the accuracy is even more questionable than for K_{1c}.

[1] *linear elastic fracture mechanics*, See appendix E

Another possibility is to use inverse modeling to derive a cohesive energy by simulating an experimental fracture test performed on a geometry resembling the geometry under investigation [36, 37]. An example of such a procedure is demonstrated in section 4.1. This procedure delivers a cohesive energy Γ, as well as a maximum traction T for a specific TSL. According to [37], Γ and T are not independent properties and need to be obtained together.

An overview of methods to derive an estimate of the cohesive energy from the fracture toughness K_{1c}, Charpy V-notch data and the Crack Tip Opening Displacement CTOD is given in appendix F.

2.2.3 Maximum traction and opening

The maximum traction of the TSL is denoted as T for mode I and S for mode II/III. The instantaneous tractions are given as $\hat{t}$ and $\hat{s}$, respectively. The ordinate values of the normalized TSL are multiplied with the maximum traction. The abscissa values need to be scaled as well to derive the TSL. For this purpose the maximum opening needs to be calculated. This is calculated through:

$$\delta_{0,\mathrm{N}} = \frac{\Gamma_{\mathrm{N}}}{T A_{\mathrm{N.TSL}}}, \qquad \text{For mode I} \tag{2.4}$$

$$\delta_{0,\mathrm{T}} = \frac{\Gamma_{\mathrm{T}}}{S A_{\mathrm{N.TSL}}}, \qquad \text{For mode II/III} \tag{2.5}$$

Where $\delta_{0,\mathrm{N}}$ and $\delta_{0,\mathrm{T}}$ are the maximum openings in mode I and mode II/III. $A_{\mathrm{N.TSL}}$ is the area under the normalized TSL or its "fullness". In cases where a trilinear TSL is used, the ordinate vale corresponding to the end of the increasing traction path is defined as δ_1, while the value at the start of the decreasing damage part is known as δ_2. Figures 2.8 show the parameters discussed in a TSL. The value of the maximum traction T and S can be obtained together with

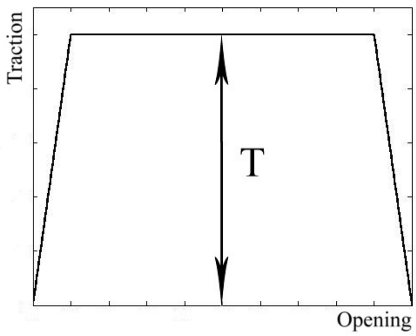

(a) Maximum traction

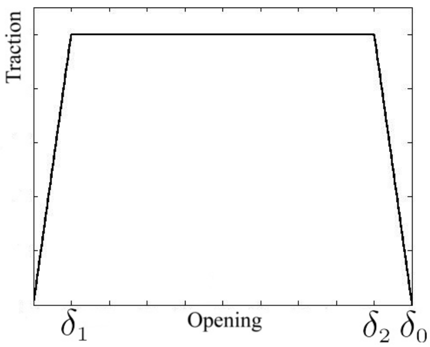

(b) Opening

Figure 2.8: Scaling of the non dimensional TSL

the cohesive energy Γ in an inverse modelling approach where its value is equal to the stress at the point of instability [38].

2.2.4 Traction separation law

As cohesive zones are a phenomenological fracture model, there is no single true model. This is also true for the normalized TSL. A large variety exists, but most share the same basic properties.

The exact shape of the normalized TSL is often reported to have no or little effect [39, 40], while others do report an influence [41, 42, 43], but mostly in the area of fracture branching. In this research a modified version of the Tvergaard Hutchinson TSL (figure 2.9c) is used. This is a common variety and it is also the one recommended in a comparative study [44] for mode I. Some of the most widely used TSL are discussed below.

Needleman

Needleman [45] proposed a TSL based on equation 2.6 in 1987. This TSL is depicted in figure 2.9a.

$$\hat{t} = \frac{27}{4} T \frac{\delta}{\delta_0} \left(1 - \frac{\delta}{\delta_0}\right)^2 \tag{2.6}$$

Needleman also proposed a second exponential model [40] in 1990 to simulate a ductile fracture process. This TSL does not have a zero traction at the moment of failure as can be observed in figure 2.9b. Equation 2.7 defines it, where $z = \frac{16}{9}e$.

$$\hat{t} = zTe \frac{\delta}{\delta_0} e^{-z\frac{\delta}{\delta_0}} \tag{2.7}$$

Tvergaard

Tvergaard et al. [27] proposed a trilinear TSL with a stable traction level for most of the opening profile. It is shown in figure 2.9c. The model is the one used in the non rate sensitive cohesive simulation performed for this research. It is defined by equation 2.8.

$$\hat{t} = T \begin{cases} \frac{\delta}{\delta_1} & ,\text{For} \quad \delta < \delta_1 \\ 1 & ,\text{For } \delta_1 \leq \delta < \delta_2 \\ \frac{\delta - \delta_2}{\delta_0} & ,\text{For } \delta_2 \leq \delta \leq \delta_0 \end{cases} \tag{2.8}$$

Scheider

An adaptation to the Tvergaard model was published by Scheider [46] in 1992, making the TSL continuously differentiable in order to avoid numerical problems. Equation 2.9 defines the TSL and figure 2.9d shows an example of it.

$$\hat{t} = T \begin{cases} 2\left(\frac{\delta}{\delta_1}\right) - \left(\frac{\delta}{\delta_1}\right)^2 & ,\text{For} \quad \delta < \delta_1 \\ 1 & ,\text{For } \delta_1 \leq \delta < \delta_2 \\ 2\left(\frac{\delta - \delta_2}{\delta_0 - \delta_2}\right)^3 - 3\left(\frac{\delta - \delta_2}{\delta_0 - \delta_2}\right)^2 + 1 & ,\text{For } \delta_2 \leq \delta \leq \delta_0 \end{cases} \tag{2.9}$$

2.3 Alternatives to using cohesive zones

Modelling of fracture in LS-DYNA can be achieved through other means then using cohesive zones. In [2] all the available alternatives were compared for their suitability in the types of simulations at hand in this research. This section offers an overview of the available alternatives based largely on the source indicated.

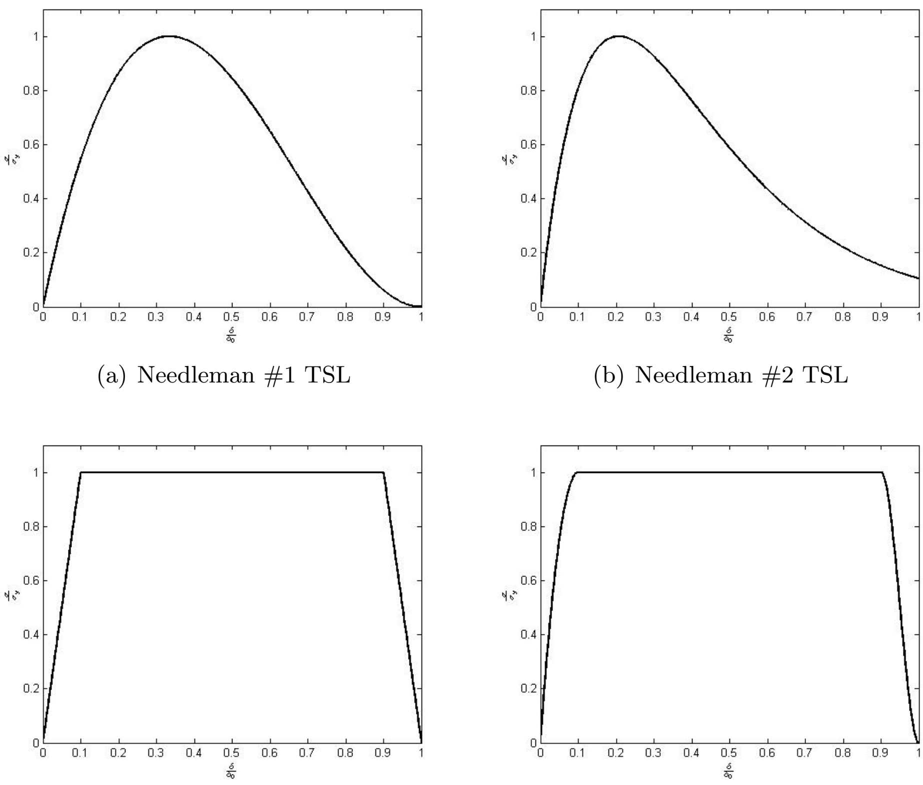

(a) Needleman #1 TSL

(b) Needleman #2 TSL

(c) Tvergaard Hutchinson TSL

(d) Scheider TSL

Figure 2.9: Four different examples of traction-separation laws

Element Erosion

Element erosion techniques are based on the deletion of elements after a certain criterion has been met. For fracture this criterion is likely to be a maximum strain value. Th advantage of this technique is its ease of implementation and it allows an arbitrary fracture path not defined at the time of the start of simulations. The main drawback is the loss off mass and inertia in exactly those areas where the influence on the rate of fracture is the strongest; at the tip of the fracture. Mesh dependence can also be an issue, but this can be overcome as is done in [47], where a Rice-Tracey failure criterion is used with a correction for element size.

Nodal release

Nodal release is a technique where nodes are doubled along element boundaries leading to a separation of the elements on both sides of the duplicated boundary after reaching a certain criterion. This criterion can be a certain strain, crack tip opening- displacement or angle. A drawback is the necessity to define the fracture path a-priory. In [48] the nodal release and shell element erosion methods are compared for LS-DYNA.

Continuum softening

Cohesive softening is a continuum approach to fracture mechanics where softening of the stress-strain relationship is introduced after a fracture criterion is reached. Elements remain intact and there is no true separation of the material. The advantage is that the method does not require knowledge of the fracture path a-priori. The disadvantages include the inability to model separation and the potential for mesh dependence unless special techniques known as localization limiters are used. LS-DYNA offers a variety of continuum damage models based on the Gurson void model [29] and a smeared crack approach.

Cohesive zones

Cohesive zones were already discussed in detail in the beginning of this chapter. LS-DYNA offers several non rate sensitive cohesive zone models and allows custom cohesive zone models to be implemented. The advantages and disadvantages of cohesive zones as a tool to model fracture were discussed in [33]. The advantages of the cohesive zone method as compared to other fracture mechanical approaches are as follows:

1. Cohesive zones are phenomenological and can therefore be used to model a wide variety of materials and fracture mechanisms

2. Cohesive properties are geometry independent and may be transferred from a small scale test specimen to a large scale component. Transferability of parameters is possible as long as the fracture mechanism remains the same and a similar level of constraint is present. This last requirement results from the difference in fracture energy for fracture in plane strain and plane stress[2]. If triaxiality is taken into account in the cohesive zone model, as is done in [32, 33], the last condition can be circumvented.

3. The number of parameters involved with cohesive zones is low as compared to many other approaches.

4. There is no mesh dependence for sufficiently small cohesive zone elements in the fracture length direction.

There are however also disadvantages and uncertainties associated with using cohesive zones.

1. The phenomenological nature of the model causes some uncertainties with regard to the physics of the process.

2. Mixed mode behaviour is not yet established with sufficient evidence

3. Arbitrary fracture through any surface within elements is generally not possible unless special techniques are used as is done in [49, 50, 51]. this is not an issue in situations where the crack path is known a-priori with a high degree of accuracy.

4. Separation of plastic material behaviour into a cohesive zone and bulk material is problematic.

[2]See appendix D

Chapter 3

Experiments

At TNO Defence, Security and Safety, experiments were carried out to investigate the fracture behaviour of thin sheets of aluminium 2024 T3 and duplex steel DIN 1.4462. Section G first covers the material properties. As a first step, centre cracked panel tests were performed, these are discussed in section 3.1. Secondly, as part of a wider investigation into fracture in aircrafts, tests were carried out on pressurised aluminium barrels. These tests and the results are discussed in section 3.2.

3.1 Dynamic fracture of prestressed plates

Centre crack panel tests were performed on aluminium 2024 T3 and duplex steel DIN 1.4462 plates 800 mm wide and 1500 mm long. The thickness varied between 1 and 1.5 mm Plates were pre-stressed to the stresses as indicated in table 3.1. Figures 3.1a and 3.1b show the test setup used in the plate tests and a schematic drawing thereof.

Material	Test	t_h (mm)	Force (kN)	Stress $\left(\frac{N}{mm^2}\right)$
Aluminium	V3-01	1	160	200
Aluminium	V3-02	1	160	200
Steel	V1	1.5	690	575

Table 3.1: Plate tests summary

An initial fracture was created in the stressed plate using an explosive charge placed against the plate and a fixed “anvil” bar on the other side as depicted in figure 3.2a and 3.2b. This setup induces a 200 mm wide fracture in shear.

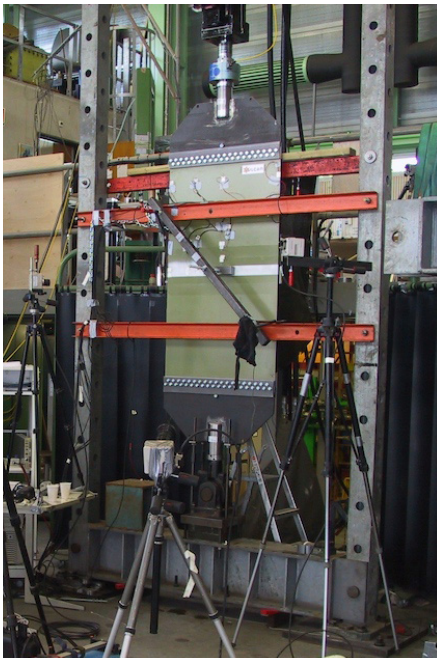

(a) Before fracture

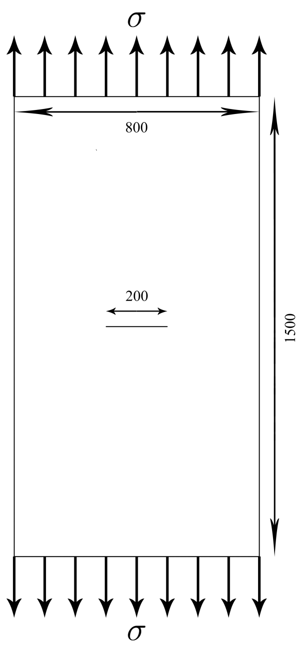

(b) Scematic

Figure 3.1: Plate test test setup

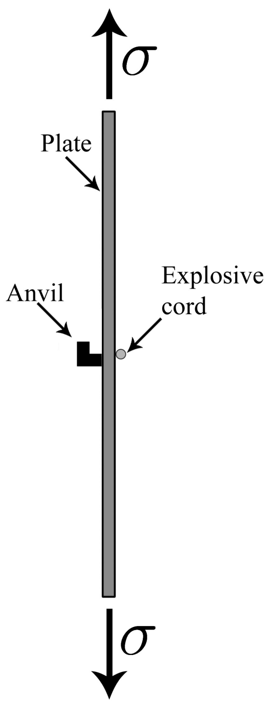

(a) Before initiation

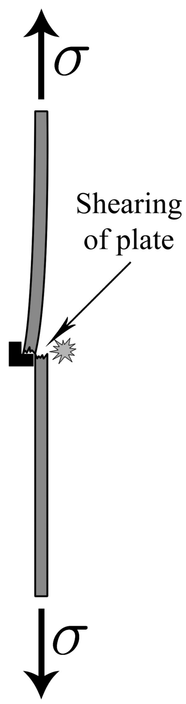

(b) After initiation

Figure 3.2: Fracture initiation using explosives

High speed video recorded the entire length of the fractures progressing in both directions. Substantial periodical out of plane plate movement was observed as a result of the explosive initiation. Fracture speeds data was derived from the highspeed footage, but not all frames could be used as smoke and flames obscured the initial fracture progress and strain gauges placed on top of the fracture path covered substantial parts of the fracture trajectory. Fracture was not perfectly symmetrical and upon reaching the end of the plate at one side, the fracture at the other side would cease to progress and the plate would hang for a substantial amount of time before the rest of the plate was torn off, this would indicate that the test rig was unable to cope with the sudden large deformations and the condition of equal force was violated from the point of the first fracture reaching the panel side on. As a consequence, it was only possible to derive one fracture progression data set per plate. Figure 3.3 shows several of the frames used for obtaining fracture data in an aluminium plate test. Figure 3.4 shows the setup after fracture is complete.

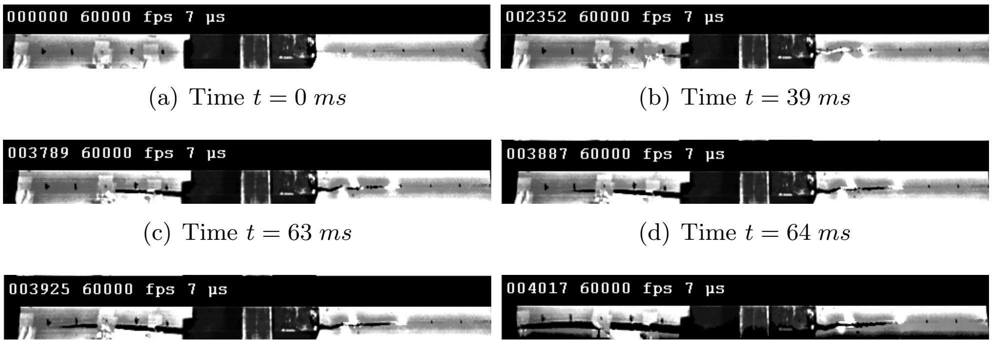

(a) Time $t = 0\ ms$

(b) Time $t = 39\ ms$

(c) Time $t = 63\ ms$

(d) Time $t = 64\ ms$

(e) Time $t = 65\ ms$

(f) Time $t = 67\ ms$

Figure 3.3: Fracture progress in an aluminium plate

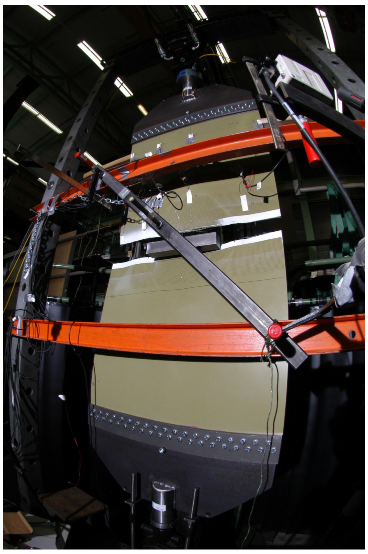

Figure 3.4: Plate after test

The fracture velocity is obtained by simple numerical differentiation along the fracture path. Figure 3.5 shows the velocity profile for the aluminium and the steel test together. The initialfracture speeds found are much lower than realistic at around 5 m/s. Only near the edges of the plate an acceleration occurs to a maximum of around 80 m/s. The curves for the steel and aluminium tests are almost identical which is an implausible result given the difference in fracture toughness of the two materials. This is likely to be attributed to the method of initiation. More detailed velocity curves can be found in appendix K.2. All tests are described in more detail in [52]. Scanning electron microscope images have been made of the fracture

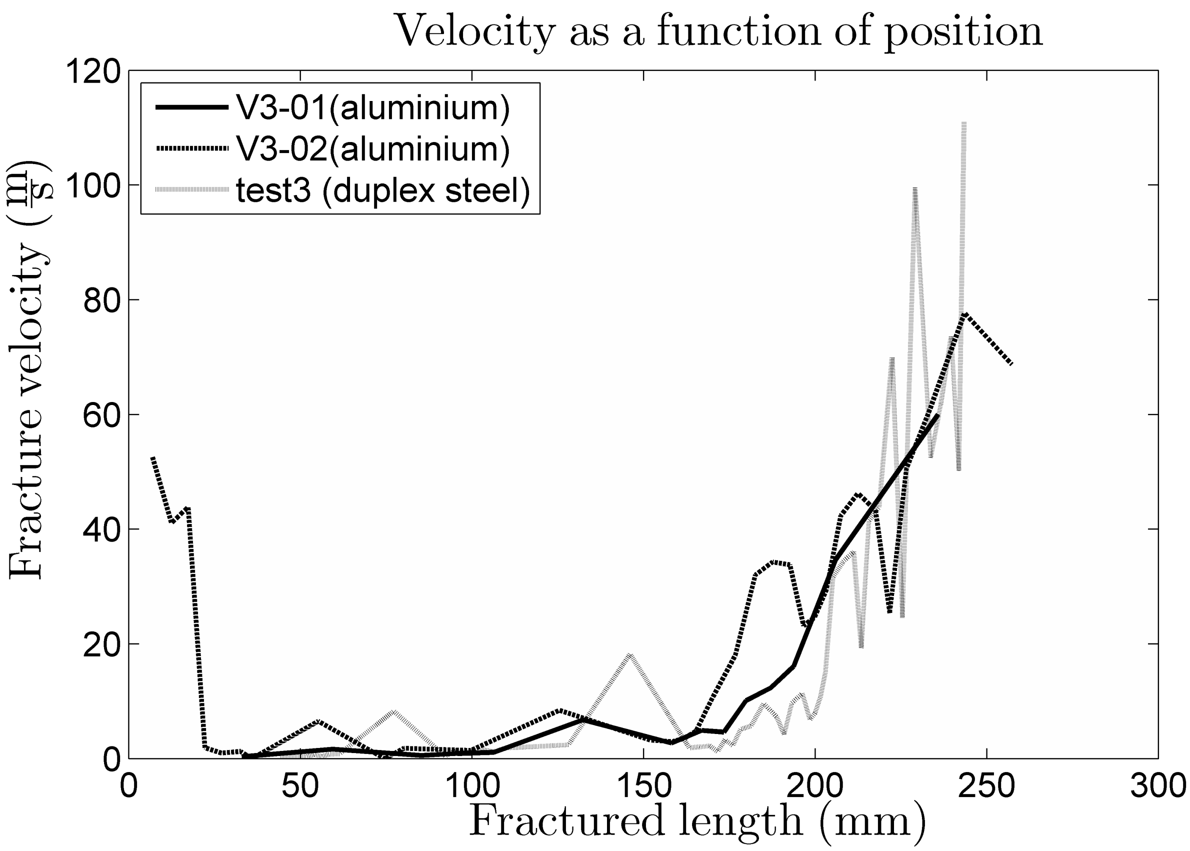

Figure 3.5: Plate test fracture rates

surfaces to confirm mode I ductile failure. For the steel test, these are shown in figure 3.6 and for aluminium in figure 3.7. All these images were taken from the fracture surface close to the edge of the plate, where the fracture velocity was the highest. Figure 3.8a shows a possible impurity present in the material, acting as a nucleation site. Figure 3.8b is a close up of the aluminium fracture surface, showing the walls in between the coalesced microvoids forming the tell tail dimple-like surface of mode I ductile fracture.

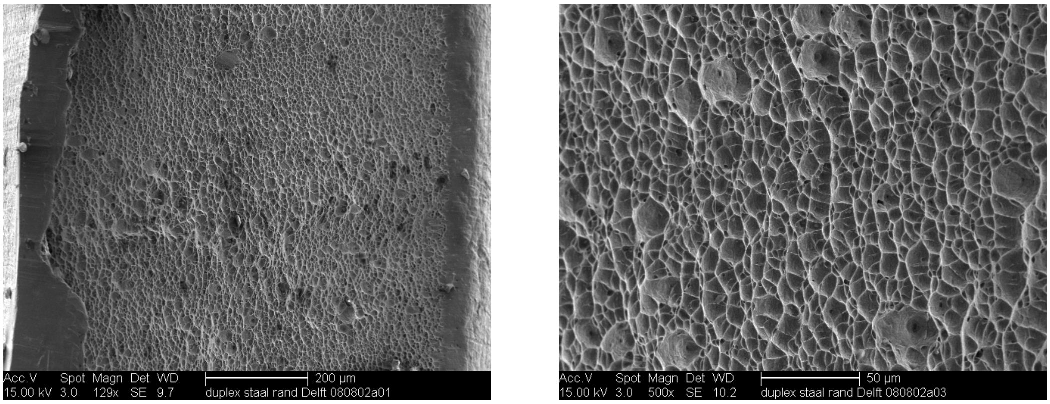

(a) Complete face

(b) detail

Figure 3.6: SEM images of the fracture face in a steel plate test

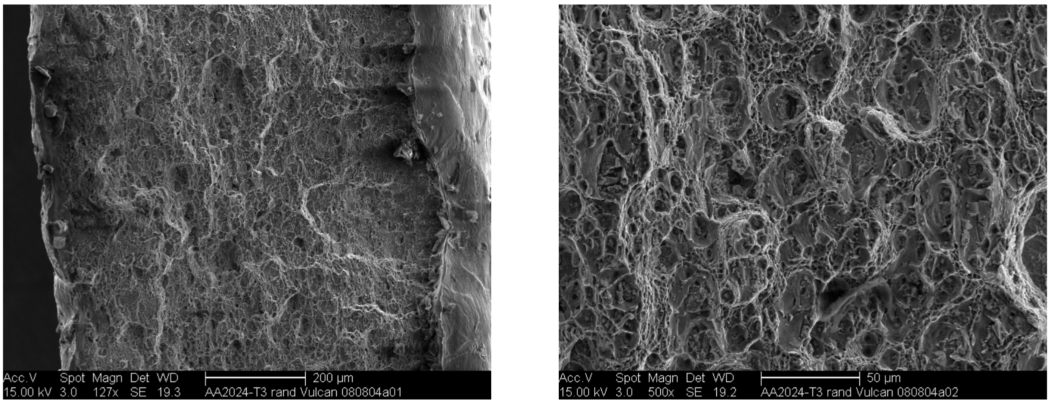

(a) Complete face

(b) detail

Figure 3.7: SEM images of the fracture face in an aluminium plate test

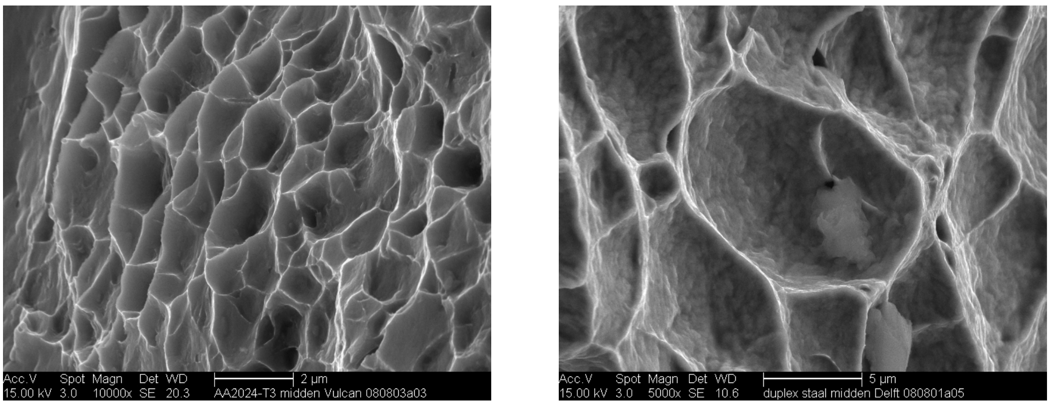

(a) Aluminium at very high resolution

(b) possible source of nucleation

Figure 3.8: SEM imagery at high magnification

3.2 Dynamic fracture in pressurised barrels

Two, one third of full scale, fracture experiments were performed on pressurized aluminium barrels, representing an aeroplane fuselage. The work was done at TNO under the "EU VULCAN project" framework, which aims to study the vulnerability of aeroplane fuselages in case of an internal explosion and fire. The barrels were made of the same aluminium 2024 T3 "bare", as the plates in the previous section. Details of the geometries are given in table 3.2. Figures 3.9a and 3.9b show the test setup. An internal pressure was applied to the barrel of a magnitude as indicated in table 3.2.

	Pressure $(\frac{N}{mm})$	Initial notch $(2a)$ (mm)	Height (mm)	Diameter (mm)	Thickness (t_h) (mm)
Test02alu01	310	280	1030	1225	1
Test03alu02	230	200	1030	1225	1

Table 3.2: Vulcan Barrel test setup details

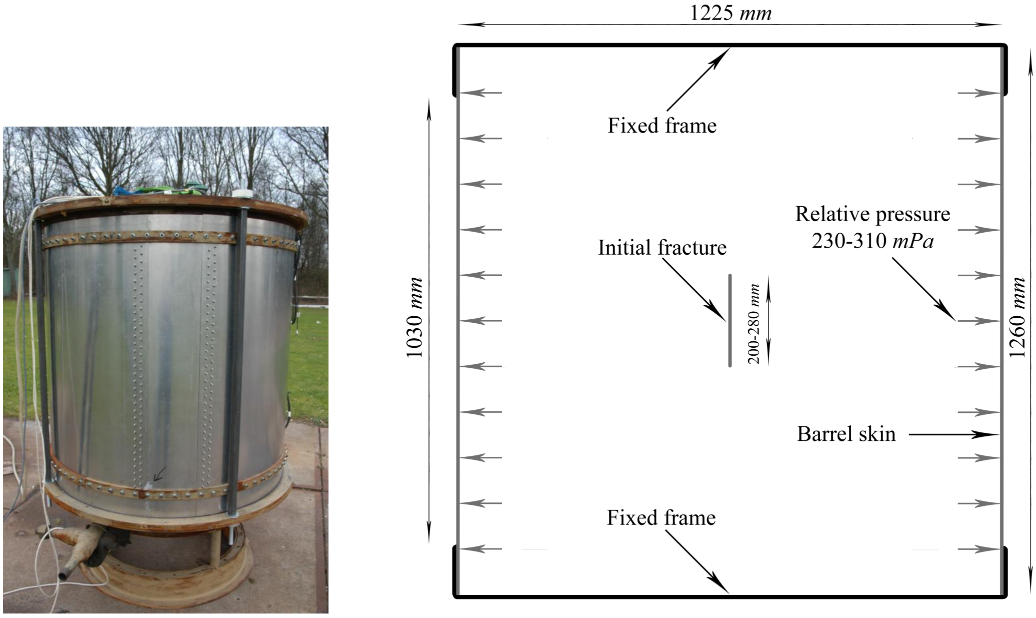

(a) Before fracture (b) Scematic

Figure 3.9: Vulcan barrel test setup

Fracture was initiated in the same way as was done with the prestressed plate test, creating an initial notch in shear of length 2a. Fracture thereafter continued vertically up and down, thus fracturing in mode I, until reaching the end of the barrel. There mode III fractures occurred along the edge of the barrel, while the barrel opened up in two flaps that can still be distinguished in figure 3.10a. The top and bottom plate of the barrel were firmly fixed relative to one another in the vertical direction. The skin of the barrel was fixed to the end plates with the help of bolts. Local bulging at the fracture in the barrel caused membrane stresses high enough to pull the bolts through the skin material for up to 30 *mm* at both sides. Figure 3.10b shows this at a point exactly below the initial fracture. The outward deflection of the posts supporting the end caps was caused by impact with the outward moving aluminium flaps.

(a) Barrel after test

(b) Bolts pulled through skin material

Figure 3.10: Vulcan barrel test result

Continuous gas pressure measurements were performed, showing a linear decay in pressure from the initial value to ambient levels in approximately 12 ms for both tests. High speed footage was taken of the barrels at some distance and in close-up of the fracture. As the scope of the close-up was rather narrow and the fracture deviated from a perfect vertical line slightly, the data sets were not complete. Simultaneous triggering of all cameras allowed the data set from *test03alu02* to be completed using footage from the wide angle camera. *Test02alu01* had its wide angle camera orientated in such a way that this was not possible. Figure 3.11 shows four frames of the high speed footage taken at 70.000 frames per second. The central, non fracturing object in the frames is part of the anvil structure.

Fracture progress data is obtained by marking the location of the visual fracture front at frames where this is visible. Smoke, flames and glare from the studio lights hampered this, which resulted in less than smooth velocity profile. Although it cannot be ruled out that fluctuations were physically present in the rate of fracture, the period of two inter-observation time steps, in the fluctuations seems to suggest the origin to lie in the measuring instead. The fracture velocity obtained for both barrel tests is plotted against the additional fractured length in figure 3.12. Higher resolution graphs can be found in appendix K.1. The fracture rate has been obtained by means of simple numerical differentiation. Figure 3.12 shows an initial spike in fracture rate for both *test03alu02* as *Test02alu01* of around 500 m/s. The fracture rate decreased thereafter to a value around 300 m/s for *Test02alu01* and 200 m/s for *test03alu02*.

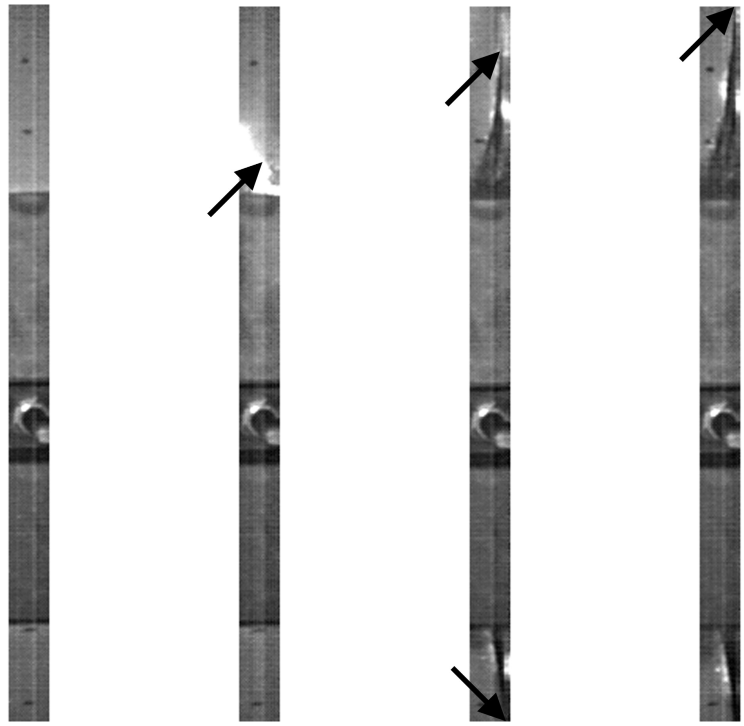

(a) $t = 0\ ms$ (b) $t = 0.3\ ms$ (c) $t = 0.7\ ms$ (d) $t = 0.9\ ms$

Figure 3.11: High speed close-up of *Test02alu01*

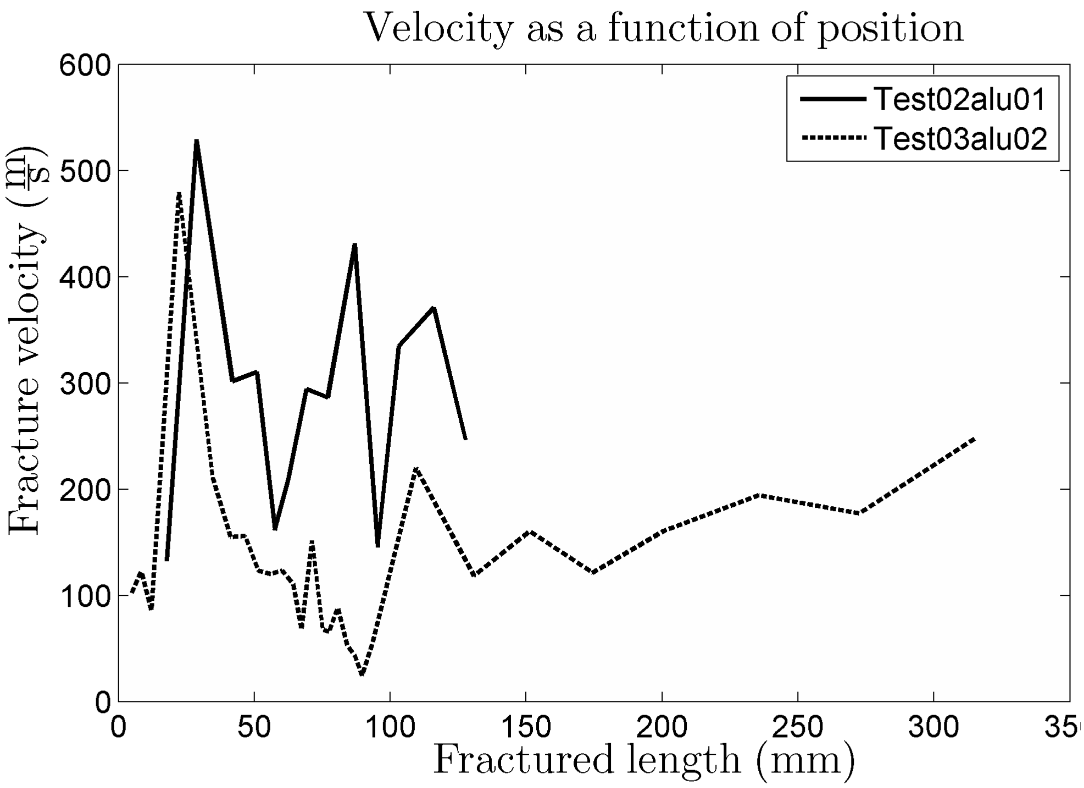

Figure 3.12: Vulcan barrel test fracture rates

Chapter 4

Finite element Simulations

In this section, the experiments of chapter 3 are simulated using the FEM and standard rate independent cohesive zones. It will be shown that the existing rate independent cohesive zones over predict the rate of fracture dramatically. As a first step the cohesive properties of aluminium 2024 T3 and duplex steel DIN 1.4462 are derived. The procedures used and the values obtained are given in section 4.1. Attention also needs to be paid to correct modelling of bulk material behaviour; different models exist, and parameters for these models need to be obtained. This is discussed in appendix H.

The finite element simulations of the experiments described in chapter 3 are presented in section 4.2 and 4.3 for the plate and barrel experiments, respectively. Obtaining the fracture propagation rate curve from finite element simulations is not a straight forward procedure and the steps required to derive them are explained in section 4.4. Section 4.5 describes the way solid cohesive elements are placed within a shell bulk mesh. Finally the differences in fracture velocity between experiments and finite element simulations are discussed in section 4.6.

4.1 Derivation of static cohesive parameters

4.1.1 Aluminium 2024 T3

The object of this section is to derive the cohesive energy Γ_{N} and traction T for a mode I opening. No data or estimates were found for the other modes. These are set equal to the mode I parameters therefor in the simulations. As is pointed out in [37], the two parameters are not independent from one and another, but need to be derived together. Two sources give estimates of these values. they are given in table 4.1

Source	Γ_{N} $\left(\frac{kJ}{m^2}\right)$	T $\left(\frac{N}{mm^2}\right)$
[53]	19.0	$2.7 \cdot \sigma_y = 2.7 \cdot 345 = 931.5$
[54]	17.0	$2.0 \cdot \sigma_y = 2.0 \cdot 285 = 570.0$

Table 4.1: Reported cohesive properties of thin sheet aluminium 2024 T3

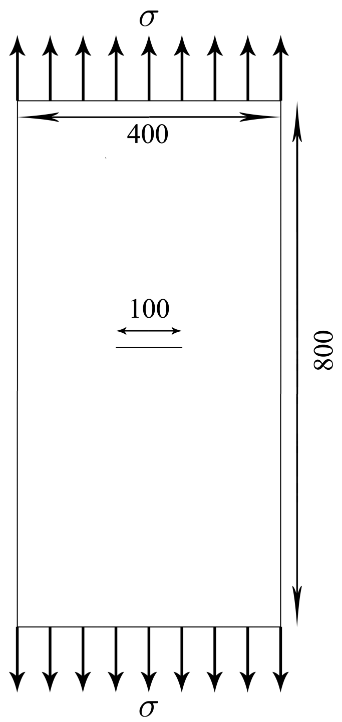

Figure 4.1: Geometry of test B24LT-06

The values quoted in table 4.1 give significant differences in fracture velocity, mainly because of the maximum traction reported in [54]. To check the values obtained from the sources mentioned, an inverse simulation is performed on one of the centre cracked panel test as performed by the TU-Delft [55]. The test number is *B24LT-06* and the plate was 400 mm wide, 800 mm tall and 1 mm thick with a 100 mm wide initial fracture as illustrated in figure 4.1. The panel with a centre crack is subjected to an increasing load and both the increase of the fracture as the displacement of the load applicator is monitored. In the beginning, the fracture extends as a function of stress, but as the stress increases, the fracture releases more potential energy per unit of fracture increase until this becomes equal to the amount of energy needed to fracture the same unit length of fracture. At this point, no additional external energy is needed to propagate the fracture and the fracture accelerates independent of the externally applied load.

At the point of instability, the static material fracture energy can be determined [23]. Simulations were performed with varied cohesive properties, and the combination giving the same point of instability as the experiment, was then utilized for the cohesive zone model. Figure 4.2 shows the displacement versus the theoretical stress in the whole cross section and the point of instability. The line through this point is then transferred to figure 4.3, to determine the correct parameter using the procedure mentioned above.

The cohesive parameters obtained from this procedure are as follows: $\Gamma = 19\ \frac{N}{mm}$ and $T = 755\ \frac{N}{mm^2}$, which fall in between the values of table 4.1 and are used as the cohesive properties of 1 mm thick aluminium 2024 T3 throughout the rest of the research.

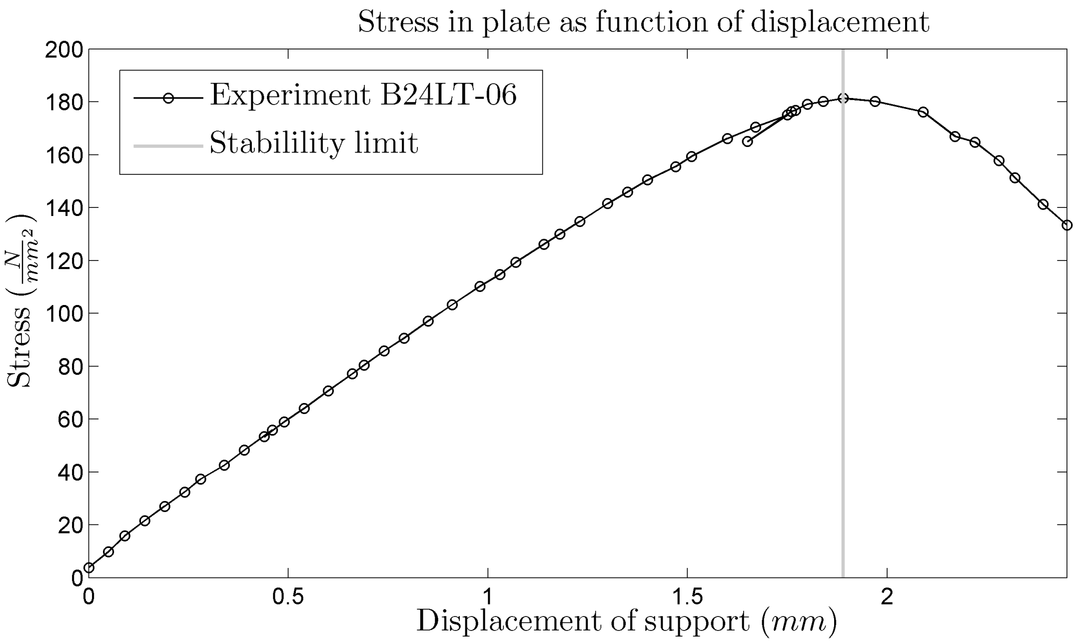

Figure 4.2: The point of instability

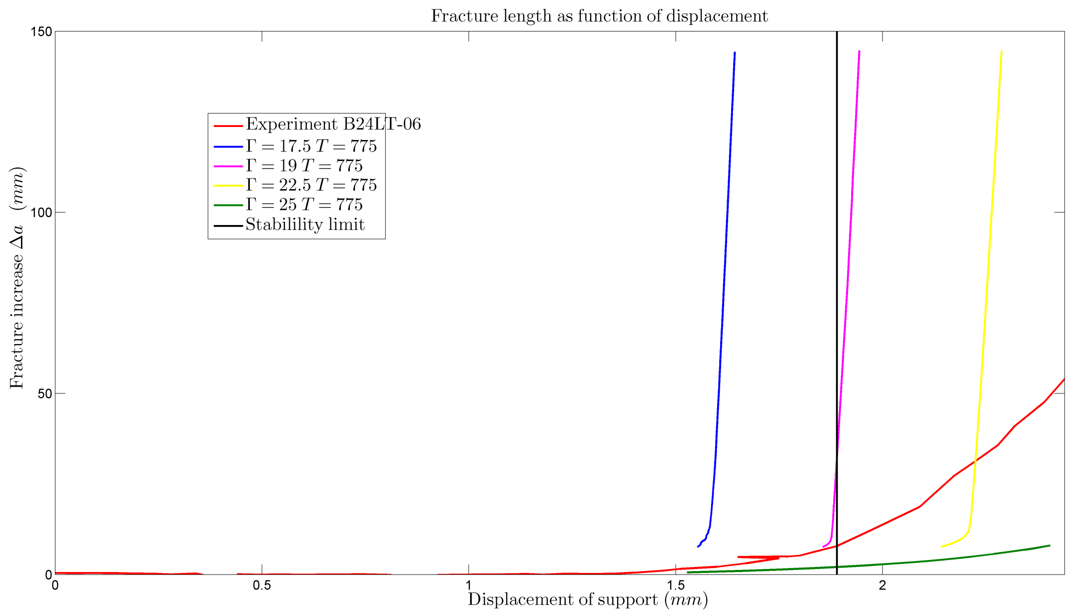

Figure 4.3: Determining the cohesive properties through inverse modelling

4.1.2 Steel

For duplex steel DIN 1.4462, no centre cracked panel tests are available, nor is any other kind of other data set where the cohesive properties may be inferred from using inverse modelling. As was pointed out earlier, it is possible to obtain a rough estimate of the cohesive energy using the techniques presented in appendix F.

A CTOD of 1.57mm [56] has been measured for duplex steel 1.4462. As outlined in section F.3, it is possible to convert this to a critical J value. Equation F.9 has an unknown in the form of constant M. [57] Reports a value of M = 1.5 for duplex steel 1.4162, an alloy with comparable properties to 1.4462. [58] has a slightly different version of equation (F.9) in the form of

$$\Gamma \approx J = \delta_t \frac{\sigma_{\mathrm{y}} + \sigma_{\mathrm{ult}}}{2} \cdot \mathrm{M}_* \tag{4.1}$$

This formulation is in fact identical to the one of equation F.11. $\mathrm{M}_* = 1.4$. σ_{ult} Is a factor 1.41 [56] higher then σ_{y}, a relationship that allows M_* to be converted to a representative value $\mathrm{M} = 1.68$.

The M values thus obtained lie in the range 1.5 to 1.68. An M_* value of 1.4 as suggested by Wellman in section F.3 for test pieces in unknown stress states seems reasonable.

$$\Gamma \approx J = \delta_t \frac{\sigma_{\mathrm{y}} + \sigma_{\mathrm{ult}}}{2} \cdot \mathrm{M}_* = 1.57\ \frac{460 + 640}{2} \cdot 1.4 = 1230\ \frac{N}{mm} \tag{4.2}$$

Another way of obtaining the fracture toughness is the Charpy V-notch conversion process of section F.2. The Charpy V-notch data available for duplex steel 1.4462 is presented in figure 4.4a. A CVN curve was fitted and converted to a fracture toughness curve that is depicted in figure 4.4b. This is in turn converted to a critical energy release rate, or cohesive energy estimate. Figures 4.4c and 4.4d show the cohesive energy derived at room temperature and at $-20°C$ respectively. For room temperature, a cohesive energy of 400 - 420 $\frac{N}{mm}$ was found. At $-20°C$, this reduces to 280 $\frac{N}{mm}$.

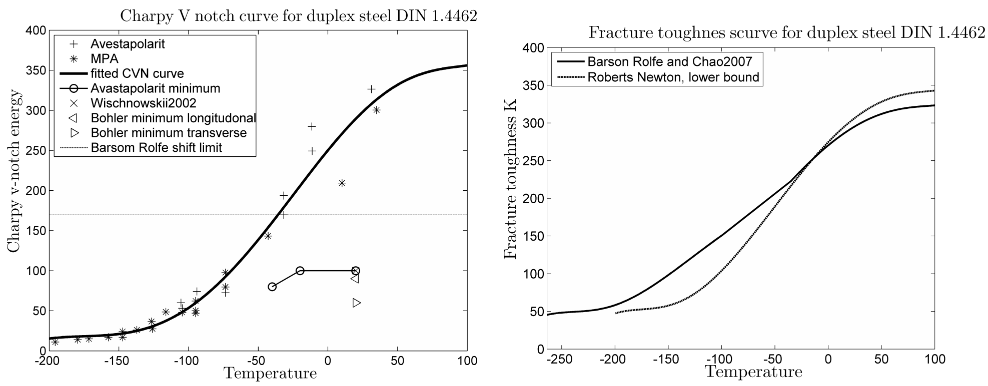

(a) CVN data available
(b) Fracture toughness

Figure 4.4: Obtaining fracture toughness data from Charpy V-notch data

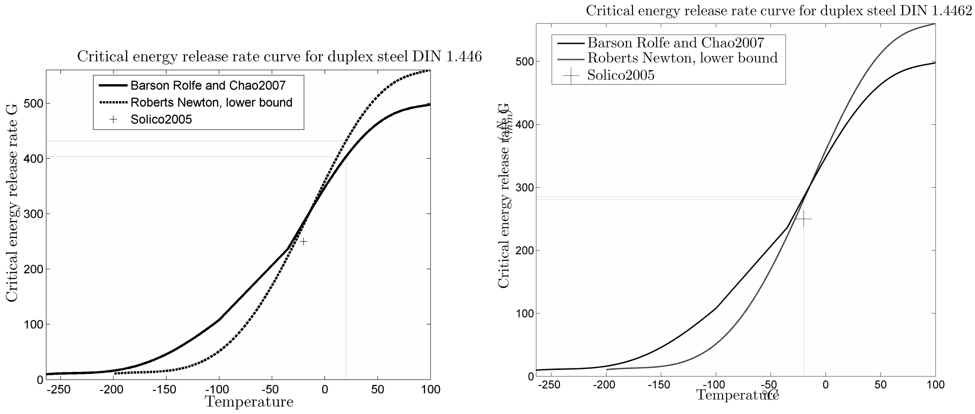

(a) Toughness at $20°C$ (b) Toughness at $-20°C$

Figure 4.5: Derived fracture toughness values for DIN 1.4462

Significant differences exist between the cohesive energy levels obtained (420 - 1230 $\frac{N}{mm}$). This large variation was also present in the Charpy V-notch data as presented in figure 4.4a. The cohesive energy is an important factor in the rate of fracture. This uncertainty in cohesive energy, together with the unknown maximum traction, prevents any meaningful finite element simulation from being performed in an effort to predict the fracture propagation rate.

4.2 Plate test

The experiments performed on prestressed plates as described in section 3.1 and 4.1 were analyzed in finite element simulations. The mesh used in the centre cracked plate simulations is presented in figure 4.7. It consists of one layer of eight noded fully integrated solids. The mesh is progressively refined in the vicinity of the central fracture path. This fracture path is defined a-priori by a layer of rate independent cohesive zone elements.

To take advantage of the three fold symmetry in a centre cracked panel, only a part of the the panel is modelled, and zero strength shell layers are applied to set the relevant symmetry boundary conditions on the symmetry planes. Only two symmetries can be exploited as the third plane lies across the cohesive zone and this proved problematic to exploit. The two remaining planes of symmetry lie in the through thickness direction of the plate and across the centre of the plate in the width direction, thus cutting the fracture plane in half.

An initial fracture is either present at the beginning of the test or explosively notched when the plate is in a prestressed state. Both cases are simulated using an initial notch in the finite element mesh. This notch is held closed using nodal constraints in the case of the explosively notched prestressed plate. Figure 4.7 shows the mesh used.

4.2.1 Aluminium prestressed plate test simulation

The aluminium plate test of paragraph 3.1 was reproduced in a finite element simulation. A stress of 200 $\frac{N}{mm^2}$ was built up during the initial millisecond of the simulation when a critical damping was also applied. At 1 millisecond the fracture was initiated by removing the constraints

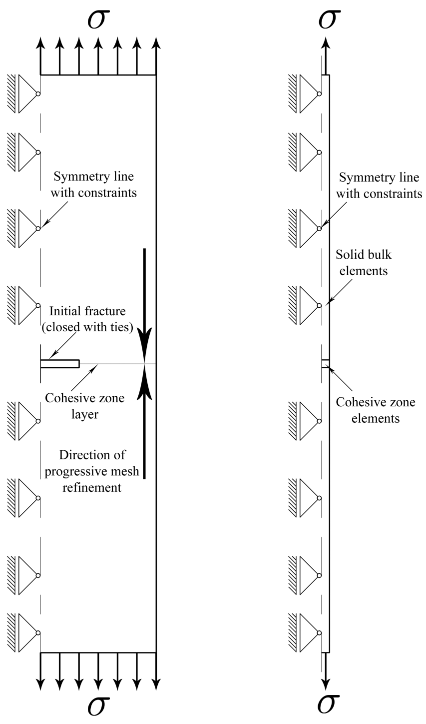

(a) Front (b) Side

Figure 4.6: plate geometry sketch

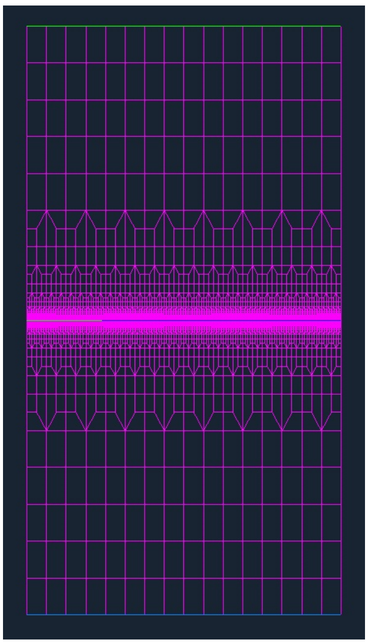

Figure 4.7: Plate mesh

between the two sides of the initial notch, creating a 200 mm initial fracture. This simulates the explosive notch forming process.

The cohesive layer was modelled using a rate independent cohesive zone formulation, and the amount of cohesive energy was varied. The surrounding bulk material was modelled with a plastic isotropic material model as described in H.3. Results of the aluminium plate simulations are given in figure 4.8. The cohesive energy level for static fracture is equal to 19 $\frac{N}{mm}$ and this value resulted in velocities in excess of 1800 $\frac{m}{s}$, as is clear from figure 4.8. Increasing the cohesive energy lowered the velocity, though it proved impossible to reproduce the results of the experimental tests where speed below 80 m/s were found as can be seen in figure 3.5. Values of the cohesive energy, $\Gamma \geq 50\ \frac{N}{mm}$, did not fracture or arrested after a short distance.

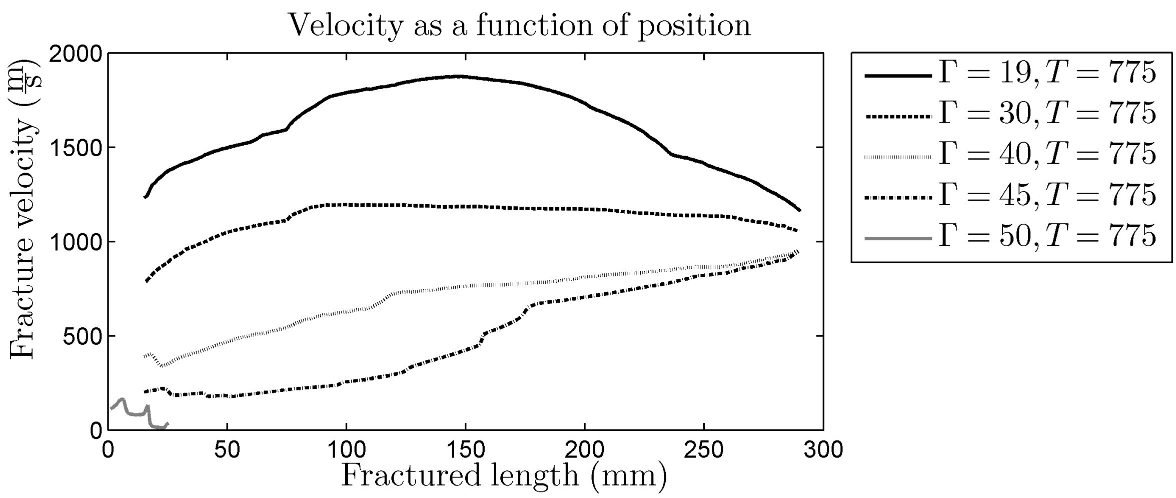

Figure 4.8: Simulated fracture speeds in aluminium, plate test

4.2.2 Steel prestressed plate test simulation

The different fracture toughness levels derived for duplex steel were simulated in a plate test. The stress in the plate was built up and maintained as was done with the aluminium plate test case. The stress was set equal to 575 $\frac{N}{mm^2}$, as was done in the experiments. This placed the whole plate in a condition of yielding as the yield stress is only 460 $\frac{N}{mm^2}$. After opening of the initial fracture, this would result in a stress of 767 $\frac{N}{mm^2}$ for the unfractured cross-section. This value exceeds the representative ultimate tensile strength of the material of 640 $\frac{N}{mm^2}$. As is pointed out in section G, the quoted material properties of duplex steel 1.4462 vary greatly, especially with regard to the ultimate tensile strength. The test piece was obviously of higher quality then required by norm, but no tests were performed to ascertain precisely what these properties were. This poses considerable difficulties in simulations and future experiments on duplex steel fracture should therefore be accompanied by a strength test of the specific batch.

Simulations using the characteristic yield strength from the norm, and the plastic-kinematic properties as found in section H.3 yielded a continuously accelerating fracture without a stable maximum velocity as can be seen in figure 4.9. A reduction of the externally applied stresses to 80% of the yield stress, led to the material being unable to fracture in the simulations. This is consistent with an earlier experimental plate tests, where a plate loaded to 350 $\frac{N}{mm^2}$ failed to result in a propagating fracture after being initiated.

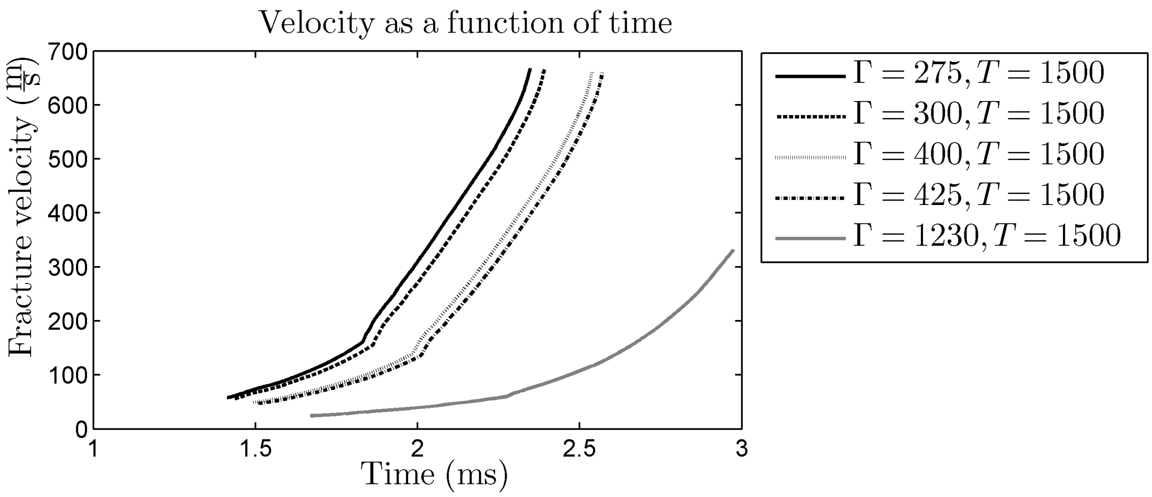

Figure 4.9: Simulated fracture speeds in duplex steel plate test

The cohesive energies used to derive figure 4.9 were chosen in the range as found in section G.2. As no estimation could be made for the maximum traction, a value approximately three times the yield stress was chosen. The maximum traction typically ranges from 2 to 3 times the yield stress. Even the very high cohesive energy of $\Gamma = 1230\ \frac{N}{mm}$ combined with a maximum traction T at the high end of the range, showed speeds in excess of 300 m/s, and failed to reproduce the experimentally observed fracture rate of approximately 80 m/s.

4.3 Barrel test

4.3.1 Mesh layout

The barrel mesh consists of a ring of shell elements with a mesh refinement at both fracture planes. This is visible in figure 4.10a, where the refinements are in separate parts and coloured green. Fracture is initiated at the longitudinal fracture path, at the other end of the halved model at the place indicated. Figure 4.10b shows the two different fracture paths lined with cohesive elements, one longitudinal and the other around the circumference of the barrel. As the fracture reaches the end of the longitudinal fracture path, fracture can continue around the top of the barrel and open up the barrel in a double door type fashion. This failure mode was observed in tests and accidents with pressure vessels[1].

There are two different planes of symmetry in the model that could be exploited to reduce the number of elements needed in the simulations and thus the time it takes to run them. One plane of symmetry was exploited and lies through the longitudinal direction of the barrel. The plane of symmetry cutting the circumference of the barrel in two proved problematic because the cut lies through the centre of the longitudinal fracture path in the barrel. This plane of symmetry was therefore not exploited. Figure 4.11 shows a sketch of the finite element model used with details of the boundaries, symmetry plane and fracture. As can be seen in figure 4.11, the cohesive zone layer is more complicated then the one for the plate type meshes. Because only solid cohesive zone elements are supported within LS-DYNA, a transition between the shell elements of the bulk of the mesh and the solid cohesive zone elements needs to be made. This is discussed further in section 4.5.

[1]See sections 1.1.1 and 3

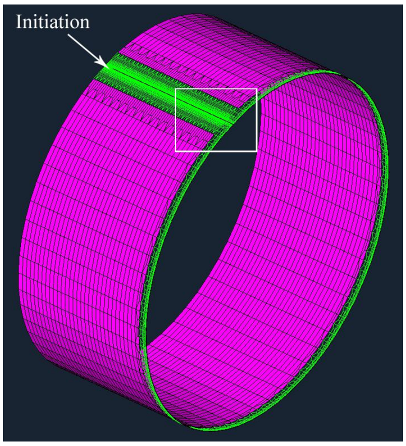

(a) Overview of barrel mesh

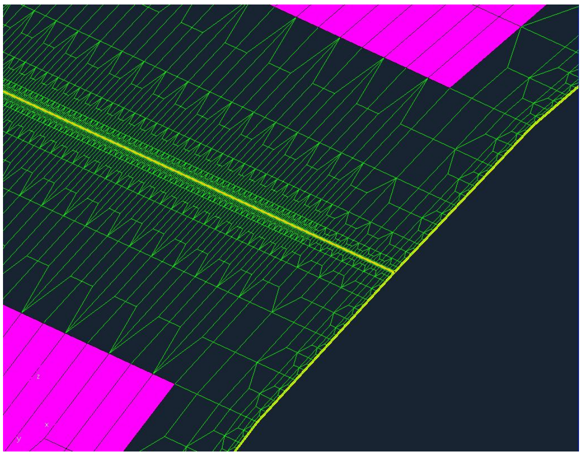

(b) Detail A, CZ layers

Figure 4.10: Barrel mesh

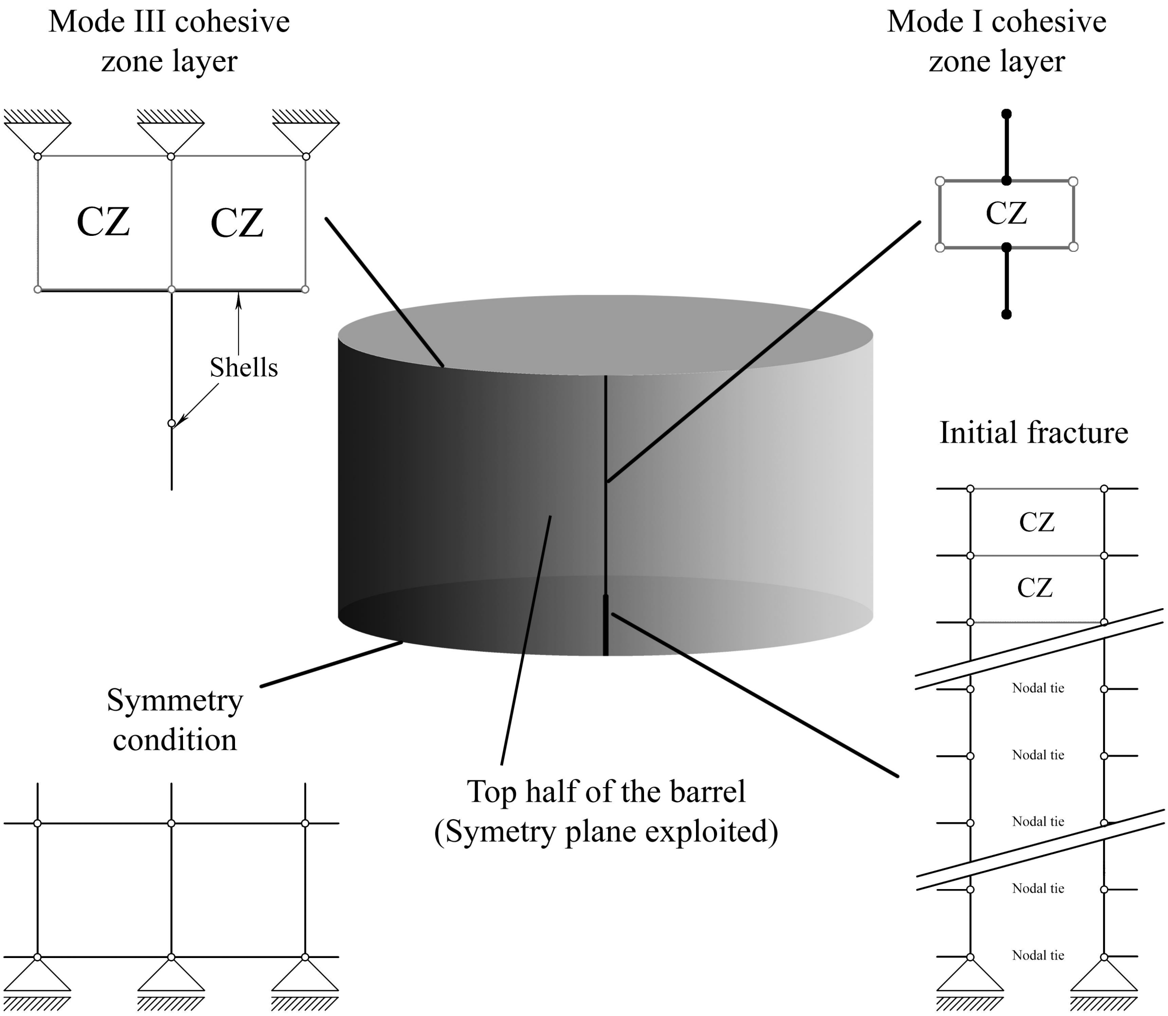

Figure 4.11: Barrel simulation details sketch

Boundary conditions are applied along the edge of the longitudinal cut in the model and restricts movement in the longitudinal direction. A second set is situated at the other end of the model and prohibits movement in all directions. This is consistent with the 30 mm thick steel plate[2], confining the aluminium skin of the barrel in all directions. A third set of boundary conditions imposes a traction on all shells forming the circumference of the barrel and represent a pressure build up inside the barrel. A fourth set is used to close and open an initial fracture when required. This is done by tying both sides of an initial fracture by nodal constraints called *spotwelds* in LS-DYNA.

[2]See figures 3.9a and 3.9b

4.3.2 Aluminium barrel test simulation

The geometry of the barrel test of paragraph 3 was discretized in a finite element mesh and an internal pressure was built up during the initial millisecond of the simulation when a condition of critical damping was also present. At 1 millisecond the fracture was initiated by removal of the constraints between the two sides of the initial notch. From that point on the fracture could propagate unimpeded and the internal pressure was set according to the curves as given in figure 4.12. These curves represent the pressure data derived from the actual barrel tests performed.

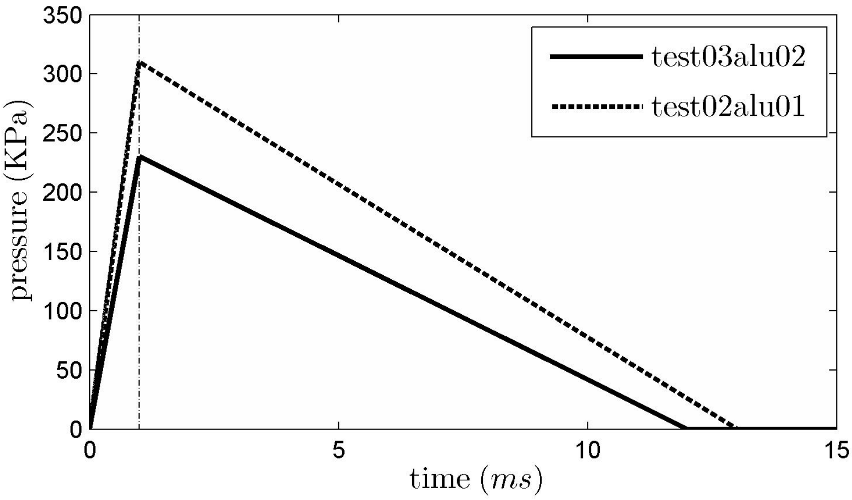

Figure 4.12: Pressure curve for barrel tests

The bulk material was modelled using a simplified Johnson-Cook model with features and properties as listed in appendix H.2. The cohesive zones were of the standard *MAT_COHESIVE_-GENERAL* type, as described in [59]. This type of eight noded cohesive element is rate insensitive and isotropic properties were specified. A maximum traction of 755 $\frac{N}{mm^2}$ and a cohesive energy of 19 $\frac{N}{mm}$ was used. *MAT_COHESIVE_GENERAL* uses an arbitrary piecewise user defined TSL. In this research a tri-linear TSL was used, according to the Tvergaard model as described in section 2.2.4.

The simulated fracture velocities are shown in figure 4.13. The higher pressure test shows a maximum velocity of about 1200 m/s, while the lower pressure test stabilizes at 1100 m/s.

4.4 Capturing the speed of fracture

This research depends heavily on the possibility of obtaining the rate of fracture in finite element calculations. LS-DYNA, nor its post processor LS-PREPOST [60] has a build in solution to monitor the progress of fractures. Calculating fracture propagation profiles is a task left to the user. To do this, the first step is to obtain the time the fracture passed certain points along the fracture path at known distances from the initial fracture front. This can be accomplished in several ways but the highest fidelity can be reached by considering each individual fracture increment separately.

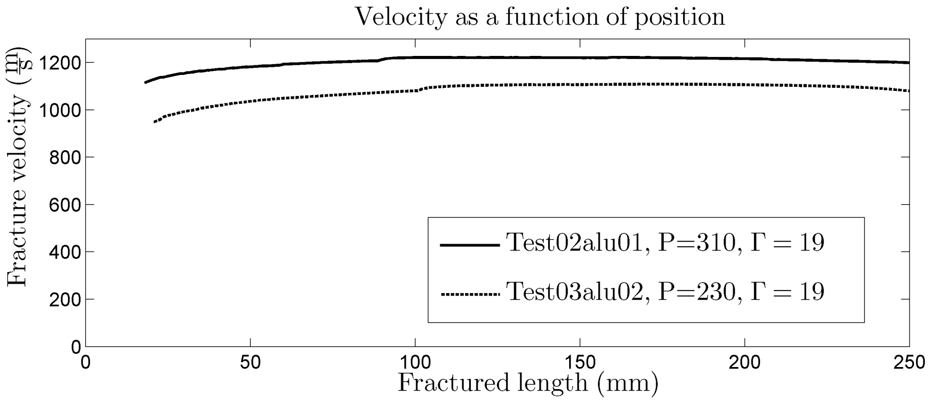

Figure 4.13: Simulated fracture speeds in aluminium, barrel test

A fracture grows as cohesive zone elements fail in its path, and LS-DYNA reports elemental failures in its message log. Only the time of failure and the element number are reported. Attributing the failure message to a specific fracture and calculating the added length of the fracture is performed by various MATLAB programs parsing the message logs, looking up the element number in the mesh file and adding the relevant distance to the fracture tip positions. Simple numerical differentiation is then used to derive a crude fracture velocity profile.

$$velocity_{\mathrm{n}} = \frac{position_{\mathrm{n+1}} - position_{\mathrm{n}}}{t_{\mathrm{fail,n+1}} - t_{\mathrm{fail,n}}} \tag{4.3}$$

The data derived consists of a series of locations and times of failure along with a crude fracture velocity estimate. The problem is, that the dependent variable is time in this format, and fracture tip location is the independent variable. This poses problems with deriving derivations and the smoothing of data. Equation 4.3 goes to infinity as the time between failures approaches zero. As we are dealing with discrete time steps, it can occur that consecutive elements fail in the same time step, and so share a time of failure. This can be solved by adding all the fracture increases into a single "event" per timestep, thus preventing local displacement jumps and making the fracture tip displacement curve continually differentiable. Equation 4.3 now produces finite solutions across the domain, yet the results are still highly unstable. Higher order methods cannot be used to correct this as they require constantly spaced time steps.

The unstable fracture velocity is not the result of numerical problems but is a consequence of the way the data is obtained. The time step is approximately constant during the solving of the finite element model, and the number of timesteps between failures is a natural number by definition. Only time steps with at least one failure are present in the fracture data profile. As simple numerical differentiation is used, this results in the fracture velocity profile to have a semi discrete form with velocity values equal to $V = \frac{\Delta x}{n \cdot \Delta t}$ where $n = \in \{\mathbb{N} > 0\}$. Even a constant velocity fracture will produce an unstable, almost discrete, velocity profile if the number of time steps per element failure is not very high. A solution would be to take very small time steps, but this would also increase the required calculation time, which can quickly become unacceptably long if the desired level of smoothness increases. Increasing the number of time steps does not alter the shape or magnitude of the velocity profile but does smooth it as was confirmed with a number of simulations.

4.4.1 Smoothing

Another option is the application of a filtering technique. The filter needs to be applied to the failure time series as the smoothing of the fracture tip position series has no effect because it is already linear for the regular meshes used. A discrete Gaussian convolution filter was written to process the time data.

$$f_i^* = \sum_{j=-\sigma\cdot m}^{-\sigma\cdot m} f_{i+j} \cdot g_j \cdot Q_i \tag{4.4}$$

Where $\bar{f}$ is an array containing n entries of all the times of failure for the cohesive zone elements, $\bar{f}^*$ is the smoothed time array, $\bar{g}$ is a array with $n = 2 \cdot \sigma \cdot m + 1$ elements, with its values according to a Gaussian distribution centred at $g_{j=0}$ and a standard deviation of σ elements. m is the number of standard deviations of accuracy considered in the infinite Gaussian interval. $\bar{g}$ is scaled by factor Q_g so that the sum of the product $g_j \cdot Q_i$ is equal to unity, or:

$$Q_i = \frac{1}{\sum g_j} \tag{4.5}$$

The elements of $\bar{g}$ are obtained from the *Gaussian* or *normal* probability density function, that can be written in its zero centred form as

$$g_j = \frac{1}{\sigma\sqrt{2\,\pi}}\, e^{-\frac{j^2}{2\,\sigma^2}} \tag{4.6}$$

Where $j =\in \mathbb{Z}$.

It is clear that equation 4.4 is impossible for values of i smaller then $\sigma \cdot m$ or larger the $n - sigma \cdot m$. This leads to a clipping of the time data. To reduce the amount of clipping, the value of m is dynamically reduced at the edges of the $\bar{f}^*$ tensor. Values of f_i^* where $i < \sigma$ or $n - i > \sigma$ are still omitted because their inclusion could potentially yield unrealistic spikes in the data. An example of the problematic nature of the fracture velocity together with smoothed curves derived using different standard deviations and edge clipping turned on and off, can be seen in figure 4.14.

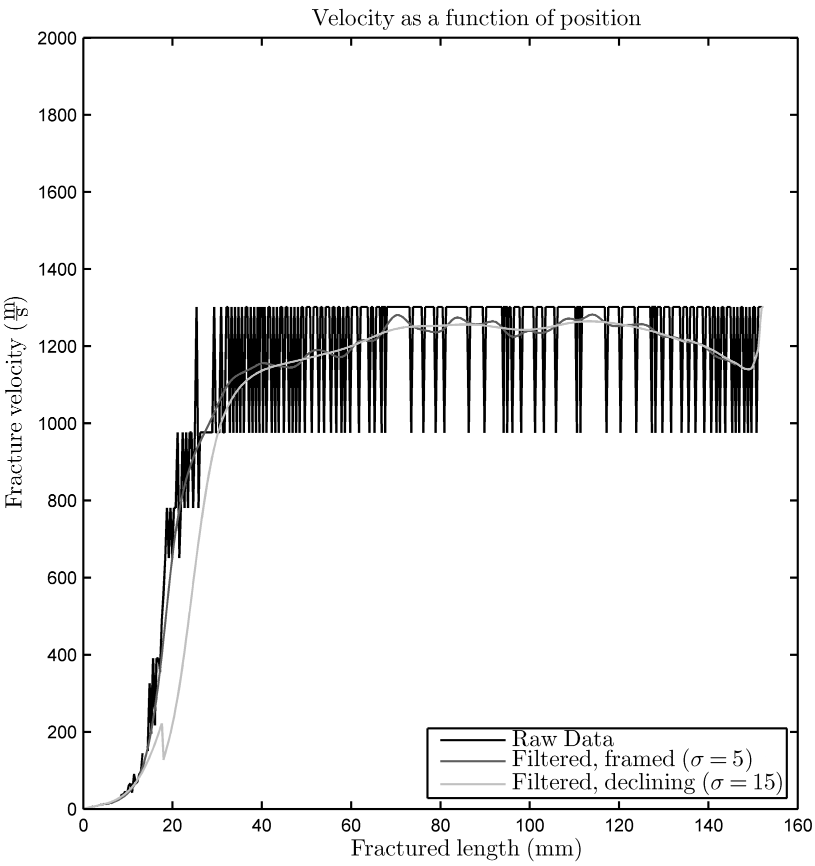

Figure 4.14: Example of a smoothed data set

4.5 Connecting shells to cohesive zones

In the existing meshes for the barrel geometry, two rows of cohesive zone elements run parallel to each other along the length of the fracture, their top and bottom faces are lined with shell elements with a certain strength, inertia and stiffness. These are then in turn connected to the shells making up the bulk of the barrel mesh. This situation is depicted in figure 4.15a for an unloaded cross-section.

A problem arises when the cohesive zone layer is loaded. The shells lining the cohesive zones lack the required stiffness to load the whole cross-section of the cohesive zone. In fact, the nodes at the ends remain stationary until failure of the cohesive zone element. This situation is depicted in figure 4.15b.

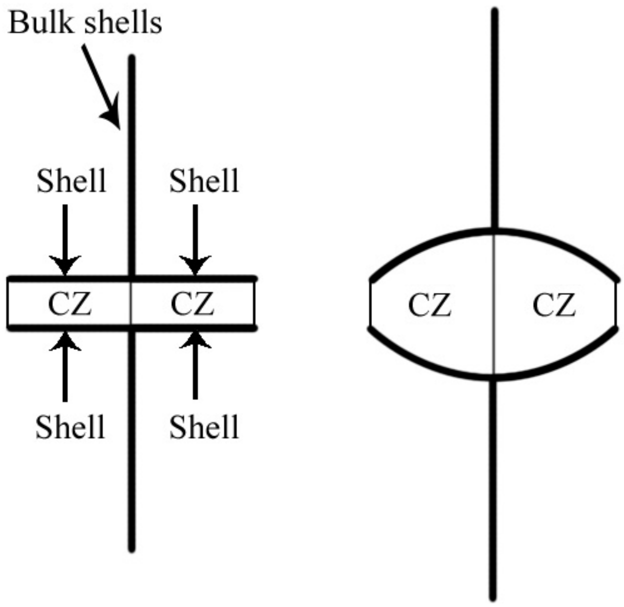

(a) Unloaded state (b) Loaded state

Figure 4.15: Problems with original shell - solid interface

The amount of dissipated energy is effected by this problem as the displacement is evaluated at the four gauss points of the cohesive zone. When any of the gauss points reaches the maximum opening allowed, the complete element fails, not dissipating the remaining opening - traction energy in the three remaining gauss points. It is possible to fail an element only when all gauss points have failed, but the flexibility of the covering shells makes this impossible as a fracture may pass with half the element remaining intact and continuing to exert a traction on the fracture flanks and thus slowing the fracture down in a physical impossible way.

Solutions were sought to solve the before mentioned problem. As a first approach the stiffness of the covering shells was increased and the width of the cohesive zones decreased. The maximum cohesive energy and traction were scaled to correct for the decrease in width. It is noted that the layers of shells covering the cohesive zones constitute an increase of the material around the fracture without a physical counterpart. An increase in this shell stiffness would drive the model further from reality. A shortening of the cohesive zone width has an opposite and thus positive effect, but has problems with regard to scaling associated with it. To test the performance of the proposed solutions, simulations were ran where the width of the cohesive zone elements and stiffness of the covering shells were varied. Figure 4.16 shows a collection of results of the simulations performed, the numbers in the description indicate the relative level of the given quantity as compared to the original (defective) mesh. The cohesive energy was scaled to keep the energy dissipation equal for al simulations. The fourth item in the graph "New mesh" is obtained by using a newly derived interface based on nodal constraints, that will be discussed in the following section. This interface does not suffer from the problems as outlined in this section and is therefore a benchmark to judge the other techniques.

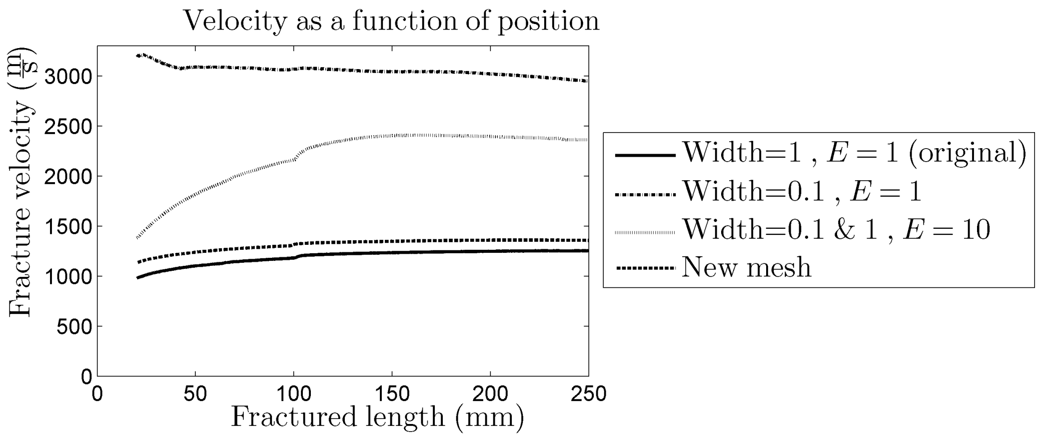

Figure 4.16: Velocity graphs of different shell solid interface solutions

Efforts to correct for the bending of the covering shells proved to be contra-productive. Another reason for using the (more laborious) nodal constraints method is the fact that reducing the width of the cohesive zones or increasing the stiffness of the covering shells, also lowers the Courant [3] limit as these are likely the time step defining elements.

4.5.1 Newly developed interface

A nodal constraint to circumvent the problems outlined in the previous section, exists within LS-DYNA, but this feature is not recognized by the mesher. For this purpose a MATLAB procedure was written that generates a fully operational cohesive zone mesh that can be imported into any bulk mesh and stitched into it. The source code is given in appendix M.

The nodal constraint procedure used is called "*CONSTRAINED_SHELL_TO_SOLID*" and is used to tie a number of nodes lying in a straight line and belonging to solid elements to a single node lying on the straight line as well and belonging to a shell. The relative position of the single node on the straight line to the two outer nodes of the nodes belonging to the solid elements is then fixed throughout the calculation. Rotation along the central shell node is free and in a situation where moments can exist along this axis the solution is not possible, however this is not the case in a barrel subjected to hoop stress.

[3]See § 5.4.2.

Figure 4.17 shows a single cohesive zone element tied to two shells in this manner. Node 5, belonging to the shell is forced to remain in the middle of nodes 1 and 2, belonging to the cohesive zone element. Node 6 is fixed to the centre of the line 3 - 4. In this way the cohesive zone is bound to the shell mesh. Imposing additional constraints to restrict rotation is not possible as there is a limit of one constraint per node. The hoop stress in the barrel resists a rotation of the cohesive zone however, resulting in correct mode I opening behaviour as can be observed in figure 6.5.

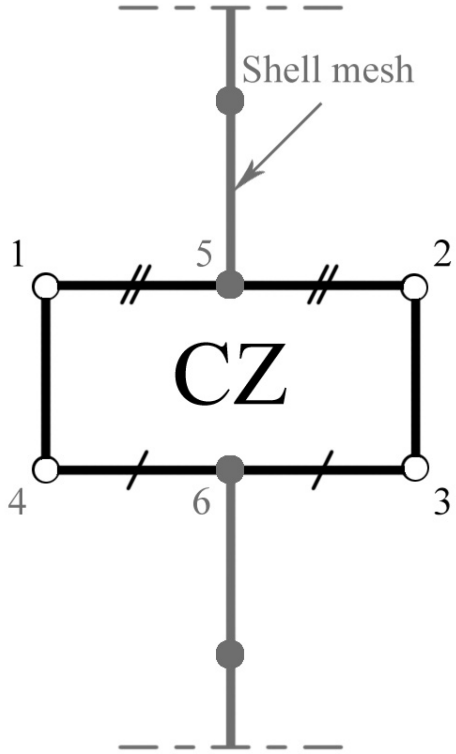

Figure 4.17: Sketch of the cohesive zone interface

LS-DYNA outputs a warning if a cohesive zone has no other elements connected to each of its nodes. Even though the solution with constraints alone is a perfectly valid configuration, it will result in a warning for every cohesive element at the start of the calculation. To prevent this, a zero stiffness and inertia shell is placed on the upper and lower surface of the cohesive zone. This type of element is not included in the stiffness matrix. A 10 element mesh as produced by the code is shown in figure 4.18.

4.6 Discrepancies between experiments and simulations

Significant differences exist between the speeds of fracture as observed in experiments and in simulations. The differences are illustrated below in figures 4.19. It can be observed that the simulations using a rate independent cohesive zone model overestimate the fracture velocity by an order of magnitude. These differences may be explained by the fact that at higher opening rates, a strengthening of the material in the fracture front may develop, resulting in a greater dissipation of energy. The cohesive zones available in LS-DYNA are unable to reproduce such a rate effect and a custom material will need to be developed for LS-DYNA to capture this effect.

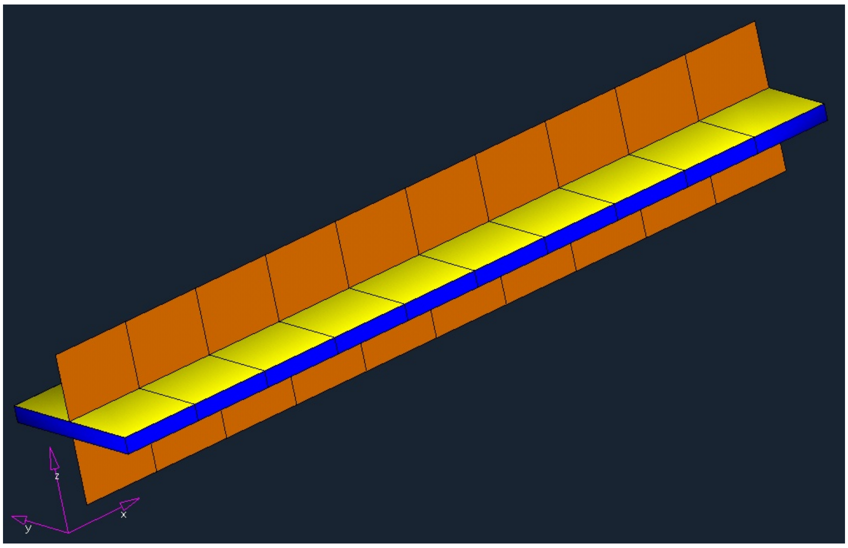

Figure 4.18: Sum mesh of ten cohesive elements

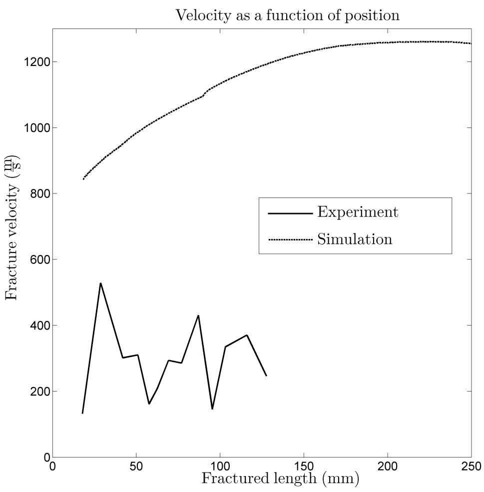

(a) Test02alu01

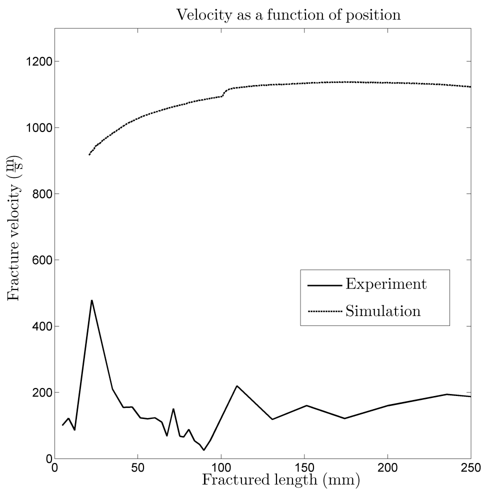

(b) Test03alu02

Figure 4.19: Experiment and simulation in barrel tests

Apart from the overall difference in speed between the simulations and the experiments, Differences related to the method of initiation were observed:

1. Substantial out of plane movement was observed in the plate tests and fracture propagation was jerky and slow as compared to the barrel test. Also the initial shear fracture was rather blunt and the fracture did not reach a stable velocity level. This makes the plate test an unsuitable candidate for comparison with simulation data. The barrel tests do not suffer from these drawbacks, and is therefore to be preferred in future experiments.

2. Due to the initial explosive load in the experiments, momentum is imparted onto the material next to the fracture, leading to a initial spike in fracture speed. Simulated fracture is started with the removal of constraints between two adjacent initial fracture sides and lacks this extra energy. Simulations require a certain time before the material bulges enough out of plane [4], and the fracture speed increases. This difference in initiation leads to a different speed profile in the initial fracture speeds.

3. A second possible source of difference in fracture speed directly after initiation is the damage to the material surrounding the initial fracture. Also the initial notch is not a clean and sharp cut. These disturbances are not accounted for in the finite element simulations.

The difficulties as presented in this section have rendered the prestressed plate test unusable as a fracture speed experiments. The fact that aluminium plates fracture at the same speed as steel plates, while their fracture toughness is an order of magnitude lower, shows the inability of the experimental setup to perform as a valid material dependent fracture test. Therefore the results of the tests performed on it cannot be used as a validation or data source for any cohesive zone material model. As this test was the only one available for duplex steel DIN 1.4462 and the static cohesive properties of this material are also uncertain, it is impossible to develop a rate dependent cohesive zone model for duplex steel DIN 1.4462 at this time on the basis of the data available.

[4] See § 6.3.

Chapter 5

Development of a rate dependent model

This chapter deals with the implementation of a rate dependent cohesive zone model in the commercial finite element code LS-DYNA. To this end, an overview is given of existing rate dependent models in section 5.1. A Perzyna visco-plastic model has been chosen as explained in section 5.2. This was originally developed as a continuum material model, and has been adapted to a cohesive zone formulation. This is done in section 5.3.

An overview of the time-space FE discretization of the balance equation is given in section 5.4. Section 5.5 deals with the numericals aspects of the Perzyna model as it is implemented in a LS-DYNA custom cohesive element model.

5.1 Strain rate dependent models

As has been found in section 4.6, it is not possible to obtain fracture velocities as observed in experiments using the same cohesive energy as for static cases. If the cohesive energy obtained for static fracture is used throughout the simulation of a dynamic fracture, the fracture rates obtained dramatically overestimate the rate of fracture. A possible explanation is that the cohesive energy increases as a result of the higher opening rates associated with dynamic fracture.

During fracture propagation the fracture speed and hence the opening rate may vary. Therefore a static increase in the cohesive energy to a “dynamic” value can never capture the total behaviour of dynamic fracture [1]. In order to describe the total behaviour, a rate dependent cohesive energy is suggested. This allows the cohesive energy to be equal to its static value at initiation, and increase as the fracture accelerates. Rate dependence is a property exhibited by many materials, so it seems a logical phenomenon to incorporate in a cohesive zone model.

Because a static increase of cohesive energy is not able to describe the fracture in its entire path from initiation to complete failure, a rate dependent cohesive energy is suggested. At initiation the cohesive energy can then be equal to a static energy level, while as the fracture accelerates, the energy dissipation increases. Rate dependent models are thus able to describe the entire fracture path and provide the potential for an energetic upper bound to the rate of fracture propagation. Rate dependence is a property exhibited by many materials in a continuum sense. Including it in techniques describing the fracture of the material seems logical.

[1] See also § 6.5.1.

In Section 5.1.1 an overview of existing rate dependent cohesive zone models is given, many of which were derived for use with brittle materials however. It is also possible to derive a cohesive zone model from a continuum material model. Section 5.1.2 gives an overview of likely candidates for this purpose.

5.1.1 Description of existing rate dependent cohesive zone models

Several existing rate dependent cohesive zones models are presented in this section

Anvari

Anvari et al.[61] introduced a rate and triaxiality dependent cohesive zone model for a specific material. A test series was performed on smooth round bars made out of aluminium 6XXX series alloy using split-Hopkinson tension bar tests. The results were used to obtain parameters for a microscopic fracture, Gurson model. The Scheider TSL [46] was then fitted to the predictions of the Gurson model. The end result is a static TSL with a modifier on the maximum traction and cohesive energy.

$$\frac{\Gamma_0}{h} = \begin{cases} 237.6\left(\frac{\dot{\varepsilon}}{\dot{\varepsilon}_0}\right)^m & \text{, For } H < 1.2 \\ 1.43H^{-1.36}\sigma_0\left(\frac{\dot{\varepsilon}}{\dot{\varepsilon}_0}\right)^m & \text{, For } H \geq 1.2 \end{cases} \tag{5.1}$$

$$T = \begin{cases} 474\left(\frac{\dot{\varepsilon}}{\dot{\varepsilon}_0}\right)^m & \text{, For } H < 1.2 \\ (1.1\ln(H) + 2.1)\,\sigma_0\left(\frac{\dot{\varepsilon}}{\dot{\varepsilon}_0}\right)^m & \text{, For } H \geq 1.2 \end{cases} \tag{5.2}$$

H in equation 5.1 and 5.2, is the triaxiality. H is defined in [61] as [SIC]

$$H = \frac{1 + \frac{\sigma_{11}}{\sigma_{22}}}{\sqrt{3}\left(1 - \frac{\sigma_{11}}{\sigma_{22}}\right)} \tag{5.3}$$

The Anvari model requires the strain and stress state of neighbouring continuum elements.

Zhang

Zhang et al.[41] developed a mode I cohesive zone formulation for ductile dynamic fracture propagation using a "multi-scale" approach. This entails that the fracture process zone is separated into two separate regions, the first being the plastic region, governed by a hardening traction-opening function and the second a damage region, described by a decreasing damage function. A graphical depiction of these zones is given in figure 5.1a. The rate sensitive plastic zone formulation is expressed as

$$\hat{t} = \sigma_{\mathrm{ult}}\left(\frac{\delta}{\delta_c}\right)^n\left(1 + \beta_n\dot{\delta}\right) \tag{5.4}$$

Where n is a hardening exponent, β_n the viscosity for plastic deformation and δ_c is the critical opening displacement. The damage region is controlled by

$$\hat{t} = \sigma_{\mathrm{m}}\left(1 - \frac{\delta}{\delta_c}\right)^m\left(1 + \beta_m\dot{\delta}\right) \tag{5.5}$$

Where m is softening index, β_m the viscous coefficient and σ_m is the ultimate tensile strength for the damage zone. The two intersecting functions are shown in figure 5.1b. The transition to the damage region occurs at the intersection of equation 5.4 and 5.5.

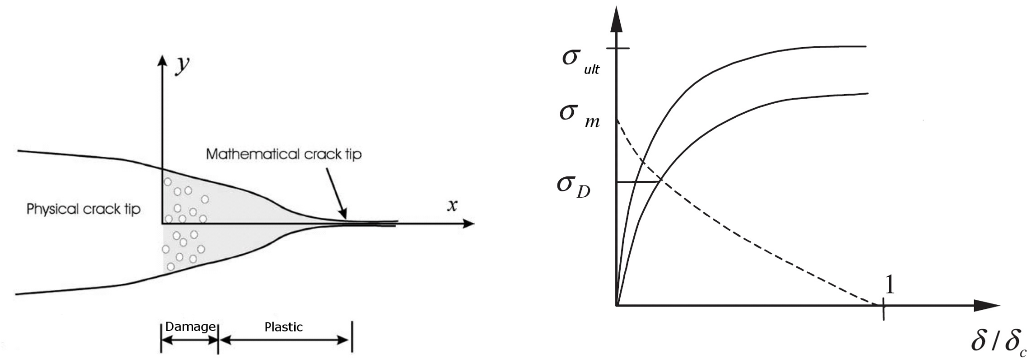

(a) Multi-scale cohesve formulation (b) Intersection of plastic and damage region

Figure 5.1: The Zhang et al. rate dependent cohesive zone model

Corigliano

Corigliano et al.[62] developed a cohesive zone element with an initially linear elastic response until the yield stress and a visco-plastic formulation thereafter, based on the Perzyna model. An example graph is shown in figure 5.2. A noteworthy feature is the increase of the maximum opening at increased opening rates. The model does not distinguish between a potentially more stable traction level at cohesion and a steeper reduction at decohesion or damage. This is expressed in the triangular shape of the TSL and is a feature associated with brittle fracture behaviour where a constant traction level as a result of ductility in the material response is absent [44].

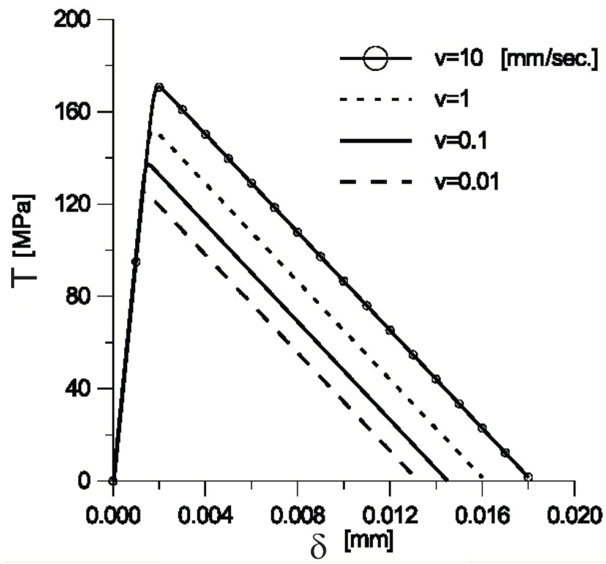

Figure 5.2: Example Corigliano element showing rate dependence

Xu

Xu et al. [63] developed a rate dependent cohesive zone for modelling adhesive bonding in mode I failure. It is based on a standard linear solid model; a spring in parallel with a maxwell[2] element. A schematic is depicted in figure 5.3a. It can be observed that the model has two asymptotic stiffnesses associated with it, one for infinitely fast and the other for infinitely slow loading; for $\lim_{\dot{\delta}\to\infty} E_{\mathrm{eq}} = E_1 + E_2$ and for $\lim_{\dot{\delta}\to 0} E_{\mathrm{eq}} = E_1$. E_1 is the derivative of the non rate dependent TSL, and E_2 presents a secondary cohesive zone stiffness. The dashpot is governed by μ, a parameter that can be used to set a reference opening rate. Figure 5.3b shows an example calculation for different opening rates.

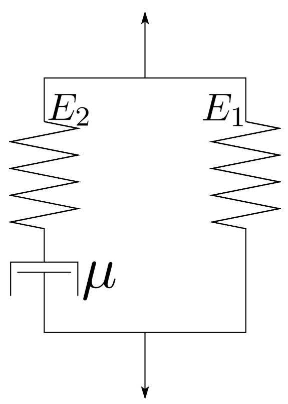

(a) Schematics of model

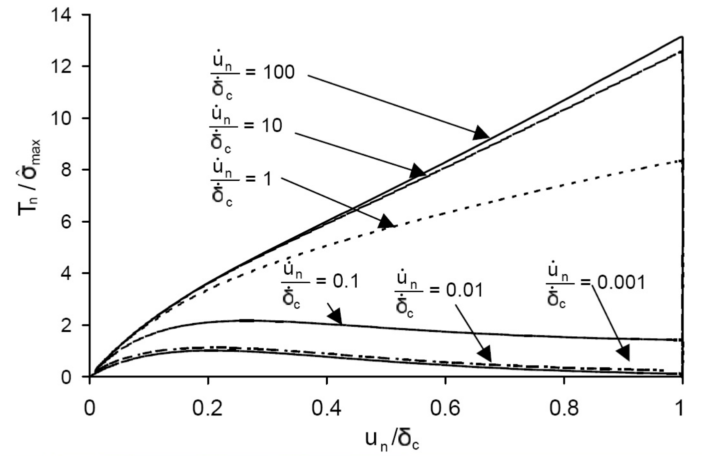

(b) Example showing effect of rate dependency

Figure 5.3: The Xu et al. rate dependent cohesive zone model

Liechti

Liechti et al. [64] defined a cohesive zone based on a non linear Kelvin-Voight[3] unit. A schematic drawing of the model is given in figure 5.4. A displacement imposed on the unit will cause an opposing traction consisting of a reversible, elastic and a dissipative, plastic component

$$\hat{t} = \hat{t}_{\mathrm{spring}}(\delta) + \hat{t}_{\mathrm{dashpot}}(\dot{\delta}) \tag{5.6}$$

The non-linear spring traction $\hat{t}_{\mathrm{spring}}(\delta)$ can be a regular static TSL. The rate dependency is defined by the dashpot. Liechte et al. proposed a tri-linear set of equations to define the non-linear dashpot.

$$\hat{t}_{\mathrm{dashpot}}(\dot{\delta}) = \begin{cases} c_1\dot{\delta} & \text{, For } \quad \dot{\delta} \le \dot{\delta}_1 \\ \hat{t}\left(\dot{\delta}_1\right) + c_2\left(\dot{\delta} - \dot{\delta}_1\right) & \text{, For } \dot{\delta}_1 \le \dot{\delta} \le \dot{\delta}_2 \\ \hat{t}\left(\dot{\delta}_2\right) + c_2\left(\dot{\delta} - \dot{\delta}_2\right) & \text{, For } \dot{\delta}_2 \le \dot{\delta} \end{cases} \tag{5.7}$$

[2]Spring and dashpot in series, named after James Clerk Maxwell who proposed the model in 1867
[3]Spring and dashpot in parallel, named after Baron William Thomson Kelvin and Woldemar Voigt

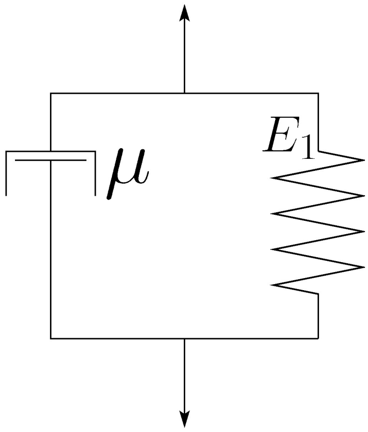

Figure 5.4: Non linear Kelvin-Voigt unit

Rahul-Kumar

Rahul-Kumar et al. [65] introduced a cohesive zone model where the traction is a product of an arbitrary TSL and a rate dependent expression.

$$\hat{t} = \hat{t}_{\text{TSL}}\left(\delta\right)\left(1 + \left(\frac{\dot{\delta}}{\dot{\delta}_0}\right)^n\right) \tag{5.8}$$

Fagerström

Fagerström et al.[66] created a "prototype viscous interface model" based on the Perzyna [67] system of visco-plastic equations and a linear damage formulation based on the plastic material opening. The system of equations is given as

$$\begin{aligned}
\dot{\boldsymbol{\delta}}_{\boldsymbol{vp}} &= \frac{1}{c^*}\left(\frac{\langle F_{qs}\rangle}{\sigma_y}\right)^{\frac{1}{m}}\frac{\boldsymbol{M}}{|\boldsymbol{M}|} && (5.9)\\
F_{qs} &= \sigma_y\left(\frac{\langle\hat{Q}_n\rangle}{\sigma_y}\right)^2 + \sigma_y\left(\frac{\hat{Q}_t}{\gamma\sigma_y}\right)^2 - \sigma_y && (5.10)\\
\boldsymbol{M} &= \frac{\partial F_{qs}}{\partial\hat{\boldsymbol{Q}}} = 2\frac{\langle\hat{Q}_n\rangle}{\sigma_y}\boldsymbol{e_n} + 2\frac{\langle\hat{Q}_t\rangle}{\gamma^2\sigma_y}\boldsymbol{e_t} && (5.11)\\
\hat{\boldsymbol{Q}} &= \boldsymbol{K}\cdot\boldsymbol{\delta}_{\text{el}} && (5.12)
\end{aligned}$$

A damage parameter α is defined with the help of damage calibrating parameter S.

$$\dot{\delta}_{\mathbf{vp}} = S\dot{\alpha}\boldsymbol{M} \tag{5.13}$$

$\dot{\alpha}$ is used to describe the decreasing tractions as an element is opening up according to

$$\hat{\boldsymbol{t}} = \boldsymbol{t}\cdot(1-\alpha) \tag{5.14}$$

Equations 5.12 and 5.13 combine into a visco-plastic cohesive zone model with a close resemblance to the Corigliano model. An example graph, showing the effect of opening rate is given in figure (5.5)

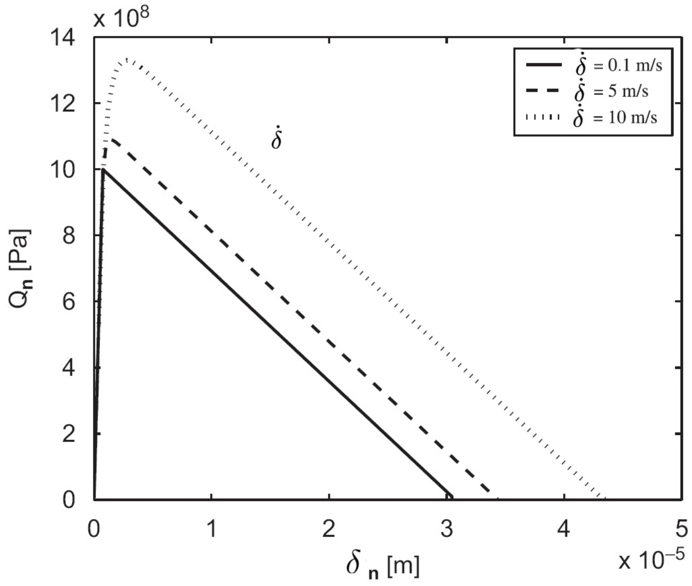

Figure 5.5: The rate dependent Fagerström model

5.1.2 Description of existing rate dependent continuum models

Apart from the existing rate sensitive cohesive zone models as as described in section 5.1.1, it is also possible to convert a continuum material model to a cohesive zone form. Two existing rate dependent continuum models were identified for this purpose and these will be discussed hereafter.

Perzyna

Perzyna et al. [67] developed a visco-plastic strain rate dependent material model with work hardening. The system of constitutive equations describing the model is given in equations 5.15 to 5.19.

$$\psi(\sigma_{eq}) = \left\langle \frac{\sigma_{eq} - \sigma_y}{\sigma_0} \right\rangle^{N_{\mathrm{pz}}} \tag{5.15}$$

$$\boldsymbol{M} = \frac{\partial \sigma_{eq}}{\partial \boldsymbol{\sigma}} \tag{5.16}$$

$$\dot{\boldsymbol{\varepsilon}}_{\boldsymbol{vp}} = \frac{1}{\eta}\psi(\sigma_{eq})\boldsymbol{M} \tag{5.17}$$

$$\dot{\boldsymbol{q}} = \frac{1}{\eta}\psi(\sigma_{eq})\boldsymbol{M}h_{pz} \tag{5.18}$$

$$\dot{\boldsymbol{\sigma}}_{\boldsymbol{el}} = \dot{\boldsymbol{\sigma}} - \dot{\boldsymbol{\sigma}}_{\boldsymbol{vp}} = \boldsymbol{E} : (\dot{\boldsymbol{\varepsilon}} - \dot{\boldsymbol{\varepsilon}}_{\boldsymbol{vp}}) \tag{5.19}$$

Where $\psi(\sigma_{eq})$, as defined in equation 5.15 is known as the overstress function. The brackets in this function are Mc Cauley[4] brackets. The overstress function describes the relative stress level above the elastic limit and it can be easily seen that the function is equal to zero if the equivalent stress is below the yield stress. The equivalent stress formulation σ_{eq} will be The tensor $\boldsymbol{M}$ in equation 5.16 represents the normality rule.

[4]The Mc Cauley brackets indicate that the value of the bracketed part is equal to the value of the function within the brackets if it is a positive number, otherwise it is equal to zero. Mathematically this may be expressed as $\langle g(x) \rangle = \frac{|g(x)|+g(x)}{2}$

Equation 5.17 describes the amount of strain increase that does not lead to an elastic strain increase. When any material is loaded to a level below its yield limit, the value $\dot{\varepsilon}_{vp}$ is equal to zero and the response of the material is fully elastic. When the stress is increased past the elastic limit however, the overstress function 5.15 rises, causing the visco-plastic strain rate $\dot{\varepsilon}_{vp}$ to increase as well. Combined with equation 5.19, this means that for a steady strain rate, and a rising strain, the visco-plastic strain rate will become equal or greater than the actual strain rate. The material will therefore display a decreasing stiffness past its yield stress, with an ever increasing part of the material response being plastic rather than elastic, until the visco-plastic strain rate is equal to the actual strain rate and the material is fully plastic. At this point, ceteris paribus, the stress has reached an asymptotic value equal to the ultimate stress level $\sigma_{\text{ult}}(\dot{\varepsilon}_{eq})$ at the given strain rate. $\boldsymbol{E}$ in equation 5.19 is the fourth order stiffness tensor.

The equivalent stress formulation σ_{eq} is not specified in [67]. For an isotropic metal, the von Mises [68] yield stress is a logical choice.

$\dot{\mathbf{q}}$ represents the evolution of the work hardening. It is integrated to calculate $\boldsymbol{q}$ with integration constant one. $\boldsymbol{q}$ is multiplied to the yield stresses in the calculation of σ_{eq} to describe a strengthening of the material through plastic work. Section 5.5 describes this in more detail. Work hardening is an increase in the yield stress of a material as a result of repeated plastic work being done. Because this thesis is focused on single dramatic failure by fracture and not on fractured growth by cyclic loading, work hardening is not expected to play a role. It is implemented however in the developed material model to allow it to be used in more situations.

Chaboche

The Chaboche model [69] is a continuum visco-plastic model, and is defined by the the following system of equations.

$$\dot{\varepsilon} = \left\langle \frac{f}{Z} \right\rangle^{n} \cdot \operatorname{sign}(\sigma - \chi) \tag{5.20}$$

$$f = -\langle -j(\sigma - \chi) + R + K \rangle \tag{5.21}$$

$$J(\sigma - \chi) = |\sigma - \chi| \tag{5.22}$$

$$\chi = \chi_1 + \chi_2 \tag{5.23}$$

$$\dot{\chi}_i = C_i \left(a_i \dot{\varepsilon}_p - \chi_i \dot{P} \right) \qquad i = 1, 2 \tag{5.24}$$

$$\dot{P} = |\dot{\varepsilon}_p| \tag{5.25}$$

$$\dot{R} = b(Q - R)\dot{P} \tag{5.26}$$

Where j is the von Mises stress, k is the initial yield stress,χ is the kinematic hardening variable and R is the isotropic hardening. Apart from the multi stage kinematic hardening, The model is almost identical to the Perzyna model after some rearranging.

5.2 Choice of cohesive formulation

The rate dependent models discussed in section 5.1 share the property of their empirical nature. Selection of the model is therefore different than selecting the physically “right” model. Nevertheless, a choice of rate dependent cohesive zone model can be made based on the features the model provides and its applicability both to the material to be modelled as the finite element software used. The different models are compared based on the following set criteria.

Continuous: A model with this property has a continuously differentiable response to discontinuous opening rates. Continuous models have the advantage that discontinuities in the opening or strain rates do not result in corresponding discontinuities in the increased traction. This is an important feature in cohesive zones as they are in an elastic or destroyed state the vast majority of the time steps, but experience a sudden jump in opening rates as the fracture tip reaches them. Especially when the time steps are large this would lead to physically unrealistic jumps in the increased traction as well.

Rate sensitive maximum opening: All rate sensitive models offer a rate sensitive maximum traction, but some also include a rate sensitive maximum opening. The possibility of having a rate sensitive maximum opening is favourable property of any model. However, it is unknown if duplex steel or aluminium 2024 T3 exhibit this property. Including this feature would create more unknowns without the possibility of acquiring their values due to the limited amount of (experimental) data. Therefore the possibility of including a rate sensitive maximum opening is considered an advantage nor a disadvantage for the purpose of this research.

Visco-Plasticity: Visco-plasticity is a model for rate dependent plasticity. Visco-plasticity is not an advantage in itself, though visco-plastic models intrinsicly feature some of the favourable properties discussed in this section such as plasticity, a continuous response and the possibility to use it for ductile fracture. Figure 5.6 shows the continuous response of a visco-plastic, Perzyna type model subjected to a discontinuous opening rate.

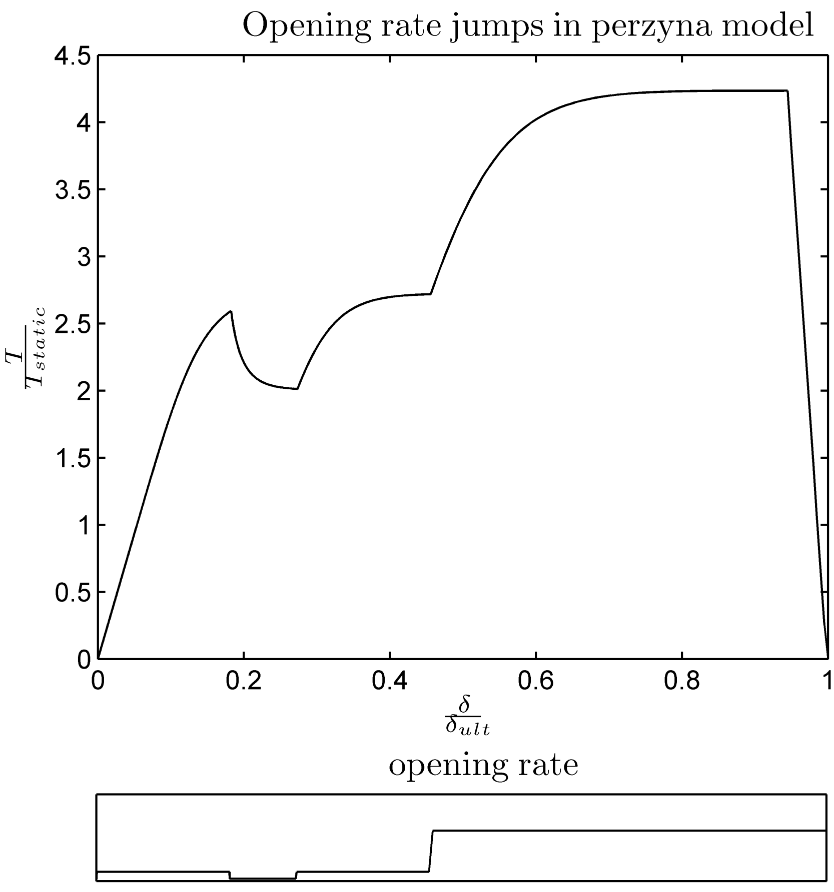

Figure 5.6: The effect of discontinious opening rates on a perzyna model

Triaxiality: The triaxiality of the stress state influences the cohesive zone behaviour; an increase of triaxiality leads to a higher cohesive energy and its inclusion in the cohesive zone model can offer a more realistic model behaviour. However the influence of triaxiality is not known for the materials examined in this research. and inclusion of triaxiality would only lead to more unsolvable unknowns. Apart from this concern, it is not possible to include triaxiality in custom cohesive zone models in LS-DYNA in any case; the required knowledge of the triaxiality of the material is not available within the cohesive zone elements and it is not possible to obtain this information from adjacent bulk material due to limitations of LS-DYNA.

Ductile: While most rate dependent models were developed for brittle materials, Some were developed for specifically for ductile fracture; exhibiting a plateau in the TSL. Duplex steel DIN 1.4462 and aluminium 2024 T3 are examples of ductile materials at room temperature. Fracture of these materials needs to be simulated in cohesive zone models with traction separation laws capable of reproducing the constant traction levels associated with the void coalescence fracture process.

Plastic: Some of the models are fully plastic instead of non linear elastic. Plasticity indicates that after plastic deformation and subsequent unloading, the plastic deformation remains. Non linear elastic models do not have a remaining deformation after loading past the yield traction and subsequent unloading. If the unloading path is also equal to the loading path, as is the case in these models, this means there is no energy dissipation in cyclic loading below the ultimate opening limit. This is undesirable behaviour from a physical reality standpoint, and therefore ductility is required of the rate dependent cohesive zone model used for this research.

The features of the different models discussed in section 5.1 are summarized in table 5.1

	Continuous	r.s. opening	Visco-plastic	Triaxciality	Ductile	Plastic
Anvari				Yes	Yes	
Zhang					Yes	
Corigliano	Yes	Yes	Yes			yes
Liechti						
Rahul-kumar						Possible
Fagerström	Yes	Yes	Yes			yes
Chaboche	Yes	Possible	Yes	Possible	Possible	yes
Perzyna	Yes	Possible	Yes	Possible	Possible	yes

Table 5.1: Feature comparison chart for rate dependent models

Based on the considerations brought forward in this section, it was decided that the rate dependent cohesive zone model for usage in this research is not to have triaxiality dependence. Furthermore, both plasticity and the ability to model ductile fracture processes are deemed paramount. The only models able to fulfill these criteria are the Perzyna and the Chaboche model. Neither of these models is originally a cohesive zone element model, and their usage will involve an adaption from a continuum form.

The Chaboche model was decided against because of its close resemblance to the Perzyna model, with the only mayor difference being the more complex kinematic hardening equation.

In a situation of limited experimental data available for the calibration of the added parameters, this is not an advantageous property. The rate dependent cohesive zone model as used in this research will therefore be based on the Perzyna model.

5.3 Rewriting the Perzyna model to a cohesive zone formulation

The Perzyna visco-plastic model presented in section 5.1.2 was defined in terms of strains $\boldsymbol{\varepsilon}$ and stresses $\boldsymbol{\sigma}$ In a cohesive zone element model, the openings $\boldsymbol{\delta}$ need to be related to tractions $\hat{\boldsymbol{t}}$ instead. The system of continuum equations 5.15 to 5.19 is transformed into the following cohesive zone element model.

$$\begin{aligned}
\psi(\hat{t}_{eq}) &= \left\langle \frac{\hat{t}_{eq}}{T} - 1 \right\rangle^{N_{\mathrm{pz}}} && (5.27)\\
\boldsymbol{M} &= \frac{\partial \hat{t}_{eq}}{\partial \hat{\boldsymbol{t}}} && (5.28)\\
\dot{\boldsymbol{\delta}}_{\boldsymbol{vp}} &= \frac{1}{\eta}\psi(\hat{t}_{eq})\boldsymbol{M} && (5.29)\\
\dot{\boldsymbol{q}} &= \frac{1}{\eta}\psi(\hat{t}_{eq})\boldsymbol{M} \cdot h_{pz} && (5.30)\\
\dot{\hat{\boldsymbol{t}}}_{\boldsymbol{el}} &= \dot{\hat{\boldsymbol{t}}} - \dot{\hat{\boldsymbol{t}}}_{\boldsymbol{vp}} = K(\dot{\boldsymbol{\delta}} - \dot{\boldsymbol{\delta}}_{\boldsymbol{vp}}) && (5.31)
\end{aligned}$$

Where K is the stiffness of the cohesive zone. Equation 5.27 was simplified by setting the reference traction level equal to the yield traction.

5.3.1 Equivalent traction

The Perzyna model uses a single stress parameter $\hat{t}_{eq}$ to describe the three dimensional stress state. It is not specified what this should be, as different materials require different failure criteria. A logical first approach for metals is to use the *von Mises* yield stress

von Mises yield stress

The von Mises yield stress σ_v [68, 70] is based on limiting the value of the second invariant of the deviator tensor to the known shear stress of a material. This means σ_v is independent of the hydrostatic stress and it describes at which deviation from a hydrostatic stress situation yielding will start to occur. The yield stress in pure tension is a factor $\sqrt{3}$ higher than the shear strength, so the equivalent von Mises stress σ_v can be calculated as a function of the second invariant in a three dimensional stress state:

$$\sigma_v = \sqrt{3J_2} \tag{5.32}$$

This can be written out as a function of the Cauchy stress tensor components.

$$(\sigma_{11} - \sigma_{22})^2 + (\sigma_{22} - \sigma_{33})^2 + (\sigma_{11} - \sigma_{33})^2 + 6(\sigma_{23}^2 + \sigma_{31}^2 + \sigma_{12}^2) = 2\sigma_v \tag{5.33}$$

Because the von Mises stress is to be implemented in a cohesive zone, only three Cauchy stress tensor components are taken into account. The first two act along two perpendicular vectors lieing in the plane of the cohesive zone and are associated with Mode II/III deformations, the vector of the third stress is perpendicular to the other two and the plane of the cohesive zone and is associated with Mode I fracture opening. Roman numerals are used as sub indices to distinguish between modes and Gauchy stress components. The three tractions are related to their Cauchy tensor counterparts through:

$$\begin{aligned}\hat{t}_{\mathrm{I}} &= \sigma_{11}\\ \hat{t}_{\mathrm{II}} &= \sigma_{13}\\ \hat{t}_{\mathrm{III}} &= \sigma_{12}\end{aligned} \tag{5.34}$$

Combining equation 5.33 and 5.34, leads to:

$$\hat{t}_v = \sqrt{3\hat{t}_{\mathrm{III}}^2 + 3\hat{t}_{\mathrm{II}}^2 + \hat{t}_{\mathrm{I}}^2} \tag{5.35}$$

Dividing equation 5.35 by $\hat{t}_y$ yields the yield criterion, where a value of one or higher indicates yielding.

$$\frac{\hat{t}_v}{\hat{t}_y} = \sqrt{\frac{3\hat{t}_{\mathrm{III}}^2}{\hat{t}_y^2} + \frac{3\hat{t}_{\mathrm{II}}^2}{\hat{t}_y^2} + \frac{\hat{t}_{\mathrm{I}}^2}{\hat{t}_y^2}} \tag{5.36}$$

In stead of the yield traction $\hat{t}_y$ we want to write equation 5.36 in terms of the maximum traction T and S, the maximum cohesive traction in Mode I and Mode II/III respectively. The von Mises yield criterion has a fixed relationship between the yielding force in shear and in tension, this couples T and S as well. Setting the maximum traction in Mode I, T, equal to the yield traction $\hat{t}_y$ leads to

$$\begin{aligned}T &= \hat{t}_y\\ S &= \sqrt{\frac{\hat{t}_y^2}{3}}\end{aligned} \tag{5.37}$$

Combining equation 5.36 and 5.37 and multiplying both sides with T leads to:

$$\hat{t}_{eq} = \hat{t}_v = T\sqrt{\frac{\hat{t}_{\mathrm{III}}^2}{S^2} + \frac{\hat{t}_{\mathrm{II}}^2}{S^2} + \frac{\hat{t}_{\mathrm{I}}^2}{T^2}} \tag{5.38}$$

The drawback of this formulation is the coupling of the parameters S and T. For the use of equation 5.38 as a cohesive zone equivalent traction, the two need to be independent of one another. A failure criterion that offers independent yield stress levels in orthogonal directions would be able to provide such flexibility. The quadratic Hill criterion is such a model

Hill yield stress

The quadratic Hill [70] criterion is anisotropic yield model and is an extension of the von Mises yield criterion. It is presented below in equation 5.39.

$$\begin{aligned}F(\sigma_{22}-\sigma_{33})^2 + G(\sigma_{33}-\sigma_{11})^2 + H(\sigma_{11}-\sigma_{22})^2\\ + 2L\sigma_{23}^2 + 2M\sigma_{31}^2 + 2N\sigma_{12}^2 = 1\end{aligned} \tag{5.39}$$

With the parameters F to N defined as:

$$
\begin{aligned}
F &= \frac{1}{2}\left[\frac{1}{(\sigma_2^y)^2} + \frac{1}{(\sigma_3^y)^2} - \frac{1}{(\sigma_1^y)^2}\right] \\
G &= \frac{1}{2}\left[\frac{1}{(\sigma_3^y)^2} + \frac{1}{(\sigma_1^y)^2} - \frac{1}{(\sigma_2^y)^2}\right] \\
H &= \frac{1}{2}\left[\frac{1}{(\sigma_1^y)^2} + \frac{1}{(\sigma_2^y)^2} - \frac{1}{(\sigma_3^y)^2}\right] \\
L &= \frac{1}{2\ (\sigma_{23}^y)^2} \\
M &= \frac{1}{2\ (\sigma_{13}^y)^2} \\
N &= \frac{1}{2\ (\sigma_{12}^y)^2}
\end{aligned}
\tag{5.40}
$$

Transcribing equation 5.39 with the help of the cohesive zone stress definition equation 5.34 yields:

$$G \cdot \hat{t}_{\mathrm{I}}^2 + H \cdot \hat{t}_{\mathrm{I}}^2 + 2M \cdot \hat{t}_{\mathrm{II}}^2 + 2N \cdot \hat{t}_{\mathrm{III}}^2 = 1 \tag{5.41}$$

The maximum traction T and S are now set as the yield stress in normal and shear loading respectively.

$$
\begin{aligned}
\sigma_1^y = \sigma_2^y = \sigma_3^y &= T \\
\sigma_{23}^y = \sigma_{13}^y = \sigma_{12}^y &= S
\end{aligned}
\tag{5.42}
$$

Applying equations 5.42 to equations 5.40 yields:

$$
\begin{aligned}
F = G = H &= 1/2\left[\frac{1}{T^2}\right] \\
L = M = N &= 1/2\left[\frac{1}{S^2}\right]
\end{aligned}
\tag{5.43}
$$

Combining equations 5.43 and 5.41 gives the anisotropic, Hill based, cohesive zone failure criterion.

$$\frac{\hat{t}_{\mathrm{III}}^2}{\mathrm{S}^2} + \frac{\hat{t}_{\mathrm{II}}^2}{\mathrm{S}^2} + \frac{\hat{t}_{\mathrm{I}}^2}{\mathrm{T}^2} = 1 \tag{5.44}$$

We can take the square root of both sides of equation 5.44 and then multiply with T to arrive at an equivalent stress formulation.

$$\hat{t}_{eq} = T\sqrt{\frac{\hat{t}_{\mathrm{III}}^2}{\mathrm{S}^2} + \frac{\hat{t}_{\mathrm{II}}^2}{\mathrm{S}^2} + \frac{\hat{t}_{\mathrm{I}}^2}{\mathrm{T}^2}} \tag{5.45}$$

This equation is identical to the one obtained from the von Mises failure criterion, equation 5.38. There is one mayor difference however, the values of S and T may be set independently in the Hill equivalent stress definition. This allows different maximum tractions to be defined for Mode I and Mode II/III opening directions. This feature is critical for the cohesive zone to be able to accurately model fracture in all modes. If S and T are set conforming to (5.37), the Hill criterion reverts back to the von Mises criterion.

Fracture growth is independent of normal compressive traction and Mc Cauley brackets are added to equation 5.45 to take this into account numerically.

$$\hat{t}_{eq} = T\sqrt{\frac{\hat{t}_{\mathrm{III}}^2}{\mathrm{S}^2} + \frac{\hat{t}_{\mathrm{II}}^2}{\mathrm{S}^2} + \left\langle \frac{\hat{t}_{\mathrm{I}}^2}{\mathrm{T}^2} \right\rangle} \tag{5.46}$$

Figure 5.7 gives a graphical representation of yield surface expressed in equation 5.46. The maximum tractions were set as $T = 2, S = 1$.

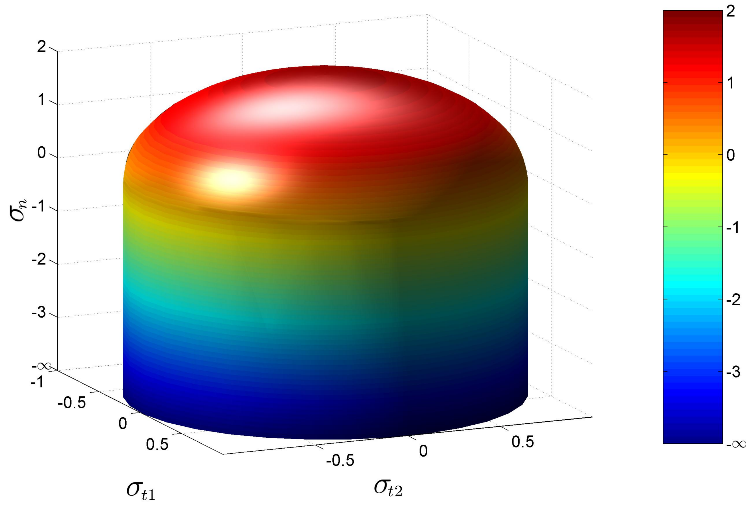

Figure 5.7: Hill yield surface for cohesive zones

A final modification needs to be made to be able to account for work hardening. Contrary to the name, this relation does not need to be a positive one; for example, LS-DYNA does not pass temperature information to cohesive elements, but as temperature is a linear function of dissipated energy or work, a negative work hardening parameter may be used to take into account thermal softening. The inclusion of work hardening transforms equation 5.46 into the required equivalent stress formulation for use in the rate sensitive cohesive zone model.

$$\sigma_{eq} = T\sqrt{\frac{\left(\frac{\hat{t}_{\mathrm{III}}}{q_{\mathrm{III}}}\right)^2}{\mathrm{S}^2} + \frac{\left(\frac{\hat{t}_{\mathrm{II}}}{q_{\mathrm{II}}}\right)^2}{\mathrm{S}^2} + \left\langle \frac{\left(\frac{\hat{t}_{\mathrm{I}}}{q_{\mathrm{I}}}\right)^2}{\mathrm{T}^2} \right\rangle} \tag{5.47}$$

5.4 Finite element method

5.4.1 formulation

The principle of virtual work can be used to derive the FEM formulation. In this section the governing equation is derived with special attention to the implementation of cohesive zone elements. The procedure as put forward in [71, 72]. The strong form of the governing equation follows directly from the virtual work equilibrium.

$$\int_{\Omega} (\nabla \cdot \boldsymbol{\sigma} - \rho \ddot{\boldsymbol{u}})\, \delta \boldsymbol{u} d\Omega - \int_{\Gamma} (\boldsymbol{T}_{\Gamma} - \boldsymbol{\sigma n})\, d\boldsymbol{u} d\Gamma = 0 \tag{5.48}$$

Ω denotes the volume of the domain, Γ its boundary and $\boldsymbol{n}$ the vector normal to it. On the boundary tractions may be present an these are denoted as $\boldsymbol{T_\Gamma}$. $\boldsymbol{\sigma}$ is the Cauchy stress tensor. $\boldsymbol{u}$ is the displacement vector and $\ddot{\boldsymbol{u}}$ its second derivative with respect to time. Application of the divergence theorem[5] and integration by parts to equation 5.48 yields the weak form of the governing equation

$$\int_\Omega (\boldsymbol{\sigma} : \delta \boldsymbol{E} + \rho \ddot{\boldsymbol{u}} \cdot \delta \boldsymbol{u})\, d\Omega - \int_{\Gamma_{\text{ext}}} \boldsymbol{T}_{\text{ext}} \cdot \delta \boldsymbol{u}\, d\Gamma - \int_{\Gamma_{\text{coh}}} \boldsymbol{T}_{\text{coh}} \cdot \delta \Delta \boldsymbol{u}\, d\Gamma = 0 \tag{5.49}$$

In equation 5.49,the boundary Γ is subdivided; Γ_{ext} is the part of the boundary with an external traction $\boldsymbol{T}_{\text{ext}}$, and Γ_{coh} where cohesive tractions $\boldsymbol{T}_{\text{coh}}$ and displacement jumps $\delta \boldsymbol{u}$ are present ($\Gamma_{\text{ext}} \cap \Gamma_{\text{coh}} = 0$). $\boldsymbol{E}$ is the Lagrangian strain tensor.

The cohesive zone and surrounding bulk elements may show large displacements and therefore it is necessary to perform a pull back to the undeformed geometry. Equation 5.49 is modified with the help of the Piola-Kirchoff stress tensor $\boldsymbol{S_{\text{pk}}}$.

$$\int_\Omega (\boldsymbol{S_{\text{pk}}} : \delta \boldsymbol{E} + \rho \ddot{\boldsymbol{u}} \cdot \delta \boldsymbol{u})\, d\Omega - \int_{\Gamma_{\text{ext}}} \boldsymbol{T}_{\text{ext}} \cdot \delta \boldsymbol{u}\, d\Gamma - \int_{\Gamma_{\text{coh}}} \boldsymbol{T}_{\text{coh}} \cdot \delta \Delta \boldsymbol{u}\, d\Gamma = 0 \tag{5.50}$$

The Piola-Kirchoff stress tensor $\boldsymbol{S_{\text{pk}}}$ is obtained from the Cauchy stress tensor $\boldsymbol{\sigma}$ [73] by:

$$\boldsymbol{S_{\text{pk}}} = j \boldsymbol{F^{-1}} \boldsymbol{\sigma} \boldsymbol{F^{-T}} \tag{5.51}$$

Where $\boldsymbol{F}$ is the deformation gradient tensor and j its determinant. Equation 5.50 is made discrete in space with the help of the shape functions

$$\boldsymbol{a} = N^{-1} u \tag{5.52}$$
$$\dot{\boldsymbol{a}} = N^{-1} u \tag{5.53}$$
$$\ddot{\boldsymbol{a}} = N^{-1} u \tag{5.54}$$
$$\tag{5.55}$$

$\boldsymbol{R_{\text{ext}}}$, $\boldsymbol{R_{\text{int}}}$ and $\boldsymbol{R_{\text{coh}}}$ are the external, global internal and cohesive force vectors, respectively, and $\boldsymbol{M}$ is the mass matrix. The central difference time integration procedure is used to calculate the displacement field at the next time step.

$$\ddot{\boldsymbol{a}}_{\boldsymbol{n}} = \boldsymbol{M^{-1}} (\boldsymbol{R_{\text{ext},n}} - \boldsymbol{R_{\text{int},n}} + \boldsymbol{R_{\text{coh},n}}) \tag{5.56}$$
$$\dot{\boldsymbol{a}}_{\boldsymbol{n+1/2}} = \dot{\boldsymbol{a}}_{\boldsymbol{n-1/2}} + \ddot{\boldsymbol{a}}_{\boldsymbol{n}} \Delta t_n \tag{5.57}$$
$$\Delta t_{n+1/2} = \frac{\Delta t_n + \Delta t_{n+1}}{2} \tag{5.58}$$
$$\boldsymbol{a}_{\boldsymbol{n+1}} = \boldsymbol{a}_{\boldsymbol{n}} + \dot{\boldsymbol{a}}_{\boldsymbol{n+1/2}} \Delta t_{n+1/2} \tag{5.59}$$

The nodal displacements obtained by equation 5.59 are then used to update the geometry.

5.4.2 Time step calculation

The disadvantage of explicit methods is the existence of a maximum permissible time step. This limit is a convergence requirement based on the time it takes a stress wave to cross the smallest

[5] For a continuously differentiable vector field $\boldsymbol{F}$ present in a subset of $\mathbb{R}^n$, with $n = 3$, the divergence theorem is expressed as $\iiint_\Omega (\nabla \cdot \boldsymbol{F})\, d\Omega = \iint_\Gamma \boldsymbol{F}\, \boldsymbol{n}\, ds$

elemental distance. Because all elements share a single time step, the maximum time step is based on the smallest maximum time step of all the elements. In LS-Dyna this is calculated as

$$\Delta t^{n+1} = a \cdot \min\{\Delta t_1^n, \Delta t_2^n, \ldots, \Delta t_{\text{N-1}}^n, \Delta t_{\text{N}}^n\} \tag{5.60}$$

The smallest maximum time step value of the current time step thus serves as the limit for the following timestep. For stability reasons a factor a is applied, often equal to 0.9 or even 0.67 in the case of high explosive loading. N is the number of elements in the model.

The maximum time step requirement is known as the Courant limit [74]. In one dimensional form it is expressed as:

$$a \geq \frac{c_0 \Delta t}{l_e} \tag{5.61}$$

a is known as the Courant *number* and is also the constant used in equation 5.60. c_0 is the speed of sound in a medium, and in mediums with a constant bulk modulus is equal to:

$$c_0 = \sqrt{\frac{E(1-\nu)}{(1+\nu)(1-2\nu)\rho}} \tag{5.62}$$

The three dimensional Courant limit as used by LS-DYNA is defined as [60].

$$\Delta t = \frac{l_e}{Q + \sqrt{Q^2 + c_0^2}} \tag{5.63}$$

The quantity l_e is the smallest dimension of the element, this is known as the characteristic length and is calculated as

$$l_e = \begin{cases} \frac{V_e}{A_{e,\max}} & \text{, For 8 node solids} \\ \text{minimum length} & \text{, For 4 node tetrahedras} \end{cases} \tag{5.64}$$

With V_e and $A_{e,\max}$ being the elemental volume and the largest surface area of one side respectively. Q in equation 5.63 describes the increase in stiffness as a result of isotropic compression. An additional lowering of the maximum timestep may be necessary as a result of the inclusion of cohesive zones [72]. It is not published how this is implemented in LS-DYNA or how zero volume cohesive zones are treated.

5.5 Time integration of the cz

The Perzyna equations as modified for use in cohesive zone models as described in equations 5.27 to 5.31, have been implemented as a user defined subroutine in LS-DYNA. This is used to define an opening rate dependent opening-traction relationship at Gauss point level. Two distinct phases can be distinguished; a visco-plastic hardening phase based on the Perzyna equations and a subsequent softening-damage phase. The softening phase linearly decreases the tractions to zero when the combined maximum opening defined by some mixed mode law has been reached. In this section the governing equations of the model are presented. Figure 5.8 shows a flow chart of the total total model flow.

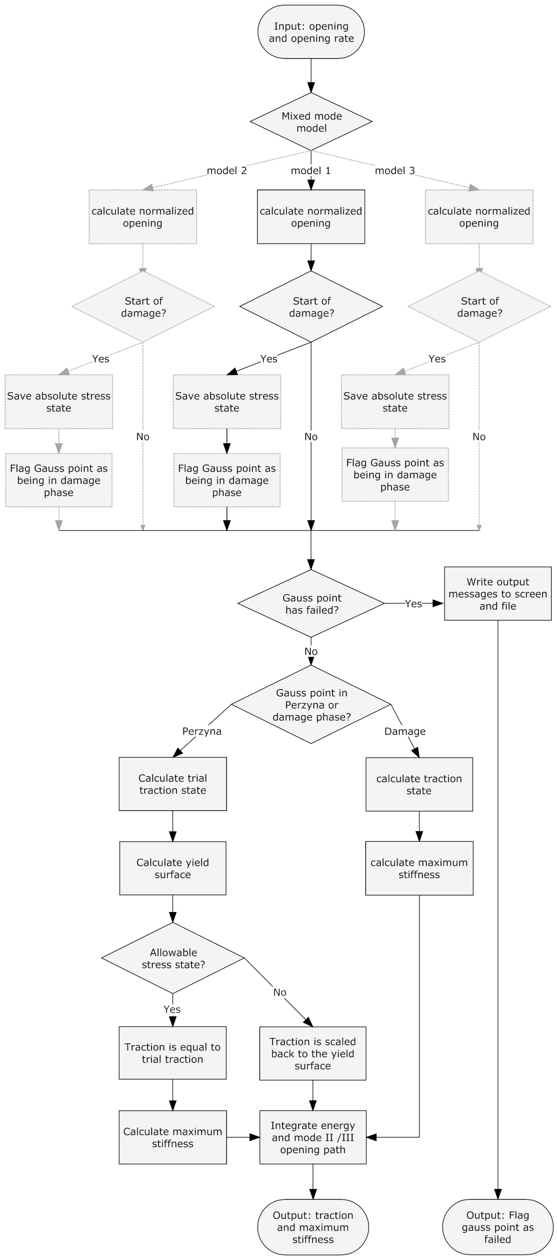

Figure 5.8: Program flow diagram

5.5.1 Visco-plastic hardening phase

The Perzyna phase of the model describes the visco-plastic behaviour of the cohesive zone element until its opening is sufficiently large so a decrease of tractions starts to occur. In the Perzyna phase, a trial traction state $\hat{\boldsymbol{t}}_{\mathbf{trial},\boldsymbol{n}}$ is obtained as a function of the opening $\boldsymbol{\delta}$ and the opening rate $\dot{\boldsymbol{\delta}}$ for each element not in its traction reduction, or damage phase. Figure 5.9 shows the role of the Perzyna phase in the overall model flow.

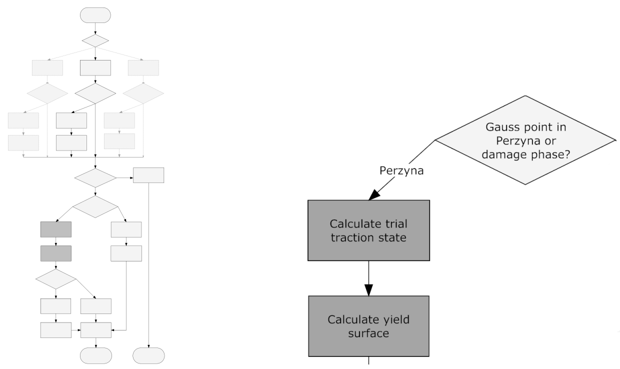

(a) Overall (b) Detail

Figure 5.9: Perzyna phase in program flow

As a first step, the equivalent traction is calculated at the current time step using the traction distribution of the previous time step.

$$\hat{t}_{eq,n} = T\sqrt{\frac{\frac{\hat{t}^2_{\mathrm{III},n-1}}{q_{\mathrm{III,n\text{-}1}}}}{S^2} + \frac{\frac{\hat{t}^2_{\mathrm{II},n-1}}{q_{\mathrm{II,n\text{-}1}}}}{S^2} + \frac{\frac{\hat{t}^2_{\mathrm{I},n-1}}{q_{\mathrm{I,n\text{-}1}}}}{T^2}} \tag{5.65}$$

The partial derivatives of $\hat{t}_{eq,n}$ to $\hat{\boldsymbol{t}}_{\boldsymbol{n-1}}$ are calculated next.

$$\begin{aligned}
\frac{\partial \hat{t}_{eq,n}}{\partial \hat{t}_{\mathrm{III},n-1}} &= \frac{T\hat{t}_{\mathrm{III},n-1}}{q_{\mathrm{III,n\text{-}1}} S^2 \sqrt{\frac{\frac{\hat{t}^2_{\mathrm{III},n-1}}{q_{\mathrm{III,n\text{-}1}}}}{S^2} + \frac{\frac{\hat{t}^2_{\mathrm{II},n-1}}{q_{\mathrm{II,n\text{-}1}}}}{S^2} + \frac{\frac{\hat{t}^2_{\mathrm{I},n-1}}{q_{\mathrm{I,n\text{-}1}}}}{T^2}}} \\
\frac{\partial \hat{t}_{eq,n}}{\partial \hat{t}_{\mathrm{II},n-1}} &= \frac{T\hat{t}_{\mathrm{II},n-1}}{q_{\mathrm{II,n\text{-}1}} S^2 \sqrt{\frac{\frac{\hat{t}^2_{\mathrm{III},n-1}}{q_{\mathrm{III,n\text{-}1}}}}{S^2} + \frac{\frac{\hat{t}^2_{\mathrm{II},n-1}}{q_{\mathrm{II,n\text{-}1}}}}{S^2} + \frac{\frac{\hat{t}^2_{\mathrm{I},n-1}}{q_{\mathrm{I,n\text{-}1}}}}{T^2}}} \\
\frac{\partial \hat{t}_{eq,n}}{\partial \hat{t}_{\mathrm{I},n-1}} &= \frac{\hat{t}_{\mathrm{I},n-1}}{q_{\mathrm{I,n\text{-}1}} T \sqrt{\frac{\frac{\hat{t}^2_{\mathrm{III},n-1}}{q_{\mathrm{III,n\text{-}1}}}}{S^2} + \frac{\frac{\hat{t}^2_{\mathrm{II},n-1}}{q_{\mathrm{II,n\text{-}1}}}}{S^2} + \frac{\frac{\hat{t}^2_{\mathrm{I},n-1}}{q_{\mathrm{I,n\text{-}1}}}}{T^2}}}
\end{aligned} \tag{5.66}$$

The value of the overstress function at the current time step is then determined by:

$$\psi_n(\hat{t}_{eq}) = \left\langle \frac{\hat{t}_{eq,n}}{T} - 1 \right\rangle^{N_{\mathrm{pz}}} \tag{5.67}$$

The increase in work hardening, $\dot{\boldsymbol{q}}_{\boldsymbol{n}}$ is calculated next.

$$\dot{\boldsymbol{q}}_{\boldsymbol{n}} = \frac{1}{\eta}\psi_n(\hat{t}_{eq,n}) \cdot \frac{\partial \hat{t}_{eq,n}}{\partial \hat{\boldsymbol{t}}_{\boldsymbol{n-1}}} h_{\mathrm{pz}} \tag{5.68}$$

And integrated to obtain $\boldsymbol{q}_{\boldsymbol{n}}$.

$$\boldsymbol{q}_{\boldsymbol{n}} = \boldsymbol{q}_{\boldsymbol{n-1}} + \dot{\boldsymbol{q}}_{\boldsymbol{n}}\Delta t \tag{5.69}$$

The visco-plastic part of the opening rate $\dot{\boldsymbol{\delta}}$ is determined through:

$$\dot{\boldsymbol{\delta}}_{\boldsymbol{vp,n}} = \frac{1}{\eta}\psi_n\left(\hat{t}_{eq,n}\right) \cdot \frac{\partial \hat{t}_{eq,n}}{\partial \hat{\boldsymbol{t}}_{\boldsymbol{n-1}}} \tag{5.70}$$

Next a trial traction distribution at $t = t_n$ is calculated. For the Mode I stress, an optional penalty parameter C_{pen} is considered for compression tractions to prevent negative volumes from occurring.

$$\hat{t}_{\mathrm{trial,II,III},n} = \hat{t}_{\mathrm{II,III},n-1} + K_1\left(\dot{\delta}_{\mathrm{II,III},n} - \dot{\delta}_{vp,\mathrm{II,III},n}\right)\Delta t \tag{5.71}$$

And

$$\hat{t}_{\mathrm{trial,I},n} = \begin{cases} \hat{t}_{\mathrm{I},n} + K_1(\dot{\delta}_{\mathrm{I},n-1} - \dot{\delta}_{vp,\mathrm{I},n})\Delta t & \text{, Without penalty} \\ \hat{t}_{\mathrm{I},n} + K_1(\dot{\delta}_{\mathrm{I},n-1} - \dot{\delta}_{vp,\mathrm{I},n})C_{\mathrm{pen}}\Delta t & \text{, With penalty} \end{cases} \tag{5.72}$$

Return mapping

In equation 5.71 and 5.72 a trail traction state $\hat{\boldsymbol{t}}_{\mathrm{trial},\boldsymbol{n}}$ was obtained. Because the integration is explicit, it may occur for large timesteps that the traction state exceeds the theoretical dynamic traction limit. In this section a return mapping scheme is discussed that has been implemented to overcome this effect. In figure 5.10 the position of the return mapping scheme in the overall model layout is drawn.

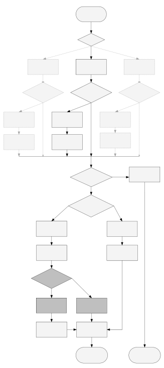

(a) Overall

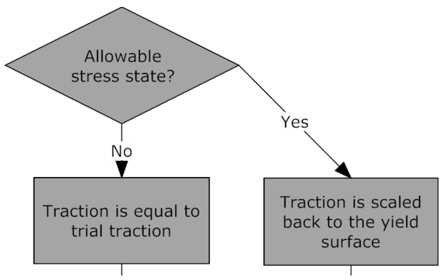

(b) Detail

Figure 5.10: Return mapping in program flow

The integration scheme uses the traction distribution from the previous time step to calculate the overstress $\psi_n(\hat{t}_{eq})$ and therefore the position of the yield surface and the plastic opening increment. If the number of time steps per element is low and the plastic opening rate changes rapidly, this can cause the new traction distribution to lie outside the space enclosed by the dynamic limit surface. This typically results in a vibration in the traction levels around the traction levels belonging to the dynamic limit. Figure 5.11 shows a typical example of this behaviour.

The problem can solved by the implementation of a return strategy. For simplicity a radial method based solution is implemented in the newly developed cohesive zone element model. This section describes the return mapping procedure that allows even large time steps to be stable.

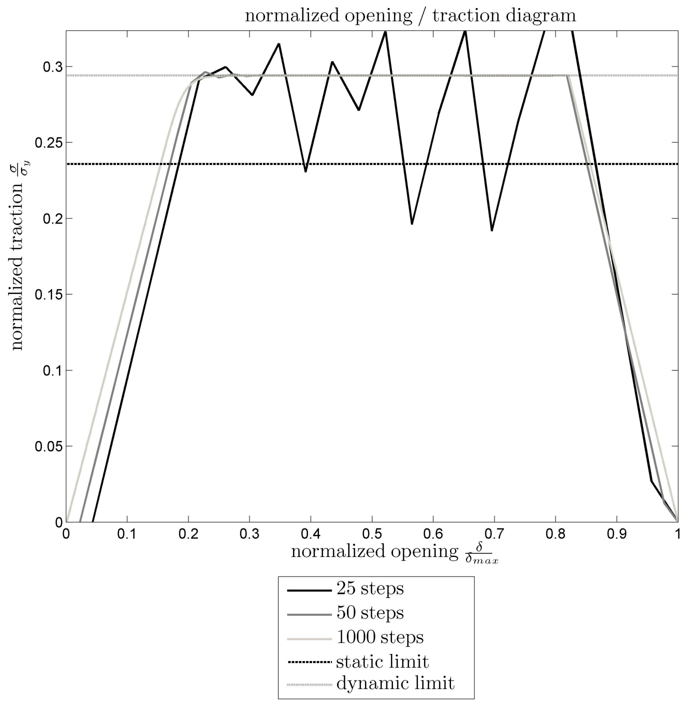

Figure 5.11: Opening / traction curve without return mapping

Under the Perzyna model, a material under loading experiences opening rate hardening. This hardening increases the ultimate traction resistance, until an asymptotic value is reached. This ultimate traction is a function of the "regular"- and the visco-plastic material properties as well as the opening rate. According to equations 5.71 and 5.72, stresses can only increase as long as the visco-plastic opening rate is lower than the actual opening rate. At the dynamic limit traction level, the following equation must hold:

$$\dot{\boldsymbol{\delta}}_{\boldsymbol{vp,n}} = \dot{\boldsymbol{\delta}}_{\boldsymbol{n}} \tag{5.73}$$

If we combine equation 5.73 with equation 5.70, we obtain:

$$\dot{\boldsymbol{\delta}}_{\boldsymbol{n}} = \frac{1}{\eta}\psi_n(\hat{t}_{eq,n})\frac{\partial \hat{t}_{eq,n}}{\partial \hat{\boldsymbol{t}}_{\boldsymbol{n-1}}} \tag{5.74}$$

Rewriting equation 5.74 and combining it with equation 5.67, yields the following equation, expressing the asymptotic maximum overstress level as a function of the opening rate in three directions.

$$\hat{t}_{eq,\max,n} = T + T\sum_i \sqrt[N_{\mathrm{pz}}]{\frac{\dot{\delta}_{i,n}\eta}{\frac{\partial \hat{t}_{eq}}{\partial \hat{t}_{i,n-1}}}} \tag{5.75}$$

where i loops over all the elements of $\dot{\delta}_{i,n}$ and $\frac{\partial \hat{t}_{eq}}{\partial \hat{t}_{i,n-1}}$ where $\frac{\partial \hat{t}_{eq}}{\partial \hat{t}_{i,n-1}} \neq 0$

Next we test the derived equivalent traction $\hat{t}_{eq}$ from equation 5.65 against the maximum allowable equivalent traction $\hat{t}_{eq,\max,n}$. Equation 5.76 assigns the values of $\hat{t}_{\text{trial},\mathrm{II},\mathrm{III},\text{n}}$ to $\hat{t}_{\mathrm{II},\mathrm{III},\text{n}}$ unless these values exceed the limits of the dynamic traction limit, If the latter is the case, the tractions $\hat{t}_{\mathrm{II},\mathrm{III},n}$ will be set equal to maximum allowable tractions on the yield surface.

$$\hat{t}_{\mathrm{II},\mathrm{III},n} = \frac{\hat{t}_{\text{trial},\mathrm{II},\mathrm{III},n}}{\left\langle \frac{\hat{t}_{eq,n}}{\hat{t}_{eq,\max,n}} - 1 \right\rangle + 1} \tag{5.76}$$

For the normal opening direction belonging to $\hat{t}_{\mathrm{I},n}$ an additional test is applied to allow for normal compression without yielding.

$$\hat{t}_{\mathrm{I},n} = \begin{cases} \hat{t}_{\text{trial},\mathrm{I},n} & , \text{For } \hat{t}_{\text{trial},\mathrm{I},n} \leq 0 \\ \frac{\hat{t}_{\text{trial},\mathrm{I},n}}{\langle \frac{\hat{t}_{eq,n}}{\hat{t}_{eq,\max,n}} - 1 \rangle + 1} & , \text{For } \hat{t}_{\text{trial},\mathrm{I},n} > 0 \end{cases} \tag{5.77}$$

The return mapping strategy is demonstrated in figure 5.12. Based on the traction state at the time $t = t_{n-1}$, and displacement jump $\Delta\delta_n$, a new trial traction state outside the original dynamic limit surface is reached; $\hat{t}_{\text{trial}}$. The position of the dynamic limit surface is then recalculated based on the traction state at the present timestep. If the trial traction state falls within the new surface, no further action needs to be taken, and the trial traction state becomes the actual traction state. If he trial state is inadmissible however, The trial traction state is scaled back.

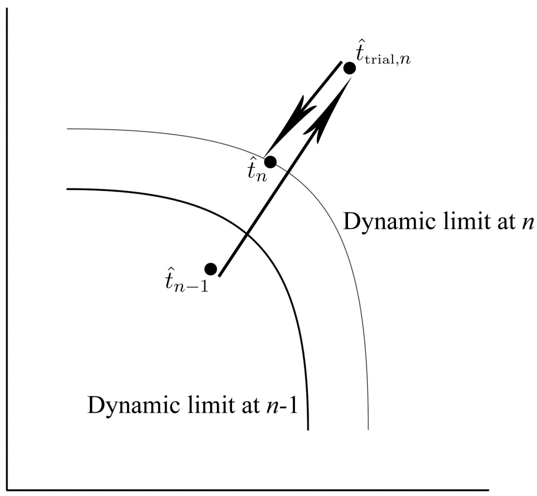

Figure 5.12: Return strategy for inadmissible stress states

The return strategy employed here differs from the classical return mapping strategies as it only prevents traction levels to exceed the theoretic maximum traction of the dynamic traction limit. Figure 5.13 shows the effect of the strategy on the stability of the time integration. It shows a dramatic improvement over the explicit integration scheme without return mapping in place as shown in figure 5.11.

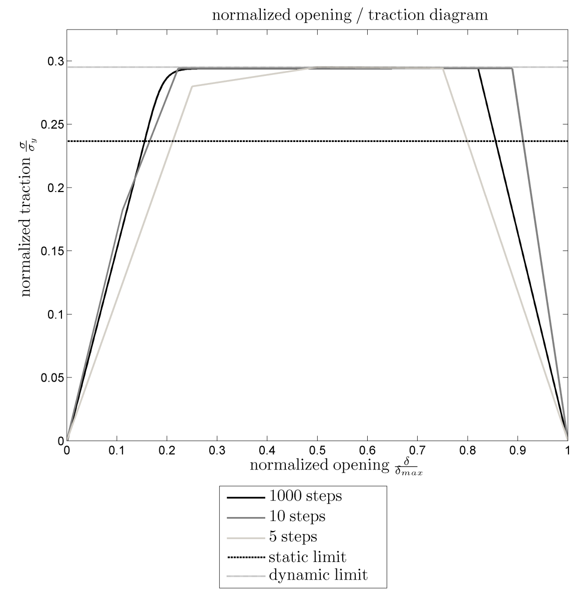

Figure 5.13: Opening / traction curve with return mapping

The end result of the technique outlined in this section is a stable visco-plastic, opening rate sensitive, Perzyna type model. A more realistic complex loading regime with different maximum tractions in Mode I and Mode Ⅱ/Ⅲ is shown in figure 5.14.

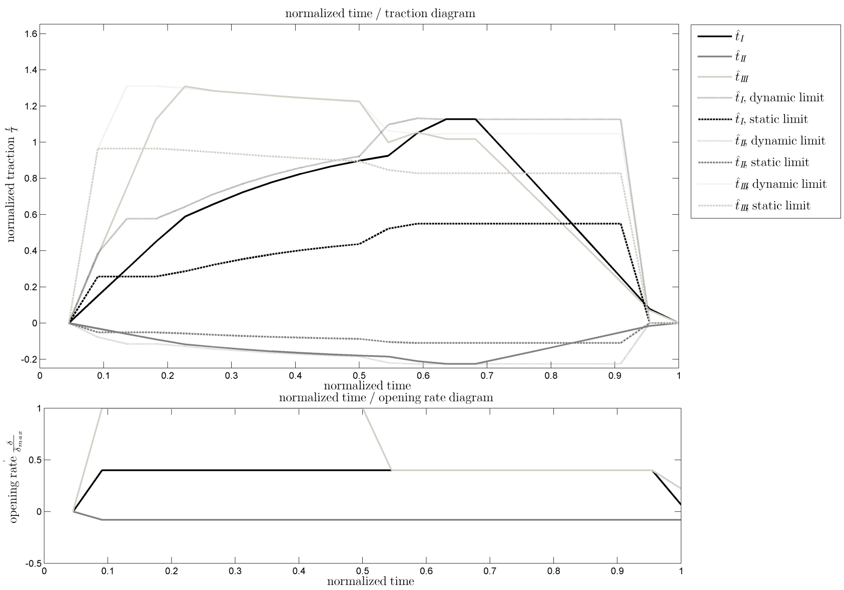

Figure 5.14: Stabilized Perzyna with complex loading regime, 50 time steps

5.5.2 Softening phase

The softening, or damage phase follows the visco-plastic hardening phase after a certain condition with regard to the cohesive zone opening has been met. It is necessary to combine the three opening directions of the cohesive zone into a single combined opening as is explained hereafter, and perform a check for the onset of softening on this single, combined quantity.

5.5.3 Mixed mode opening

The cohesive zone model has three opening directions, two tangential and one normal to the plane of fracture. These openings are not independent from one and another, as a tangential opening influences the maximum opening in the normal direction. These three openings need to be combined into a single combined opening so it can be tested against a combined maximum opening. This task is performed by a mixed mode law, and as the cohesive zones approach to fracture mechanics is phenomenological in nature, there need not be a single, true mixed mode law. The position of the mixed mode handling equations in the overall model flow is shown in figure 5.15.

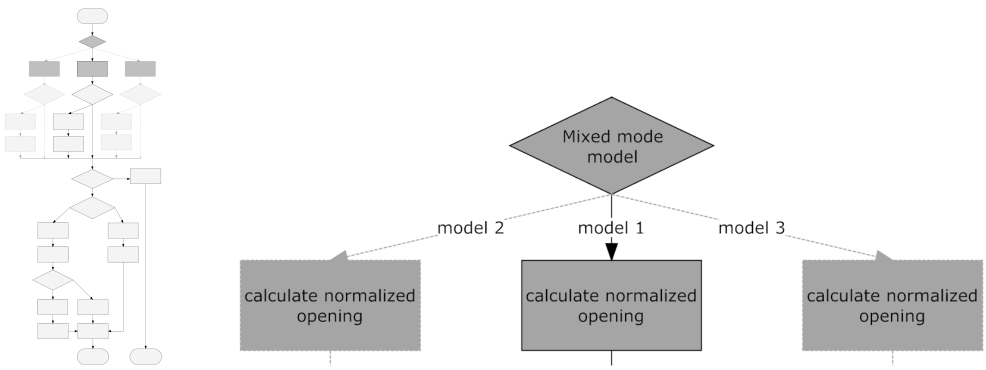

(a) Overall (b) Detail

Figure 5.15: Mixed mode in program flow

An opening is not treated equally in all directions. Mode I, normal compressive traction is excluded as this does not constitute a force that promotes fracture. Opening in mode II and III, the tangential directions do not physically differ in nature if their sign is negative. This is only a matter of direction relative to some arbitrarily chosen coordinate system.

For the calculation of the combined opening, the instantaneous value of the normal opening is used. The tangential openings need to be treated differently, as a reversal of opening direction first constitutes an unloading, but becomes a reloading again if it passes the point of zero opening. The tangential openings are integrated according to

$$\hat{\delta}_{\mathrm{II},\mathrm{III}} = \int \dot{\delta}_{\mathrm{II},\mathrm{III}} \Delta t \cdot \mathrm{sign}\left(\sigma_{\mathrm{II},\mathrm{III}}\right) \tag{5.78}$$

Figure 5.16a shows the preservation effect of tangential opening integration. If opening direction reversals occur, the traction is reduced according to the loading stiffness until the maximum traction is reached in the other direction. For clarity the situation shown, excludes visco-plasticity. In reality this effect is taken into account. Figure 5.16b shows the effects of equation 5.78, independent of choice of coordinate system, increasing openings lead to an increasing value of $\hat{\delta}$. At opening reversals, the integral reduces, but is increased by the same amount when it has reached the maximum opening in the opposite direction. The effect of this is, that the mode Ⅱ /Ⅲ traction, ends up at the same point in the normalized TSL as it was, when opening reversal started.

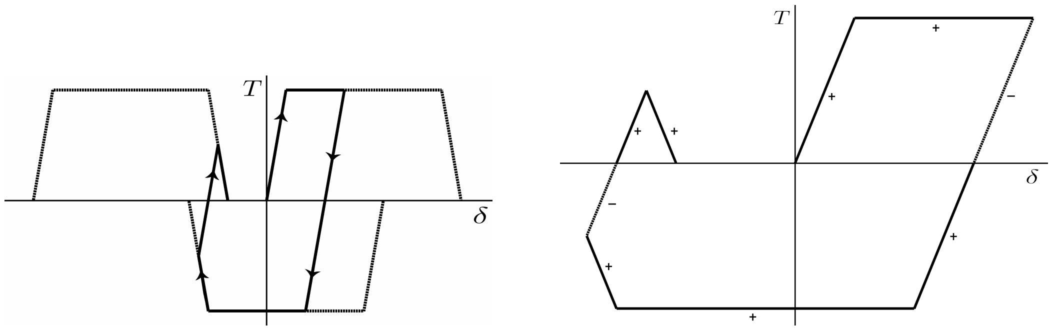

(a) Opening reversal behaviour (b) Sign of $\dot{\delta} \cdot \mathrm{sign}\,(\sigma)$

Figure 5.16: Loading and unloading in tangential directions (mode Ⅱ /Ⅲ)

There are three different mixed mode laws available for selection in the existing cohesive models in LS-DYNA. For the sake of uniformity, these three laws are also available in the newly developed opening rate sensitive cohesive zone model. A description of each follows hereafter.

Power law formulation

The power law formulation expresses every stress state into a corresponding maximum opening according to formula 5.79

$$\delta_{0,n} = \frac{1+\beta_n^2}{\mathrm{A}_{\mathrm{N.TSL}}} \frac{1}{\sqrt[\mathrm{XMU}]{\left(\frac{T}{\Gamma_\mathrm{N}}\right)^{\mathrm{XMU}} + \left(\frac{S\beta_n^2}{\Gamma_\mathrm{T}}\right)^{\mathrm{XMU}}}} \tag{5.79}$$

Exponent *XMU* is a parameter expressing an increased fracture toughness in multi-mode fracture situations. A value equal to one is a reasonable and safe first approach. β is known as the "mode mixity" and is defined as

$$\beta_n = \frac{\sqrt{\hat{\delta}_{\mathrm{II},n} + \hat{\delta}_{\mathrm{III},n}}}{\delta_{\mathrm{I},n}} \tag{5.80}$$

The maximum value of the combined opening $\delta_{0,n}$ is used to check the instantaneous value of the mixed mode opening at every time step. The instantaneous mixed mode opening is expressed by equation 5.81.

$$\delta_{\mathrm{eq},n} = \sqrt{\hat{\delta}_{\mathrm{III},n} + \hat{\delta}_{\mathrm{II},n} + \langle \delta_{\mathrm{I},n} \rangle} \tag{5.81}$$

The nondimensional combined opening is calculated by.

$$\lambda_n = \frac{\delta_{eq,n}}{\delta_0, n} \tag{5.82}$$

Benzeggagh Kenane law

An alternative formulation, resembling the power law, is the Benzeggagh Kenane law [75]. It differs from the power law only with respect to the maximum combined opening calculation. This is expressed as in equation 5.83.

$$\delta_{0,n} = \frac{1+\beta_n^2}{\mathrm{A}_{\mathrm{N.TSL}}\left(T+\beta_n^2 S\right)} \left(\Gamma_{\mathrm{N}} + \left(\Gamma_{\mathrm{T}} - \Gamma_{\mathrm{N}}\right) \left(\frac{\beta_n^2 S}{T+\beta_n S}\right)^{\mathrm{XMU}}\right) \tag{5.83}$$

The instantaneous value of the combined opening is identical to the power law equation 5.81, and a normalized opening is calculated according to equation 5.82.

Dimensionless effective parameter approach

The third mixed mode laws, differs from the first two, in the sense that it expresses the current opening distribution not as a instantaneous and maximum value, but rather as a dimensionless effective opening parameter λ directly.

$$\lambda_n = \sqrt{\left(\frac{\hat{\delta}_{\mathrm{III},n}}{\delta_{0,\mathrm{T}}}\right)^2 + \left(\frac{\hat{\delta}_{\mathrm{II},n}}{\delta_{0,\mathrm{T}}}\right)^2 + \left\langle\frac{\delta_{\mathrm{I},n}}{\delta_{0,\mathrm{N}}}\right\rangle^2} \tag{5.84}$$

$\delta_{0,\mathrm{N}}$ and $\delta_{0,\mathrm{T}}$ are the maximum openings in mode I and mode II/III respectively, and are calculated according to

$$\delta_{0,\mathrm{N}} = \frac{\Gamma_{\mathrm{N}}}{\mathrm{A}_{\mathrm{N.TSL}} T} \tag{5.85}$$

$$\delta_{0,\mathrm{T}} = \frac{\Gamma_{\mathrm{T}}}{\mathrm{A}_{\mathrm{N.TSL}} S} \tag{5.86}$$

Onset of softening phase

The Perzyna model describes an increase in the traction as a result of an increase in the opening rate. It does not describe an increase in maximum opening however. In fact it does not have any failure criterion at all, and as the opening goes to infinity, the resulting traction will go towards a finite asymptotical value unequal to zero. A cohesive zone model based on the Perzyna model, must therefore take into account failure through other means. Figure 5.17 graphically presents the place of this failure criterion in the total program flow as was given in figure 5.8.

The maximum opening was chosen to be constant and this is a logical basis for a failure criterion. Using this criterion by itself could cause instability due to the sudden drop in traction and is problematic in explicit finite element code as a sudden drop in traction combined with an increasing opening implies a very large negative stiffness. To assure stability an absolute upper bound to this stiffness for the following time step is passed to the finite element code by the material model at each time step. As it is unknown if an element will fail the next time step, it is necessary to always expect this drop in traction levels to occur. Having a large upper bound for the stiffness, forces the finite element code to choose a very small time step. This in turn increases the absolute stiffness upper bound even more as the traction jump occurs within one time step by definition. This process continues until the lower bound for the finite element code time step has been reached.

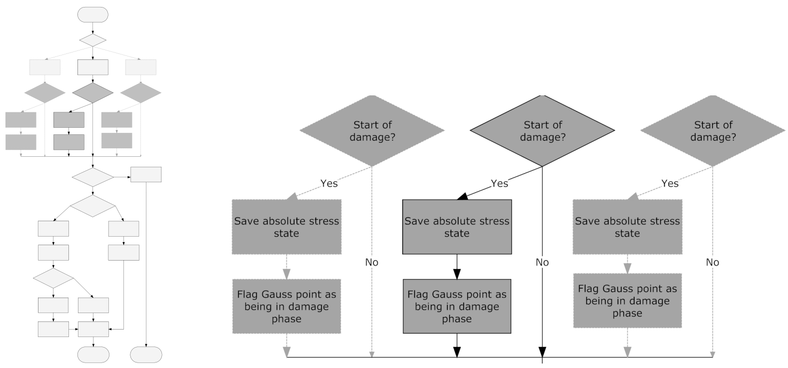

(a) Overall (b) Detail

Figure 5.17: Damage phase start in program flow

To circumvent the difficulties presented above, an unloading stiffness K_2 is introduced to reduce the tractions more gradually at the end of the opening range of the material. The unloading stiffness K_2 behaves in the same way as the loading stiffness K_1. Having a decreasing traction, or damage, zone at the end of the opening range is physically not unrealistic and in fact as shown in section 2.2 many, if not all cohesive zone traction separation laws exhibit this behaviour.

The onset of damage is triggered by a check on the instantaneous combined opening $\delta_{\text{eq},n}$. The opening necessary to reduce the stresses of an infinitely slowly loaded, cohesive zone element $\Delta\delta_{\text{damage},n}$ according to the damage stiffness K_2 is added to this opening and the sum is checked against the maximum allowable opening $\delta_{0,n}$. The additional opening in the damage zone is calculated as

$$\begin{aligned}\Delta\delta^2_{\text{damage},n} \quad = \quad & \left(\hat{\delta}_{\text{III},n} + \frac{\text{Min}\left(S, \hat{t}_{\text{III},n} \cdot \text{Sign}\left(\hat{t}_{\text{III},n} \cdot \hat{\delta}_{\text{III},n}\right)\right)}{K_2}\right)^2 \\ & + \left(\hat{\delta}_{\text{II},n} + \frac{\text{Min}\left(S, \hat{t}_{\text{II},n} \cdot \text{Sign}\left(\hat{t}_{\text{II},n} \cdot \hat{\delta}_{\text{II},n}\right)\right)}{K_2}\right)^2 \\ & + \left\langle \delta_{\text{I},n} + \frac{\text{Min}\left(S, \hat{t}_{\text{I},n} \cdot \text{Sign}\left(\hat{t}_{\text{I},n} \cdot \delta_{\text{I},n}\right)\right)}{K_2} \right\rangle^2 \end{aligned} \tag{5.87}$$

And the check for onset of damage becomes

$$\delta_{\text{eq},n} + \Delta\delta_{\text{damage},n} \geq \delta_{0,n} \tag{5.88}$$

When condition 5.88 is met, the gauss point is permanently flagged as damaged. This excludes it from any further visco-plastic traction increases. A linear damage law as described in section 5.5.4 will govern the gauss point instead. This damage law requires the absolute traction levels $|\hat{\boldsymbol{t}}_{\boldsymbol{n}}|$ and the relative combined opening λ_n to be obtained at the moment of damage initiation

$$\hat{\boldsymbol{t}}_{\mathbf{dam}} = |\hat{\boldsymbol{t}}_{\boldsymbol{n}}| \tag{5.89}$$

$$\lambda_{\text{dam}} = \lambda_n \tag{5.90}$$

5.5.4 Traction reduction in the softening phase

When a gauss point is governed by the softening phase system of equations, its traction levels are linearly decreased over a certain combined opening length. When the maximum combined opening is reached and the tractions are equal to zero, a flag is set to inform LS-DYNA the gauss point has failed. The position of the softening phase set of equation is shown in figure 5.18.

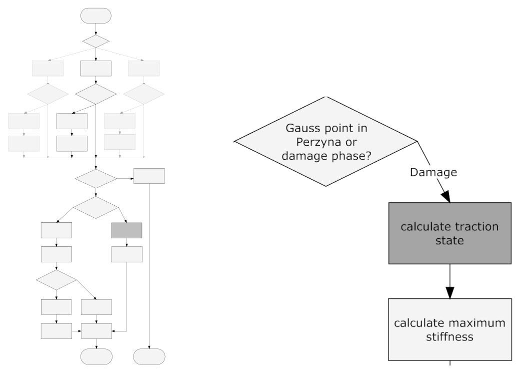

(a) Overall (b) Detail

Figure 5.18: Softening phase in program flow

After the onset of softening, a damage term d reduces the tractions linearly to zero as the normalized opening λ_n reaches the maximum normalized opening $\lambda_{0,n}$.

$$d_n = \left\langle \mathrm{Min}\left(d_{n-1}, 1 - \frac{\lambda_{\mathrm{dam}} - \lambda_n}{1 - \lambda_n}\right)\right\rangle \tag{5.91}$$

A trial traction state $\hat{\boldsymbol{t}}_{\mathbf{trial}}$ is obtained trough equation 5.71 and 5.72. The tractions at the current timestep are obtained from the trial traction state by checking them against a decreasing yield surface criterion $\hat{t}_i \leq |\hat{t}_{\mathrm{dam},i}| \cdot d_n$

$$\hat{t}_{i,n} = \begin{cases} \hat{t}_{\mathrm{trial},i,n} & ,\mathrm{For}\ |\hat{t}_{\mathrm{trial},i,n}| \leq \hat{t}_{\mathrm{dam},i} \cdot d_n \\ \hat{t}_{\mathrm{dam},i} \cdot \mathrm{Sign}\left(\hat{t}_{\mathrm{trial},i,n}\right) \cdot d_n & ,\mathrm{For}\ |\hat{t}_{\mathrm{trial},i,n}| > \hat{t}_{\mathrm{dam},i} \cdot d_n \end{cases} \tag{5.92}$$

The scheme as outlined in this section produces a linear decay of tractions to zero from the onset of softening to the final failure of the element. This softening zone corresponds with the decreasing traction phase in a traditional TSL. Elastic unloading is still possible in the softening phase, but tractions are bounded by a decreasing damage yield surface. Softening is an irreversible phenomenon as decreasing damage is impossible. The opening length of the softening zone corresponds with the opening length of the softening zone of a rate insensitive cohesive zone TSL with the same softening or damage stiffness K_2. This can be seen in figure 5.19, where the softening opening length $\lambda_{\mathrm{dam}}$is constant for a series of opening-traction curves at increasingly high opening rates.

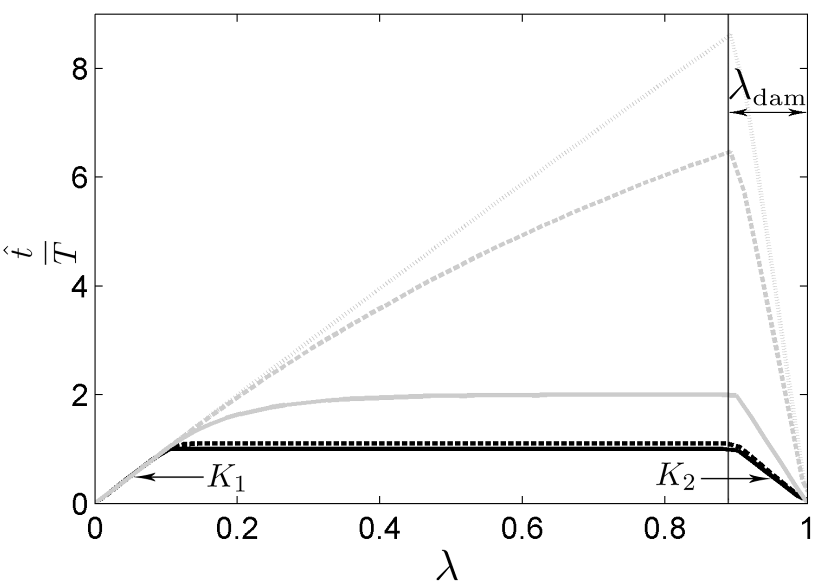

Figure 5.19: Stiffness definition

5.5.5 Maximum stiffness

As discussed in section 5.4.2, the maximum stable time step of an explicit finite element scheme is dependent on the stiffness of the elements[6]. For the finite element to be able to calculate the maximum allowable timestep, an upper bound to the stiffness in any direction of each element is considered. For user defined (cohesive zone) elements, this upper bound must be calculated by the user defined code and passed back to the finite element solver. The position of the equations in shown in figure 5.20. Equation 5.93 calculates an upper bound to the expected elemental

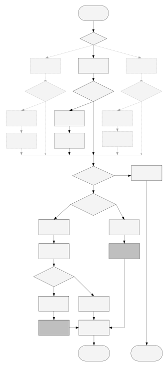

Figure 5.20: Maximum stiffness in program flow

stiffness.

$$K_{\mathrm{ub}} = \begin{cases} \dfrac{\mathrm{Max}\left\{K_1, K_2 \cdot \mathrm{Max}\left\{\frac{\hat{t}_{\mathrm{I,dam}}}{T}, \frac{\hat{t}_{\mathrm{II,dam}}}{S}, \frac{\hat{t}_{\mathrm{III,dam}}}{S}, 1.0\right\}\right\}}{C_{\mathrm{ts}}^2} & \text{, No penalty} \cup \hat{t}_{\mathrm{I},n} \geq 0 \\ \dfrac{\mathrm{Max}\left\{K_1 \cdot C_{\mathrm{pen}}, K_2 \cdot \mathrm{Max}\left\{\frac{\hat{t}_{\mathrm{I,dam}}}{T}, \frac{\hat{t}_{\mathrm{II,dam}}}{S}, \frac{\hat{t}_{\mathrm{III,dam}}}{S}, 1.0\right\}\right\}}{C_{\mathrm{ts}}^2} & \text{, With penalty} \cap \hat{t}_{\mathrm{I},n} < 0 \end{cases} \tag{5.93}$$

An additional factor C_{ts} provides the possibility of an artificial increase of the element upper bound stiffness. This does not alter the behaviour of the element but allows the user to impose a reduced timestep as long as the artificially stiffened element set has not failed completely. This saves calculation resources as the timestep can increase again when the stiffened elements are destroyed.

[6]See equation 5.62.

Chapter 6

Testing and validation

The model as presented in chapter 5 was first tested on single elements to check for its proper functioning in known limit cases and in general. Also the mixed mode behaviour was verified. The results of these tests can be found in section 6.1. As cohesive zones are phenomenological in nature, its parameters need to be determined empirically. Section 6.2 deals with the selection of appropriate experimental data sets for this purpose. In section 4.1 the static cz parameters were determined, in section 6.3 the corresponding Perzyna parameters are determined. The now calibrated model is tested against an experimental data set not used in the calibration in section 6.4. In section 6.5 a parameter study is performed on both the rate dependent as the regular cohesive zone element type *MAT_COHESIVE_GENERAL*.

6.1 One element testing

To test the new material model, simulations were performed with a single cohesive element. The element is a cube with all sides 1 unit long. This form factor deviates from the standard cohesive geometry where the thickness dimension is usually substantially smaller then the others. Based on the LS-DYNA manual this was not expected to influence the validity of the simulation.

A discrepancy was found however between the integrated opening rate and the reported actual opening in mode Ⅱ / Ⅲ; a factor two difference was found for small openings:

$$\delta_n \neq \sum_{m=1}^{n} \dot{\delta}_m \Delta t_m \tag{6.1}$$

This was later traced to the way the element rigid body velocity is calculated and subtracted from the opening rates in LS-DYNA. To circumvent the problem in this chapter, the (correct) opening was differentiated at every time step to provide a consistent opening rate for mode Ⅱ / Ⅲ openings. For typical cohesive zone element form factors, this adaptation is not necessary as the discrepancy vanishes for these cohesive element geometries.

$$\dot{\delta}_n = \frac{\delta_n - \delta_{n-1}}{\Delta t_{n-1}} \tag{6.2}$$

6.1.1 Mode I loading

To subject the element to Mode I loading the nodes belonging to the top and bottom face of the element were subjected to a outward displacement normal to their relevant planes. To test the performance of the model, two limit cases exist that the model must obey. These two extremes are an elastic model with no plasticity until damage and an elastic-plastic model with an elastic response until the yield stress σ_y (or maximum traction T), and a fully plastic response thereafter until damage. The visco-plastic cohesive element operates within these two extremes and this is controlled by the value of the fluidity parameter η. Rewriting equation 5.75 to a single loading direction and a maximum traction equal to unity yields

$$\hat{t}_{\max} = T\left(\sqrt[N_{\text{pz}}]{\dot{\delta}\eta} + 1\right) \tag{6.3}$$

It is clear from equation 6.3 that setting the fluidity $\eta = 0$ yields a elastic-plastic model while a fluidity $\eta = \infty$ yields a fully elastic description. To test for the proper function of the model these two cases are simulated. Because the reciprocal value of η needs to be calculated, a value of zero is numerically impossible as is the infinite value. The two values tested approach these limits however and are equal to $\eta = 1.0 \cdot 10^5$ and $\eta = 1.0 \cdot 10^{-5}$. The cohesive energy Γ was set to 0.9, the Perzyna exponant N_{pz} to unity and both the loading as the damage stiffness K_1 and K_2 were set to 10. The resulting opening δ should therefore approach 1.0 in both cases, with a small error present due to the discrete time steps. The displacement / traction diagram is drawn in figure 6.1. Table 6.1 lists the analytically calculated results together with the results found in the simulations.

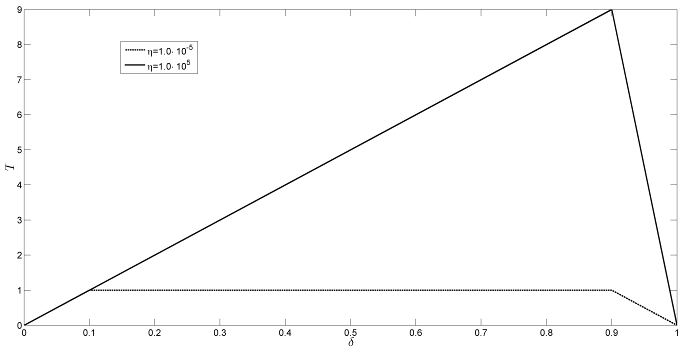

Figure 6.1: Single element test in mode I, 2 extreme cases

	Calculated value			Simulated		
η	$\hat{t}_{\max}$	Γ	δ	$\hat{t}_{\max}$	Γ	δ
$1.0 \cdot 10^5$	9.0000	4.5000	1	8.9967	4.4990	1.0000
$1.0 \cdot 10^{-5}$	1.0000	0.90000	1	1.0000	0.90000	1.0000

Table 6.1: Single element test in mode I results

Unfortunately no experimental benchmarks exist to calibrate the model and derive an estimation for N_{pz} and η directly. The proper response of the model to the opening rate with assumed parameters can be tested however. Figure 6.2 shows the response of the element subjected to a prescribed opening applied at varied rates. Figure 6.3 shows the observed maximum tractions along with the theoretical limit as described by equation 6.3. It should be noted that the points belonging to the two highest opening rates do not lie on the limit line, the reason for this deviation is apparent from figure 6.2; the element fails before the maximum traction can be approached. Based on the tests performed, the strain rate sensitive cohesive element has proven to work as designed

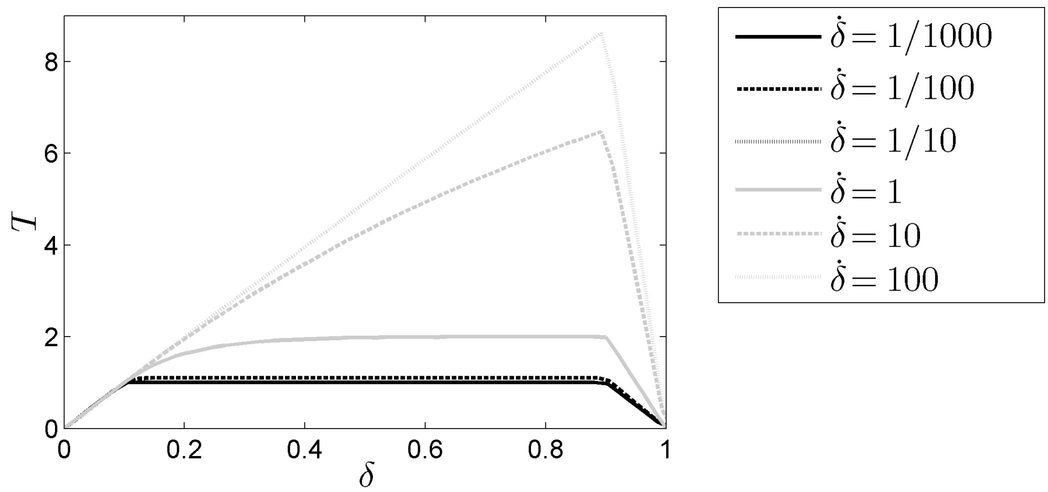

Figure 6.2: Mode I traction curve as a function of opening rate

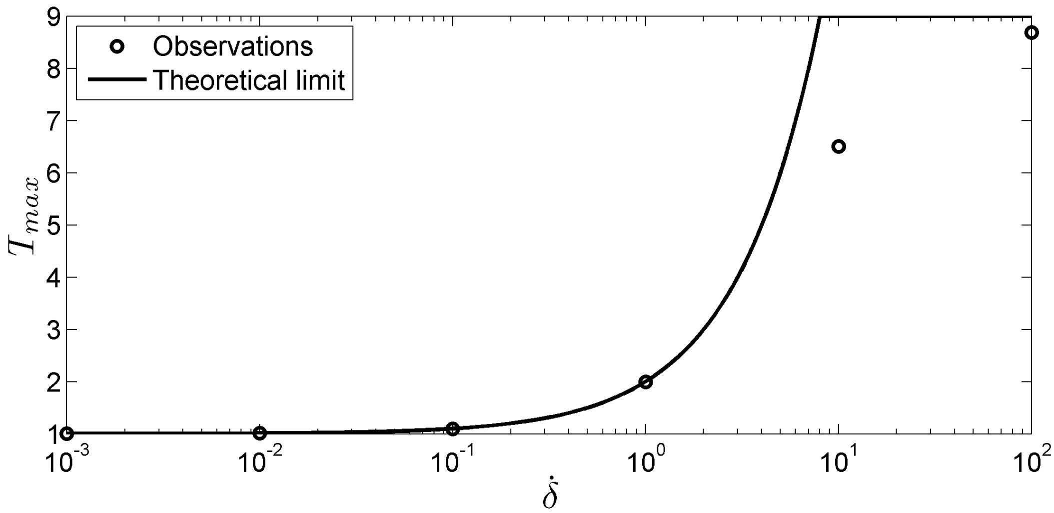

Figure 6.3: Mode I traction curve as a function of maximum opening

6.1.2 Mode II / III loading

As was done for mode I testing, the limits of the model were tested for both mode II and III opening, by applying the relevant shearing deformation to the top and bottom faces of the cohesive zone element and setting the fluidity according to $\eta = 1.0 \cdot 10^5$ and $\eta = 1.0 \cdot 10^{-5}$. The results of these calculations are given in table 6.2.

Mode		Calculated value			Simulated		
	η	$\hat{s}_{\max}$	Γ	δ	$\hat{s}_{\max}$	Γ	δ
II	$1.0 \cdot 10^5$	9.0000	4.5000	1	8.9968	4.4997	1.0000
II	$1.0 \cdot 10^{-5}$	1.0000	0.90000	1	1.0000	0.90013	1.0000
III	$1.0 \cdot 10^5$	9.0000	4.5000	1	8.9968	4.4997	1.0000
III	$1.0 \cdot 10^{-5}$	1.0000	0.90000	1	1.0000	0.90013	1.0000

Table 6.2: Single element test in mode II and III results

It can be observed from table 6.2 that the results of the simulations in mode II and III are identical and conform to the expected solutions calculated.

6.1.3 Mixed mode loading

One of the features of the the newly developed cohesive zone element model is its ability to cope with mixed mode openings. The openings in the three modes are combined to ascertain the visco-plastic state of the element according to equation 5.65. For the start of damage and final failure of the element, a single failure criterion must also be in place. The user has the option of choosing three different varieties as detailed in section 5.5.3. These mixed mode laws revert to a single law if the exponent XMU in equations 5.79 and 5.83 is set to 1, the maximum traction is set equal for the normal and tangential opening directions, or $S = T = 1$ and the cohesive energy is equal to $\Gamma_{\mathrm{N}} = \Gamma_{\mathrm{T}} = 0.9$. The opening is controlled by a displacement vector forcing a combined mode I and II opening with a $\frac{\dot{\delta}_{\mathrm{N}}}{\dot{\delta}_{\mathrm{T}}}$ ratio of 0.75. These simulations were performed for each of the available mixed mode models and the results are given in table 6.3, Where model 1 signifies the Power law, 2 the Benzeggagh Kenane law and 3 the dimensionless effective parameter approach.

	Mode I			Mode II		
Model	$\hat{t}_{\max}$	Γ_{N}	δ_{N}	$\hat{s}_{\max}$	Γ_{T}	δ_{T}
1	0.7072	0.5077	0.6022	0.7070	0.5090	0.7985
2	0.7072	0.5077	0.6022	0.7070	0.5090	0.7985
3	0.7072	0.5077	0.6022	0.7070	0.5090	0.7985

Table 6.3: Single element test, mixed mode results

As was expected, the response of each of the three models is identical. Because the values for the maximum tractions and cohesive energy were set equal in the normal and tangential directions, equations 6.4 and 6.5 hold and should both be equal to 1.

$$|\delta| = \sqrt{\delta_{\mathrm{N}}^2 + \delta_{\mathrm{T}}^2} = \sqrt{0.6022^2 + 0.7985^2} = 1.0000 \tag{6.4}$$

$$|\hat{t}| = \sqrt{t^2 + s^2} = \sqrt{0.7072^2 + 0.7070^2} = 1.0000 \tag{6.5}$$

6.1.4 Time step dependence

The final single element test performed is the effect of the number of time steps per cohesive zone element. The element was loaded in one of the tangential directions and an opening was applied until failure. The number of time steps was varied between 1200 and 100.000. The fluidity was set as $\eta = 1.0 \cdot 10^5$. The results are listed in table 6.4, and show a linear convergence of the solution.

Time steps	$\hat{s}_{\max}$	Γ_{T}	δ_{T}
1200	8.9975	4.5057	1.000164
11000	8.9968	4.4997	1.000025
100000	8.9964	4.4988	1.000003

Table 6.4: Single element test, influence of time step size

6.2 Selection of experimental data

For aluminium 2024 T3 there are reliable estimates of the cohesive energy and maximum traction in mode I available. This is not the case for duplex steel DIN 1.4462, where we have only a very rough estimate of the cohesive energy based on fracture toughness conversion. There is the possibility of simulating experiments already performed and varying the parameters until the simulated prediction matches the observations. This procedure is known as inverse modelling. For this to be successful, appropriate datasets are required from experiments with the relevant material.

6.2.1 Duplex steel DIN 1.4462

The only experiment available for duplex steel DIN 1.4462 is the plate test as described in section 3.1. As was indicated in that section, the test was not a properly conditioned centre crack panel test, and the results were obscured by significant out of plane movement and questionable boundary conditions. It is therefore not a suitable set for inverse modelling and because of this there is no possibility of obtaining the needed parameters for duplex steel without new experiments.

6.2.2 Aluminium 2024 T3

For aluminium 2024 T3, much more data is available. The two Vulcan barrel tests for example as mentioned in section 3 offer excellent data, though the first one has only a limited part of the fracture path captured on the high speed video due to the camera setup and the fracture vearing slightly off a perfectly straight course. Apart from this, a series of centre cracked panel test are available from the TU Delft [55] and a NASA study [76]. The TU Delft study offers the best opportunity to derive the cohesive energy and static maximum traction as it reports the most data and it states the moment of the fracture becoming unstable. This study was used to verify the cohesive properties as reported by others and discussed in G.1.

The second aluminium barrel test, *Test03alu02* has a complete data set and is used to calibrate the opening rate parameters, η and N_{pz}. The first aluminium barrel test *Test02alu01* is then used to verify the results of the model for a different geometry and internal pressure then the one used to calibrate the model.

6.3 Derivation of Perzyna parameters

Only a single Vulcan barrel test data set is available to calibrate the Perzyna type parameters of the model; the fluidity η and the exponent N_{pz}. To be able to find these values through inverse modelling, first an estimation is made of their approximate values

Equation 5.75 for one dimension is expressible as

$$\frac{\hat{t}_{\max}}{T} = \sqrt[N_{\mathrm{pz}}]{\dot{\delta}_n \eta} + 1 \tag{6.6}$$

Because of the high stiffness in the the cohesive element used, $K_1 = \frac{E}{t_{\mathrm{cz}}}$ the TSL is almost square, therefore the area under the non dimensional TSL is close to being equal to unity. If we increase the maximum traction T and we do not alter the maximum opening, the cohesive energy increases almost proportionally and we may write

$$\frac{\Gamma_{\mathrm{dynamic}}}{\Gamma_{\mathrm{static}}} \approx \frac{\hat{t}_{\max}}{T} = \sqrt[N_{\mathrm{pz}}]{\dot{\delta}_n \eta} + 1 \tag{6.7}$$

Increasing both the cohesive energy as the maximum traction by the same factor, a number of simulations have been performed using a rate insensitive cohesive zone model to match the simulations with the experimentally observed fracture propagation rates. The values of the base cohesive properties Γ and T were set equal to the static cohesive properties obtained in section 4.1. The results of these simulations are presented in figure 6.4. As is clear from the graph no good match was achieved, the highest possible increase factor was 1.64, higher values led to fracture arrest in the initial fracture phase.

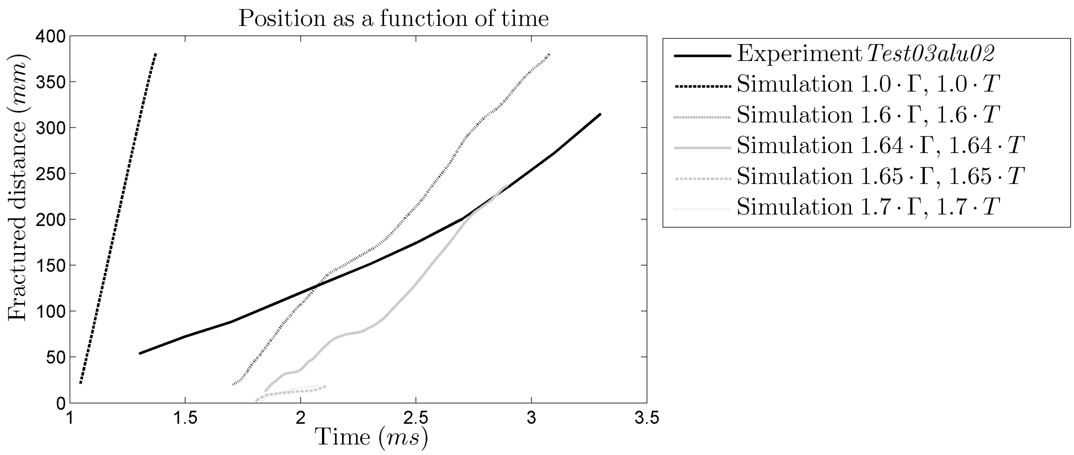

Figure 6.4: Increase of static energy to match experiment Test03alu02

The fact that an increase of 1.64 is insufficient to bring the fracture rate down in the developed fracture phase to observed levels, and a value of 1.65 is too high to allow for the fracture to propagate through its initiation phase, is an indication that the increase must not be a static value, but rather be an opening rate dependent quantity. In figure 6.4, at approximately 2.7 ms, the fracture propagation and velocity for the simulation and the 1.6 increase are close. For a cohesive element lying in this region of the 1.6 times increase simulation, the opening between the bottom and top nodes of the element were extracted and the results are plotted in figure 6.5.

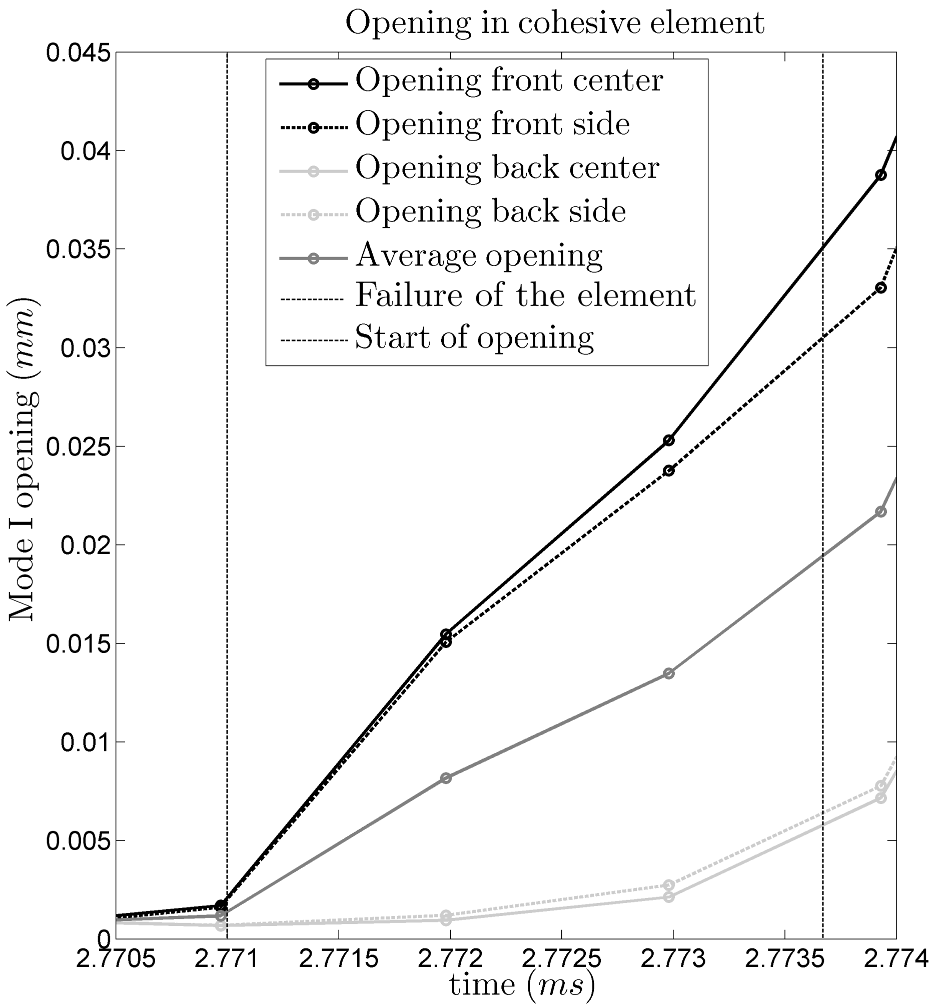

Figure 6.5: Opening rate of cohesive zone in Vulcan barrel test

It is apparent that not all nodes of one flank are moving in unison. The openings of a cohesive element are calculated according to the movement of the centre of the bottom and top flank as visualized in figure 6.6. An average value is thus calculated and this serves as the elemental opening. A normal opening rate of 7.12 $\frac{mm}{ms}$ was derived from it. Armed with this value, it is possible to rewrite equation 6.6 to give an initial estimate of the fluidity η as a function of an assumed exponent N_{pz} and a level of traction higher then the static maximum traction. This quantity is denoted $F_{\text{over}} = \hat{t}_{\max} - T$ the initial estimate for F_{over} comes from the $\frac{\hat{t}_{\max}}{T}$ ratio used in the simulation to acquire the opening rate and the estimate of F_{over} is equal to 0.6.

$$
\begin{aligned}
\frac{\hat{t}_{\max}}{T} &= F_{\text{over}} + 1 &=& \sqrt[N_{\text{pz}}]{\dot{\delta}_n \eta} + 1 \\
& \quad {F_{\text{over}}}^{N_{\text{pz}}} &=& \dot{\delta}_n \eta \\
\frac{{F_{\text{over}}}^{N_{\text{pz}}}}{\dot{\delta}_n} &= \frac{{F_{\text{over}}}^{N_{\text{pz}}}}{7.12} &=& \eta
\end{aligned}
\tag{6.8}
$$

The reason for introducing the quantity F_{over} is that the dynamic increase of the maximum traction T and cohesive energy Γ are now a function of F_{over} and $\dot{\delta}$ alone. A value for N_{pz} can now be found without effecting the dynamic increase in cohesive properties. Once a value for N_{pz} is determined, the corresponding fluidity η can be calculated by:

$$\eta = \frac{F_{\text{over}}^{N_{\text{pz}}}}{\dot{\delta}_n} \tag{6.9}$$

N_{pz} is still unknown but needs to be equal to at least 1. A least squares solution was sought iteratively between the simulations and the smoothed experimental data. Table 6.5 lists the combinations of N_{pz} and F_{over} simulated. The best fit was found for $N_{\text{pz}} = 2.875$ and $F_{\text{over}} = 1.325$. The three best fits are plotted in figure 6.7 along with the experimental data set. The corresponding fluidity η is obtained from equation 6.9 and is equal to 0.31547.

$F_{\text{over}} \backslash N_{\text{pz}}$	12.5	10	7.5	5	2.875	2.75	2.625	2.5	3	2	1.5	1
0.4	X											
0.5		X	X	X								
0.6			X	X				X				
0.7				X								
0.8				X				X				
0.9				X								
1.0				X								
1.1								X				
1.2				X							X	
1.3									X	X	X	X
1.325					X	X	X					
1.35					X	X	X					
1.375					X	X	X					
1.4								X	X	X	X	X
1.5								X	X	X		

Table 6.5: Simulations performed in inverse modelling of Perzyna parameters

While good agreement exists when the velocity is plotted against the position, the simulations have a delay before fracture takes off after initiation of about 0.7 - 0.9 ms. This was found to be caused by the need for a bulge before fracture can start. This bulge takes some time to form in the simulations, while in the explosively triggered experiment it would have been created almost instantaneous. Figure 6.8 shows the moment just before the fracture starts to propagate, at 0.9 ms after the initial fracture was opened up. Figure 6.9a shows the out of plane deflection of three nodes as defined in figure 6.8. Formation of the bulge takes approximately 0.9 ms after which the fracture starts to propagate. In figure 6.9b the experimental data has been plotted

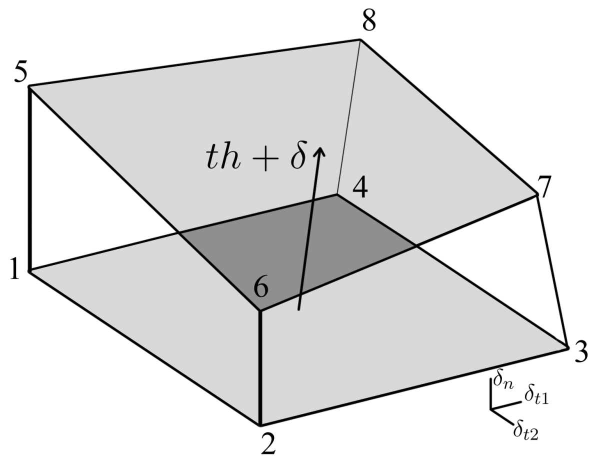

Figure 6.6: definition scetch of CZ

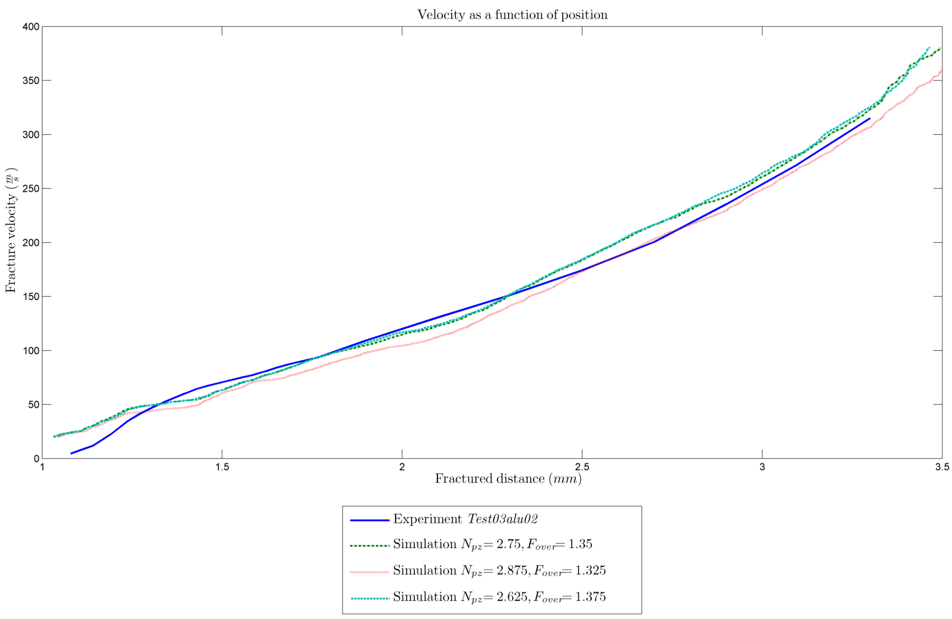

Figure 6.7: *Test03alu02* inverse modelling

against the best fit simulation, where this last graph has been transposed in time $-0.9\ ms$ to correct for the delay caused by the necessary bulging in the simulations. This shows a good relationship between experiment and the simulations with the Perzyna parameters as obtained in this section.

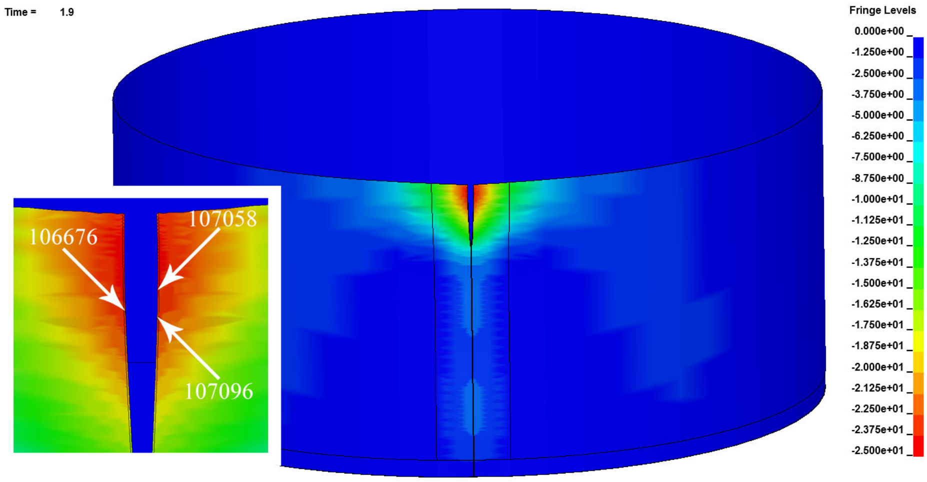

Figure 6.8: Bulge formation at initiation

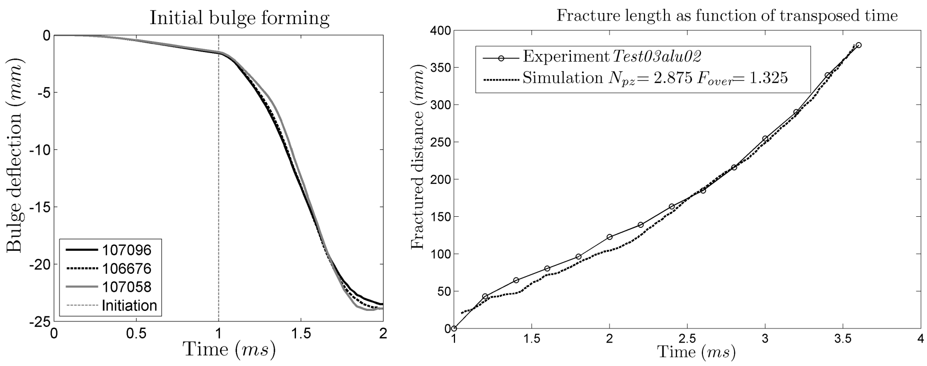

(a) Bulge deflection in time

(b) Fracture velocity

Figure 6.9: Simulation of *Test03alu02* using $N_{\text{pz}} = 2.875$ and $F_{\text{over}} = 1.325$

6.4 Validation

When this report was written, only a single experiment was available to test the predictions of the new opening rate sensitive model. As was explained in section 6.2, this is the Vulcan barrel test *Test03alu02*, with a limited data set. This barrel test was performed with a higher pressure of 310 $\frac{N}{mm}$ and a larger initial notch of $2a = 280\ mm$ than *Test02alu01*, where a pressure of 230 $\frac{N}{mm}$ and an initial notch of $2a = 200\ mm$ was used. Figure 6.10a shows the experimental data plotted against a simulation using the now calibrated, opening rate sensitive, cohesive zone model. Because there is only experimental data available on the initial piece of the fracture growth, and the initiation is the phase where the simulation and the experiment differ most, there can be no definitive answer to the question of the validity of the new cohesive zone model and the parameters derived for it.

Figure 6.10a has two different fracture speed velocity curves, they were derived from two different observations of the same experiment. Determining the exact position of the fracture tip was problematic, resulting in a high variability in fracture velocity. The boundary between the bulging and the start of fracture in the simulations is less clear than for the calibration simulations. A delay of about 0.4 - 0.5 ms was found, and the simulation has been shifted in time by $-0.5\ ms$ in figure 6.10b. This figure shows a reasonable agreement between simulation and experiment, but more test data is required to check the validity of the model.

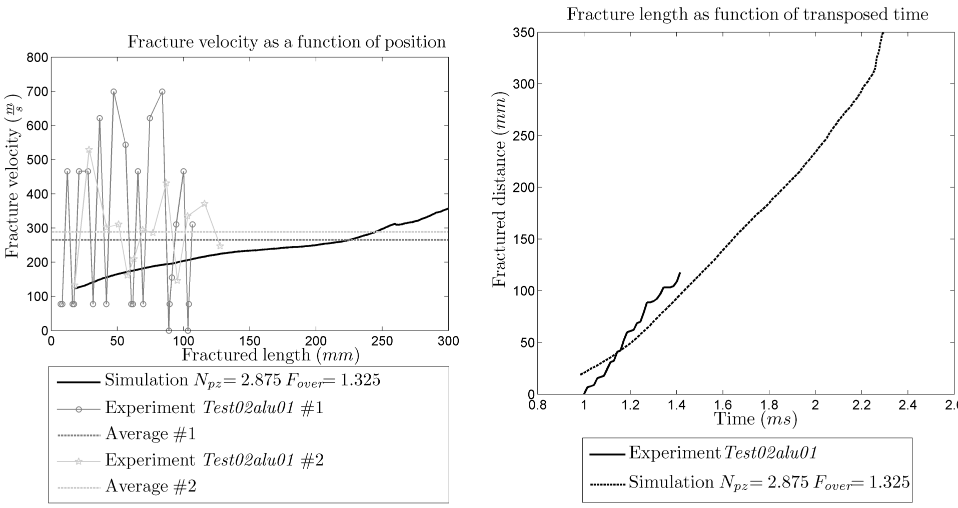

(a) Velocity / position graph (b) Velocity in time

Figure 6.10: Simulation of *Test02alu01* using $N_{\text{pz}} = 2.875$ and $F_{\text{over}} = 1.325$

6.5 Parameter study

A parameter study has been performed to quantify the influence of different parameters relevant to the fracture rate derived from simulations for both the non rate sensitive *MAT_COHESIVE_-GENERAL* and the new Perzyna type rate sensitive cohesive zone model. Unless stated otherwise, all tests were performed on the barrel mesh and geometry with an initial fracture length $a = 140\ mm$, an internal relative pressure of $0.165\ \frac{N}{mm^2}$, a cohesive energy $\Gamma = 19\ \frac{N}{mm}$, a maximum traction $T = 2.1 \cdot \sigma_y = 775\ \frac{N}{mm^2}$ and a plastic kinematic bulk material curve fitted to the Johnson Cook model as described in appendix H.3.

6.5.1 Cohesive energy

The first parameter examined is the cohesive energy Γ. Figure 6.11a shows the result of a series of simulations using MAT_COHESIVE_GENERAL, while the results using the new model are given in 6.11b. Both pictures show the expected decrease in fracture velocity with an increase of cohesive energy Γ. Another observation is that for high cohesive energies, there can be no fracture propagation. This is a direct consequence of the fact that if the amount of energy dissipated per unit length of fracture exceeds the potential energy released, it is energetically not possible for a fracture to continue.

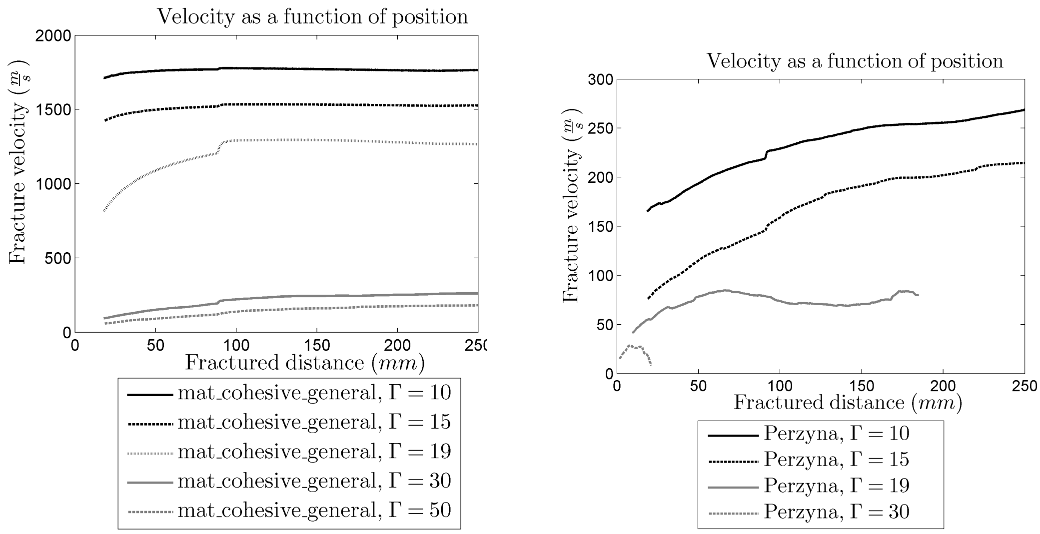

(a) *MAT_COHESIVE_GENERAL* (b) Rate dependent model

Figure 6.11: The effect of the cohesive energy Γ on the fracture velocity

A last observation is the much lower fracture rate with the new model, this is also as expected, the dynamic increase in cohesive energy as a result of high opening rates is an intended feature of the model. Figure 6.12 gives the maximum velocities observed as a function of the cohesive energy.

Straight lines have been curve fitted through the results and show the negative relationship as discussed between cohesive energy and velocity. A noteworthy feature is the fact that there appears to be a possibility for the *MAT_COHESIVE_GENERAL* model to continue at high cohesive energies. This is not as expected as in the analytical stress intensity approach to

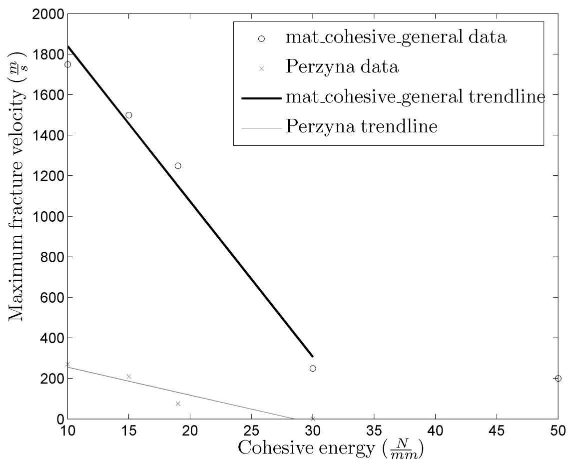

Figure 6.12: Effect of cohesive energy on maximum fracture velocity

fracture mechanics, appendix E.1.1, the stress intensity K is a linear function of the stress and thus the potential energy. It is therefore doubtful that the increasing cohesive energy, and thus the fracture resistance R, is non linear: Other simulations using *MAT_COHESIVE_GENERAL* did not show such a non linearity and it is well possible that more simulations would disprove the existence of it. The Perzyna model shows a more or less linear relationship as expected.

6.5.2 Pressure

The second quantity varied is the relative pressure in the barrel. This has a linear relationship with the hoop stress in the barrel skin through equation 6.10 with r being the radius and t_h the thickness of the barrel skin. Figure 6.13a gives the results of the calculations with *MAT_COHESIVE_GENERAL* and figure 6.13b those obtained with the rate sensitive Perzyna model.

$$\sigma_{\text{hoop}} = \frac{Pr}{t_h} \tag{6.10}$$

It is apparent from figure 6.13a, that the non rate sensitive model has a maximum fracture velocity independent of all but the lowest pressures. Even though this effect was observed in experiments described in section 1.3.2, it remains a physically doubtful observation. The two barrel tests performed within the scope of the Vulcan project had different initial fractures, but this should have no effect on the maximum stable velocity reached, but there was a difference in fracture rate between the two experiments, indicating that there is indeed a pressure dependence for the fracture rate. The rate sensitive calculations do show such a relationship. The maximum fracture velocities are taken once more and plotted as a function of the pressure. This is shown in figure 6.14. The mentioned pressure independence for *MAT_COHESIVE_GENERAL* is likely to be caused by the existence of a limiting velocity.

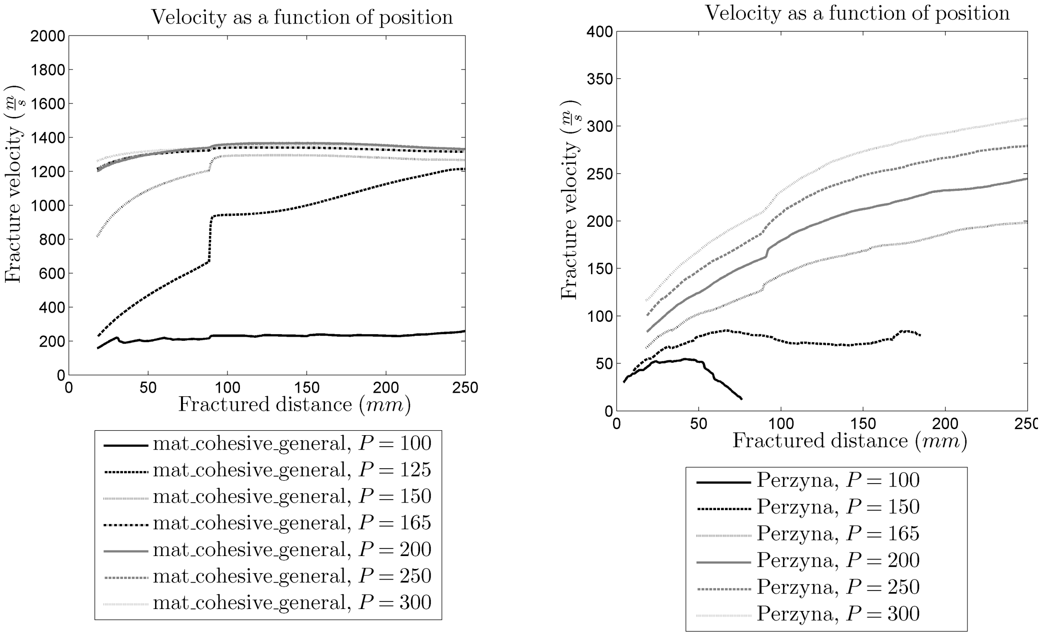

(a) *MAT_COHESIVE_GENERAL* (b) Rate dependent model

Figure 6.13: Effect of the pressure P on the fracture velocity

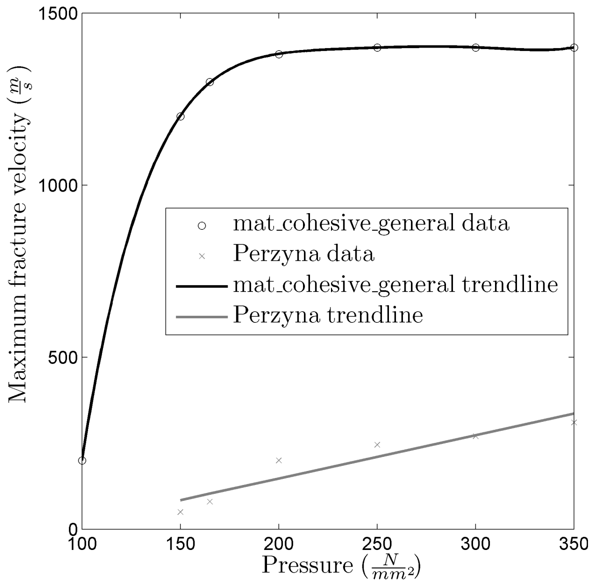

Figure 6.14: Effect of pressure P on maximum fracture velocity

6.5.3 Stiffness

The effect of the stiffness of the cohesive zone is studied in this section for *MAT_COHESIVE_-GENERAL* and the Perzyna model. Cohesive element stiffness is a parameter present in both models, but in *MAT_COHESIVE_GENERAL* it is an implicit quantity defined by the chosen traction separation law and parameters. In the strain rate sensitive model, it is declared directly. Two stiffnesses exist, the initial stiffness K_1 and the slope of the decreasing traction at the end of the TSL, or "damage stiffness" K_2. These need not be equal to each other but have been in this report.

It is argued by many authors[1] that the shape of the TSL does not have an important influence on the simulations performed with it, though this is disputed especially with regards to the initial stiffness and possible numerical problems are associated with high values. Throughout the course of this research the stiffness was chosen in such a way that the non zero thickness cohesive layer initially behaves equal to the surrounding bulk material. To achieve this, the stiffness was set according to equation 6.11.

$$K_1 = K_2 = \frac{E}{t_{\mathrm{cz}}} \tag{6.11}$$

Simulations have been performed with *MAT_COHESIVE_GENERAL* with a varied stiffness, the results of which can be seen in figure 6.15. Table 6.6 shows the implicit stiffness and the TSL parameters used to set it; λ_1, λ_2 and λ_0. Also given is the area under the non dimensional TSL $A_{\mathrm{N.TSL}}$. As the initial stiffness K_1 is equal to the damage stiffness K_2, $A_{\mathrm{N.TSL}}$ is equal to λ_2.

$K_{1,2}$ $\left(\frac{N}{mm}\right)$	λ_1 -	λ_2 -	A_{TSL} -
$\frac{E}{t_{cz}} \cdot 10^{-1}$	0.30	0.70	0.70
$\frac{E}{t_{cz}}$	0.04	0.996	0.996
$\frac{E}{t_{cz}} \cdot 10^{1}$	0.004	0.9996	0.9996
$\frac{E}{t_{cz}} \cdot 10^{2}$	0.0004	0.99996	0.99996

Table 6.6: Effect of stiffness on TSL

The influence of the stiffness appears to be very small, especially when it is considered that there is a $1.0 \cdot 10^5$ factor between the lowest and the highest stiffness used in the simulations. Very high stiffnesses do lead to a delayed reaching of the maximum velocity.

[1]See section 2.2.3

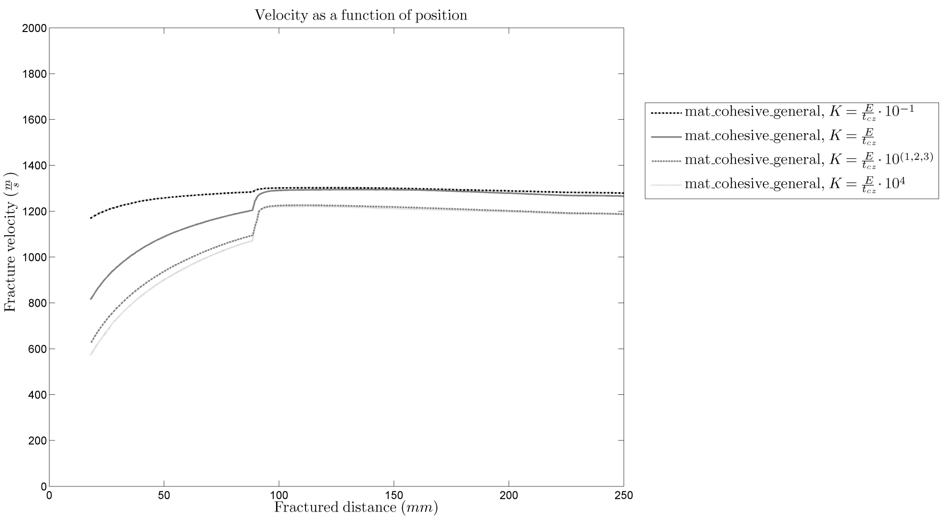

Figure 6.15: Effect of CZ stiffness on fracture velocity

6.5.4 Maximum traction

The effect of the maximum traction T on the fracture velocity is now investigated for cohesive elements of the type *MAT_COHESIVE_GENERAL*. As the maximum traction increases, so does the size of the plastic zone surrounding the fracture tip. It is therefore expected that more energy is being dissipated and a negative relation ship exists between it and the fracture rate. Figure 6.16 gives the results of these calculations. Typical values for T lie between 2 and 3 times the yield stress of the material. A value lower than one results in the absence of a plastic zone and dissipation in the bulk material.

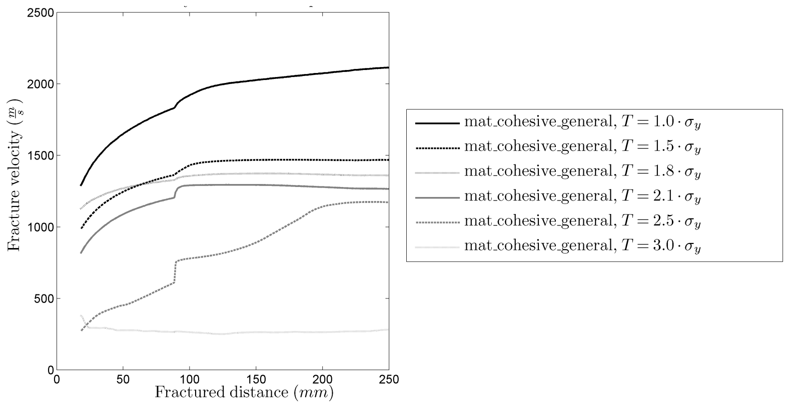

Figure 6.16: Effect of maximum traction on fracture velocity

From figure 6.16 a relatively small influence is observed for values surrounding the value of $2.1 \cdot \sigma_y$, the value obtained in section 4.1, and used in this research. As expected the value of $1.0 \cdot \sigma_y$ results in very high propagation rates, while $3.0 \cdot \sigma_y$ seems to result in fracture rates not consistent with the ones obtained with values for T surrounding $2.1 \cdot \sigma_y$. It is noted that the simulation with $T = 3.0 \cdot \sigma_y$ gives a solution closer to the fracture rates observed in experiments. Yet, $T = 3.1 \cdot \sigma_y$ leads to fracture arrest, Figure 6.17 gives the maximum fracture rates observed as a function of T. A linear trend line has been added, but it is clear that for $1.5 \cdot \sigma_y < T < 2.5 \cdot \sigma_y$ the simulations are relatively insensitive for changes in the maximum traction, while $T = 3.0 \cdot \sigma_y$ proves to be highly unstable.

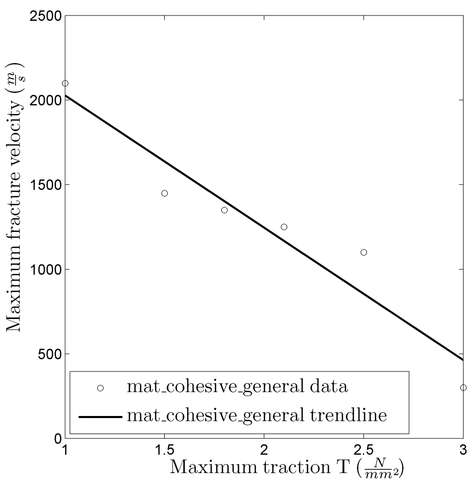

Figure 6.17: Effect of maximum traction on maximum fracture velocity

6.5.5 Fluidity

The fluidity η influences the maximum dynamic traction as a function of the opening rate $\dot{\delta}$. This can be observed in figure 6.18. For this graph, the maximum opening δ and the static traction T was set equal to 1 and the stiffness k_1 and k_2 to 10.

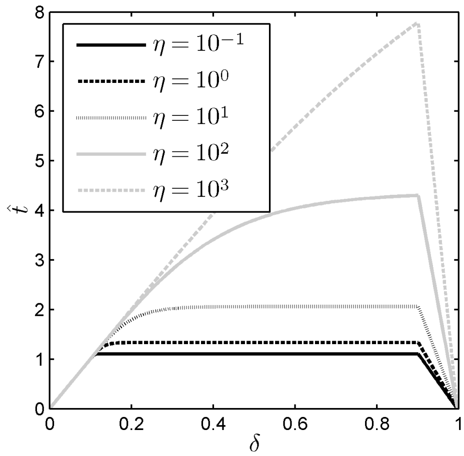

Figure 6.18: The influence of the fluidity η

6.5.6 Perzyna exponent

The exponent in the perzyna model N_{pz}, has two effects: It influences the maximum dynamic traction levels, and it changes how fast these traction levels are reached; instantaneous or more gradual. In figure 6.19, N_{pz} is varied and this results in a similar graph as in figure 6.18. This is caused by the before mentioned effect on the maximum dynamic traction. The effect of N_pz on

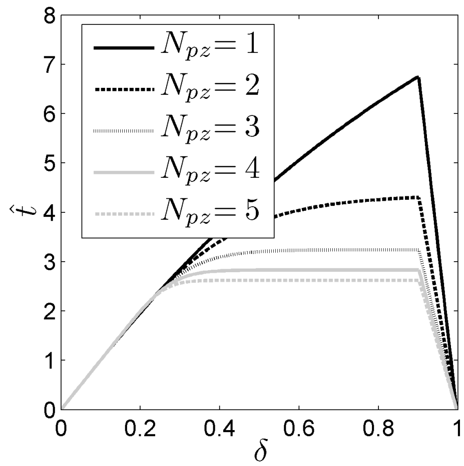

Figure 6.19: The influence of the Perzyna exponent N_{pz}

the shape of the traction separation curve is better illustrated by setting the dynamic traction level constant. This is done in figure 6.20 following the same procedure as was done in section 6.3.

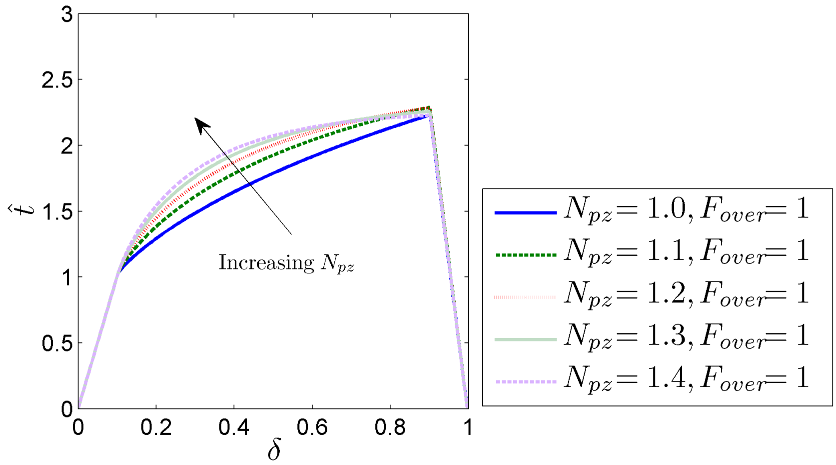

Figure 6.20: The influence of the Perzyna exponent N_{pz} with a constant maximum dynamic traction

6.5.7 Bulk material

A large number of material models exist within LS-DYNA to simulate the material surrounding the fracture, or the *bulk* material. As energy is being dissipated in the plastic zone surrounding the fracture tip, the plastic properties of this material are influencing the amount of energy dissipated and this influences the energy left for the fracture to propagate and thus its speed. In this section three different bulk materials are examined, first the fully elastic *MAT_ELASTIC*, secondly a elasto-plastic material formulation with isotropic hardening and a Cowper Symonds based strain rate dependence: *MAT_PLASTIC_KINEMATIC* and finally the Johnson Cook material model *MAT_SIMPLIFIED_JOHNSON_COOK*. These models are discussed in more detail in appendix H along with the parameters used.

A very comprehensive research yielded definitive Johnson Cook parameters that were used as a bulk material formulation initially. This material model does not output elemental data and it is not possible to view stress states in post processing. By means of curve fitting, plastic-kinematic parameters were obtained that describe the Johnson Cook model data well. Figure 6.21 shows the fracture velocity as obtained from the simulations. In figure 6.21 simulations using *MAT_PLASTIC_KINEMATIC* and *MAT_SIMPLIFIED_JOHNSON_COOK* are denoted "PK" and "JC" respectively.

It is clear from figure 6.21 that the bulk material has an influence on the rate of fracture. A difference in fracture speed simulated between the elastic and the johnson-Cook model of over 100% is present. Furthermore, the curve fitted plastic-kinematic model shows good agreement with the Johnson cook model. Increasing the yield stress past $\sigma = 369$ results in increased rates of fracture progress until the limit as formed by the elastic model. It can be concluded that knowledge of the bulk properties is necessary for obtaining correct fracture rate estimates.

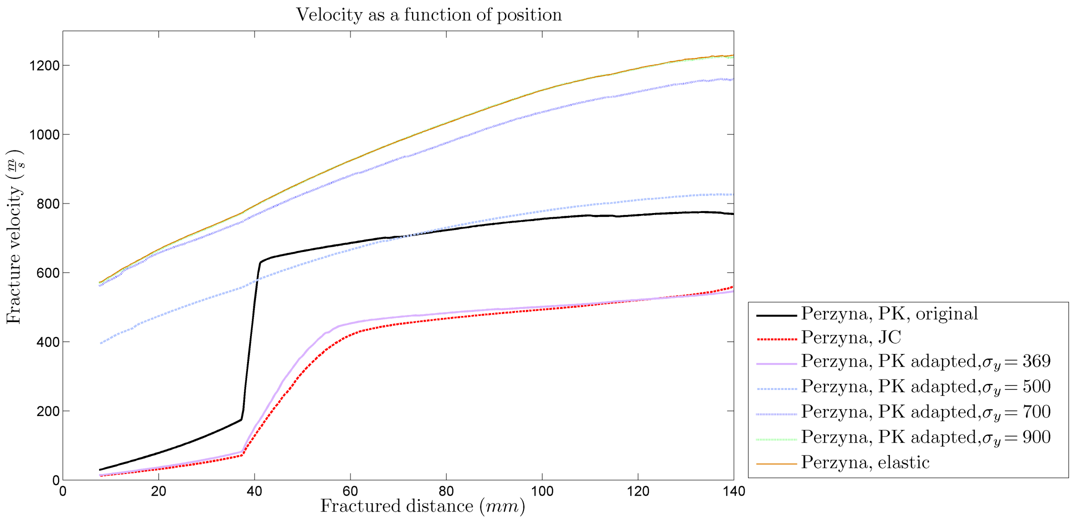

Figure 6.21: Effect of bulk material on fracture velocity

Chapter 7

Conclusions and recommendations

Based on the research performed and literature, conclusions are drawn in section 7.1. Recommendations for future work are given in 7.2.

7.1 Conclusions

Existing analytical and empirical formulae cannot be used to predict the speed of fracture in sheets of aluminium 2024 T3 and duplex steel DIN 1.4462 as observed in experiments. These formulae are either highly overconservative, as they are upper bounds for brittle fracture with fracture velocity estimations in excess of 2000 m/s, or have verified ranges of validity not extending to the types of geometry under research. Fracture propagation rates observed in experiments on pressurized steel gas pipelines fall below 360 m/s at room temperature. Numerical simulations using rate insensitive cohesive zone models with static cohesive properties also dramatically overpredict the rate of fracture.

Based on the visco-plastic Perzyna model, a new rate sensitive cohesive zone element model was derived with a yield surface defined by the Hill criterion. Loading in all three modes of fracture is taken into account, as is unloading and reloading and work hardening. To improve the numerical stability an atypical implementation of the radial return method is employed. The implemented model was tested and found to behave as designed and conforming to limit cases.

The cohesive energy and traction for 1 mm thick plates of aluminium 2024 T3 were obtained from an inverse modelation of a centre cracked plate test. A cohesive energy $\Gamma_{\text{N}} = 19 \ \frac{N}{mm}$ and a maximum traction $T = 2.1 \cdot \sigma_y = 775 \ \frac{N}{mm^2}$ was obtained, these values are in agreement with values reported in literature The visco-plastic properties were derived based on a single Vulcan barrel test as: $N_{\text{pz}} = 2.875 \ (-)$ and $\eta = 3.1546 \frac{[Nms}{mm^2}$. Because of shortcomings in the experimental procedure on duplex steed DIN 1.4462 centre cracked panel testing, no data is available for this material. Subsequent verification of the newly developed cohesive zone element model showed a significant improvement in predictive accuracy over non-rate sensitive models, though further experimental verification is necessary.

A parameter study was performed and both the existing and the new model show a heavy dependence on the cohesive energy for the fracture propagation rate as expected. However,the rate insensitive model showed a non linearity in the dependence of the fracture speed on cohesive energy, allowing fracture to continue at high cohesive energies. The rate insensitive model also showed an independence on the rate of fracture with respect to internal pressure inside a pressure vessel beyond a certain limit value. The rate sensitive model however, shows a linear relationship at all pressures tested. The Vulcan barrel experiments seem to confirm this linear behaviour, but the evidence is insufficient to draw definitive conclusions.

The material model used for the bulk material has an influence on the fracture rate and a difference of 60% procent in fracture velocity was found between an elastic and an elasto-plastic Johnson Cook model with validated parameters. Fracture rate simulations offer little value if the correct visco-plastic properties of the bulk material are unknown.

7.2 Recommendations for future work

The single most important conclusion to be drawn is the fact that simulations using the newly developed cohesive zone model offer a good approximation of the fracture speeds observed in experiments, but the limited amount of available test data forms an impediment for more rigorous verification. As a new series of barrel tests is scheduled, a first priority would be to use these to verify and if necessary update the visco-plastic properties. Recommendations are presented below on future work to be performed with regard to improvement of the simulations and experimental procedures used, in section 7.2.1 and 7.2.2 respectively.

7.2.1 Recommendations for simulations

At this time, LS-DYNA only allows cohesive formulations to be used in 8-noded solids, but a 4 noded shell type element would be more appropriate in thin plate structures. This would eliminate the need for time consuming interface solutions that might also be potential sources of error. This last aspect could be investigated by comparing a shell element type mesh with a corresponding solid element mesh.

The mixed mode performance of the model was not investigated fully as the relevant properties were not available. As this research was focussed on mode I fracture behaviour, this was not an important issue, but in future work the mode II and III cohesive properties could be investigated more extensively.

An assumption was made by making the maximum opening rate insensitive. This assumption remains untested and should be checked with the help of experiments and literature.

Mesh size dependence was not examined, but unlike continuum softening models, cohesive zones do not experience a dependence however if the mesh is sufficiently fine. This remains to be checked for the meshes used in this research.

The integration of the constitutive equations was done using a explicit scheme together with a radial return algorithm based on the dynamic traction limit. The accuracy could be improved by implementing an implicit, backward Euler scheme as was done in [77].

7.2.2 Recommendations for experiments

The plate test originally intended to serve as a source of data for this report, showed questionable results, with unrealistically low fracture rates that were likely caused by significant periodic out of plane deflection of the plate and damage to the material caused by the explosive initiation.

The Vulcan barrel tests showed good results and reproducible fracture rate estimates without external deflections interfering with crack growth. This type of experiment should have preference over the panel tests if possible. The method of initiation for the barrel tests performed so far was identical to the plate tests, but the problems associated with the latter were not present in the barrel test, likely due to the curved geometry and the internal pressure resisting out of plane movement and the hoop stress being able to continuously load the fracture, while the test rig was not necessarily able to keep the force exerted at a constant level.

Barrel tests simulation require knowledge of the cohesive properties of the material. Barrel tests should be accompanied therefore with initially notched plate tests where the load, deflection and fracture extension is monitored. These quantities allow the cohesive energy and traction to be inferred by inverse modelling. A fracture toughness derived from Charpy V-notch testing or linear elastic fracture mechanics shows large variations and and does not provide a maximum traction estimate.

Bulk material behaviour is an important factor in the speed of fracture. At least the strain hardening characteristics should be well defined. The strain rates present in the fracture process zone, are so high that most testing facilities are unable to test them. Very long split Hopkinson bar tests setups are required.

Fracture may not proceed in a perfectly straight line, a wide angle high speed camera is always required apart from the close up near the initiation side. To serve as an input for the finite element simulations, the pressure should be monitored inside the barrel on several points.

Appendix A

Design of a pressurized barrel test setup

A second series of pressurized barrel test was proposed and is partially completed at this time. The setup was made according to the design study presented below. The tests showed the setup to function as designed with perfectly straight running fractures as can be seen in figures A.1. Because no anvil structure was used, the two flanks of the fracture remained intact and unrealistic behaviour of the material surrounding the initial fracture was prevented.

(a) Overview (b) Detail

Figure A.1: New fracture test results

In figure A.1b there appears to be bifurcation of the fracture. This is not a fracture of the aluminium skin of the barrel however, but of the paint cover applied to improve contrast. It is an indication of large strains in the material surrounding the fracture.

A.1 Introduction

Additional tests are proposed within the *European 6th Vulcan framework*. Because of problems related to explosive notching of prestressed plates as described in section 3.1, the focus has now shifted towards barrel test setups. Barrel tests previously performed, were initiated with the help of explosives, cutting a initial fracture by shearing[1]. The anvil structure necessary for creating before mentioned initial fracture is obstructing the outward deflection of the barrel and is responsible for shattering of the barrel skin in a manner not consistent with air plane fuselage explosions, which the test setup aims to emulate. An additional concern is that an explosively created notch has an out of plane deflection on its boundaries and may not accurately simulate a sharp fracture due to fatigue or a penetrating particle. A last consideration is the fact that passenger aircraft have insulation and panelling, making an explosive placed directly against the pressure hull by one of the passengers an unlikely scenario, as the distance to the air plane has been found to have a considerable influence, This effect should be isolated from the tests.

For the new series of tests, a pre-machined, sharp notch is proposed with initial fracture dimensions chosen in such a way as to avoid pre explosive failure due to static pressure alone, with a reasonable amount of confidence. The initial notch is cut and the fracture tips are then extended a further 3 mm using a jeweller's saw or surgeon's blade. This procedure to achieve sharp fracture tips is used because fatigue pre-cracking is prohibitively expensive and this is a well known alternative [78].

The challenge in designing a pre-notched barrel lies in the fact that it must not fail under just its static pressure load and does fail when subjected to an explosive load. Also the appropriate explosive load needs to be determined within the limits of practicality and test site clearance.

[1]See chapter 3

A.2 Static load design

The initial fracture length chosen, should be such that the fracture does not propagate under the static pressure alone that is applied to simulate the overpressure of an aircraft at cruise altitude[2]. Design formula exist to check for the stability of initial fractures. These are presented next.

A.2.1 Design formula

Separate design formula exist for pipes and plates. The barrel geometry used in the tests is in between these geometries. The formulae were taken from [79] and are presented below

Plate fracture sensitivity

This formula is an example of *linear elastic fracture mechanics* and the fracture toughness of the material $K_{\mathrm{I,R}}$ must exceed the geometry dependent stress intensity factor $K_{\mathrm{I,S}}$, in order to prevent fracture. A plate of width W with an initial fracture $2a$ perpendicular to an uniform externally applied stress σ has a stress intensity factor according to

$$K_{\mathrm{I,S}} = C\sigma\sqrt{\pi a} \tag{A.1}$$

Where C is a geometry dependent constant, two different approximations are given, together with the relevant ranges of validity and confidence.

Brown The Brown C approximation has a maximum fault of less then 0.5% for $\frac{a}{W} \leq 0.35$

$$C = 1 + 0.256\left(\frac{a}{W}\right) - 1.152\left(\frac{a}{W}\right)^2 + 12.200\left(\frac{a}{W}\right)^3 \tag{A.2}$$

Fedderson The Fedderson C approximation has a fault of less then 0.3% for $\frac{a}{W} \leq 0.35$

$$C = \sqrt{\sec\frac{\pi a}{W}} \tag{A.3}$$

Pipe fracture sensitivity

For axial through thickness fractures in pipes a separate formula exist. The radius of the pipe is denoted as R, the initial fracture as $2a$, the thickness of the pipe wall as t and the applied hoop stress as σ_{H}. No information is given on the range of validity with regards to the maximum r/t_h ratio.

$$K_{\mathrm{I,S}} = \sigma_{\mathrm{H}}\, M_{\mathrm{f}}\sqrt{\pi a} \tag{A.4}$$

The hoop stress σ_{H} can be calculated from:

$$\sigma_{\mathrm{H}} = \frac{Pr}{t_h} \tag{A.5}$$

Where P is equal to the relative pressure in the pipe. M_{f} can be calculated with the help of equation A.6.

$$M_{\mathrm{f}} = \sqrt{1 + 1.225\left(\frac{a^2}{rt_h}\right) - 0.0135\left(\frac{a^4}{r^2t_h^2}\right)} \tag{A.6}$$

[2]Cruise altitude is approximately 10.000 km, air pressure is less than a third of the ambient pressure at sea level. The relative pressure on the hull is approximately 55 KPa.

A.2.2 Finite element calculations

Finite element simulations were also performed with an existing rate insensitive cohesive zone model. The size of the initial fracture $2a$ and the relative internal pressure P was varied. The initial fractures were held closed with nodal ties called spotwelds in LS-DYNA. These ties are destroyed at $t = 0.1$ ms as immediate destruction is ignored by the finite element package. The static pressure is increased from ambient levels to the required level in the first 0.5 ms, critical damping is applied during the first 1 ms. Simulations were run for a further 3 ms to determine the stability of the initial fracture. Table A.1 shows the result of these calculations. A ($*$) indicates that the specific simulation was not performed as its stability was already known by simulations at different pressures with the same geometry.

P $\left(\frac{N}{mm^2}\right)$	$a = 140$ mm -	$a = 100$ mm -	$a = 66$ mm -	$a = 39$ mm -	$a = 28$ mm -
0.200	$*$	$*$	1583	4	1
0.165	1537	1456	937	2	0
0.135	878	818	869	1	$*$
0.100	364	311	8	$*$	$*$

Table A.1: Number of fractured elements at initial fracture stability simulations

Table A.1 shows a small number of failed elements for certain pressure/initial fracture length combinations. It was checked if this fracture increase represented a slow fracture or an arrested initial fracture increase. It was found that as much as 8 elements failed, representing a fracture increase of around 8 mm, while the fracture proved stable afterwards. Table A.2 lists the stability of the fractures.

P $\left(\frac{N}{mm^2}\right)$	$a = 140$ mm	$a = 100$ mm	$a = 66$ mm	$a = 39$ mm	$a = 28$ mm
0.200	No	No	No	Yes	Yes
0.165	No	No	No	Yes	Yes
0.135	No	No	No	Yes	Yes
0.100	No	No	Yes	Yes	Yes

Table A.2: Stability of initial fracture as observed in finite element simulations

A.3 Initial fracture size recommendation

Similar tables can be drawn for the results of the analytical formulae A.1 and A.4. The exact value of the material's fracture resistance $K_{\mathrm{I,R}}$ varies depending on the source. A reliable value of 60 $\frac{N}{mm}\sqrt{m}$ has been found in a study by the TU Delft [55], where a large number of plates of aluminium 2024 T3 were tested with centre cracks in comparable geometries. If the cohesive zone energy, $\Gamma = 19$, is converted to a fracture resistance however[3], a value of 37.5 $\frac{N}{mm}\sqrt{m}$ is found. The calculations were performed for both values. Table A.3 and A.4 show the stability as derived for plates, and table A.5 and A.6 for pipes. For stable combinations, the number in parenthesis indicates the maximum stable length in mm.

[3]See appendix F for the procedure

P $\left(\frac{N}{mm^2}\right)$	$a = 140\ mm$	$a = 100\ mm$	$a = 66\ mm$	$a = 39\ mm$	$a = 28\ mm$
0.200	No	No	yes (76)	yes (76)	yes (76)
0.165	No	yes (110)	yes (110)	yes (110)	yes (110)
0.135	yes (154)	yes (154)	yes (154)	yes (154)	yes (154)
0.100	yes (235)	yes (235)	yes (235)	yes (235)	yes (235)

Table A.3: Stability of initial fracture size based on plate formula and $K_{\mathrm{I,R}} = 60\ \frac{N}{mm}\sqrt{m}$

P $\left(\frac{N}{mm^2}\right)$	$a = 140\ mm$	$a = 100\ mm$	$a = 66\ mm$	$a = 39\ mm$	$a = 28\ mm$
0.200	No	No	No	No	yes (30)
0.165	No	No	No	yes (45)	yes (45)
0.135	No	No	yes (66)	yes (66)	yes (66)
0.100	No	yes (116)	yes (116)	yes (116)	yes (116)

Table A.4: Stability of initial fracture size based on plate formula and $K_{\mathrm{I,R}} = 37.5\ \frac{N}{mm}\sqrt{m}$

P $\left(\frac{N}{mm^2}\right)$	$a = 140\ mm$	$a = 100\ mm$	$a = 66\ mm$	$a = 39\ mm$	$a = 28\ mm$
0.200	No	No	No	No	yes (29)
0.165	No	No	No	No	yes (34)
0.135	No	No	No	yes (40)	yes (40)
0.100	No	No	No	yes (51)	yes (51)

Table A.5: Stability of initial fracture size based on pipe formula and $K_{\mathrm{I,R}} = 60\ \frac{N}{mm}\sqrt{m}$

P $\left(\frac{N}{mm^2}\right)$	$a = 140\ mm$	$a = 100\ mm$	$a = 66\ mm$	$a = 39\ mm$	$a = 28\ mm$
0.200	No	No	No	No	No
0.165	No	No	No	No	No
0.135	No	No	No	No	No
0.100	No	No	No	No	yes (35)

Table A.6: Stability of initial fracture size based on pipe formula and $K_{\mathrm{I,R}} = 37.5\ \frac{N}{mm}\sqrt{m}$

Based on the finite element simulations and the design formula calculations, a barrel with an initial fracture of $a = 28\ mm$ and an initial relative pressure of $0.165\ \frac{N}{mm^2}$, is deemed not to fracture by its static pressure load alone. Finite element simulations show stability at least up to 39 mm for the higher pressure $P = 0.200\ \frac{N}{mm^2}$. Both the plate and pipe formula, equation A.1 and A.4 show stability for this initial fracture length an pressure as well, based on the empirically derived fracture toughness of $K_{\mathrm{I,R}} = 60\ \frac{N}{mm}\sqrt{m}$. When the lower fracture toughness $K_{\mathrm{I,R}} = 37.5\ \frac{N}{mm}\sqrt{m}$ is used, the plate formula predicts stability as well, however the plate formula fails. Designing according to this combination of formula and fracture toughness yields unrealistically small values for the maximum initial notch. As pointed out in section A.2.1, the range of validity is unknown and its typical use lies in pipes with considerably larger radius to wall-thickness ratios. Combined with the fact that a fracture toughness of $K_{\mathrm{I,R}} = 60\ \frac{N}{mm}\sqrt{m}$ was found in testing, and the pipe formula does show stability for this value, this results in an initial fracture of $a = 28\ mm$ to be recommended for the barrel test on aluminium 2024 T3 at a relative pressure of $0.165\ \frac{N}{mm^2}$. The total length of the fracture is equal to $2 \cdot a = 2 \cdot 28 = 56\ mm$. As the machined notch is to be extended a further 3 mm with a fine saw or knife at either side, the fracture cut initially should be 50 mm long in total.

A.4 Explosive load recommendation

An explosive device is introduced into the centre of the barrel and is required to produce a failure of the barrel through a propagating fracture. The initial fracture of $a = 28\ mm$ is calculated to be non propagating in static stress alone, but will need to fracture as a result of the explosion. To obtain the minimum explosive load needed to produce failure in this mechanism, finite element simulations were performed in LS-DYNA.

The effect of an explosion in a barrel of the geometry at hand were taken from [80], where 4 increasingly powerful explosive devices, known hereafter as $EL_{1,2,3,4}$[4] in order of increasing explosive potential, were simulated and their resulting pressure profiles were calculated for 5 different points on the barrel perimeter. Their locations are given in figure A.2. Symmetry allows this to equate to 7 different load profiles to be set to the barrel skin in the finite element model. Because the mesh used also exploits the symmetry of the barrel, this number reduces to 4. Figure A.3 gives an normalized example of such a profile. The higher velocity blast wave and following pressure wave can be clearly distinguished.

The wall of the barrel was subdivided into 4 concentric zones, loaded according the the explosive load profiles resulting from $EL_{1,2,3,4}$, summed with a static pressure of $0.165\ \frac{N}{mm^2}$. The initial fracture was open from the beginning of the simulation and the static load was built up under critical damping conditions. The transient explosive loads were then applied and the stability of the fracture considered. Table A.7 shows the effect of the explosive loads $EL_{1,2,3,4}$ on the fracture using an opening rate insensitive cohesive element type.

If the newly developed rate sensitive cohesive elements are used, there is a difference in the magnitude of the fracture with explosive load EL_3, as can be seen in table A.8.

Based on table A.7, the explosive load EL_3 is sufficient to produce complete fracture in the longitudinal direction. As higher loads increase the likelihood of failure occurring through other mechanisms then fracture starting from the initial notch, higher loads are not recommended.

[4]For security reasons the size and characteristics of the explosive loads are not given

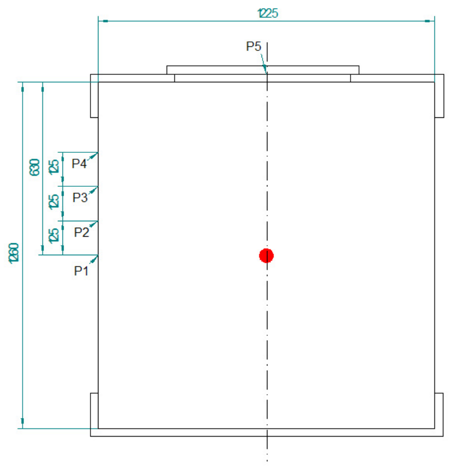

Figure A.2: Points of the calculated load profiles

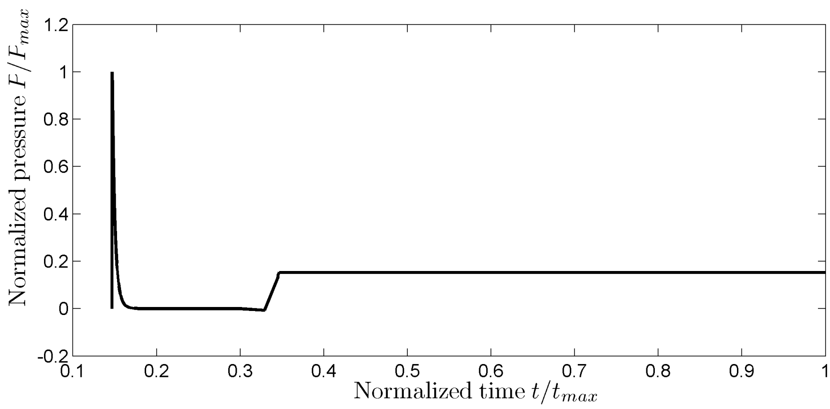

Figure A.3: Example pressure profile of a confined explosive

load	Effect
EL_1	No Fracture
EL_2	No Fracture
EL_3	Complete Fracture
EL_4	Complete Fracture

Table A.7: Effect of explosive load on fracture using ordinary CZ elements

load	Effect
EL_1	No Fracture
EL_2	No Fracture
EL_3	partial Fracture, $\Delta a \approx 70\ mm$
EL_4	Complete Fracture

Table A.8: Effect of explosive load on fracture using ordinary CZ elements

There exists however a possibility of fracture not being complete as de pressurisation might occur before complete fracture can occur as indicated in table A.8. There are however uncertainties with regards to the validity of the Perzyna parameters used and the de-pressurisation profile. The difference in fracture velocity predicted for the tests with EL_3 and EL_4 using both cohesive zone formulations is presented in figure A.4

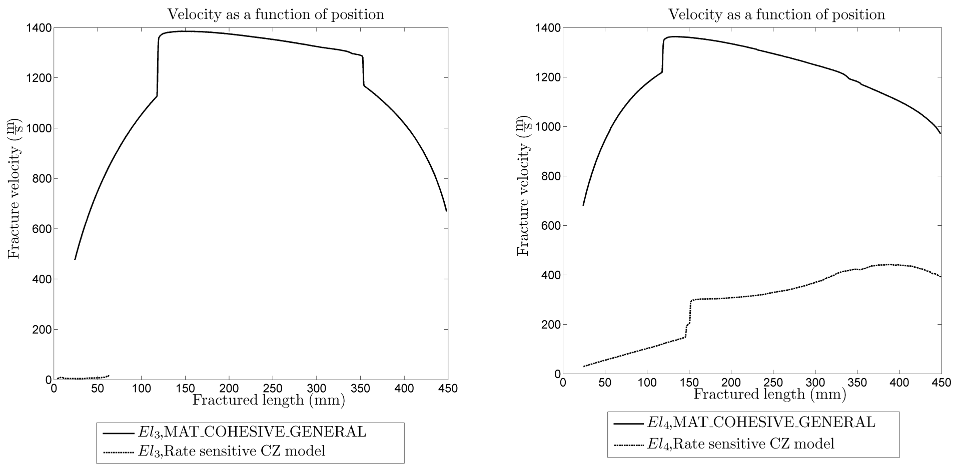

(a) El_3 (b) El_4

Figure A.4: Fracture velocity with two different types of CZ

As indicated, an uncertainty exists with regard to the loading profile; the diminishing pressure after fracture onset is not known exactly. Earlier tests on barrels used pressure transducers to record the pressure profile. These recorded a linear decay in pressure in 12 ms, but were placed in a location where they experienced the decay in pressure delayed. In all calculations on the fracture velocity as presented in this chapter a liner decay in pressure is assumed starting from the arrival of the pressure wave at each point and reaching a zero overpressure at $t = 12\ ms$.

A.5 Chapter conclusion

Designing a barrel that will not fracture under static loading and is sure to fail under explosive loading with its magnitude limited by the constraints of the test terrain, poses difficulties as high safety factors with regard to initial failure cut into the certainty of complete failure after detonation. Based on the calculations and simulations as presented in this chapter an initial fracture of $2a = 56\ mm$ is recommended. Explosive load EL_4 will lead to complete failure with a high degree of certainty. EL_3 might not produce complete fracture but creates a more valuable experiment as it gives more certainty with regards to the minimum required explosive load.

Appendix B

Conference paper

A summary of this report [81] has been entered and accepted as a paper to the of 12th International Conference on Fracture in Ottowa, Canada from the 12th to the 17th of July 2009. The full text is given in this appendix on the subsequent pages. The author contributed to another conference paper to the 17th European Conference on Fracture held in Brno, the Czech Republic, from 2nd to the 5th of September 2008 [82].

Cohesive modeling of ductile dynamic failure of pressurized metallic structures

O. R. van der Meulen[a,b,c,1], J. Mediavilla Varas[c], J. Weerheijm[c,d], and F. Soetens[a,b]

[a] *Eindhoven University of Technology, Faculty of Architecture, Building and Planning, Eindhoven, The Netherlands*
[b] *TNO Built Environment and Geosciences, Delft, The Netherlands*
[c] *TNO Defense, Security and Safety, Rijswijk, The Netherlands*
[d] *Delft University of Technology, Faculty of Civil Engineering and Geosciences, Delft, The Netherlands*

Abstract

Dynamic crack propagation of pressurized aluminum vessels has been studied. Rate insensitive cohesive zone models overpredict the rate of fracture. This was the motivation to implement a new Perzyna cohesive zone model, which is able to explain the low measured crack speeds.

1 Introduction

Fracture mechanics is used successfully to predict the progress of slow fracture processes as fatigue. Fast fracture of ductile materials, on the other hand, proves more difficult to predict accurately. This paper describes a series of tests on aluminium pressure vessels, representing airplane fuselages and a new rate sensitive cohesive zone model to model these.

Accurate estimations of the rate of fracture are of particular interest to the oil and gas industry. Uncontrolled pipeline failure may fail to arrest for many kilometers, if the fracture speed exceeds the gas depressurization speed. Industry formulas to determine the potential for this to occur exist, but are based on empirical measurements and need to be validated for higher strength steels [1].

Another field of application is the research on the severity of occurrences of boiling liquid expanding vapor explosions, also known as BLEVE [2]. In road vehicles carrying liquefied gasses at pressure, a notch resulting from some accident may cause complete containment failure in a matter of milliseconds, leaving the liquefied gas in an unstable superheated state, which then regasifies almost instantaneous, equivalent to a powerful explosion. The severity and even the very occurrence, of a BLEVE are controlled for a great part by the fracture propagation rate.

1.1 Analytical boundaries to the speed of fracture

Analytical boundaries to the speed of fracture do exist, and it is generally accepted that the Rayleigh wave speed serves as an absolute upper bound [3]:

$$c_R = c_S \frac{0.862 + 1.14\nu}{1 + \nu}. \tag{1}$$

where,

$$c_S = \sqrt{\frac{E}{2\rho\,(1 + \nu)}}. \tag{2}$$

[1] Corresponding author
Email address: o.r.v.d.meulen@tue.nl

This yields an upper bound for steel and aluminum of 3000 and 2800 m/s respectively. Attempts to lower the upper bound fracture propagation rate by using the Griffith model have resulted in an asymptotic upper bound for brittle fracture and fracture lengths orders greater then the initial crack length [4]:

$$c_{\text{limit}} = 0.38c_0. \tag{3}$$

where C_0 is the material sound speed:

$$C_0 = \sqrt{\frac{\mu}{\rho}}. \tag{4}$$

This lowers the upper bound to fracture speeds of 2000 m/s for steel and 1900 m/s for aluminum. This is still many times faster than the speeds observed in experiments, which lie in the range of 300 - 500 m/s [5].

2 Experiments on pressurized barrels

The EU VULCAN projects aims at studying the vulnerability of airplane fuselages in case of an internal explosion and fire. In this framework, tests were carried out at TNO DSS[2] on pressurized aluminum 2024 T3 barrels to obtain the speed of fracture in airplane fuselages. The dimensions and internal pressures of the barrels are given in Table 2. High speed cameras were used to monitor the fracture propagation. Fracture was triggered with the use of explosives and a static anvil bar, creating an initial notch in shear of length $2a$. figure 1a shows a post mortem of the test setup. figure 1b shows the fracture surface of another test performed on the same batch of one millimeter thick aluminum, indicating ductile failure through void coalescence as the fracture mechanism. The recorded fracture speeds were less than 300 m/s (see later figure 6 and Figure 7).

Test	Pressure	2a	Height	Diameter	Thickness
	kPa	mm	mm	mm	mm
Test02alu1	310	280	1030	1200	1
Test03alu2	230	200	1030	1200	1

Table 1: Test barrel geometry and load.

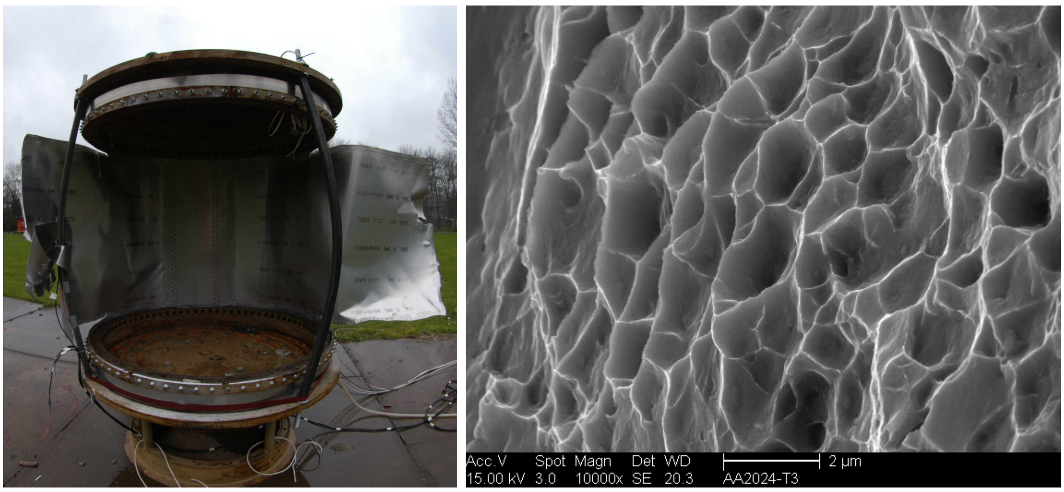

(a) Barrel test after fracture (b) Close-up of fracture surface.

Figure 1: The results of fracture

[2]TNO Defense, Security and Safety, Rijswijk, The Netherlands

3 Shortcomings of standard CZ models for dynamic crack propagation

To predict the dynamic crack behavior of the pressurized barrels described in section 2, the nonlinear explicit finite element code LS-DYNA has been used. Explicit finite element codes are especially well suited for highly transient phenomenon as fast fracture. Fracture is modeled by means of the *cohesive zone* (CZ) approach. The cohesive zone serves to incorporate all nonlinearities in the fracture process zone in a single row of elements of negligible width. Cohesive zones are used as intermediate elements in between two bulk meshes and define a possible fracture path. The cohesive behavior is defined by a cohesive energy Γ, a maximum traction T, and a non-dimensional traction separation law or TSL. The maximum traction and cohesive energy are not independent from one another and need to be obtained together [6]. Figure 2 depicts the type of TSL used in this research. The cohesive properties of aluminum

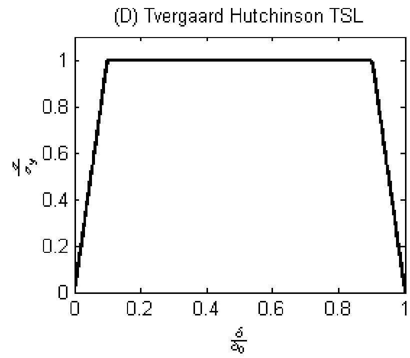

Figure 2: CZ law model with a tri-linear traction-separation law

2024 T3 were obtained from reference [7], where an inverse modeling technique was applied to a centre cracked tension test, with a similar thickness as that of our barrel tests. A cohesive energy $\Gamma = 18$ N/mm and a maximum traction of $T = 2.1\sigma_y$, with σ_y being the material yield stress. This value is comparable to the value reported in [8, 9] of $\Gamma = 17$ - 19 N/mm, and $T = 2$ - $2.7\sigma_y$.

Using these cohesive properties to do simulations of the barrel experiments of section 2, leads to a gross overestimation of the actual fracture speed, roughly $c = 1100$ m/s, instead of the 300 m/s measured. See figure 3. To reproduce the test data, a significantly higher cohesive energy is needed, $\Gamma = 100$ N/mm. This indicates than in dynamic fracture the cohesive energy must be higher than in the static case. Nevertheless, no experimental data on the fracture energy at high rates was available to confirm these findings.

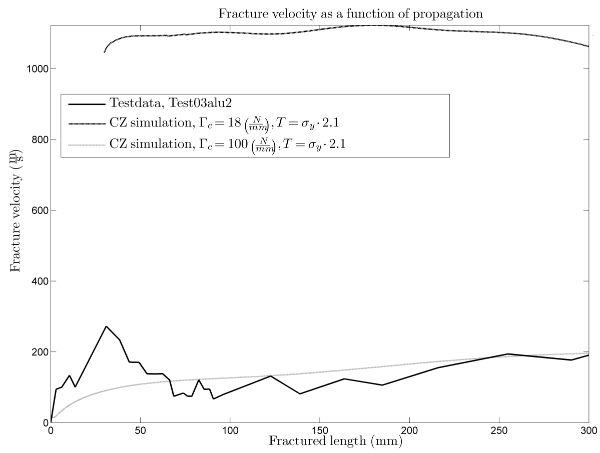

Figure 3: Test data with regular and increased cohesive energy level simulations.

4 Motivation for using a rate dependent cohesive zone model

During dynamic crack propagation, the material undergoes rapid strain rate changes. As many mechanical properties, the fracture energy is also rate sensitive. Thus using one constant static fracture energy during dynamic crack propagation is not realistic. We believe this rate sensitivity is partly responsible for the discrepancies in crack speed between experiments and conventional (non-strain rate sensitive) cohesive zone models. This is the motivation of the work presented in this paper. A user defined rate sensitive cohesive zone model has been developed in LS-DYNA, namely a visco-plastic Perzyna type cohesive model.

4.1 Constitutive equations

The continuum Perzyna model was adapted for use in cohesive zones and is defined by the following set of partial differential equations. Note that work hardening has been excluded. The variable $\hat{t}$ denotes a traction (3 components), not a stress tensor (9 components).

$$\psi(\hat{t}_{eq}) = \left\langle \frac{\hat{t}_{eq}}{T} - 1 \right\rangle^{N_{\mathrm{pz}}}. \tag{5}$$

$$\dot{\boldsymbol{\delta}}_{\boldsymbol{vp}} = \frac{1}{\eta}\psi(\hat{t}_{eq})\frac{\partial \hat{t}_{eq}}{\partial \hat{\boldsymbol{t}}}. \tag{6}$$

$$\dot{\hat{\boldsymbol{t}}}_{\boldsymbol{el}} = \dot{\hat{\boldsymbol{t}}} - \dot{\hat{\boldsymbol{t}}}_{\boldsymbol{vp}} = K(\dot{\boldsymbol{\delta}} - \dot{\boldsymbol{\delta}}_{\boldsymbol{vp}}). \tag{7}$$

This system of differential equation is numerically integrated using a simple Euler forward type integration. First the equivalent traction is calculated:

$$\hat{t}_{eq,n} = T\sqrt{\frac{\hat{t}^2_{\mathrm{III},n-1}}{S^2} + \frac{\hat{t}^2_{\mathrm{II},n-1}}{S^2} + \frac{\hat{t}^2_{\mathrm{I},n-1}}{T^2}}. \tag{8}$$

And then the overstress function:

$$\psi_n(\hat{t}_{eq}) = \left\langle \frac{\hat{t}_{eq,n}}{T} - 1 \right\rangle^{N_{\mathrm{pz}}}. \tag{9}$$

Followed by the normal to the yield surface:

$$\begin{aligned}
\frac{\partial \hat{t}_{eq,n}}{\partial \hat{t}_{\mathrm{III},n-1}} &= \frac{T\hat{t}_{\mathrm{III},n-1}}{S^2\sqrt{\frac{\hat{t}^2_{\mathrm{III},n-1}}{S^2} + \frac{\hat{t}^2_{\mathrm{II},n-1}}{S^2} + \frac{\hat{t}^2_{\mathrm{I},n-1}}{T^2}}}, \\
\frac{\partial \hat{t}_{eq,n}}{\partial \hat{t}_{\mathrm{II},n-1}} &= \frac{T\hat{t}_{\mathrm{II},n-1}}{S^2\sqrt{\frac{\hat{t}^2_{\mathrm{III},n-1}}{S^2} + \frac{\hat{t}^2_{\mathrm{II},n-1}}{S^2} + \frac{\hat{t}^2_{\mathrm{I},n-1}}{T^2}}}, \\
\frac{\partial \hat{t}_{eq,n}}{\partial \hat{t}_{\mathrm{I},n-1}} &= \frac{\hat{t}_{\mathrm{I},n-1}}{T\sqrt{\frac{\hat{t}^2_{\mathrm{III},n-1}}{S^2} + \frac{\hat{t}^2_{\mathrm{II},n-1}}{S^2} + \frac{\hat{t}^2_{\mathrm{I},n-1}}{T^2}}}.
\end{aligned} \tag{10}$$

And the plastic part of the opening rate:

$$\dot{\boldsymbol{\delta}}_{\boldsymbol{vp,n}} = \frac{1}{\eta}\psi_n\left(\hat{t}_{eq,n}\right) \cdot \frac{\partial \hat{t}_{eq,n}}{\partial \hat{\boldsymbol{t}}_{\boldsymbol{n-1}}}. \tag{11}$$

Finally the traction update is computed:

$$\hat{t}_{\mathrm{II,III},n} = \hat{t}_{\mathrm{II,III},n-1} + K_1\left(\dot{\delta}_{\mathrm{II,III},n} - \dot{\delta}_{vp,\mathrm{II,III},n}\right)\Delta t. \tag{12}$$

An additional penalty term is included for normal compression forces to avoid penetration:

$$\hat{t}_{\mathrm{I},n} = \begin{cases} \hat{t}_{\mathrm{I},n} + K_1(\dot{\delta}_{\mathrm{I},n-1} - \dot{\delta}_{vp,\mathrm{I},n})\Delta t & \text{, Without penalty} \\ \hat{t}_{\mathrm{I},n} + K_1(\dot{\delta}_{\mathrm{I},n-1} - \dot{\delta}_{vp,\mathrm{I},n})C_{\mathrm{pen}}\Delta t & \text{, With penalty} \end{cases} \tag{13}$$

with K_1 being the elastic stiffness of the cohesive zone.

The maximum opening is independent of the opening rate and can be calculated from the cohesive energy, the shape of the TSL and the maximum traction. To calculate the maximum combined opening, a power law equation is used:

$$\delta_{0,n} = \frac{1+\beta_n^2}{\mathrm{A}_{\mathrm{N.TSL}}} \frac{1}{\sqrt[\mathrm{XMU}]{\left(\frac{T}{\Gamma_{\mathrm{N}}}\right)^{\mathrm{XMU}} + \left(\frac{S\beta_n^2}{\Gamma_{\mathrm{T}}}\right)^{\mathrm{XMU}}}}. \tag{14}$$

where $A_{\mathrm{N.TSL}}$ is the area under the normalized TSL and β is the "mode mixity", expressing a ratio between normal and tangential opening:

$$\beta_n = \frac{\sqrt{\hat{\delta}_{\mathrm{II},n} + \hat{\delta}_{\mathrm{III},n}}}{\delta_{\mathrm{I},n}}. \tag{15}$$

The current combined opening is expressed as:

$$\delta_{\mathrm{eq},n} = \sqrt{\hat{\delta}_{\mathrm{III},n} + \hat{\delta}_{\mathrm{II},n} + \langle \delta_{\mathrm{I},n} \rangle}. \tag{16}$$

The normal opening δ_I is enclosed by McCauley brackets to exclude compressive forces. The tangential opening directions are integrated according to:

$$\hat{\delta}_{\mathrm{II,III}} = \int \dot{\delta}_{\mathrm{II,III}} \Delta t \cdot \mathrm{sign}\left(\sigma_{\mathrm{II,III}}\right). \tag{17}$$

The declining stress part of the cohesive zone model is described by a damage opening distance δ_{dam}. At each time step, the sum of the current opening δ_{eq} and the damage opening distance δ_{dam}, is checked against the maximum opening δ_0. When this is exceeded, the element is no longer governed by the visco-plastic system of equations, but rather by a linear damage formulation. As can be seen in figure 5, the failure opening is equal for all opening rates.

4.2 Gauss point tests

The opening rate dependent cohesive zone model described in section 4.1 has been tested at single gauss point level. this is shown in figure 4. The maximum traction T and the fracture energy Γ (the area below the $\hat{t}$ - δ curve) increases with the opening rate, while leaving the maximum opening unchanged. This causes the cohesive energy to rise and bring the speed of fracture down.

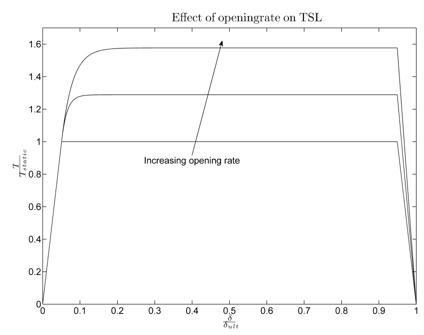

Figure 4: Perzyna cohesive zone model. an increase in the maximum traction and fracture energy is observed at increasing opening rates.

Another interesting feature of the Perzyna model is that it is able to cope with discontinuities in opening rate, while returning a continuous stress response. This can be observed from figure 5.

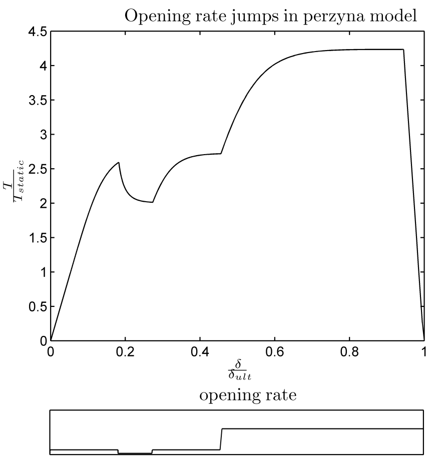

Figure 5: Perzyna type cohesive zone's response to a discontinuous opening rate.

4.3 Parameter determination

The Perzyna cohesive zone model has two additional parameters as compared to standard cohesive zone formulations, i.e. the apparent viscosity η and the Perzyna exponent N_{pz}, which need to be obtained.

The two tests with pressurized barrels [10] served as the basis for this. From one of the tests, "Test03alu2", depicted in figure 6, we were able to estimate the Perzyna parameters $\eta = 0.315$ and the Perzyna exponent $N_{\mathrm{pz}} = 2.875$. For comparison, a simulation with a standard cohesive zone with identical cohesive properties is also included. The differences in crack speed of the two models are very large.

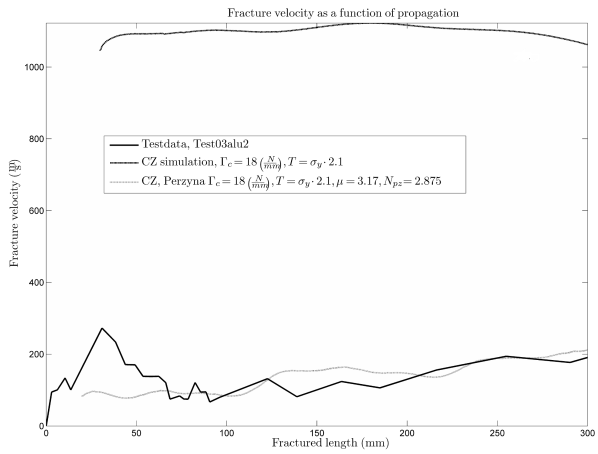

Figure 6: Custom cohesive zone model trained by experimental data.

4.4 Model validation

The visco-plastic Perzyna parameters obtained in 4.3 were used to do a simulation of the second barrel test. The results of which are presented in figure 7. The experimental data curve seems to converge to the fracture speed values obtained with the newly developed visco-plastic cohesive zone model. Unfortunately, the experimental data set is far from complete; the fracture ran outside the scope of the recording high speed cameras.

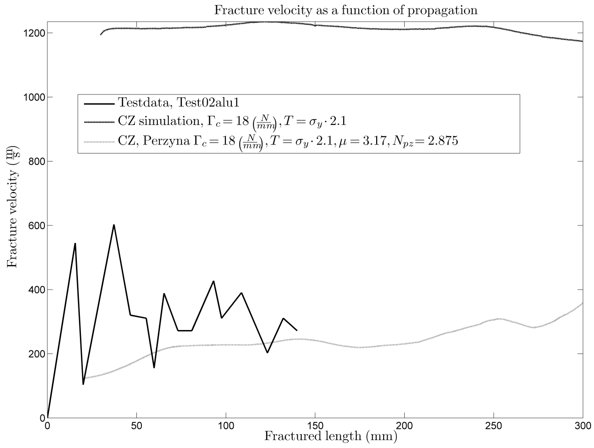

Figure 7: Testing the custom cohesive zone model against experimental data.

The difference in initial velocity of the tests and the simulations may be explained by the method of initiation. Both barrel test fractures were started with the help of explosives, the simulations however, were started using a set of constraints, holding an initial notch closed until the designated time of failure. At that time a bulge started forming, allowing the fracture to speed up as it is formed. The explosive charge not only created the required bulge almost instantaneous, it would have also imparted kinetic energy to the material surrounding the fracture. This explains the initial peak in fracture propagation rates.

5 Future work

Recently an new tests series was performed on barrels made out of aluminium 2024 T3, Glare 3 3/2 0.4, and CFRP composite to compare their relevant performance as an airplane fuselage material in cases of internal explosions. Figure 8 shows the preliminary test results. Additional results are presented at ICF12 and in [11].

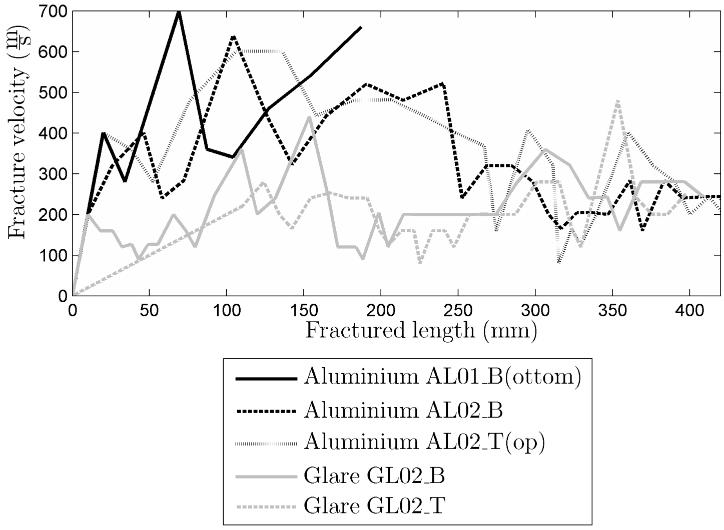

Figure 8: Barrel with an initial notch $2a = 56\ mm$ and an internal pressure of $200\ kPa$ subjected to an internal explosion equivalent to 54 grammes of TNT.

6 Conclusions

Two tests on pressurized aluminum barrels made out of 2024 T3 were performed. Using conventional cohesive zone formulations and the static cohesive energy level, we were unable to reproduce the experimental fracture propagation rates. Reproducing the observed fracture speed required cohesive energy levels as much as five times as high. A visco-plastic, opening rate sensitive CZ model has been developed for LS-DYNA. The new visco-plastic CZ model accurately predicts the stable fracture propagation rates in barrel tests made of aluminum 2024 temper T3.

acknowledgements

The authors wish to express their gratitude to the EU VULCAN project, for its financial support.

References

[1] G. Demofonti, G. Mannucci, C.M. Spinelly, L. Barantsi, and H.G. Hillenbrand. Large-diameter x100 gas line pipes: Fracture propagnation evaluation by full-scale burst test. Technical report, Europipe, 2000.

[2] A.C. van den Berg, M.M. van der Voort, J. Weerheijm, and N.H.A. Versloot. Bleve blast by expansion-controlled evaporation. *Process Safety Progress*, 25:44–51, 2005.

[3] D. Sherman. Macroscopic and microscopic examination of the relationship between crack velocity and path and rayleigh surface wave speed in single crystal silicon. *Journal of the Mechanics and Physics of Solids*, 53(12):2742–2757, December 2005.

[4] D. Hull and P. Beardmore. Velocity of propagation of cleavage cracks in tungsten. *International Journal of Fracture*, 2(2):468–487, June 1966.

[5] J. Mediavilla, J. van Deursen, and J. Weerheijm. Mechanical aspects of the initiation of a bleve. Technical report, TNO Defence, Security and Safety, 2008.

[6] W. Brocks. Ductile crack extension in thin-walled structures six lectures cism course "nonlinear fracture mechanics models". Technical report, GKSS Research Centre, Geesthacht, July 2008.

[7] T.J. de Vries and C.A.J.R. Vermeeren. R-curve testdata: 2024-t3, 7075-t6, glare 2 and glare 3. Technical report, TU-Delft, 1995. LR M-705.

[8] Sushovan Roychowdhury, Yamuna Das, Arun Roy, Robert H, and Dodds. Ductile tearing in thin aluminum panels: experiments and analyses using large-displacement, 3-d surface cohesive elements. *Engineering Fracture Mechanics*, 69:983–1002, 2002.

[9] W. Brocks and Th. Siegmund. Effects of geometry and material on the energy dissipation rate. In M. Fuentes, M. Elices, A. Martn Meizoso, and J. M. Martnez-Esnaola, editors, *Fracture Mechanics: Applications and Challenges : Invited Papers Presented at the 13th European Conference on Fracture*, San Sebastian, September 2000. ECF, Elsevier.

[10] Jesus Mediavilla, Jaap Weerheijm, Ronald van der Meulen, F. Soetens, C. Wentze, and J. van Deursen. Dynamic crack propagation: an experimental-numerical approach. In J. Pokluda, P. Lukáš, P. Sandera, and I. DLouhý, editors, *17th European Conference on Fracture. Book of Abstracts and Proceedings on CD ROM*, pages 2039–2046, 2008.

[11] J. Mediavilla, F. Soetens, O. R. van der Meulen, and M. Sagimon. Dynamic crack propagation of glare and cfrp fuselage materials. In *Proceedings of: Deformation and Fracture of Composites Conference (DFC10)*, Sheffield United kingdom, April 2009. Sheffield University.

Appendix C

LS-DYNA manual

To facilitate the usage of the newly developed rate sensitive cohesive zone model a short manual has been written. The format is intentionally made to be as close as possible to the one used in the LS-DYNA keyword manual [59]. Copyright restrictions prohibit the redistribution of the compiled LS-DYNA program with the user defined cohesive zone model included, but any registered LS-DYNA user may download the partially compiled files for their operating system from the LSTC ftp servers after requesting a login, and replace the dummy subroutine with the code as given in apendix L. A make-file is included and the compiling is a straightforward procedure.

There are five required cards to be filled out, the first two of which are generic for all custom materials. Units are provided as an example, Internally there is no concept of unit in the finite element code, but the user must make sure he is consistent with units in the input file and when evaluating output. The units presented here are consistent with an input file based on millimetres, milliseconds an Newtons. Possible ranges for the parameters are also given along with a recommended value. A value not set explicitly is treated as 0.0 by default, which may not be a possible value and result in failure. No safeguards are included to test for this as this would have to be done at every time step at every gauss point, due to the way custom materials are included in LS-DYNA. The user must therefore manually specify all values that are unequal to 0.0. The recommended values represent a suggestion in the absence of more precise information or preference by the user, not a strong recommendation.

Cohesive zones are intermediate elements relating a movement between their upper and lower faces to a traction according some cohesive law. This difference in movement represents an opening, which is considered in three directions as depicted in figure C.2. The first four nodes defined in the mesh are considered the bottom flank and the last four the top. Care must be taken to ensure the cohesive elements are orientated correctly.

The non strain rate sensitive material behaviour is governed by a tri-linear Tvergaard Hutchinson TSL as depicted in non dimensional form in figure C.1a. *KLOAD* (K_1) and *KULOAD* (K_2) define the loading and unloading stiffness of the TSL respectively. The cohesive energy in mode I *GIC* (Γ_{N}) and the other two modes *GIIC* (Γ_{T}) are equal to the energy underneath the TSL as shown in figure C.1b. T (T) and S (S) represent the maximum traction in mode I and II/III respectively and figure C.1c shows this for mode I. The maximum opening δ, figure C.1d, is a function of all the parameters named before and cannot be set directly.

The visco-plastic properties are determined by the apparent fluidity and Perzyna exponent. The cohesive model takes the inverse of the fluidity as an argument for reasons of computational efficiency. Therefore *FLDTY* is equal to $(\frac{}{\mu})$ and *PEX* to (N_{pz}). Work hardening can be set using the *WORKH* card.

Mixed mode loading is handled by one of three models as given below and can be selected by the *TES* parameter. For more information on the three models the reader is pointed to section 5.5.3. The first two models take an additional argument in the form of exponent *xmu*.

TES = 0.0 Power law formulation.

TES = 1.0 Benzeggagh Kenane law.

TES = 2.0 Dimensionless effective parameter approach.

A optional penalty term for mode I compressive openings is provided. The value entered in the *STFSF* is increased by 1.0 and all compressive displacements will produce tractions multiplied with this number.

In Practical applications, the cohesive zone elements will most likely define the maximum time step. If a certain range of cohesive elements needs more time steps than the internal time step calculation scheme offers, an increased number of time steps can be forced by scaling the maximum expected elemental stiffness reported to LS-DYNA, without effecting the actual stiffness. *DTCTRL* is the parameter controlling this mechanism and it acts as a factor on the Courant limit specified to the total model. The advantage of using *DTCTRL* is the fact that when all the artificially stiffened elements have failed, the time step returns to normal levels.

The last three card entries control the outputs generated by LS-DYNA. *SCREEN*, *MESSAG* and *HSP* are used to set the information to be outputted to the computer screen, message file and error log respectively. 4 levels of detail are offered for all these output methods,

0.0 Warnings only; only possible errors produced by the model are reported. Used mainly for debug purposes.

1.0 Summary; the element and time of failure is reported for each gauss point.

2.0 Detailed; a full report of failure, giving maximum tractions, energy dissipated, opening and work hardening as well as the element number and time of failure.

3.0 Suppress all outputs. The custom code will not output. Please note LS-DYNA will still report failed elements.

The LS-DYNA keys are presented in tables C.1. A LS-DYNA manual style short description of the parameters can be found in table C.2.

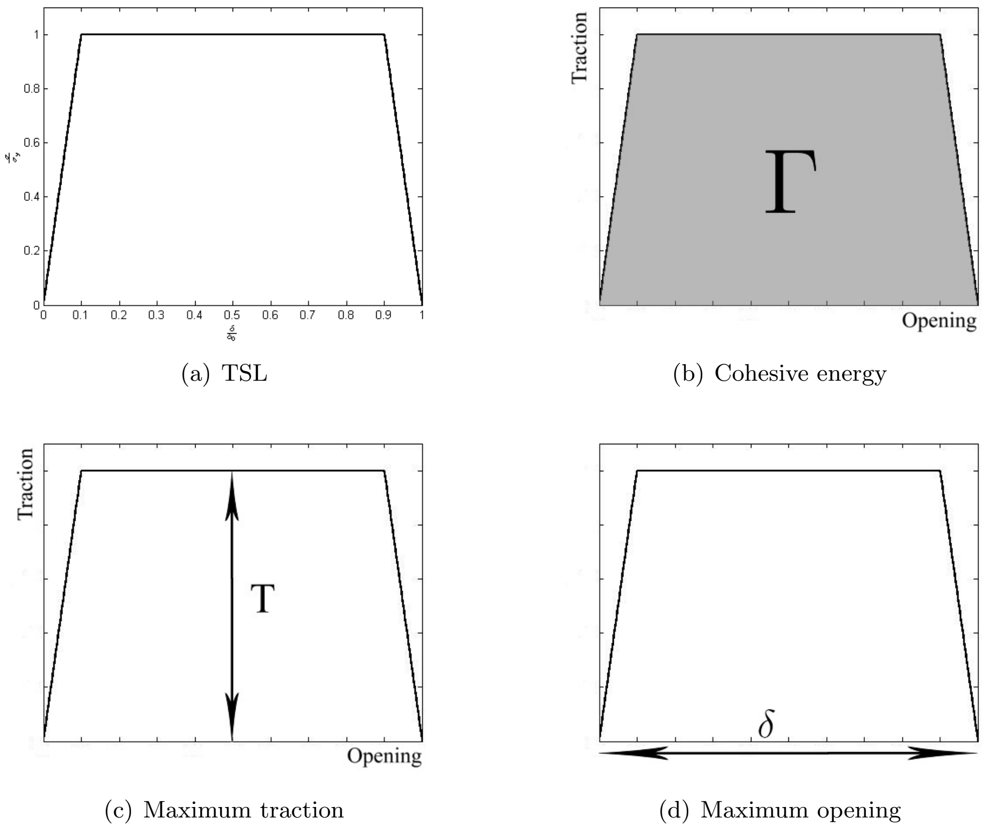

(a) TSL

(b) Cohesive energy

(c) Maximum traction

(d) Maximum opening

Figure C.1: Cohesive properties of the model

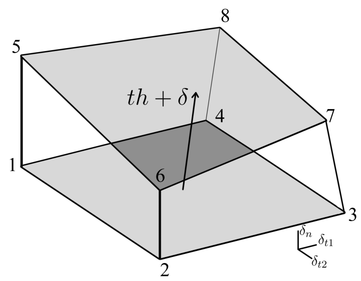

Figure C.2: Cohesive zone opening

card1	1	2	3	4	5	6	7	8
Variable	MID	RO	MT	LMC	NHV			
Unit	-	$\frac{N}{mm^3}$	-	-	-			
Range	-	$\mathbb{R}^+$	45.0	18.0	14.0			
Recomm.	-	-	45.0	18.0	14.0			

card2	1	2	3	4	5	6	7	8
Variable	IVECT	IFAIL						
Unit	-	-						
Range	$\in \{0,1\}$	$\in \{0,1\}$						
Recomm.	1.0	1.0						

card3	1	2	3	4	5	6	7	8
Variable	RHOSTO	NFAIL	GIC	GIIC	T	S	KLOAD	KULOAD
Unit	-	-	$\frac{N}{mm}$	$\frac{N}{mm}$	$\frac{N}{mm^2}$	$\frac{N}{mm^2}$	$\frac{N}{mm}$	$\frac{N}{mm}$
Range	$\in \{0,1\}$	$\in \{1,2,3,4\}$	$\mathbb{R}^+$	$\mathbb{R}^+$	$\mathbb{R}^+$	$\mathbb{R}^+$	$\mathbb{R}^+$	$\mathbb{R}^+$
Recomm.	1.0	1.0	-	-	-	-	-	-

card4	1	2	3	4	5	6	7	8
Variable	FLDTY	PEX	WORKH	TES	XMU	STFSF	DTCTRL	SCREEN
Unit	$\frac{mm^2}{N \cdot ms}$	-	-	-	-	-	-	-
Range	$\mathbb{R}^+$	$\mathbb{R}^+$	$\mathbb{R}^+$	$\in \{0,1,2\}$	$\mathbb{R} \geq 1$	$\mathbb{R}^+$	$\mathbb{R}^+$	$\in \{0,1,2,3\}$
Recomm.	-	-	0.0	2.0	1.0	0.0	1.0	1.0

card5	1	2	3	4	5	6	7	8
Variable	MESSAG	HSP						
Unit	-	-						
Range	$\in \{0,1,2,3\}$	$\in \{0,1,2,3\}$						
Recomm.	2.0	3.0						

Table C.1: LS-Dyna material deck for custom perzyna cohesive zone model

VARIABLE	DESCRIPTION
MID	Material identification. A unique number or label not exceeding 8 characters.
RO	Mass density.
MT	User defined material model number, must be set to 45.0
LMC	number of material variables in card 3, 4 and 5, must be set to 18.0
NHV	Number of history variables used, 14 are in use, 3 are added for undocumented LS-DYNA peculiarities
IVECT	Flag for a vectorized material model, model is scalar so 0.0
IFAIL	Flag if element failure is possible at all, this overrides NFAIL, (default=1.0)
ROSTO	Flag for density option. = 0.0: Density per unit volume. = 1.0: Density per unit area.
NFAIL	Number of failed gauss points before element failure (1.0 = default) (0.0 means no failure)
GIC	Cohesive energy in mode I, Γ_n.
GIIC	Cohesive energy in mode II/III, Γ_t.
T	Maximum traction in mode I.
S	Maximum traction in mode II/III.
KLOAD	Initial stiffness of cohesive zone, recommended is $\frac{E}{t_{\mathrm{cz}}}$.
KULOAD	Negative stiffness of damaging static cohesive zone, determines length of damage opening path.
FLDTY	Perzyna fluidity parameter, but reciprocally defined, so enter 1/FLDTY
PEX	Perzyna model exponent
WORKH	Work hardening parameter

VARIABLE	DESCRIPTION
TES	Type of mixed mode law used, see section 5.5.3 = 0.0: Power law formulation. = 1.0: Benzeggagh Kenane law. = 2.0: Dimensionless effective parameter approach.
XMU	Exponent in the power failure criterion, for TES=1.0 and 0.0 only
STFSF	penetration stiffness multiplier for forces in normal compression. Internally, 1 is added. (0 = default)
DTCTRL	Factor on maximum timestep, ignored if resulting timestep is greater then allowed by Courant limit of another element(type). Parameter influences reported maximum stiffness.
SCREEN	Print to screen at gauss point failure. = 0.0: Warnings only. = 1.0: Summary. = 2.0: Detailed. = 3.0: Nothing.
MESSAG	Append to "MESSAG" file at gauss point failure. = 0.0: Warnings only. = 1.0: Summary. = 2.0: Detailed. = 3.0: Nothing.
HSP	Append to "HSP" file at gauss point failure. = 0.0: Warnings only. = 1.0: Summary. = 2.0: Detailed. = 3.0: Nothing.

Table C.2: LS-Dyna material card names for custom Perzyna cohesive zone

Appendix D

Plane strain, Plane stress

Two distinct assumptions of stress or strain distribution in the thickness direction of a plate exist. These states are computationally exclusive and physically effect the observed ductility of the material. In traditional fracture mechanics the assumed state influenced the choice of computational model and in present day FEM modulation the choice of (shell) element used. When a material is loaded in tension and the region near the crack tip starts to deform plastically, because of equal-volume considerations, a contracting force perpendicular to the load force is exerted. No force normal to a free surface may exist, therefore, near free surfaces, the opposing force to the contracting force can not be generated and the material will have to deform laterally as a consequence. The lack of restraint also induces a biaxial stress state in these zones that differs from the more or fully triaxial stress state near the centre of the material. This phenomena is demonstrated by the existence of shear lips in post mortem crack plane observations. Because of the biaxiality, the material is locally more ductile and demonstrates a larger yield strain. This results 45° "hills" called shear lips running along the sides of the crack plane. The two states are discussed below in more detail.

Plain stress

> " A condition of a body in which the state of stress is such that two of the principal stresses are always parallel to a given plane and are constant in the normal direction. "

This state is found in relatively thin plates and due to the lack of lateral support as described above, the material will contract resulting in a smaller effective cross-section subjected to the stresses exerted on it. Also, when the edge disturbance is large compared to the full thickness of the plate, the area of biaxiality is large compared to the tri-axially loaded centre that may not even fully develop. As material loaded triaxially fractures more brittle, a thin plate fractures more ductile then a thick plate with the same material properties.

Plane strain

> " A condition of a body in which the displacements of all points in the body are parallel to a given plane, and the values of theses displacements do not depend on the distance perpendicular to the plane. "

The cross-section of the body under loading will change relatively little. Also the biaxially loaded zones as a consequence of the vicinity to the free edge will be relatively small. The triaxial stress state is able to fully develop and this results in a more brittle fracture.

Appendix E

Classical fracture mechanics

The field of fracture mechanics is concerned with the behaviour of cracked bodies under loading. It delivers quantitative answers to questions relating to structures with fractures or initial flaws. These questions often arise in an effort to predict the safe (remaining) life of a structure subjected to (cyclic) loading or its necessary inspection regime. Examples of this are offshore platforms subjected to wave loads and air planes undergoing pressurisation/depressurisation cycles of the pressure hull.

The classical approach primarily aims to describe the growth of non dynamic fatigue fracture and calculating the the stress level at which a certain (flawded) geometry may start to exhibit continued dynamic fracture. In the early days of fracture mechanical research, the process was thought of as progressing at the very tip of the fracture and later on also in the area surrounding it. The material was thought to behave linear elastically throughout.

Energy cannot be formed or lost, just transformed from one type to another. This fact is expressed in the the first law of thermodynamics.

> The increase in the internal energy of a system is equal to the amount of energy added by heating the system, minus the amount lost as a result of the work done by the system on its surroundings.

This means, that if we choose support conditions for a fracturing body in such a manner that the surroundings are not performing any work, all energy gained by fracturing like the loss of potential energy in a body under tension, should be transformed into another type of energy, for example the kinetic energy of the material moving away from the crack. An energy balance can therefore be used to predict at what stress level fracturing delivers more energy than needed to form a fracture. At this level of stress, the material is susceptible to fracture. This concept is used in *linear elastic fracture mechanics* or *LEFM* and comes in two flavours that are in all respects two different expressions of the same thing. These 'two' methods omit plasticity, but are easy to understand and visualize and remain in use. They are discussed briefly below for just these reasons.

E.1 The energy balance approach

An infinitely large plate of unit thickness is subjected to an uniform tensile stress in one in-plane direction. Now a fracture with length $2a$ is introduced perpendicular to said stress. This situation is depicted in figure E.1. It is clear that the introduction of the fracture influences the stress

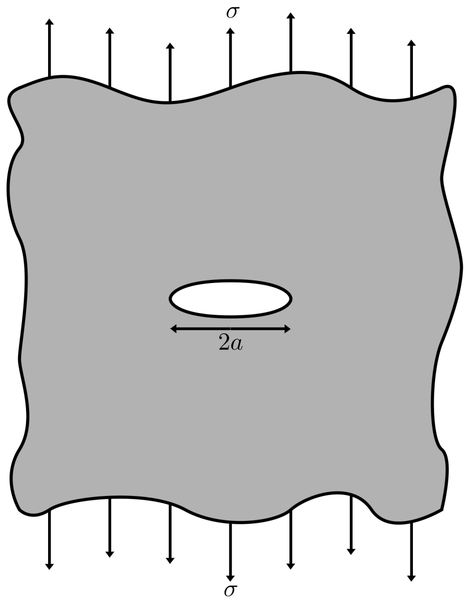

Figure E.1: Fracture in an infinite plate

distribution, and as no forces can exist on a free boundary, none can be present at the fracture flanks. This local relaxation of the material constitutes a drop in potential energy per unit thickness which can be calculated by equation E.1

$$\Delta energy = 1/2\varepsilon \cdot \sigma \tag{E.1}$$

Assuming the area of relaxation to be a circle with radius a and linear elasticity, equation E.1 becomes

$$\Delta \text{energy} = 1/2 \cdot \varepsilon \cdot \frac{\varepsilon}{E} \cdot \pi a^2 = 1/2 \frac{\pi \sigma^2 a^2}{E} \tag{E.2}$$

In actuality this is an oversimplification and the drop in potential energy U_a is actually equal to

$$U_a = \frac{\pi \sigma^2 a^2}{E} \tag{E.3}$$

As an infinite plate has no surroundings to exert forces on it or perform work, this drop in potential energy can be used fully as an increase in energy of another kind. If we consider a material without plasticity, this energy would be in the form of a surface energy. If we define the surface energy per unit area as γ_e, the total increase in surface energy U_γ must be lower then the drop in potential energy to allow a fracture to grow.

$$U_\gamma = 4a\gamma_e \tag{E.4}$$

This relationship combined with equation E.3 becomes

$$4a\gamma_e < \frac{\pi \sigma^2 a^2}{E} \tag{E.5}$$

Figure E.2 shows an example contour plot of this relationship. A value of 1 or higher indicates enough energy being available for propagation of a fracture. $\frac{U_\gamma}{U_e} > 1$ therefore defines the region of combinations of stress intensity and fracture length for which further crack growth is possible

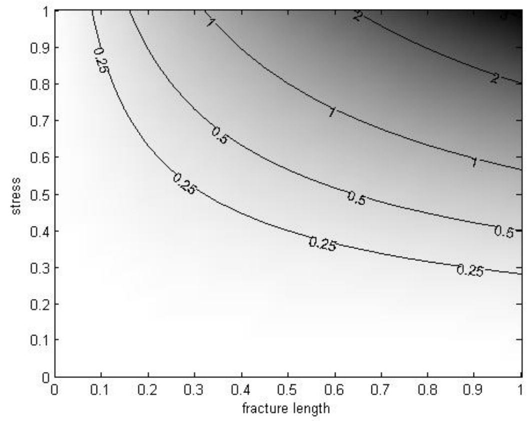

Figure E.2: Fracture stability as a function of initial fracture and stress stae

The theory was extended by Irwin to include plasticity to cover not only brittle, but also ductile materials. He defined the derivative to the crack length 2a of the right hand side of equation E.5 to be equal to the *energy release rate* G and the derivative of the left hand side of the same equation to be the *crack resistance* R.

$$G = \frac{d}{d(2a)}\left(\frac{\pi\sigma^2 a^2}{E}\right) = \frac{\pi\sigma^2 a}{E} \tag{E.6}$$

$$R = \frac{d}{d(2a)}(4a\gamma_e) = 2a\gamma_e \tag{E.7}$$

He then added plasticity by including the strain work done per unit of fracture surface area to the definition of R, equation E.7, to arrive at

$$R = 2(\gamma_e + \gamma_p) \tag{E.8}$$

E.1.1 The stress intensity approach

The energy balance approach assumes an ideally sharp crack which deviates from reality in most instances and it is unable to capture situations with low fracture speeds such as fatigue fracture. Irwin suggested an alternative approach to LEFM and developed the stress intensity approach. In it, the *stress intensity factor* K takes a central role. This factor describes the stresses in the vicinity of the crack tip in relation to the stress in the surrounding material. It was established from dimensional analysis that it must be a function of the form:

$$K = \sigma\sqrt{\pi a} \cdot f() \tag{E.9}$$

Where $f()$ is a function of the geometry of both the entire object considered as well as the fracture. This function f() has been established for many types of geometry and specimen size. For a fracture in an infinite plate,$f() = 1$ and equation E.9 becomes $K = \sigma\sqrt{\pi a}$. This bares a striking resemblance to the equation for the energy release rate G given in equation E.7, for the same infinitely large plate. If the two are combined, a relationship between the two appears in the form of:

$$\sqrt{GE} = K \tag{E.10}$$

As the energy release rate G needed for stable crack growth should at least be equal to the crack resistance R, it follows from equation E.10, that the minimal stress intensity needed for fracture

K_c is equal to

$$\sqrt{RE} = K_c \tag{E.11}$$

This combines with the definition of R for a ductile material to form the definition of the critical stress intensity K_c, equation E.7, to form

$$K_c = \sqrt{2E \cdot (\gamma_e + \gamma_p)} \tag{E.12}$$

The value K_c can be experimentally determined for a given material and geometry. Within a certain range of validity, the value derived for K_c, can then be used as a quasi material constant for the fracture toughness.

Equation E.10 allows us to switch between the energy and stress intensity approach to linear elastic fracture mechanics. In practice the stress intensity approach is most commonly used, but it can always be transformed to an energy based form if this is more practical for a certain application.

E.2 Elastic plastic fracture mechanics

In cases where plasticity plays an important role, the performance of linear elastic models as discussed in section E.1 and E.1.1 becomes poor. Even including a plastic term in the energy dissipation function is not sufficient to model large scale plasticity or a a plastic zone ahead of the crack tip that is large compared to the thickness of a plate.

To model these kind of situations, *elastic plastic fracture mechanics* has to be used. Besides the difference in accounting for plasticity, it differs from LEFM in the sense that *EPFM* uses a local description of failure as opposed to the single parameter energy based concepts of LEFM (K,G and R).

Two approaches to EPFM have gained widespread use, one in Anglo-Saxon lands, the *Cracktip opening displacement method* and the US *J-integral* approach by Rice. EPFM is of interest in the scope of this paper as it is able to provide a measure of energy released during fracture in a local sense.

A full mathematical derivation of the J integral is beyond the scope of this chapter[1], but its main properties are discussed. The J-integral model is build around the conservation of energy. The amount of potential energy available for fracture formation U_{P} in a region of a stressed plate in encompassing the full plastic zone is expressible as

$$U_{\mathrm{P}} = U_0 + U_{\mathrm{a}} - U_{\mathrm{ext}} \tag{E.13}$$

where U_0 is the initial energy before the fracture was present in the area, U_{a} represents the change in elastic energy since fracture introduction and U_{ext} is the work performed by the surroundings. The J integral describes the energy dissipated by the fracture process or:

$$J = -\frac{dU_{\mathrm{P}}}{da} = \frac{d}{da}\left(U_{\mathrm{ext}} - U_{\mathrm{a}}\right) \tag{E.14}$$

[1] The interested reader is referred to [79].

Appendix F

Fracture toughness conversion

As was discussed in section 2.2.2, it is often problematic to obtain values for the cohesive energy. Because a correct maximum traction is also necessary for a proper simulation, an inverse modelling approach is to be recommended. In situations where the necessary information is unavailable and an estimation of the cohesive energy needs to be made, the techniques as explained in this appendix may be used.

F.1 Conversion between K and G

A direct relationship exists between the fracture toughness K_{I} and critical energy release rate G [79],

$$G = \begin{cases} \frac{K_{\mathrm{I}}^2}{E}, & \text{for plane stress} \\ \frac{K_{\mathrm{I}}^2}{E}\left(1-\nu^2\right), & \text{for plane strain} \end{cases} \tag{F.1}$$

The validity of equation F.1 is restricted to LEFM conditions. The critical energy release rate in mode I fracture G_{1c} is equal to the elastic portion of the J integral J_{el}, or:

$$J_{el} = G_{1c} \tag{F.2}$$

Ignoring the contribution of the plastic energy dissipation J_{pl} yields a crude underestimation of the true cohesive energy.

$$\Gamma \approx J_{el} \tag{F.3}$$

F.2 Charpy V conversion

One of the most well known and most abundant measures of fracture toughness available is the Charpy V-notch value or curve. It is derived from the Charpy v-notch test, in which an impactor is swung from a pendulum through a notched test peace. The difference in release and maximum height after half a period signifies an amount of energy dissipated by the test peace fracture process. Geometry end test setup is closely regulated in ASTM norm E23 [83]. An example of the setup is given in figure F.1

A Charpy test results in a qualitative description of the materials fracture toughness. Formulas exist [84, 85, 86] to convert the derived values to units used in fracture toughness calculations, but these are somewhat empirical in nature. The main strength of the test lies in its simplicity of preparation and execution and because of this, it is relatively inexpensive to perform. As a result of this and the fact that it is included in many norms, Charpy values are available for most materials, where dedicated fracture toughness data is lacking.

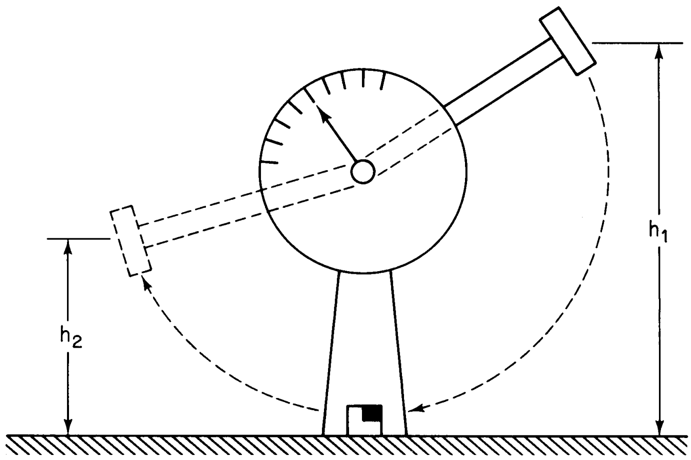

Figure F.1: Charpy V-notch test rig

Most often Charpy tests are performed to establish the materials response to low temperatures with regard to its ductility. Steel, like many materials has three distinct zones in its response to low temperatures, namely the lower, and the upper shelf and a transition zone. These zones can be observed in figure F.2. From this it is clear that there exists a certain temperature (range), below which a material behaves brittle. Charpy tests values are therefore always a function of temperature for materials that have a ductile to brittle transition like steels.

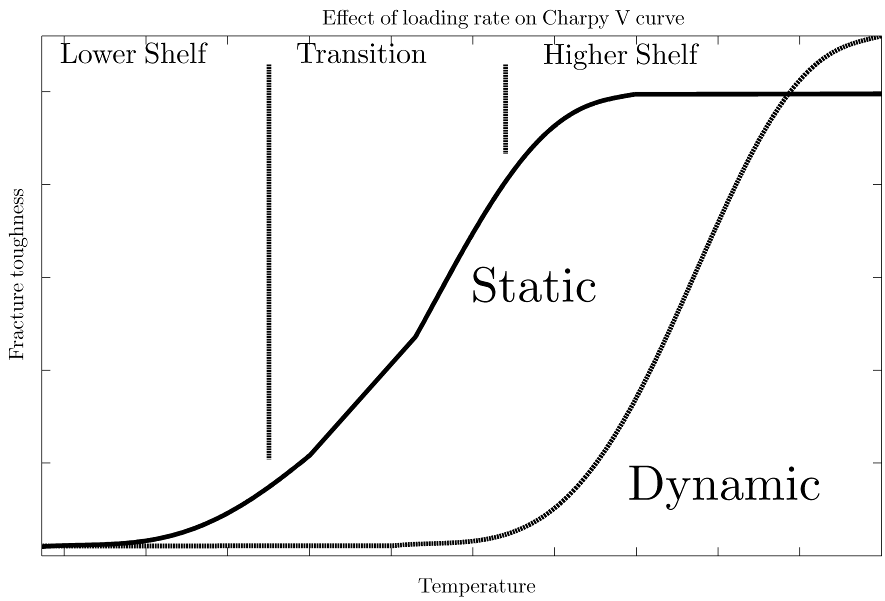

Figure F.2: Effect of loading rate on a CVN curve

Figure F.2 also indicates that increased loading rates shift the Charpy V-notch or *CVN* curve towards the higher temperatures. This may be counter intuitive, as this report deals with increased fracture toughness at higher strain rates. This perceived contradiction disappears at higher temperatures well above the transition zone, here the fracture toughness increases at increased loading rates [86]

It was indicated that there are empirical formulae to convert Charpy V data to fracture toughness values in usable units for fracture calculations. The best known of these is the two-stage correlation procedure by Barsom and Rolfe [86]. This procedure will be explained below as well as a lower bound approach by Roberts and Newton [85].

The Barsom and Rolfe correlation procedure splits the CVN curve in two parts according to the maximum CVN criterion given in equation F.4

$$\mathrm{CVN} \leq 0.3687 \cdot \sigma_y \tag{F.4}$$

The part of the CVN curve satisfying F.4 is deemed either the lower shelf or the lower part of the transition regime. K_{1c} values are obtained in this part of the curve by

$$\mathrm{K}_{1c} = \sqrt{0.64\, E \cdot \mathrm{CVN}} \tag{F.5}$$

But the temperature coordinates of these points need to be shifted towards absolute zero according to

$$\Delta T = 119 - \sigma_y \cdot 0.12 \tag{F.6}$$

The upper shelf CVN values, are treated differently. The exact boundaries of the upper shelf region are unclear and it is not clear if any point not satisfying equation F.4 is to be treated as "upper shelf". This is implicitly done in [87] however and this approach will be followed in this report.

"Upper shelf" CVN curve values are converted using

$$\mathrm{K}_{1c} = 0.804\sigma_y \sqrt{\frac{\mathrm{CVN}}{\sigma_y} - 0.0098} \tag{F.7}$$

Equations F.5 and F.7 define a complete conversion rule set for CVN curves if the assumption with regards to the start of the upper shelf region is valid. There is however no alternative if it does not.

A lower bound solution, valid for all the CVN regions was formulated by Roberts and Newton [85] in the form of equation F.8

$$\mathrm{K}_{1c} = 8.47\,(\mathrm{CVN})^{0.63} \tag{F.8}$$

The critical fracture intensity for mode I K_{1c} may then be used to derive an estimate of the cohesive energy using equations F.1 and F.2.

F.3 CTOD converion

A fracture toughness description popular mainly in the united kingdom is the Crack Tip Opening Displacement or, *CTOD*. An initially sharp fracture tip deforms plastically, or *blunts* under the influence of plastic deformation. As fracture is controlled by the stresses near the tip of the fracture and these stresses always exceed the elastic limit. The amount of blunting is an indication of the stress field in the vicinity of the tip. Fracture can only occur if a certain critical stress level has been reached. This implies that there exists a critical amount of blunting, below which fracture can not occur. This critical crack tip opening displacement δ_t is the CTOD and is deemed a material property.

Under both LEFM as EPFM conditions, various sources have proposed relations between the CTOD δ_t and the critical integral J. They all take the form [79]

$$\Gamma \approx J = \delta_t \sigma_y \cdot \mathrm{M} \tag{F.9}$$

Where M is a constant varying between 1.15 and 2.95. δ_t is measured as the distance between the two flanks of a fracture, at a distance from the actual fracture tip so that 45° lines originating from the measuring point intersect at the fracture tip.

Finite element simulations by Wellman [88] have improved on equation F.9. He defined a flow stress σ_{flow} according to

$$\sigma_{\text{flow}} = \frac{\sigma_y + \sigma_{\text{ult}}}{2} \tag{F.10}$$

Furthermore he discovered that the value for M lies between 1.2 for plane stress and 1.6 for plane strain. He suggests a value of 1.4 for any circumstance where the state of the stress is not exactly known. The fracture toughness can now be calculated as.

$$\Gamma \approx J = \delta_t \sigma_{\text{flow}} \cdot \mathrm{M} \tag{F.11}$$

Appendix G

Material properties

The research performed in the research was focussed on two different materials; aluminium 2024 T3 "bare" and duplex steel DIN 1.4462. These materials and their detailed properties are discussed in this chapter.

G.1 Aluminium 2024 T3

Aluminium 2024 temper condition T3 is an alloy known for its damage tolerance [78] combined with a high yield strength. This made it a common aviation alloy used in commercial aircraft for over 50 years [76]. The material is used in many different parts of aircrafts, such as the fuselage and the wings as can be seen in figure G.1 for a Fokker 100.

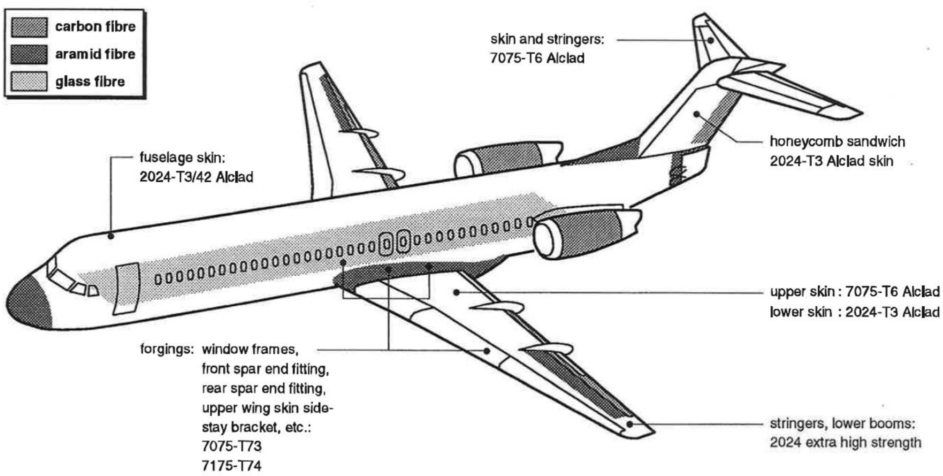

Figure G.1: Aluminium alloy usage in a Fokker 100 aircraft

The chemical composition ranges are given in table G.1. The mechanical properties are listed in table G.2 and were taken from [89, 55, 90]. Isotropic values are used as there is no bulk material available to model the anisotropicy of the material as well as its rate dependence in LS-DYNA. The anisotropicy is caused by rolling of the material into sheets; different properties are found along and across the rolling direction.

The temper of the aluminium, T3, entails a solution heat treatment, followed by cold working and an (natural) ageing process. As the solubility of different alloying materials increases with

	Al	Cr	Cu	Fe	Mg	Mn	Si	Ti	Zn
Min	90.7	-	3.8	-	1.2	0.3	-	-	-
Max	94.7	0.1	4.9	0.5	1.8	0.9	0.5	0.15	0 .25

Table G.1: Chemical composition of aluminium 2024 T3

$\sigma_{\mathrm{y}}\left(\frac{\mathrm{N}}{\mathrm{mm}^2}\right)$	$\sigma_{\mathrm{ult}}\left(\frac{\mathrm{N}}{\mathrm{mm}^2}\right)$	$E\left(\frac{\mathrm{kN}}{\mathrm{mm}^2}\right)$	$\rho\left(\frac{\mathrm{kN}}{\mathrm{m}^3}\right)$	$\varepsilon_{\mathrm{ult}}(\%)$
369	475	78	2.8	18

Table G.2: Mechanical properties of aluminium 2024 T3 bare

temperature, a stable homogeneous alloy can be produced at a high temperature, that becomes over saturated at room temperature. The alloying agents cannot fit into the metal roster and form precipitates that obstruct deformation in the metal grid. This leads to drastically increased strength. The suffix “bare” indicates that no cladding is present. In an effort to increase the chemical resistance or to provide a more suitable base for surface treatments, a layer of pure aluminium may be deposited on the outer surfaces. This material condition is then known as “alclad”

G.2 Duplex steel 1.4462

Duplex stainless steels were developed in an effort to combine high corrosion resistance with good mechanical properties. They are a breed of steels popular in petrochemical industries, transportation and in general engineering. The combination of good corrosive as well as mechanical properties is reached trough their “Duplex” microsture; approximately equivalent volume fractions of Ferrite and Austenite exist in the material. This two phase micro structure also delivers a higher resistance to pitting and stress corrosion compared to conventional stainless steels.

Duplex steels are characterized by a high chrome and molybdenum content, increasing the materials resistance to intergranular and pitting corrosion respectively. The addition of a nitrogen fraction raises the ultimate stress without effecting the fracture toughness. Within the Duplex family of steels, sub-groups exist with higher and lower contents of chrome and molybdenum, but the most popular duplex steel, accounting for over 80% of its ussage is the material discust in this section: DIN 1.4462. This steel combines the before mentioned benefits with satisfactory weldability, frabricational properties and economics

As it is such a popular alloy, it is produced by many produces and has a large amount of different names. The exact composition also varies from source to source. Table G.3 lists the most frequently used names for the duplex steel at hand, and table G.4 shows the chemical composition ranges as encountered in [56, 91, 92, 93, 94].

Standard	Name
DIN, EN	1.4462
ASTM	S31803
	S2205
NF	Z3 CND 22-05 Az
Böhler	A903 extra
SS	2377
	2205
AISI	F51

Table G.3: Different names of 1.4462

	C	Si	Mn	P	S	Cr	Ni	Mo	N	Fe
Min	0.017	0.33	1.12	0.021	0.001	21	4.5	2.5	0.1	66
Max	0.03	0.6	1.48	0.028	0.01	23	6.5	6.6	0 .2	69

Table G.4: Chemical composition of DIN 1.4462

As can be expected from the substantial differences in composition; a wide range of values for the material properties also exist. Properties were taken from [56, 91, 92, 93, 94] and the characteristic strength properties are plotted in figure (G.2). A large variation can be observed, especially with respect to the ultimate tensile strength. This poses difficulties as the formulas to calculate the fracture toughness from the Charpy V-notch test data are sensitive to these parameters. Also the reported Charpy V-notch toughness itself has a large spread. The minimum values for the yield and ultimate strength as guaranteed by some producers [92, 93] are used in this research. The Young's modulus also shows some variability amongst sources, a mean value of 210 $\frac{kN}{mm^2}$ is taken. Table G.5 lists the mechanical properties as used.

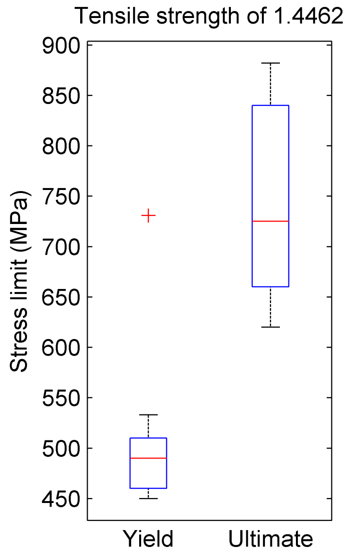

Figure G.2: Boxplot of stress resistance

$\sigma_y\left(\frac{N}{mm^2}\right)$	$\sigma_{ult}\left(\frac{N}{mm^2}\right)$	$E\left(\frac{kN}{mm^2}\right)$	$\rho\left(\frac{kN}{m^3}\right)$	$\varepsilon_{ult}(\%)$
460	640	210	7.8	24

Table G.5: Mechanical properties of DIN 1.4462

Appendix H

Bulk material

The material surrounding the cohesive zones in a finite element mesh is known as *bulk* material. Different material models exist that may be used to describe the material. The material models used during the course of this research are discussed in this chapter and the material parameters are given for aluminium 2024 T3 and duplex steel DIN 1.4461 were available.

H.1 Elastic

MAT_ELASTIC is the simplest material model available in LS-DYNA. It models an isotropic elastic material, without the option of a criterion for failure in solids. The material model's response to a deformation is governed by

$$\sigma = E\varepsilon \tag{H.1}$$

It should be self evident from equation (H.1), that no plastic region exists. It is used as a reference bulk material. Because this material can not dissipate any energy, it is useful for studying the bulk material's influence on fracture. Tables H.1 and H.2, list the properties as used.

card1	1	2	3	4	5	6	7	8
Variable	MID	RO	E	PR				
Unit	-	$\frac{\mathrm{N}}{\mathrm{mm}^3}$	$\frac{\mathrm{N}}{\mathrm{mm}^2}$	-				
Value	-	2.8E-3	7.8E+4	0.33				

Table H.1: LS-DYNA elastic material deck for aluminium 2024 T3

card1	1	2	3	4	5	6	7	8
Variable	MID	RO	E	PR				
Unit	-	$\frac{\mathrm{N}}{\mathrm{mm}^3}$	$\frac{\mathrm{N}}{\mathrm{mm}^2}$	-				
Value	-	7.85E-3	210E+3	0.3				

Table H.2: LS-DYNA elastic material deck for stainless duplex steel DIN 1.4462

VARIABLE	**DESCRIPTION**
MID	Material identification. A unique number or label not exceeding 8 characters.
RO	Mass density.
E	Youngs modulus.
PR	Poissons ratio.

Table H.3: LS-DYNA material card names for *MAT_ELASTIC*

H.2 Johnson Cook

H.2.1 Model description

The Johnson Cook material model as outlined in [95], allows us to describe a materials flow surface as a function of the strain, strain rate and temperature. It is mainly used in situations where strain rates vary over a large range, as is the case in the simulations discussed in this report.

In the JC model, stresses reaching the flow surface do not directly lead to failure. Rather a separate failure model is included to describe failure. As the JC model is used as a bulk material and failure is constricted to the cohesive zones for the purpose of this report, we do not need to include this second part of the model. The JC flow function is defined as in equation (H.2)

$$\sigma_{\mathrm{y}} = \Big(A + B\left(\hat{\varepsilon}_p\right)^n\Big)\Big(1 + C\ln\left(\dot{\varepsilon}^*\right)\Big)\Big(1 + \left(T^*\right)^m\Big) \tag{H.2}$$

With material constants A, B, C, n, m. The non dimensional temperature T is defined as

$$T^* = \frac{T - T_{\mathrm{room}}}{T_{\mathrm{melt}} - T_{\mathrm{room}}} \tag{H.3}$$

Where T, T_{room} and T_{melt} are the current, ambient and melting temperatures respectively. Due to the the assumption of adiabatic conditions, all energy dissipated is transformed into heat, and equation (H.4) must hold.

$$\Delta T = \frac{\sigma_{\mathrm{vm}}\hat{\varepsilon}_{\mathrm{p}}}{\rho C_{\mathrm{v}}} \tag{H.4}$$

With σ_{vm} being the equivalent von Mises stress from equation (5.32). Written in primary stresses, (5.32) becomes

$$\sigma_{\mathrm{vm}} = \sqrt{3J_2} = \sqrt{\frac{\left(\sigma_1 - \sigma_2\right)^2 + \left(\sigma_2 - \sigma_3\right)^2 + \left(\sigma_3 - \sigma_1\right)^2}{2}} \tag{H.5}$$

Furthermore, ρ in (H.4) is the material density, C_{v} the specific heat and $\hat{\varepsilon}_{\mathrm{p}}$ the effective plastic strain as defined in (H.6).

$$\hat{\varepsilon}_{\mathrm{p}} = \int_0^t \mathrm{d}\hat{\varepsilon}_{\mathrm{p}} \tag{H.6}$$

The incremental plastic strain $\mathrm{d}\hat{\varepsilon}_{\mathrm{p}}$ is equal to:

$$\mathrm{d}\hat{\varepsilon}_{\mathrm{p}} = \sqrt{\frac{2}{3}\mathrm{d}\varepsilon_{ij}\mathrm{d}\varepsilon_{ij}} \tag{H.7}$$

The nondimensional strainrate $\dot{\varepsilon}^*$ is equal to the strain rate divided by a reference strain rate, which is usually equal to 1 s^{-1}

$$\dot{\varepsilon}^* = \frac{\dot{\varepsilon}}{\dot{\varepsilon}_0} \tag{H.8}$$

H.2.2 LS-DYNA implementation

LS-DYNA has three different build in Johnson Cook material models. As a bulk material, *MAT_SIMPLIFIED_JOHNSON_COOK* [59] was used. This material model excludes the effect of thermal softening and uses a simple, maximum strain based, failure model. Because failure is not considered for bulk materials, and the exclusion of thermal softening is reasonable as the necessary adiabatic conditions may not exist in a thin walled pressure vessel with a rapidly decreasing pressure, the reduced model is the obvious choice.

For aluminium 2024 T3, the Johnson Cook parameters have been determined for a strain rate validity range of $\dot{\varepsilon} = 10^5$ to $10^{-5}s^{-1}$ in [96]. These serve as the basis of the data in the LS-DYNA cards in table H.4. For the duplex steel no JC parameters are available.

card1	1	2	3	4	5	6	7	8
Variable	MID	RO	E	PR	VP			
Unit	-	$\frac{N}{mm^3}$	$\frac{N}{mm^2}$	-	-			
Value	-	2.8E-3	7.8E+4	0.33	1.0			

card2	1	2	3	4	5	6	7	8
Variable	A	B	N	C	PSFAIL	SIGMAX	SIGSAT	EPSO
Unit	$\frac{N}{mm^2}$	$\frac{N}{mm^2}$	-	-	PSFAIL	$\frac{N}{mm^2}$	SIGSAT	EPSO
Value	369	684	0.73	8.3E-3	0.0	0.0	-	1.0

Table H.4: LS-DYNA Simplified Johnson Cook material deck for aluminium 2024 T3

VARIABLE	DESCRIPTION
MID	Material identification. A unique number or label not exceeding 8 characters.
RO	Mass density.
E	Youngs modulus.
PR	Poissons ratio.
VP	Formulation for rate effects: EQ.0.0: Scale yield stress (default), EQ.1.0: Viscoplastic formulation (perzyna type).
A	Johnson Cook model parameter A, see equation H.2
B	Johnson Cook model parameter B, see equation H.2
N	Johnson Cook model parameter N, see equation H.2
C	Johnson Cook model parameter C, see equation H.2
PSFAIL	Effective plastic strain at failure. If zero failure is not considered.
SIGMAX	Maximum stress obtainable from work hardening before rate effects are added (optional). This option is ignored if VP=1.0.
SIGSAT	Saturation stress which limits the maximum value of effective stress which can develop after rate effects are added (optional).
EPSO	Strain rate normalization factor.

Table H.5: LS-DYNA material card names for *MAT_SIMPLIFIED_JOHNSON_COOK*

H.3 Cowper Symonds

The Cowper Symonds model serves as a way to model strain rate dependence of a material through an equation acting on the yield stress limit of a material. It is expressible as:

$$\frac{\sigma_{\mathrm{y,dyn}}}{\sigma_{\mathrm{y}}} = 1 + \sqrt[\mathrm{p}]{\frac{\dot{\varepsilon}}{C}} \tag{H.9}$$

Equation (H.9) can be added to an elasto-plastic material formulation with isotropic hardening to form what is known as *MAT_PLASTC_KINEMATIC* in LS-DYNA. It is governed by equation (H.10).

$$\sigma_y = \left[1 + \frac{\dot{\varepsilon}}{C}\right] \left(\sigma_0 + E_p \varepsilon^p_{eff}\right) \tag{H.10}$$

Where p and C are material properties and $\dot{\varepsilon}$ is the strain rate defined as:

$$\dot{\varepsilon} = \sqrt{\dot{\varepsilon}_i j \dot{\varepsilon}_i j} \tag{H.11}$$

The plastic hardening modulus E_p is equal to:

$$E_p = \frac{E_t E}{E - E_t} \tag{H.12}$$

And ε^p_{eff} is the effective plastic strain.

$$\varepsilon^p_{eff} = \int_0^t \sqrt{\frac{2}{3} \dot{\varepsilon}^p_{ij} \dot{\varepsilon}^p_{ij}}\, dt \tag{H.13}$$

No extensive source of plastic-kinematic properties for duplex stainless steel 1.4462 exists. Simulations with plastic-kinematic bulk material are performed for duplex steel 1.4462 in [2]. These properties are given in table H.6. These properties are also used in the simulating of steel plates in this report. No claims are made to their validity.

card1	1	2	3	4	5	6	7	8
Variable	MID	RO	E	PR	SIGY	ETAN	BETA	
Unit	-	$\frac{\mathrm{N}}{\mathrm{mm}^3}$	$\frac{\mathrm{N}}{\mathrm{mm}^2}$	-	-	$\frac{\mathrm{N}}{\mathrm{mm}^2}$	$\frac{\mathrm{N}}{\mathrm{mm}^2}$	-
Value	-	7.8E-3	2.1E+5	0.3	460.0	800	1.0	

The same source also lists plastic kinematic parameters for aluminium 2024 T3. It may be observed that equation (H.10) bears some resemblance to equation (H.2) if we ignore the temperature dependent part. This allows the plastic kinematic parameters to be curve fitted to the Johnson Cook parameters. These were obtained from: [96].

Table H.7 lists the parameters used in the simulation of aluminium 2024 T3 bulk material, where the parenthesis, indicate that the data has been obtained through the curve fitting of the Johnson Cook data from table H.4. Figure H.1 shows the extend of the difference between the existing parameters and the new curve fitted values. The reason for using a curve fitted plastic-kinematic model rather then the actual Johnson Cook model, is the fact that this last model does not output elemental states in LS-DYNA.

card2	1	2	3	4	5	6	7	8
Variable	SRC	SRP	FS	VP				
Unit	-	-	$\frac{N}{mm^2}$	-				
Value	100	5	0.0	1.0				

Table H.6: LS-DYNA plastic kinematic material deck for duplex steel 1.4462

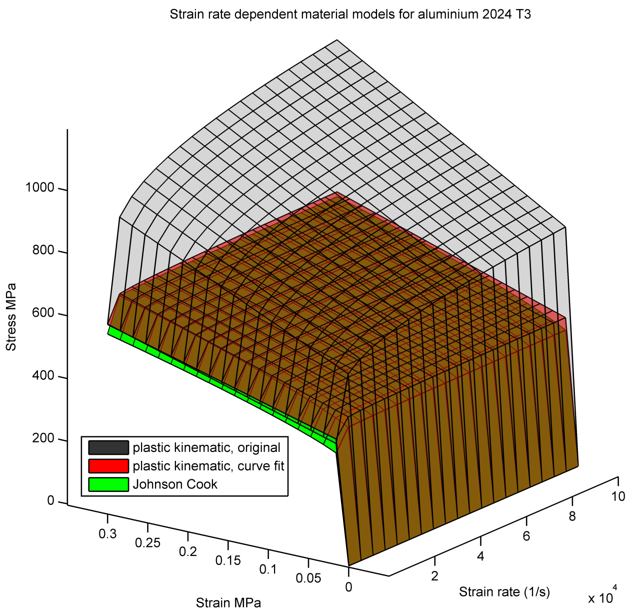

Figure H.1: Difference between the existing and new PK parameters

card1	1	2	3	4	5	6	7	8
Variable	MID	RO	E	PR	SIGY	ETAN	BETA	
Unit	-	$\frac{N}{mm^3}$	$\frac{N}{mm^2}$	-	-	$\frac{N}{mm^2}$	$\frac{N}{mm^2}$	-
Value	-	2.8E-3	7.8E+4	0.33	369.0	767.0 (684.0)	1.0	

card2	1	2	3	4	5	6	7	8
Variable	SRC	SRP	FS	VP				
Unit	-	-	$\frac{N}{mm^2}$	-				
Value	100.0 $(2.5E{+}11)$	5.0 (15.0)	0.0	1.0				

Table H.7: LS-DYNA plastic kinematic material deck for aluminium 2024 T3

VARIABLE	**DESCRIPTION**
MID	Material identification. A unique number or label not exceeding 8 characters.
RO	Mass density.
E	Youngs modulus.
PR	Poissons ratio.
SIGY	Yield stress.
ETAN	Tangent modulus.
BETA	Hardening parameter
SRC	Strain rate parameter, C, for Cowper Symonds strain rate model. If zero, rate effects are not considered.
SRP	Strain rate parameter, P, for Cowper Symonds strain rate model. If zero, rate effects are not considered.
FS	Failure strain for eroding elements.
VP	Formulation for rate effects: EQ.0.0: Scale yield stress (default), EQ.1.0: Viscoplastic formulation (perzyna type).

Table H.8: LS-DYNA material card names for *MAT_PLASTIC_KINEMATIC*

Appendix I

API Grades

The American petroleum institute publishes a norm for line pipe steel. Although the norm uses imperial units and is intended for use in the United States, it is also the common grading system for steel used in pipes worldwide. Papers in the field and industry generally refer to the X-number, such as X60 and X80 to specify a certain steel grade. Table I.1 below lists the yield and ultimate stress in metric units for steels according to the API norm [97] as well as the most important chemical requirements. The number following the X is equal to the yield stress in *pounds per square inch*.

Grade	Maximum chemical content (%)				σ_{y}	σ_{ult}
	C	Mn	S	P	$\left(\frac{N}{mm^2}\right)$	$\left(\frac{N}{mm^2}\right)$
B	0.22	1.20	0.030	0.030	241	414
X42	0.22	1.30	0.030	0.030	290	414
X46	0.22	1.40	0.030	0.030	317	434
X52	0.22	1.40	0.030	0.030	359	455
X56	0.22	1.40	0.030	0.030	386	490
X60	0.22	1.40	0.030	0.030	414	517
X65	0.22	1.45	0.030	0.030	448	531
X70	0.22	1.65	0.030	0.030	483	565
X80	0.22	1.85	0.030	0.030	552	621
X100	-	-	-	-	689	-
X120	-	-	-	-	827	-

Table I.1: API steel grades

Appendix J

LS DYNA

LS-DYNA is a general purpose multi physics finite element solver commercialized by the *Livermore Software Technology Corporation* or *LSTC*. It has its roots in the public domain finite element solver, DYNA3D, which was developed by John O. Hallquist, who worked for the Lawrence Livermore National Laboratory and was released in 1976. The source was declassified in 1978 by the US military and released into the public domain. Work on the public domain code was performed solely by Hallquist up to 1984. In 1989, Hallquist ceased work on DYNA3D development and founded LSTC. LSTC commercialized the code and continued development on it under the name LS-DYNA.

Later versions of LS-DYNA include a, somewhat limited, implicit solver as an option, but the main part of the code is aimed at explicit time integration. The advantage of explicit code over implicit code lies in its ability to describe highly non-linear, transient and dynamic phenomena. The ability to effectively solve non linear problems is necessary when either the material behaves non-linear, for example concrete at high strain rates, or when geometric non-linearities arise such as buckling of sheets. A third type of non-linearity comes from changing boundary conditions, for example as a result of contact. Transient Dynamic problems are characterized by the large influence of inertia. Examples of these are found where loads are large, sudden and short in nature such as explosions car crashes and metal extrusion.

LS-DYNA simulations are completely described by a input text file called an *keyword file*. These may link to other files. It is convenient for larger simulations to have the mesh made made by a preprocessor and have it saved in a separate file with the nodal and elemental definitions. The statements following the stars (*) are known as *keywords* and the information on the lines following them are *cards*. A trivial example of an input file is given in table J.1. A single full integration elastic solid element is defined without loads.

```
$ DEFINE SIMULATION TIME
$
*CONTROL_TERMINATION
$---1----|
$     TIME
&
& SET INITIAL TIMESTEP AND MAXIMUM COURANT NUMBER
&
*CONTROL_TIMESTEP
$---1----|----2----|
$   DTINIT     SSFAC
       0.0       0.9
$ DEFINE EIGHT NODES
$
*NODE
$---1----|----2----|----3----|----4----|----5----|----6----|----7----|----8----|
$      nid         x         y         z
       100        -1        -1        -1
       101         1        -1        -1
       103         1         1        -1
       104        -1         1        -1
       200        -1        -1         1
       201         1        -1         1
       203         1         1         1
       204        -1         1         1
$
$ DEFINE MATERIAL
*MAT_ELASTIC
$---1----|----2----|----3----|----4----|
       MID        RO         E        PR
      3001      1000       210      0.33
$
$ DEFINE SECTION
$
*SECTION_SOLID
$ full integration solid
$---1----|----2----|
$      SID      TYPE
      2001         3
$
$ DEFINE PART
*PART
---1----|----2----|----3----|
$     PID       SID       MID
     1001      2001      3001
$ DEFINE ONE ELEMENT
$
*ELEMENT_SOLID
$---1--|---2---|---3---|---4---|---5---|---6---|---7---|---8---|---9---|--10---|
     EID     PID    NID1    NID2    NID3    NID4    NID5    NID6    NID7    NID8
       1    1001     100     101     102     103     200     201     202     203
```

Table J.1: Example input file for LS-DYNA

Appendix K

Data from tests

The fracture propagation data obtained in the experiments as described in chapter 3 is presented in this appendix in a number of graphs in greater detail. Section K.1 gives the results of the pressurized barrel test, and section K.2 those of the prestressed plate tests.

K.1 Dynamic fracture in pressurized barrels

Two pressurized aluminium barrels were notched with the use of explosives and the the progression of the resulting mode I fracture was determined from high speed footage. The test itself was discussed in section 3.2. In this section the data obtained is given. Figure K.1 and K.2 show the fracture velocity as a function of fracture increase beyond the initial fracture length, and time respectively. In figure K.3 the fracture length is presented as a function of time.

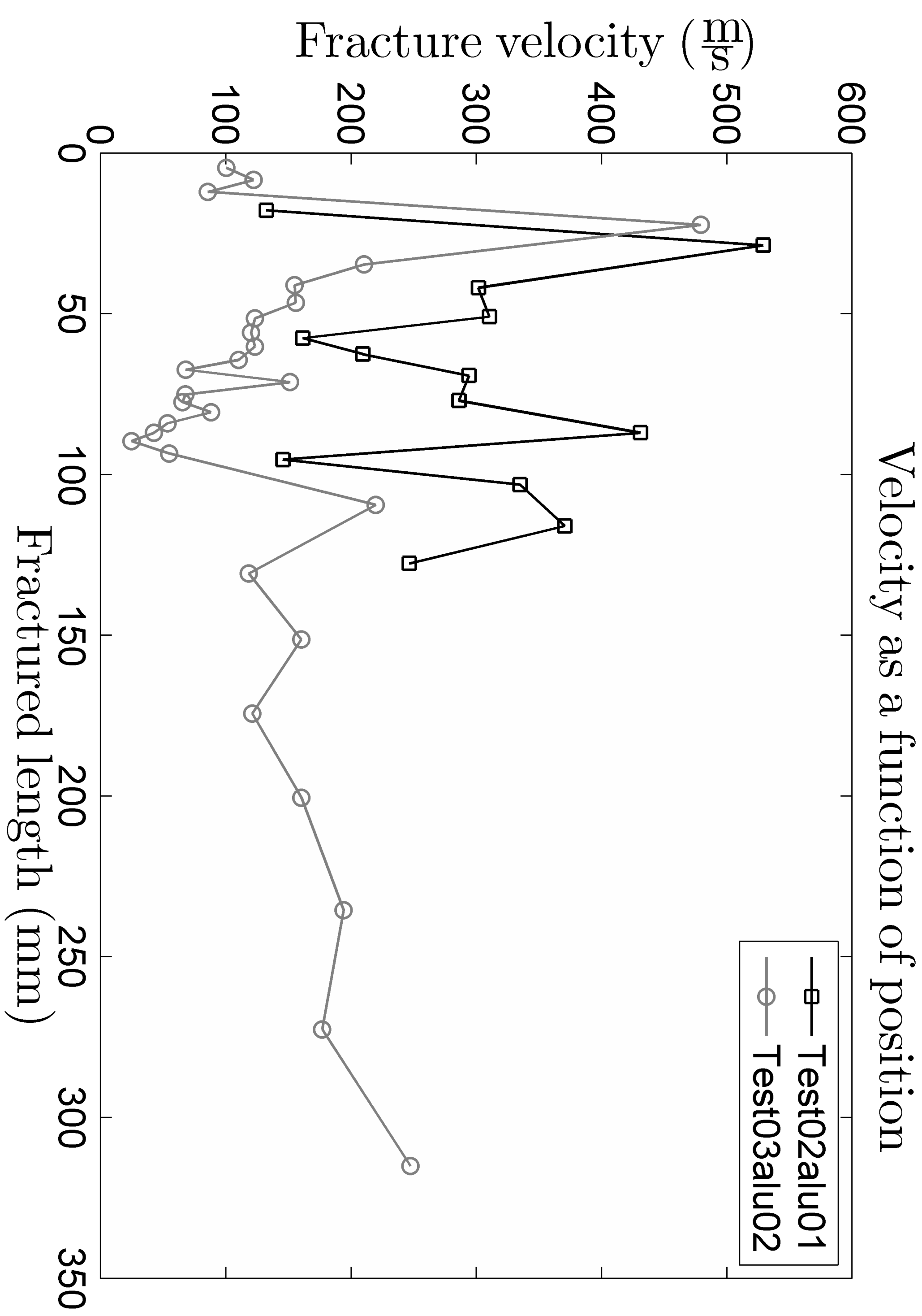

Figure K.1: Fracture velocity as a function of fracture length

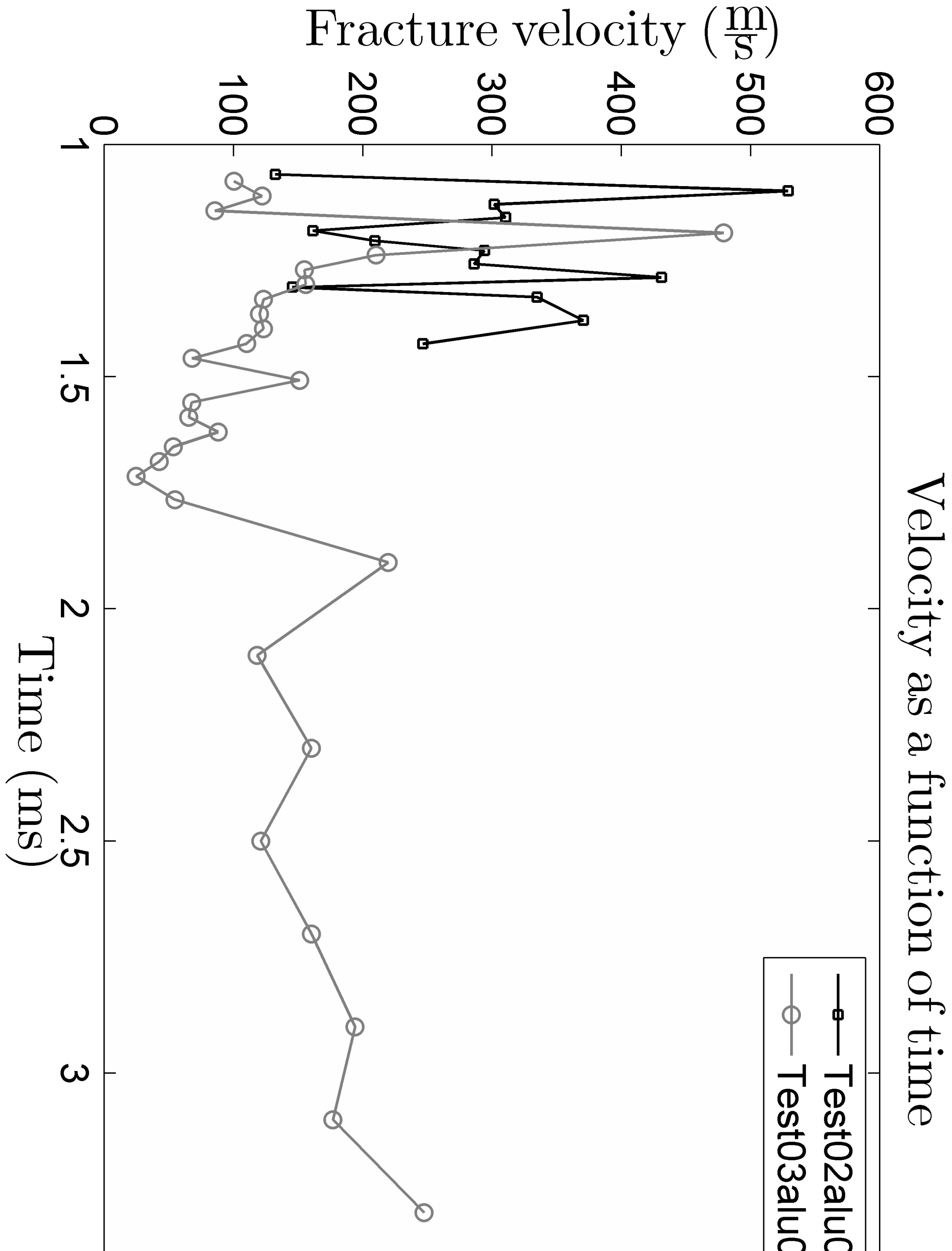

Figure K.2: Fracture velocity as a function of time

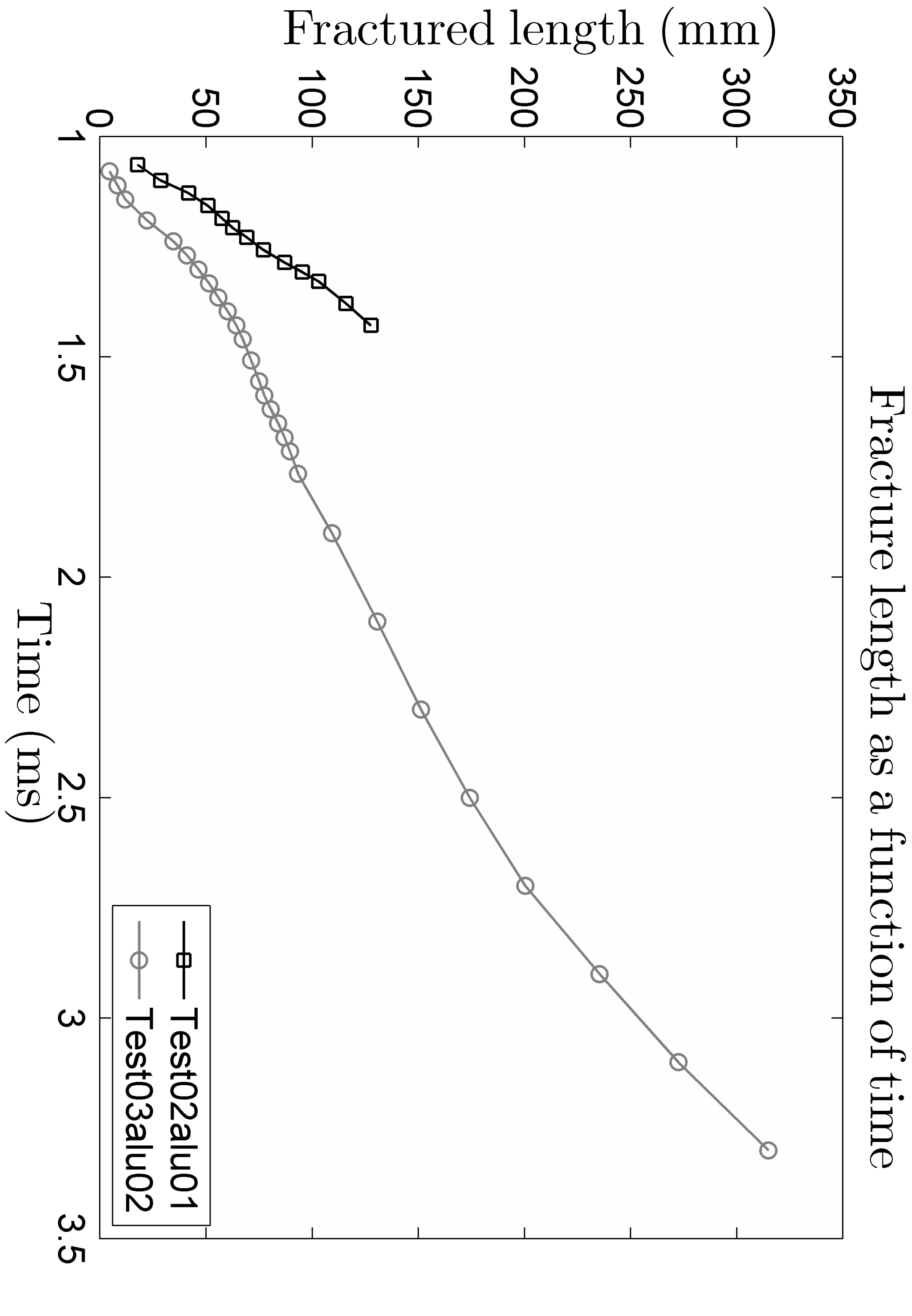

Figure K.3: Fracture length as a function of time

K.2 Dynamic fracture of prestressed plates

Explosively notched, prestressed plate tests were performed as was discussed in section 3.1. The resulting fracture rate is plotted against the added fracture length and this is presented in figure K.4 for the aluminium tests, and in figure K.5 for the duplex steel test.

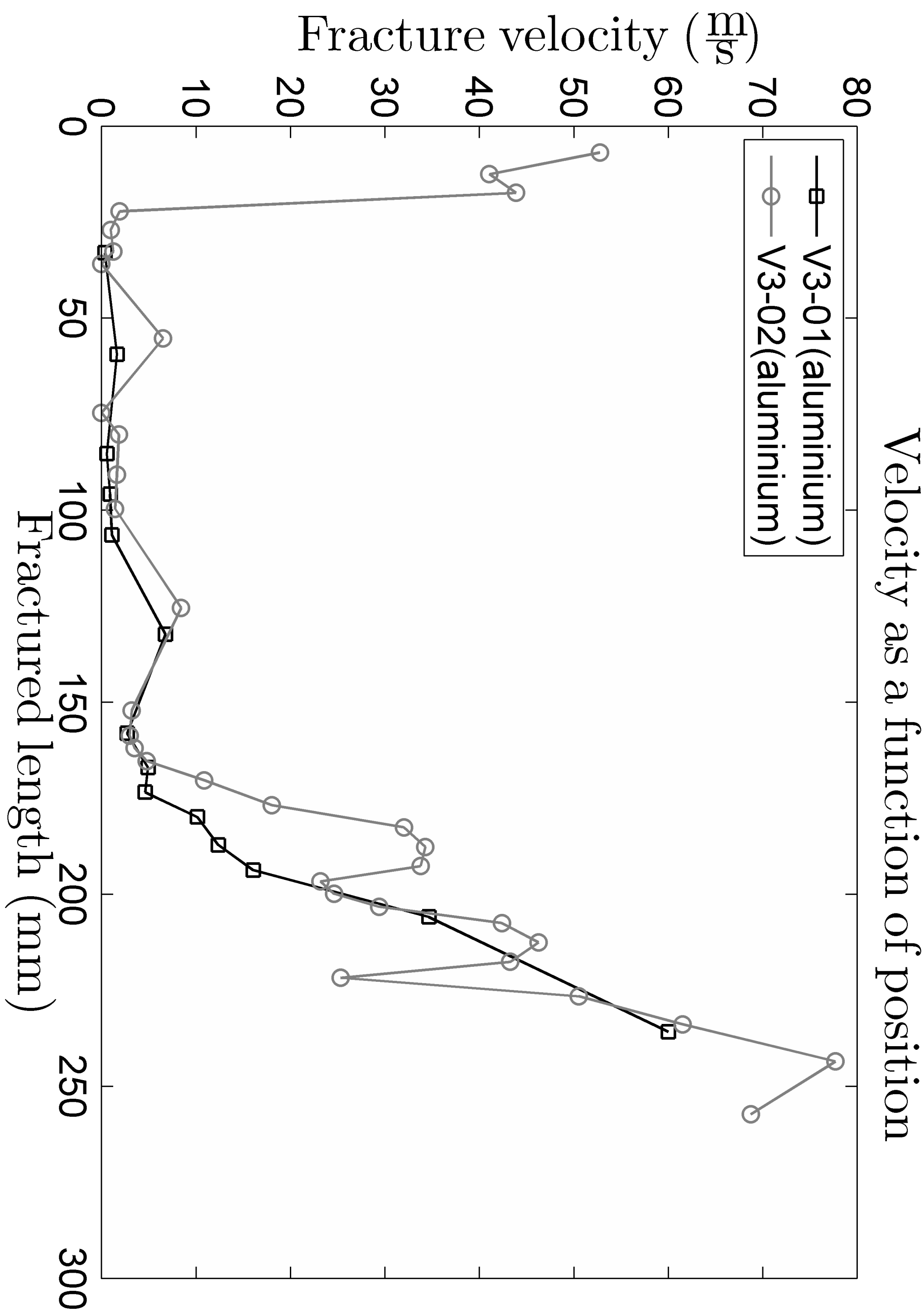

Figure K.4: Fracture velocity in aluminium plate tests as a function of fracture length

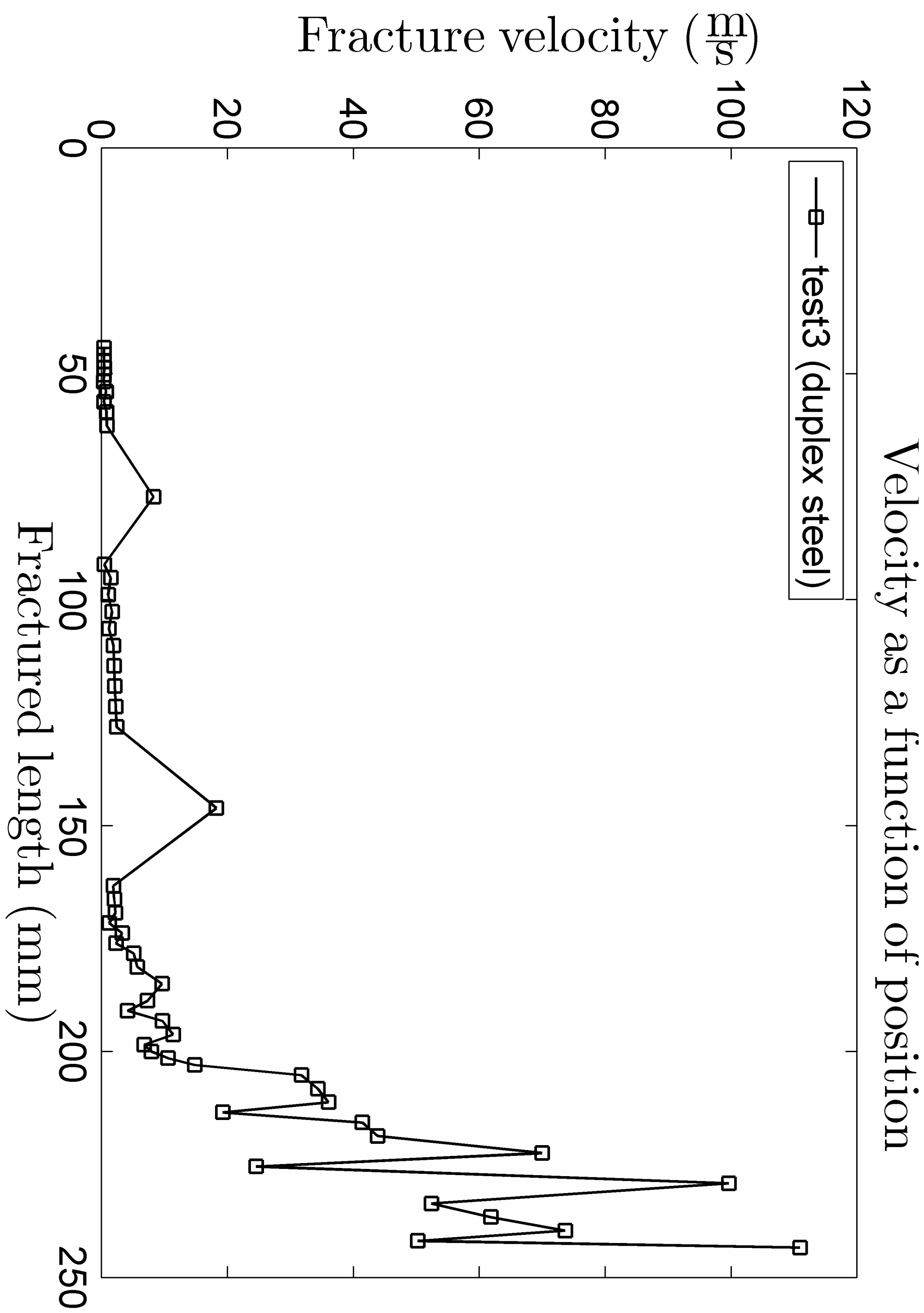

Figure K.5: Fracture velocity in steel plate test as a function of fracture length

-

Appendix L

CZ model code listing

The LS-DYNA explicit finite element code is offered as a precompiled executable and in partially compiled form. In the partially compiled form, the main part of the program is compiled, but not yet linked and there are separate uncompiled source files where alterations may still be made. Writing a custom (cohesive zone) material model involves editing these uncompiled files that include only dummy subroutines in their unedited form. The user is able to change up to ten of these dummy subroutines into custom material models. The open source part of the code is then also compiled and linked together with the closed source part of the code to obtain a single customized executable that includes the user defined materials.

Documentation is severely limited and incomplete. Writing custom material models for LS-DYNA is discouraged by LSTC, the makers of LS-DYNA, for people without special training on the subject by LSTC. This means programming is hampered by ambiguous storage conventions and undocumented behaviour of the closed source part of the code. Reverse engineering other models and trial and error led to the required level of knowledge to properly interface with the rest of the finite element code.

LS-DYNA can be instructed by the input deck to use a user defined cohesive zone material with model number N where $N = \in \{1, 2, \cdots, 49, 50\}$. LS-DYNA will then call the subroutine$UMATNC$ at runtime and provide it with information including the opening and opening rate of the element(s). The user defined material is then required to report back the resulting tractions and provide an upper bound to the elemental stiffness for the next time step.

User defined materials come in two flavours; the vectorized and scalar forms. A vectorized model is provided all inputs, for all gauss points belonging to elements with the material set to the user defined model at hand, at once in a vectorized form. Cycling over all gauss points or doing the calculations by matrix operations is left to the custom code. At each time step, the resulting tractions and stiffness bounds are passed back to the main part of the finite element code.

Though vectorized models have a distinct advantage in terms of speed, The custom cohesive zone model developed for this research has been done so in scalar form. This leads to the main part of the code calling the custom subroutine for each gauss point at every time step independently. Scalar form has the advantage that it is more transparent to read and write. Possible future revisions may well be vectorized, though accepting the loss in efficiency incurred might be less time consuming then rewriting the code. The full source as used is presented below. The code is written in Fortran 77 according to [98]. Up to Fortran 90 is supported.

```
      subroutine umat45c(IDPART,params,lft,llt,SIG,EPS,EPSDT,HSV,EMAX,
     & IFAIL,DT1SIZ,crv)
c*****************************************************************
c|  Strain rate dependent cohesive model by O.R. van der Meulen   |
c|  -----------------------------------------------------------  |
c|  Student at   : TU Delft                                       |
c|  Assignment by: TNO Defence, Security and Safety Rijswijk      |
c|  Contact at   : private(at)vandermill(dot)eu                   |
c|  The model is part of a master project, use is at own risk.    |
c|  The author, the TU Delft nor TNO guarantee the accuracy,      |
c|  suitability and correctness of the model or its source code   |
c|  All Rights Reserved                                           |
c*****************************************************************
c
c     Scalar cohesive zone with a perzyna type rate dependence
c
c***  Variables
c          IDPART ---- Part ID
c          params ---- Material constants
c          lft,llt --- Start and end of block
c                      will be set to 0 and 0 for scalar
c          SIG ------- Components of the cohesive force
c          EPS ------- Components of the displacement
c          EPSDT------ Components of the velocity
c          HSV ------- History storage
c          EMAX ------ Max. stiffness/area for time step calculation
c          IFAIL ----- =.FALSE. not failed
c                      =.TRUE. failed
c          DT1SIZ ---- Time step size
c          crv ------- Curve array (not used)
c          TIME ------ Current simulation time
c      nelmntid(1,0) - External element id (I hope)
c
c***  EPS, EPSDT, and SIG are in the local coordinate system:
c     Components 1 and 2 are in the plane of the cohesive surface
c     Component 3 is normal to the plane
c
c***  Params. storage convention
c     (1  )        Density storage convention:
                   =0, Density is per area
c                  =1, Density is per volume
c     (2) Number of integration points for element deletion:
c                  =0, No deletion
c     (3)   CZG1   Mode 1 cohesive energy
c     (4)   CZG2   Mode 2/3 cohesive energy
c     (5)   CZTX   Mode 1 maximum traction force
c     (6)   CZSX   Mode 2/3 maximum traction force
c     (7)   CZK1   Material stiffness
```

```
c     (8)   CZK2   Slope of damage curve(also a material stiffness)
c     (9)   CZETAI Reciprocal of perzyna fluidity parameter
c     (10)  CZN    Perzyna model exponent
c     (11)  CZH    Rate of strain hardening 1=default
c     (12)  TES    Type of effective seperation parameter
c     (13)  CZXMU  Exponent of the power failure criterion
c     (14)  CZPENA Penalty term for compression forces, 0=default
c     (15)  DTCTRL Factor to calculated maximum allowed timestep (0.3?)
c     Print switches:0.0:warnings,1.0:summary,2.0 detailed,3.0 nothing
c     (16)  TTYPRI Print to screen
c     (17)  MSGPRI Print to message file:"messag"
c     (18)  HSPPRI Print to extended message file: <jobname>.HSP
c
c***  HSV (history) storage convention
c     IMPORTANT  NOTE
c     In post processing, all history are moved by 1 in the direction
c     of zero, for example HSV(9) becomes history var#8.HSV(1) is lost.
c     (1)  CZDAMA   damage var.:2=intact,1=fully destroyed,0 in perzyna
c     (2)  SIGF(1)  tan1 dir. limit for abs. stress after damage starts
c     (3)  SIGF(2)  tan2 dir. limit for abs. stress after damage starts
c     (4)  SIGF(3)  norm dir. limit for abs. stress after damage starts
c     (5)  EPSINT(1)tan1. dir. integral of displacement
c     (6)  EPSINT(2)tan2. dir. integral of displacement
c     (7)  CZQ(1)   integrate strain hardening
c     (8)  CZQ(2)   integrate strain hardening
c     (9)  CZQ(3)   integrate strain hardening
c     (10) CZLABE   labda at at start of damage doctrine
c     (11) ENERGY(1)tan1 dir. energy integrator
c     (12) ENERGY(2)tan2 dir. energy integrator
c     (13) ENERGY(3)norm dir. energy integrator
c     (14) STEPCT   counter for #timesteps in perzyna and downpath
c     Perzyna overstress model:
c     The declaration below is processed by the C preprocessor and
c     is real*4 or real*8 depending on whether LS-DYNA is single or
c     double precision
c
      include 'iounits.inc'
      logical IFAIL
c     dimension inherits the mother's variable type.
      dimension params(*),SIG(*),EPS(*),EPSDT(*),HSV(*),EMAX,IFAIL,
     &          DT1SIZ
c
      DOUBLE PRECISION CZDAMA,CZDM,CZBET2,CZDF,EPSPDT(3),EPSX(3),LOWPER
     &                 ,CZLAB,CZF,CZPSI,CZQDT(3),CZDFDS(3),LAB11,LAB12,
     &                 LAB21,LAB22,CZNDA1,CZNDA2,CZDF1,CZDF2,LOWDOW,
     &                 LOWENE,HIGENE,CZFMAX,CZFTRY,SIGTRY(3),CZFSUM
c     Statement to know the simulation time, first 3 vars are not used
      common/bk28/use,less,vars,TIME
c
```

```
c***  DECLARE CONSTANTS
c     Declare warning thresholds for #timesteps in perzyna and downpath
      PARAMETER (LOWPER =10.0,LOWDOW =2.0)
c     Declare warning threshold for (dynamic/static) burned energy ratio
      PARAMETER (LOWENE =0.95 , HIGENE =100.0)
c***  PROGRAM START
c     Integrate cumulative deformation path for tangential directions
c     Usage: sign(n,-m)=-n,sign(n,m)=n,sign(-n,m)=n,sign(-n,-m)=-n
      HSV(5)=HSV(5)+EPSDT(1)*DT1SIZ*SIGN(1.0,SIG(1))
      HSV(6)=HSV(6)+EPSDT(2)*DT1SIZ*SIGN(1.0,SIG(2))
c**   Power law mixed mode model
      IF(params(12) .EQ. 0.0) THEN
c       Mixed mode relative displacement
        CZDM=SQRT(HSV(5)**2+HSV(6)**2+MAX(0.0,EPS(3))**2)
c       Mode mixity, squared
        IF(EPS(3) .NE. 0.0) THEN
          CZBET2=(sqrt(HSV(5)**2+HSV(6)**2)/EPS(3))**2
        ELSE
          IF(HSV(5) .EQ. 0.0 .AND. HSV(6) .EQ. 0.0 ) THEN
            CZBET2=0
          ELSE
            CZBET2=(sqrt(HSV(5)**2+HSV(6)**2)/(ABS(HSV(5))+
     &      ABS(HSV(6)))/2)**2
          END IF
        END IF
c       Calculate labda 1&2 on TLS for mode I
        LAB11=1.0/(((params(3)*params(7))/params(5)**2)+0.5+0.5*
     &          (params(8)/params(7)))
        LAB12=1.0-(params(8)/params(7))*LAB11
c       Calculate fullness of TLS:CZNDA
        CZNDA1=1.0-LAB11*0.5-(1.0-LAB12)*0.5
c       Ultimate combined displacement
        CZDF=((1.0+CZBET2)/CZNDA1)*((params(5)/params(3))**params(13)+
     &   ((params(6)*CZBET2)/params(4))**params(13))**(-1.0/params(13))
c       Current non dimensional combined labda on TLS (displacement)
        CZLAB=CZDM/CZDF
c       Check for end of perzyna and start of damage driven doctrine
          IF(HSV(1) .EQ. 0.0 .AND. SQRT((HSV(5)+(MIN(params(6),abs
     &    (SIG(1)))*SIGN(1.0,SIG(1)*EPSDT(1)))/params(8))**2+(HSV(6)+
     &    (MIN(params(6),abs(SIG(2)))*SIGN(1.0,SIG(2)*EPSDT(2)))/
     &    params(8))**2+MAX(EPS(3)+(MIN(params(5),abs(SIG(3)))*SIGN
     &    (1.0,EPSDT(3)))/params(8),0.0)**2) .GE. CZDF) THEN
c         Save labda at at start of damage doctrine
          HSV(10)=MIN(CZLAB,1.0)
c         Save absolute limits for sigma, SIGR can never be more again
          HSV(2)=ABS(SIG(1))
          HSV(3)=ABS(SIG(2))
          HSV(4)=ABS(SIG(3))
c         Set CZDAMA unequal to 0.0 so never downpath setup tasks again
```

```
          HSV(1)=2.0
c         Warning message for low number of timesteps in perzyna
          IF (HSV(14) .LE. LOWPER) THEN
            IF(params(16) .NE. 3.0) THEN
              write(iotty,9900)NINT(HSV(14))
            END IF
            IF(params(17) .NE. 3.0) THEN
              write(iomsg,9900)NINT(HSV(14))
            END IF
            IF(params(18) .NE. 3.0) THEN
      write(iohsp,9900)NINT(HSV(14))
            END IF
          END IF
c         Reset STEPCT (HSV(14)) to count steps in downpath from now on
          HSV(14)=0.0
        END IF
c
c**   Benzeggagh-Kenane[1996] law
      ELSE IF(params(12) .EQ. 1.0) THEN
c       Mixed mode relative displacement
        CZDM=SQRT(HSV(5)**2+HSV(6)**2+MAX(0.0,EPS(3))**2)
c       Mode mixity, squared
        IF(EPS(3) .NE. 0.0) THEN
          CZBET2=(sqrt(HSV(5)**2+HSV(6)**2)/EPS(3))**2
        ELSE
          IF(HSV(5) .EQ. 0.0 .AND. HSV(6) .EQ. 0.0 ) THEN
            CZBET2=0
          ELSE
            CZBET2=(sqrt(HSV(5)**2+HSV(6)**2)/(ABS(HSV(5))+
     &      ABS(HSV(6)))/2)**2
          END IF
        END IF
c       Calculate labda 1&2 on TLS for mode I
        LAB11=1.0/(((params(3)*params(7))/params(5)**2)+0.5+0.5*
     &          (params(8)/params(7)))
        LAB12=1.0-(params(8)/params(7))*LAB11
c       Calculate fullness of TLS:CZNDA
        CZNDA1=1.0-LAB11*0.5-(1.0-LAB12)*0.5
c       Ultimate combined displacement
        CZDF=((1.0+CZBET2)/(CZNDA1*(params(5)+CZBET2*params(6))))*
     &       (params(3)+(params(4)-params(3))*((CZBET2*params(6))/
     &       (params(5)+CZBET2*params(6)))**params(13))
c       Current non dimensional combined labda on TLS (displacement)
        CZLAB=CZDM/CZDF
c       Check for end of perzyna and start of damage driven doctrine
          IF(HSV(1) .EQ. 0.0 .AND. SQRT((HSV(5)+(MIN(params(6),abs
     &    (SIG(1)))*SIGN(1.0,SIG(1)*EPSDT(1)))/params(8))**2+(HSV(6)+
     &    (MIN(params(6),abs(SIG(2)))*SIGN(1.0,SIG(2)*EPSDT(2)))/
     &    params(8))**2+MAX(EPS(3)+(MIN(params(5),abs(SIG(3)))*SIGN
```

```
     &    (1.0,EPSDT(3)))/params(8),0.0)**2) .GE. CZDF) THEN
c         Save labda at at start of damage doctrine
          HSV(10)=MIN(CZLAB,1.0)
c         Save absolute limits for sigma, SIGR can never be more again
          HSV(2)=ABS(SIG(1))
          HSV(3)=ABS(SIG(2))
          HSV(4)=ABS(SIG(3))
c         Set CZDAMA unequal to -1 so never downpath setup tasks again
          HSV(1)=2.0
c         Warning message for low number of timesteps in perzyna
          IF (HSV(14) .LE. LOWPER) THEN
            IF(params(16) .NE. 3.0) THEN
              write(iotty,9900)NINT(HSV(14))
            END IF
            IF(params(17) .NE. 3.0) THEN
              write(iomsg,9900)NINT(HSV(14))
            END IF
            IF(params(18) .NE. 3.0) THEN
      write(iohsp,9900)NINT(HSV(14))
            END IF
          END IF
c         reset STEPCT (HSV(14)) to count steps in downpath from now on
          HSV(14)=0.0
        END IF
c**   Simpler mixed mode law
      ELSE IF(params(12) .EQ. 2.0) THEN
c       Calculate labda 1&2 on TLS for mode I
        LAB11=1.0/(((params(3)*params(7))/params(5)**2)+0.5+0.5*
     &         (params(8)/params(7)))
        LAB12=1.0-(params(8)/params(7))*LAB11
c       Calculate labda 1&2 on TLS for mode II
        LAB21=1.0/(((params(4)*params(7))/params(6)**2)+0.5+0.5*
     &         (params(8)/params(7)))
        LAB22=1.0-(params(8)/params(7))*LAB21
c       Calculate fullness of TLS:CZNDA1 & 2
        CZNDA1=1.0-LAB11*0.5-(1.0-LAB12)*0.5
        CZNDA2=1.0-LAB21*0.5-(1.0-LAB22)*0.5
c       Calculate ultimate displacements,
CZDF1=params(3)/(CZNDA1*params(5))
        CZDF2=params(4)/(CZNDA2*params(6))
c       Current non dimensional combined labda on TLS (displacement)
        CZLAB=SQRT((HSV(5)/CZDF2)**2+(HSV(6)/CZDF2)**2+
     &        MAX(EPS(3)/CZDF1,0.0)**2)
c       Check for end of perzyna and start of damage driven doctrine
          IF(HSV(1) .EQ. 0.0 .AND. SQRT(((HSV(5)+(MIN(params(6),abs
     &    (SIG(1)))*SIGN(1.0,SIG(1)*EPSDT(1)))/params(8))/CZDF2)**2+
     &    ((HSV(6)+(MIN(params(6),abs(SIG(2)))*SIGN(1.0,SIG(2)*
     &    EPSDT(2)))/params(8))/CZDF2)**2+(MAX(EPS(3)+(MIN(params(5),
     &    abs(SIG(3)))*SIGN(1.0,EPSDT(3)))/params(8),0.0)/CZDF1)**2)
```

```
     &    .GE. 1.0) THEN
c         Save labda at at start of damage doctrine
          HSV(10)=MIN(CZLAB,1.0)
c         Save absolute limits for sigma, SIGR can never be more again
          HSV(2)=ABS(SIG(1))
          HSV(3)=ABS(SIG(2))
          HSV(4)=ABS(SIG(3))
c         Set CZDAMA unequal to 0.0 so never downpath setup tasks again
          HSV(1)=2.0
c         Warning message for low number of timesteps in perzyna
          IF (HSV(14) .LE. LOWPER) THEN
            IF(params(16) .NE. 3.0) THEN
              write(iotty,9900)NINT(HSV(14))
            END IF
            IF(params(17) .NE. 3.0) THEN
              write(iomsg,9900)NINT(HSV(14))
            END IF
            IF(params(18) .NE. 3.0) THEN
      write(iohsp,9900)NINT(HSV(14))
            END IF
          END IF
c         reset STEPCT (HSV(14)) to count steps in downpath from now on
          HSV(14)=0.0
        END IF
      END IF
c
c***    CHECK FOR FAILURE OF GAUSS POINT
        IF(CZLAB .GE. 1.0 .AND. HSV(1) .NE. 1.0) THEN
c         Tell main LSDYNA code the integration point just failed
          IFAIL=.TRUE.
c         Warning message for low number of timesteps in downpath
          IF (HSV(14) .LE. LOWDOW) THEN
            IF(params(16) .NE. 3.0) THEN
              write(iotty,9901)NINT(HSV(14))
            END IF
            IF(params(17) .NE. 3.0) THEN
              write(iomsg,9901)NINT(HSV(14))
            END IF
            IF(params(18) .NE. 3.0) THEN
      write(iohsp,9901)NINT(HSV(14))
            END IF
          END IF
c         Warning message for suspiciously low amount of energy burned
          IF((HSV(11)+HSV(12)+HSV(13)) .LT. MIN(params(3),params(4))*
     &      LOWENE) THEN
            IF(params(16) .NE. 3.0) THEN
              write(iotty,9902)(HSV(11)+HSV(12)+HSV(13))/
     &        MIN(params(3),params(4))
            END IF
```

```
          IF(params(17) .NE. 3.0) THEN
            write(iomsg,9902)(HSV(11)+HSV(12)+HSV(13))/
     &        MIN(params(3),params(4))
          END IF
          IF(params(18) .NE. 3.0) THEN
      write(iohsp,9902)(HSV(11)+HSV(12)+HSV(13))/
     &        MIN(params(3),params(4))
          END IF
        END IF
c       Warning message for suspiciously high amount of energy burned
        IF((HSV(11)+HSV(12)+HSV(13)) .GT. MAX(params(3),params(4))*
     &    HIGENE) THEN
          IF(params(16) .NE. 3.0) THEN
            write(iotty,9903)(HSV(11)+HSV(12)+HSV(13))/
     &        MAX(params(3),params(4))
          END IF
          IF(params(17) .NE. 3.0) THEN
            write(iomsg,9903)(HSV(11)+HSV(12)+HSV(13))/
     &        MAX(params(3),params(4))
          END IF
          IF(params(18) .NE. 3.0) THEN
      write(iohsp,9903)(HSV(11)+HSV(12)+HSV(13))/
     &        MAX(params(3),params(4))
          END IF
        END IF
c       Write a failed element summary to screen
        IF(params(16) .EQ. 1.0) THEN
          WRITE(iotty,9800)IDPART
          WRITE(iotty,9801)TIME
        END IF
c       Write a failed element summary to message file
        IF(params(17) .EQ. 1.0) THEN
          WRITE(iomsg,9800)IDPART
          WRITE(iomsg,9801)TIME
        END IF
c       Write a failed element summary to <jobname>.HSP file
        IF(params(18) .EQ. 1.0) THEN
          WRITE(iohsp,9800)IDPART
          WRITE(iohsp,9801)TIME
        END IF
c       write a detailed failed gauss point report to screen
        IF(params(16) .EQ. 2.0) THEN
    WRITE(iotty,9700)
    WRITE(iotty,9701)IDPART
c     WRITE(iotty,9702)nelmntid(1,0)
    WRITE(iotty,9703)TIME
    WRITE(iotty,9704)HSV(13)
    WRITE(iotty,9705)HSV(11)+HSV(12)
    WRITE(iotty,9706)HSV(4)
```

```
    WRITE(iotty,9707)HSV(2)
    WRITE(iotty,9708)HSV(3)
    WRITE(iotty,9709)EPS(3)
    WRITE(iotty,9710)HSV(5)
    WRITE(iotty,9711)HSV(6)
    WRITE(iotty,9712)HSV(9)
    WRITE(iotty,9713)HSV(7)
    WRITE(iotty,9714)HSV(8)
    WRITE(iotty,9715)
          END IF
c         Write a detailed failed gauss point report to message file
          IF(params(17) .EQ. 2.0) THEN
    WRITE(iomsg,9700)
    WRITE(iomsg,9701)IDPART
c     WRITE(iomsg,9702)nelmntid(1,0)
    WRITE(iomsg,9703)TIME
    WRITE(iomsg,9704)HSV(13)
    WRITE(iomsg,9705)HSV(11)+HSV(12)
    WRITE(iomsg,9706)HSV(4)
    WRITE(iomsg,9707)HSV(2)
    WRITE(iomsg,9708)HSV(3)
    WRITE(iomsg,9709)EPS(3)
    WRITE(iomsg,9710)HSV(5)
    WRITE(iomsg,9711)HSV(6)
    WRITE(iomsg,9712)HSV(9)
    WRITE(iomsg,9713)HSV(7)
    WRITE(iomsg,9714)HSV(8)
    WRITE(iomsg,9715)
          END IF
c         Write a detailed failed gauss point report to <jobname>.HSP file
          IF(params(18) .EQ. 2.0) THEN
    WRITE(iohsp,9700)
    WRITE(iohsp,9701)IDPART
c     WRITE(iohsp,9702)nelmntid(1,0)
    WRITE(iohsp,9703)TIME
    WRITE(iohsp,9704)HSV(13)
    WRITE(iohsp,9705)HSV(11)+HSV(12)
    WRITE(iohsp,9706)HSV(4)
    WRITE(iohsp,9707)HSV(2)
    WRITE(iohsp,9708)HSV(3)
    WRITE(iohsp,9709)EPS(3)
    WRITE(iohsp,9710)HSV(5)
    WRITE(iohsp,9711)HSV(6)
    WRITE(iohsp,9712)HSV(9)
    WRITE(iohsp,9713)HSV(7)
    WRITE(iohsp,9714)HSV(8)
    WRITE(iohsp,9715)
          END IF
        END IF
```

```
c***  START OF MAIN LOOP STRESS CALCULATION
c     Detect if we are in perzyna or damage doctrine, perzyna ==0.0
      IF(HSV(1) .EQ. 0.0) THEN
c       Stress > elastic limit & allowable increase due to strain
c       Hardening divided by normal allowable stress (HILL criterion)
        CZF=sqrt((SIG(1)/(HSV(7)+1.0))**2/params(6)**2+(SIG(2)
     &  /(HSV(8)+1.0))**2/params(6)**2+max(SIG(3)/(HSV(9)+1.0),0.0)
     &  **2/params(5)**2)-1.0
c       Count number of timesteps in perzyna governed doctrine
        IF(CZF.GT.0.0 .OR. HSV(14) .GT. 0.0)THEN
          HSV(14)=HSV(14)+1.0
        END IF
c       Prevent N/0.0 error when all stresses are equal to 0.0
        IF(CZF .NE. -1.0) THEN
c         CZDFDS is the normal to the yield surface and the direction
c         of yielding vector
          CZDFDS(1)=HSV(7)**2*SIG(1)*params(5)/((CZF+1.0)*params(6)**2)
          CZDFDS(2)=HSV(8)**2*SIG(2)*params(5)/((CZF+1.0)*params(6)**2)
          CZDFDS(3)=HSV(9)**2*MAX(0.0,SIG(3)/((CZF+1.0)*params(5)))
        ELSE
c         protection against dif/0 error at first timestep
          CZDFDS(1)=0.0
          CZDFDS(2)=0.0
          CZDFDS(3)=0.0
        END IF
c       Calculate overstress
        CZPSI=MAX(0.0,CZF)**params(10)
c       Calculate increase in strain hardening this timestep
        CZQDT(1)=params(9)*MAX(0.0,CZPSI)*CZDFDS(1)*params(11)
        CZQDT(2)=params(9)*MAX(0.0,CZPSI)*CZDFDS(2)*params(11)
        CZQDT(3)=params(9)*MAX(0.0,CZPSI)*CZDFDS(3)*params(11)
c       Integrate Q (work hardening parameter)
        HSV(7)=HSV(7)+CZQDT(1)*DT1SIZ
        HSV(8)=HSV(7)+CZQDT(2)*DT1SIZ
        HSV(9)=HSV(7)+CZQDT(3)*DT1SIZ
c       Calculate amount of delta opening taken up by plasticity
        EPSPDT(1)=params(9)*MAX(0.0,CZPSI)*CZDFDS(1)
        EPSPDT(2)=params(9)*MAX(0.0,CZPSI)*CZDFDS(2)
        EPSPDT(3)=params(9)*MAX(0.0,CZPSI)*CZDFDS(3)
c       Integrate Traction in tangential directions
c       Trying the step first to prevent instability
c       (Radial return method)
        SIGTRY(1)=SIG(1)+params(7)*(EPSDT(1)-EPSPDT(1))*DT1SIZ
        SIGTRY(2)=SIG(2)+params(7)*(EPSDT(2)-EPSPDT(2))*DT1SIZ
c       Params(14)=damage=0 means undamaged in LS-Dyna,so ->1*stress
c       so we add 1 to params(14) always
c       Check for penalty parameter active and negative displacement
c       Check is inverted for calculational efficiency
        IF(params(14) .EQ. 0.0 .OR. EPS(3) .GE. 0.0) THEN
```

```
c         Integrate Traction in normal direction without penalty
          SIGTRY(3)=SIG(3)+params(7)*(EPSDT(3)-EPSPDT(3))*DT1SIZ
c         Tell LS-dyna maximum stiffness to expect(influences timestep)
           EMAX=MAX(params(7),params(8))*params(15)**(-2.0)
        ELSE
c         Integrate Traction in normal direction with penalty
          SIGTRY(3)=SIG(3)+params(7)*(params(14)+1.0)*(EPSDT(3)-
     &    EPSPDT(3))*DT1SIZ
c         Tell LS-dyna maximum stiffness to expect(influences timestep)
          EMAX=max(params(7)*(params(14)+1.0),params(8))*params(15)
     &    **(-2.0)
        END IF
c       Calculate overstress based on tried sigma steps, used for
c       Instability preventing. may not be more then any CZFMAX
        CZFTRY=sqrt((SIGTRY(1)/(HSV(7)+1.0))**2/params(6)**2+(SIGTRY(2)
     &  /(HSV(8)+1.0))**2/params(6)**2+max(SIGTRY(3)/(HSV(9)+1.0),0.0)
     &  **2/params(5)**2)-1.0
c       Test if trial F is greater then current F
          IF(CZFTRY .GT. CZF)THEN
c         Calculate max allowed overstress at given strain rate in 3d
          IF(CZDFDS(1) .EQ. 0.0)THEN
            CZFSUM=1.0
          ELSE
            CZFSUM=abs((EPSDT(1)/params(9))/CZDFDS(1))
          END IF
          IF(CZDFDS(2) .NE. 0.0)THEN
            CZFSUM=CZFSUM+abs(((EPSDT(2)/params(9))/CZDFDS(2))
          END IF
          IF(CZDFDS(3) .NE. 0.0)THEN
            CZFSUM=CZFSUM+abs(((EPSDT(3)/params(9))/CZDFDS(3))
          END IF
          CZFMAX=CZFSUM**(1.0/params(10))
c         Place SIG on boundary of poss. values if SIGTRY has passed it
          SIG(1)=SIGTRY(1)*min(1.0,(CZFMAX(1)+1.0)/(CZFTRY+1.0))
          SIG(2)=SIGTRY(2)*min(1.0,(CZFMAX(2)+1.0)/(CZFTRY+1.0))
c         Test for mode I excludes compression from scaling
          IF(SIGTRY(3) .GT. SIG(3))THEN
c           If true, value of SIGTRY(3) is impossible, scale it back
            SIG(3)=SIGTRY(3)*min(1.0,(CZFMAX(3)+1.0)/(CZFTRY+1.0))
          ELSE
c           SIGTRY(3) is possible, making the step...
            SIG(3)=SIGTRY(3)
          END IF
        ELSE
c         No limit for decreasing F
          SIG(1)=SIGTRY(1)
          SIG(2)=SIGTRY(2)
          SIG(3)=SIGTRY(3)
        END
```

```
c**   code for damage doctrine
      ELSE
c        Count number of timesteps in downpath governed doctrine
         HSV(14)=HSV(14)+1.0
c        Calculate damage, 2=intact,1=destroyed, no undamaging
         HSV(1)=MAX(1.0,MIN(HSV(1),2.0-(CZLAB-HSV(10))/(1.0-HSV(10))))
c        Calculate stress in the tangential directions, may not exceed
c        abs(value) at start downpath. is multiplied by (damage-1)
         SIG(1)=MAX(MIN(SIG(1)+EPSDT(1)*DT1SIZ*params(7),HSV(2)*
     &   (HSV(1)-1)),-HSV(2)*(HSV(1)-1))
         SIG(2)=MAX(MIN(SIG(2)+EPSDT(2)*DT1SIZ*params(7),HSV(3)*
     &   (HSV(1)-1)),-HSV(3)*(HSV(1)-1))
c        Check for penalty parameter active and negative displacement
c        Check is inverted for calculational efficientcy
c        This IF is done to accomodate penalty for mode 1 squishing
         IF(params(14) .EQ. 0.0 .OR. EPS(3) .GE. 0.0) THEN
           SIG(3)=MAX(MIN(SIG(3)+EPSDT(3)*DT1SIZ*params(7),HSV(4)*
     &    (HSV(1)-1)),-HSV(4)*(HSV(1)-1))
c          Maximum stiffness equal to static damage stiffness CZK2 times
c          the maximum ratio of overstress
           EMAX=MAX(params(7),params(8)*max(HSV(2)/params(6),HSV(3)/
     &     params(6),HSV(4)/params(5),1.0))*params(15)**(-2.0)
         ELSE
           SIG(3)=MAX(MIN(SIG(3)+EPSDT(3)*DT1SIZ*params(7)*(params(14)+
     &     1.0),HSV(4)*(HSV(1)-1)),-HSV(4)*(HSV(1)-1))
c          Maximum stiffness equal to static damage stiffness CZK2 times
c          the maximum ratio of overstress
           EMAX=max(params(8)*max(HSV(2)/params(6),HSV(3)/params(6),
     &     HSV(4)/params(5),1.0),params(7)*(params(14)+1.0))*params(15)
     &     **(-2.0)
         END IF
      END IF
c     Integrate energy
      HSV(11)=HSV(11)+EPSDT(1)*DT1SIZ*SIG(1)
      HSV(12)=HSV(12)+EPSDT(2)*DT1SIZ*SIG(2)
      HSV(13)=HSV(13)+EPSDT(3)*DT1SIZ*SIG(3)
c
c***  DEFINE FORMAT OF MESSAGES
9900  format('***WARNING #timesteps in perzyna low :',I4)
9901  format('***WARNING #timesteps in downpath low:',I4)
9902  format('***WARNING (dyn/stat) energy',
     &' low :',F10.4)
9903  format('***WARNING (dyn/stat) energy',
     &' high:',F10.4)
9800  format('A gauss point belonging to part :',I5)
9801  format('failed at time :',d)
9700  format(/'G A U S S   P O I N T   F A I L U R E   R E P O R T')
9701  format(/'part                                  =',I)
9703  format('Time                                  =',d)
```

```
9704  format('Dissipated energy in mode 1          =',d)
9705  format('Dissipated energy in mode 2&3        =',d)
9706  format('Start of damage stress in normal dir.=',d)
9707  format('and in tangential direction #1      =',d)
9708  format('and in tangential direction #2      =',d)
9709  format('Mode 1 opening at failure            =',d)
9710  format('Mode 2&3 deformation path direction 1=',d)
9711  format('Mode 2&3 deformation path direction 2=',d)
9712  format('Work hardening in normal direction   =',d)
9713  format('and in tangential direction #1      =',d)
9714  format('and in tangential direction #2      =',d)
9715  format(' ')
      return
      end
```

Appendix M

Interface source code

In this appendix the full source code of the MATLAB cohesive zone elements sub mesh generator is presented as described in section 4.5.1.

```
%OPTIONS TO BE SET BY USER
%
%Geometry of 1 unit
%
%Width of cohesive zone solid
cz_width=1;
%Height of cohesive zone solid
cz_heigth=0.1;
%Height of connecting shell (between cz and rest of mesh)
shell_heigth=0.5;
%Width of connecting shell (between cz and rest of mesh)
shell_thickness=1;
%Zero strength shells covering the cohesive zones, they feel unhappy
%without them
taco_thickness=0.1;
tacoshell_active=true;
%
%Geometry of stitched units
%
%Number of elements desired
cz_numberof=1;
%Length of one element
cz_length=0.1;
%
%Set Id start numbers
%
node_number_start=1;
element_number_start=1;
node_set_start=11;
part_id_start=21;
section_id_start=31;
%
%Set material numbers
%
```

```
mat_id_shells=1;
mat_id_cz=2;
mat_id_mat0=3;
%No adapable parameters below!
%Pre-allocating memory
home
disp('...Allocating required memory')
node=zeros(cz_numberof*8+8,3);
element_shell=zeros(cz_numberof*4,5);
element_solid=zeros(cz_numberof*1,9);
constrained_shell_to_solid=zeros(cz_numberof*2+2,2);
sid=zeros(cz_numberof*2+2,2);
%Shapes of the elements defined, dont edit, use the scaling factors in the
%user options
home
disp('...Initializing')
cz_normalized=[1,-0.5,-0.5;1,0.5,-0.5;1,-0.5,0.5;1,0.5,0.5];
shell_low_normalized=[1,0,0;1,0,-1];
shell_low_translation=[0,0,-0.5;0,0,-0.5];
shell_high_normalized=[1,0,0;1,0,1];
shell_high_translation=[0,0,0.5;0,0,0.5];
cz_dim=[0,cz_width,cz_heigth;0,cz_width,cz_heigth;0,cz_width,cz_heigth;...
    0,cz_width,cz_heigth;];
cz_dim_trans=[0,cz_width,cz_heigth;0,cz_width,cz_heigth];
node([1 2 3 4],1:3)=cz_normalized.*cz_dim;
shell_dim=[0,0,shell_heigth;0,0,shell_heigth];
node([5 8],1:3)=shell_low_normalized.*shell_dim+shell_low_translation.*...
    cz_dim_trans;
node([6 7],1:3)=shell_high_normalized.*...
    shell_dim+shell_high_translation.*cz_dim_trans;
constrained_shell_to_solid(1,:)=[5+(node_number_start-1),node_set_start];
constrained_shell_to_solid(2,:)=[6+(node_number_start-1),node_set_start+1];
sid(1,:)=[1+(node_number_start-1),2+(node_number_start-1)];
sid(2,:)=[3+(node_number_start-1),4+(node_number_start-1)];
home
disp('...Generating mesh and constraints')
for i=1:1:cz_numberof
   cz_dim=[cz_length*i,cz_width,cz_heigth;cz_length*i,cz_width,cz_heigth;...
       cz_length*i,cz_width,cz_heigth;cz_length*i,cz_width,cz_heigth;];
   cz_dim_trans=[0,cz_width,cz_heigth;0,cz_width,cz_heigth];
   shell_dim=[cz_length*i,0,shell_heigth;cz_length*i,0,shell_heigth];
   node([1+i*8 2+i*8 3+i*8 4+i*8],1:3)=cz_normalized.*cz_dim;
   node([5+i*8 8+i*8],1:3)=shell_low_normalized.*shell_dim+...
       shell_low_translation.*cz_dim_trans;
   node([6+i*8 7+i*8],1:3)=shell_high_normalized.*shell_dim+...
       shell_high_translation.*cz_dim_trans;
   element_solid(i,1:9)=[part_id_start+2,1+(i-1)*8+(node_number_start...
       -1),2+(i-1)*8+(node_number_start-1),2+i*8+(node_number_start-1)...
       ,1+i*8+(node_number_start-1),3+(i-1)*8+(node_number_start-1),4+...
```

```
        (i-1)*8+(node_number_start-1),4+i*8+(node_number_start-1),3+i*...
        8+(node_number_start-1)];
    element_shell((i-1)*4+1,1:5)=[part_id_start,5+(i-1)*8+...
        (node_number_start-1),8+(i-1)*8+(node_number_start-1),8+i*8+...
        (node_number_start-1),5+i*8+(node_number_start-1)];
    element_shell((i-1)*4+2,1:5)=[part_id_start+1,6+(i-1)*8+...
        (node_number_start-1),7+(i-1)*8+(node_number_start-1),7+i*8+...
        (node_number_start-1),6+i*8+(node_number_start-1)];
    element_shell((i-1)*4+3,1:5)=[part_id_start+3,1+(i-1)*8+...
        (node_number_start-1),2+(i-1)*8+(node_number_start-1),2+i*8+...
        (node_number_start-1),1+i*8+(node_number_start-1)];
    element_shell((i-1)*4+4,1:5)=[part_id_start+4,3+(i-1)*8+...
        (node_number_start-1),4+(i-1)*8+(node_number_start-1),4+i*8+...
        (node_number_start-1),3+i*8+(node_number_start-1)];
    constrained_shell_to_solid(i*2+1,:)=[5+i*8+(node_number_start-1),...
        i*2+node_set_start];
    constrained_shell_to_solid(i*2+2,:)=[6+i*8+(node_number_start-1),...
        i*2+node_set_start+1];
    sid(i*2+1,:)=[1+i*8+(node_number_start-1),2+i*8+(node_number_start-1)];
    sid(i*2+2,:)=[3+i*8+(node_number_start-1),4+i*8+(node_number_start-1)];
end
home
disp('...writing mesh to disk')
node_vector=(node_number_start:1:cz_numberof*8+8+(node_number_start-1))';
element_shell_vector=(element_number_start:1:cz_numberof*4+...
    (element_number_start-1))';
element_solid_vector=(element_number_start+cz_numberof*4:1:cz_numberof*...
    4+cz_numberof*1+(element_number_start-1))';
dlmwrite('testputput.txt','*KEYWORD','newline','unix','delimiter','');
dlmwrite('testputput.txt','$$cohesive zone and transition to shell mesh'...
    ,'newline','unix','delimiter','','-append');
dlmwrite('testputput.txt','$$generated by "elembuilder" a Matlab script'...
    ,'newline','unix','delimiter','','-append');
dlmwrite('testputput.txt','$$info: O.R. van der Meulen +31648176614',...
    'newline','unix','delimiter','','-append');
dlmwrite('testputput.txt','*NODE','newline','unix','delimiter','',...
    '-append');
dlmwrite('testputput.txt',[node_vector,node],'newline','unix',...
    'delimiter',',','-append','precision','%15.7f');
dlmwrite('testputput.txt','*ELEMENT_SHELL','newline','unix',...
    'delimiter','','-append');
dlmwrite('testputput.txt',[element_shell_vector element_shell],...
    'newline','unix','delimiter',',','-append','precision','%10.0f');
dlmwrite('testputput.txt','*ELEMENT_SOLID','newline','unix','delimiter',...
    '','-append');
dlmwrite('testputput.txt',[element_solid_vector element_solid],'newline'...
    ,'unix','delimiter',',','-append','precision','%10.0f');
dlmwrite('testputput.txt','*PART','newline','unix','delimiter','',...
    '-append');
```

```
dlmwrite('testputput.txt','connecting_shells_low','newline','unix',...
    'delimiter','','-append');
dlmwrite('testputput.txt',[part_id_start,section_id_start,mat_id_shells]...
    ,'newline','unix','delimiter',',','-append','precision','%10.0f');
dlmwrite('testputput.txt','connecting_shells_high','newline','unix',...
    'delimiter','','-append');
dlmwrite('testputput.txt',[part_id_start+1,section_id_start,...
    mat_id_shells],'newline','unix','delimiter',',','-append',...
    'precision','%10.0f');
dlmwrite('testputput.txt','cohesive zones ag','newline','unix',...
    'delimiter','','-append');
dlmwrite('testputput.txt',[part_id_start+2,section_id_start+1,mat_id_cz]...
    ,'newline','unix','delimiter',',','-append','precision','%10.0f');
dlmwrite('testputput.txt','mat_0 sandwitch_low','newline','unix',...
    'delimiter','','-append');
dlmwrite('testputput.txt',[part_id_start+3,section_id_start+2,...
    mat_id_mat0],'newline','unix','delimiter',',','-append','precision',...
    '%10.0f');
dlmwrite('testputput.txt','mat_0 sandwitch_high','newline','unix',...
    'delimiter','','-append');
dlmwrite('testputput.txt',[part_id_start+4,section_id_start+2,...
    mat_id_mat0],'newline','unix','delimiter',',','-append','precision',...
    '%10.0f');
dlmwrite('testputput.txt','*SECTION_SHELL_TITLE','newline','unix',...
    'delimiter','','-append');
dlmwrite('testputput.txt','connecting shells','newline','unix',...
    'delimiter','','-append');
dlmwrite('testputput.txt',section_id_start,'newline','unix','delimiter',...
    ',','-append','precision','%10.0f');
dlmwrite('testputput.txt',[shell_thickness,shell_thickness,...
    shell_thickness,shell_thickness],'newline','unix','delimiter',',',...
    '-append');
dlmwrite('testputput.txt','*SECTION_SHELL_TITLE','newline','unix',...
    'delimiter','','-append');
dlmwrite('testputput.txt','mat_0 sandwitch layer shells','newline',...
    'unix','delimiter','','-append');
dlmwrite('testputput.txt',section_id_start+2,'newline','unix',...
    'delimiter',',','-append','precision','%10.0f');
dlmwrite('testputput.txt',[taco_thickness,taco_thickness,taco_thickness,...
    taco_thickness],'newline','unix','delimiter',',','-append');
dlmwrite('testputput.txt','*SECTION_SOLID_TITLE','newline','unix',...
    'delimiter','','-append');
dlmwrite('testputput.txt','cohesive zones layer ag','newline','unix',...
    'delimiter','','-append');
dlmwrite('testputput.txt',[section_id_start+1,19],'newline','unix',...
    'delimiter',',','-append');
home
disp('...Writing constraints to disk')
disp_interval=0.1;
```

```
for i=1:1:cz_numberof*2
    dlmwrite('testputput.txt','*SET_NODE_LIST','newline','unix',...
        'delimiter','','-append');
    dlmwrite('testputput.txt',i+node_set_start-1,'newline','unix',...
        'delimiter',',','-append','precision','%10.0f');
    dlmwrite('testputput.txt',sid(i,:),'newline','unix','delimiter',',',...
        '-append','precision','%10.0f');
    dlmwrite('testputput.txt','*CONSTRAINED_SHELL_TO_SOLID','newline',...
        'unix','delimiter','','-append');
    dlmwrite('testputput.txt',constrained_shell_to_solid(i,:),'newline',...
        'unix','delimiter',',','-append','precision','%10.0f');
    if i>=cz_numberof*2*disp_interval
        home
        disp([num2str(disp_interval*100),'%'])
        disp_interval=disp_interval+0.1;
    end
end
dlmwrite('testputput.txt','*END','newline','unix','delimiter',''...
    ,'-append');
disp('...Done!')
```

Appendix N

Original assignment

The original project proposal is presented in both Dutch and English, The English version, as given in section N.1, is a translation by the author and some liberty has been taken to increase the readability of the text. The Dutch text is given in section N.2 and is a direct re-digitized copy of the original proposal as given to the author.

N.1 English

MSc project: "Visco plastic cohesive zone model"
MSc student: Ronald van der Meulen

Research topics :

1. Literature study (time: 4 weeks)
   (a) What is known about fracture propagation is steel panels / pipes? This section is aimed at experimental data; the influence of plate thickness, material (brittle or ductile), temperature and curvature is to be investigated.
   (b) Dynamic ductile fracture propagation report fracture propagation rates as derived from theoretical bounds, experimental evidence and finite element simulations.
   (c) Static and dynamic fracture propagation modelling. Primarily aimed at dynamic ductile fracture propagation
2. Perform simulations with existing LS-DYNA cohesive zone elements (time: 2 weeks) (TNO report with simulation series is available) explain shortcomings; Difference between fracture rates as observed in experiments and simulations
3. What options are available to incorporate rate dependence in the cohesive zone model? Visco-plasticity is suggested but needs to be explained by the student (time: 4 weeks) Research existing visco-plastic models and check their suitability for use within a custom LS-DYNA cohesive zone material model. If no suitable model exists, one must be developed. Report Constitutive equations. Explain the role of time integration and element stiffness in the explicit finite element solver
4. Creation of a visco-plastic cohesive zone model within LS-DYNA (time: 10 weeks) As a first step, implementation of the "*Tvergaard and Hutchinson*" cohesive zone model is suggested. This model is already available within LS-DYNA and is explained in the manual. Then implementation of the chosen visco-plastic model.

5. Check results of newly developed model. This needs to be done also against available benchmarks (time: 8 weeks) First, Perform one element simulations, then verify the results using the plate tests performed at TNO for steel and aluminium. Special attention needs to be paid to the initiation phase (plates are pre stressed and then an instantaneous initial fracture is created.) High speed recordings and strain gauge measurements are available for plate and barrel tests

6. Report Results (time: 6 weeks).

Total: 4+2+4+10+8+4=32 weeks.

N.2 Dutch

Msc project: “Visco plastic cohesive zone model”
Msc student: Ronald van der Meulen

Onderzoeksvragen/aspecten :

1. literatuur onderzoek (Tijd: 4 weken)
   (a) Wat is er bekend van scheurpropagatie in stalen panelen/buizen. Dit deel is gericht op experimentele gegevens. lnvloed van inwendige spanning, plaat dikte, materiaal (taai of brosse breuk), temperatuur, invloed kromming.
   (b) Dynamisch ductiele scheur voortplanting. Scheur snelheiden: theoretische bounds; experimenten en simulaties.
   (c) Scheurpropagatie modellering: statisch en dynamisch Met speciale aandacht aan dynamisch ductiele scheur voortplanting.

2. Toepassing (bestaand) cohesive zone element in LS Dyna (Tijd: 2 weken) (TNO studie met serie simulaties is beschikbaar) Tekortkomingen toelichten (verschillen tussen scheursnelheden van experimenten en simulaties).

3. Welke mogelijkheden zijn er om rate dependency in rekening te brengen (onze suggestie is viscoplastisch, maar keuze moet onderbouwd worden) (Tijd 4 weken) Bestaande viscoplastische modellen. Kijk naar toepasbaarheid. lndien niet toepasbaar, dan nieuw model ontwikkelen. Constitutieve vergelijkingen. Tijd integratie en stijfheid (voor rekening van expliciet tijdstap).

4. Inbouwen visco plasticity model in LS-DYNA (10 weken) Als eerste stap, implementatie van TH-CZ model in LS-DYNA handleiding. Daarna, implementatie van de gekozen CZ model.

5. Check + toepassen op benchmarks (8 weken) Eerst, one-element simulaties. Daarna, gebruiken van TNO plaattesten (staal en aluminium). Speciale aandacht voor initiatie fase. (instationaire fase) (platen onder trek-voorspanning + instantaan scheur aangebracht; high speed opnamen van scheurpropagatie aanwezig + op 4 plaatsen rekstrookmetingen uitgevoerd)

6. Rapporteren (6 weken).

Totaal: 4+2+4+10+8+4=32 weken.

Bibliography

[1] A.C. van den Berg, M.M. van der Voort, J. Weerheijm, and N.H.A. Versloot. Bleve blast by expansion-controlled evaporation. *Process Safety Progress*, 25:44–51, 2005.

[2] J. Mediavilla, J. van Deursen, and J. Weerheijm. Mechanical aspects of the initiation of a bleve. Technical report, TNO Defence, Security and Safety, 2008.

[3] C.M. Wentzel, R.M. van de Kasteele, and F. Soetens. First international conference on damage tolerance of aircraft structures. In R. Benedictus, J. Schijve, R.C. Alderliesten, and J.J. Homan, editors, *Proceedings of the First International Conference on Damage Tolerance of Aircraft Structures*, 2007.

[4] J.L. Medina-Velarde, N. Petrinic, and C. Ruiz. Parametric study of ductile crack propagation in aluminium panels. *Journal de Physique IV*, 10:409–414, 2000.

[5] G. Kay. Failure modeling of titanium 6al-4v and aluminum 2024-t3 with the johnson-cook material model. Technical report, Lawrence Livermore National Laboratory, P.O. Box 808 Livermore, CA 94551, September 2003. DOT/FAA/AR-03/57.

[6] D. Sherman. Macroscopic and microscopic examination of the relationship between crack velocity and path and rayleigh surface wave speed in single crystal silicon. *Journal of the Mechanics and Physics of Solids*, 53(12):2742–2757, December 2005.

[7] D. Hull and P. Beardmore. Velocity of propagation of cleavage cracks in tungsten. *International Journal of Fracture*, 2(2):468–487, June 1966.

[8] M.F. Kanninen, S.J. Hudak, jr., H.R. couque, R.J. Dexter, and P.E. o' Donoghue. Viscoplastic-dynamic crack propagation: Experimental and analysis research for crack arrest applications in engineering structures. *International Journal of Fracture*, 42:239–260, 1990.

[9] M.F. Kanninen. Research in progress on unstable crack propagation in pressure vessels and pipelines. *International Journal of Fracture*, 6(1):94–96, March 1970.

[10] Ludo Van Schepdael and Peter Globevnik. Explosie tankautos fase 1 : inventarisatie tankautos. Technical report, Solico, 2005.

[11] G. T. Hahn, M. Sarrate, M. F. Kanninen, and A. R. Rosenfield. A model for unstable shear crack propagation in pipes containing gas pressure. *International Journal of Fracture*, 9(2):209–222, June 1973.

[12] G. M. McClure, R. J. Eiber, and A. R. Duffy. Investigation of full-scale fracture characteristics of line pipe and correlation with laboratory tests. Phase report, American Gas Association,, March 1963.

[13] G. M. McClure, A. R. Duffy, and R. J. Eiber. Fracture resistance of line pipe. *Journal of Engineering for Industry*, 87B:265, 1965.

[14] A. R. Duffy. Full-scale studies. In *Symposium on Line Pipe Research*, number L30000. American Gas Association, March 1966.

[15] A.R. Duffy, G. M. McClure, R. J. Eiber, and W. A. Maxey. *Fracture Design Practices for Pressure Piping*. Academic Press, 1969.

[16] A. R. Duffy, R. J. Eiber, and W. A. Maxey. Recent work on flaw behavior in pressure vessels,. In *Proceedings of Symposium on Practical Fracture Mechanics for Structured Steel*, Warrington, England, 1969.

[17] G.R. Murtagian, D.H. Johnson, and H.A. Ernst. Dynamic crack propagation in steel line pipes. part i: Experimental investigation. *Engineering Fracture Mechanics*, 72:2519–2534, 2005.

[18] G.R. Murtagian and H.A. Ernst. Dynamic axial crack propagation in steel line pipes. part ii: Theoretical developments. *Engineering Fracture Mechanics*, 72:2535–2548, 2005.

[19] H. Brauer, G. Knauf, and H.G. Hillenbrand. Crack arrestors. In *Procedings of 4th International Conference on Pipeline Technology*. Europipe, May 2004.

[20] G. Demofonti, G. Mannucci, C.M. Spinelly, L. Barantsi, and H.G. Hillenbrand. Large-diameter x100 gas line pipes: Fracture propagnation evaluation by full-scale burst test. Technical report, Europipe, 2000.

[21] J.L. Medina-Velarde, N. Petrinic, and C.Ruiz. Experimental study of fast ductile crack growth in aluminium alloy 2014 panels. *Journal of Strain Analysis*, 36:561–577, 2001.

[22] ASTM International, 100 Barr Harbor Drive, PO Box C700, West Conshohocken, PA 19428-2959, United States. *Standard Test Method for Determining Plane-Strain Crack-Arrest Fracture Toughness, KIa, of Ferritic Steels*, 2006. Designation: E 1221-06.

[23] F. J. Gómez, A. Valiente, and M. Elices. Cohesive modelling of the fracture of a neutron irradiated pressure vessel steel. *Nuclear Engineering and Design*, 219:111–125, 2003.

[24] D.S. Dugdale. Yielding of steel sheets containing slits. *Journal of the Mechanics and Physics of Solids*, 8:100–104, 1960.

[25] G.I. Barenblatt. The mathematical theory of equilibrium cracks in brittle fracture. *Advances in Applied Mechanics*, 7:55–129, 1962.

[26] A. Hillerborg, M. Modeér, and P.E. Petersson. Analysis of crack formation and crack growth in concrete by means of fracture mechanics and finite elements. *Cement and Concrete Research*, 6:773–782, 1976.

[27] V. Tvergaard and J. W. Hutchinson. The relation between crack growth resistance and fracture process parameters in elastic-plastic solids. *Journal of the Mechanics and Physics of Solids*, 40(6):1377–1397, August 1992.

[28] T. Siegmund and W. Brocks. Prediction of the work of separation and implications to modeling. *International Journal of Fracture*, 99(1-2):97–116, August 1999.

[29] A.L. Gurson. Continuum theory of ductile rupture by void nucleation and growth. *International Journal of Engineering Matererial Technology*, 99:2–15, 1977.

[30] H. Yuan, G. Lin, and A. Cornec. Verification of a cohesive zone model for ductile fracture. *Journal of Engineering Materials and Technology*, 118(2):192–201, 1996.

[31] G. Lin, A. Cornec, and H. Schwalbe. Three-dimensional finite element simulation of crack extension in aluminium alloy 2024fc. *Fatigue and Fracture of Engineering Materials and Structures*, 21(10):1159–1173, October 1998.

[32] T. Siegmund and W. Brocks. A numerical study on the correlation between the work of separation and the dissipation rate in ductile fracture. *Engineering Fracture Mechanics*, 67:139–154, 2000.

[33] M. Anvari. *Simulation of dynamic fracture in aluminum structures*. PhD thesis, Norwegian university of science and technology, faculty of engineering science and technology, department of engineering design and materials, 2008.

[34] C. Shet and N. Chandra. Analysis of energy balance when using cohesive zone models to simulate fracture processes. *Journal of Engineering Materials and Technology*, 124(4):440–450, 2002.

[35] A. Turon, C.G. Dávilab, P.P. Camanhoc, and J. Costa. An engineering solution for mesh size effects in the simulation of delamination using cohesive zone models. *Engineering Fracture Mechanics*, 74(10):1665–1682, July 2007.

[36] U. Zerbst, M. Heinimannb, C. D. Donnec, and D. Steglicha. Fracture and damage mechanics modelling of thin-walled structures an overview. *Engineering Fracture Mechanics*, 76:5–43, 2009.

[37] W. Brocks. Ductile crack extension in thin-walled structures six lectures cism course "nonlinear fracture mechanics models". Technical report, GKSS Research Centre, Geesthacht, July 2008.

[38] Brian N. Coxa, Huajian Gaob, Dietmar Grossc, and Daniel Rittel. Review: Modern topics and challenges in dynamic fracture. *Journal of the Mechanics and Physics of solids*, 53:565–596, 2005.

[39] T. Siegmund and A. Needleman. A numerical study of dynamic crack growth in elastic-viscoplastic solids. *International Journal of Solids and Structures*, 34(7):769–787, March 1997.

[40] A. Needleman. An analysis of decohesion along an imperfect interface. *International Journal of Fracture*, 42:21–40, 1990.

[41] Xi Zhang, Yiu-Wing Mai, and Rob G. Jeffrey. A cohesive plastic and damage zone model for dynamic crack growth in rate-dependent materials. *International Journal of Solids and Structures*, 40:5819–5837, 2003.

[42] M. Falk, A. Needleman, and J. Rice. A critical evaluation of dynamic fracture simulations using cohesive surfaces. In *proceedings of the 5 th European Mechanics of Materials Conference*, 2001.

[43] I. Scheider and W. Brocks. The effect of the traction separation law on the results of cohesive zone crack propagation analyses. *Key Engineering Materials*, 251-252:313–318, 2003.

[44] Alfred Cornec, Ingo Scheider, and Karl-Heinz Schwalbe. On the practical application of the cohesive model. *Engineering Fracture Mechanics*, 70:1963–1987, 2003.

[45] A. Needleman. A continuum model for void nucleation by inclusion debonding. *Journal Of Applied Mechanics, Transactions of the ASME*, 54:525–531, 1987.

[46] Ingo Scheider. Cohesive model for crack propagation analyses of structures with elasticplastic material behavior. foundations and implementation. Technical Report internal report no. WMS/2000/19, GKSS Research Centre, Geesthacht, Dept. WMS, April 2001.

[47] B.C. Simonsen and R. Tornqvist. Experimental and numerical modelling of ductile crack propagation in large-scale shell structures. , 2004. 17(1): p. 1-27. *Marine Structures*, 17(1):1–27, 2004.

[48] H.S. Alsos. A comparative study on shell element deletion and element splitting. Technical report, Norwegian University of Science and Technology., 2004.

[49] Ted Belytschko, Hao Chen, Jingxiao Xuand, and Goangseup. Dynamic crack propagation based on loss of hyperbolicity and a new discontinuous enrichment. *International journal for numerical methods in engineering*, 58:1873–1905, 2003.

[50] N. Möes, J. Dolbow, and T. Belytschko. A finite element method for crack growth without remeshing. *International Journal for Numerical Methods in Engineering*, 46(1):131–150, 1999.

[51] R. de Borst. Some recent issues in computational failure mechanics. *International Journal of Numerical Methods in Engineering*, 52:63–95, 2001.

[52] J. Mediavilla. Dynamic crack propagation tests on sudden centred crack prestressed panels. Technical report, TNO Defence, Security and Safety, 2008.

[53] Sushovan Roychowdhury, Yamuna Das, Arun Roy, Robert H, and Dodds. Ductile tearing in thin aluminum panels: experiments and analyses using large-displacement, 3-d surface cohesive elements. *Engineering Fracture Mechanics*, 69:983–1002, 2002.

[54] W. Brocks and Th. Siegmund. Effects of geometry and material on the energy dissipation rate. In M. Fuentes, M. Elices, A. Martn Meizoso, and J. M. Martnez-Esnaola, editors, *Fracture Mechanics: Applications and Challenges : Invited Papers Presented at the 13th European Conference on Fracture*, San Sebastian, September 2000. ECF, Elsevier.

[55] T.J. de Vries and C.A.J.R. Vermeeren. R-curve testdata: 2024-t3, 7075-t6, glare 2 and glare 3. Technical report, TU-Delft, 1995. LR M-705.

[56] E. Erauzkin and A. M. Irisarri. Influence of microstructure on the fracture toughness and fracture topography of a duplex stainless steel. *Fatigue & Fracture of Engineering Materials & Structures*, 15(2):129–137, 1991.

[57] Henrik Sieurin, Rolf Sandström, and Elin Westin. Fracture toughness of the lean duplex stainless steel ldx 2101. *Metallurgical and Materials Transactions*, 37(10):2975–2981, October 2006.

[58] US Army Corps of Engineers, Washington, DC 20314-1000. *Engineering and Design - Inspection, Evaluation and Repair of Hydraulic Steel Structures*, December 2001. EM 1110-2-6054.

[59] Livermore software technology corporation (LSTC), Livermore Software Technology Corporation P.O. Box 712, Livermore, California 94551-0712. *Ls-dyna keyword user's manual*, 971 edition, May 2007.

[60] John O. Hallquist. *LS-DYNA theory manual.* Livermore Software Technology Corporation, 7374 Las Positas Road, Livermore, California 94551, March 2006.

[61] M. Anvari, I. Scheider, and C. Thaulow. Simulation of dynamic ductile crack growth using strain-rate and triaxiality-dependent cohesive elements. *Engineering Fracture Mechanics*, 73:2210–2228, 2006.

[62] Alberto Corigliano and Michele Ricci. Rate-dependent interface models: formulation and numerical applications. *International Journal of Solids and Structures*, 38(4):547–576, January 2001.

[63] Chongchen Xu, Thomas Siegmund, and Karthik Ramani. A bilinear cohesive zone model tailored for fracture of asphalt concrete considering viscoelastic bulk material. *International Journal of Adhesion and Adhesives*, 23(1):9–13, 2003.

[64] Kenneth M. Liechti and Jeng-Dah Wu. Mixed-mode, time-dependent rubber/metal debonding. *Journal of the Mechanics and Physics of Solids*, 49(5):1039–1072, May 2001.

[65] P. Rahul-Kumar, A. Jagota, S. J. Bennison, S. Saigal, and S. Muralidhar. Polymer interfacial fracture simulations using cohesive elements. *Acta Materialia*, 47(15-16):4161–4169, November 1999.

[66] M. Fagerström and R. Larsson. Approaches to dynamic fracture modelling at finite deformations. *Journal of the Mechanics and Physics of Solids*, 56(2):613–639, February 2007.

[67] P. Perzyna. Fundamental problems in viscoplasticity. In G. Chernyi, W. Olszak, H. Dryden, W. Prager, P. Germain, R. Probstein, L Howarth, and H. Ziegler, editors, *Advances in applied mechanics*, volume 9, pages 243–377, Warsaw, Poland, May 1966. Institute of basic technical research, Polish academy of sciences, Academic Press Inc. Library of Congress Catalog Card Number: 48-8503.

[68] R. Mises. Mechanik der festen körper im plastisch deformablen zustand. *Nachrichten von der Gesellschaft der Wissenschaten zu Göttingen, Mathematisch-Physikalische Klasse*, 1:582–592, 1913.

[69] J.L. Chaboche. On the constitutive equations of materials under monotonic or cyclic loadings. *la recherche aerospatiale*, 5(September-October):363–375, 1983.

[70] R. Hill. A theory of the yielding and plastic flow of anisotropic metals. *Proceedings of the Royal Society of London. Series A, Mathematical and Physical Sciences*, 193(1033):281–297, May 1948.

[71] X. Xu and A. Needleman. Numerical simulations of dynamic crack growth along an interface. *International Journal of Fracture*, 74(4):289–324, December 1996.

[72] Z. Zhang and G. Paulino. Cohesive zone modeling of dynamic failure in homogeneous and functionally graded materials. *International Journal of Plasticity*, 21:1195–1254, 2005.

[73] Ted Belytschko, B. Moran, W. K. Liu, Wing Kam Liu, and Brian Moran. *Nonlinear Finite Elements for Continua and Structures.* John Wiley & Sons Inc, September 2000.

[74] R. Courant, K. Friedrichs, and H. Lewy. über die partiellen differenzengleichungen der mathematischen physik. *Mathematische Annalen*, 100(1):32–74, 1928.

[75] M. L. Benzeggagh and M. Kenane. Measurement of mixed-mode delamination fracture toughness of unidirectional glass/epoxy composites with mixed-mode bending apparatus. *Composites Science and Technology*, 56(4):439–449, 1996.

[76] W.M. Johnston. Fracture tests on thin sheet 2024-t3 aliminum alloy for specimens with and without ant-buckling guides. Technical Report NASA/CR-2001-210832, Analytical Services an Materials Inc. ,Hampton, Virginia, March 2001.

[77] R. De Borst and P. H. Feenstra. Studies in anisotropic plasticity with reference to the hill criterion. *International Journal for Numerical Methods in Engineering*, 29(2):315 – 336, 1990.

[78] R.J.H. Wanhill. Damage tollerant engineering property evaluations of aerospace aluminium alloys with emphasis on fatique crack growth. Technical report, National Aerospace laboratory NLR, 1994.

[79] M. Janssen, J. Zuidema, and R.J.H. Wanhill. *Fracture Mechanics*. VSSD, 2002.

[80] R.M.M. van Wees. Vulcan, blast load on cylinder. Technical report, TNO Defence, Security and Safety, 2008.

[81] O.R. van der Meulen, J. Mediavilla Varas, J. Weerheijm, and F. Soetens. Cohesive modeling of ductile dynamic failure of pressurized metallic structures. In *proceedings of 12th International Conference on Fracture (ICF 12)*, Building M-19, 1200 Montreal Road Ottawa, ON K1A 0R6 Canada, July 2008. National Research Council Canada.

[82] Jesus Mediavilla, Jaap Weerheijm, Ronald van der Meulen, F. Soetens, C. Wentze, and J. van Deursen. Dynamic crack propagation: an experimental-numerical approach. In J. Pokluda, P. Lukáš, P. Sandera, and I. DLouhý, editors, *17th European Conference on Fracture. Book of Abstracts and Proceedings on CD ROM*, pages 2039–2046, 2008.

[83] ASTM International, 100 Barr Harbor Drive, PO Box C700, West Conshohocken, PA, 19428-2959 USA. *E23 Standard Test Methods for Notched Bar Impact Testing of Metallic Materials*, 1 edition, 2007.

[84] P. R. Sreenivasan, A. Moitra, and S. L. Mannan. Novel charpy-fracture toughness correlations for predicting reference temperature and master curve. In *Proceedings of the 11th nternational conference on fracture*. CCI Centro Congressi Internazionale s.r.l., March 2005.

[85] R. Roberts and C. Newton. Report on small-scale test correlations with kic data. *Welding research council bulletin*, 2(265):1–18, February 1981.

[86] J.M. Barsom and S.T. Rolfe. *Fracture and fatigue control in structures*. Prentice-Hall inc, Englewood cliffs, 2 edition, 1987.

[87] Y.J. Chao, J.D. Ward, and R.G. Sandsa. Charpy impact energy, fracture toughness and ductile-brittle transition temperature of dual-phase 590 steel. *Materials & Design*, 28(2):551–557, 2007.

[88] G.W. Wellman and S.T. Rolfe. Engineering aspects of ctod fracture toughness testing. *WRC Bulletin*, 299:1–36, November 1984.

[89] R.J.H. Wanhill, L. Schra, and W.G.J 't Hart. Modern aluminium sheet alloys for aerospace applications. Technical report, National Aerospace laboratory NLR, 1992. NLR TP 92057 L.

[90] Davis. *Aluminum and Aluminum Alloys (ASM Specialty Handbook).* ASM International, 1993. isbn:087170496X.

[91] V. Muthupandia, P. Bala Srinivasana, V. Shankarb, S.K. Seshadric, and S. Sundaresanc. Effect of nickel and nitrogen addition on the microstructure and mechanical properties of power beam processed duplex stainless steel (uns 31803) weld metals. *Materials Letters*, 59(18):2305–2309, August 2005.

[92] Böhler. *Böhler A903 extra stainless duplex steel product guide*, 2008.

[93] AvestaPolarit. *Duplex Stainless Steel SAF 2304, 2205, SAF 2507 product quide*, 2008.

[94] F. Wischnowskii and A. Kuhn. Stainless steel alloys strengthen critical centrifuge components. *Filtration and Separation*, 39(9):36–38, November 2002.

[95] G. R. Johnson and W. H. Cook. Fracture characteristics of three metals subjected to various strains, strain rates, temperatures and pressures. *Engineering Fracture Mechanics*, 21(1):31–48, 1985.

[96] Donald Lesuer. Experimental investigationsof material models for ti-6al-4v titanium and 2024-t3 aluminum. Technical report, U.S. Department of Transportation, Federal Aviation Administration, september 2000.

[97] American Petroleum Institute, 1220 L Street, NW Washington, DC 20005-4070 USA. *Specification for Line Pipe*, 44 edition, October 2007. ANSI/API Spec 5L / ISO 3183.

[98] Clive G. Page. *Professional Programmers Guide to Fortran77.* University of Leicester, UK, June 2005.